GRAPHENE RESONATORS FOR MASS SENSING APPLICATIONS

By

Fadoo George UNOM

Thesis submitted to the Faculty of Science, Agriculture and Engineering (SAgE) for the degree of Doctor of Philosophy (PhD)

School of Engineering

Newcastle University, United Kingdom

December 25, 2020

Abstract

Graphene's exceptional physical and mechanical properties make it an excellent nanomaterial for MEMS/NEMS devices with wide reaching applications. This thesis explores graphene as a nanomaterial, its use in mass sensing applications and the suitability of existing theoretical models to describe its behaviour as a rectangular resonator. Several local and nonlocal continuum models have been proposed in literature for the vibration analysis of graphene resonators. But with very little experimental data to validate these theoretical models, most of the solutions employed to solve these models compare their results with results from other theoretical models, leading to doubts about their validity and accuracy. In addition to providing a guide for determining the suitable theoretical model for different sized rectangular graphene resonators, this work establishes that a small-scale parameter e_0a of any value between 0 and 2 needs to be incorporated in any local continuum modelled applied to micro-sized graphene sheets to avoid overestimation of the frequency of the sheets. A fabrication route for NEMS and MEMS devices with rectangular graphene resonators up to 32 μm by 7 μm is also developed with the provision for magnetomotive actuation via Lorentz force with possible capacitive readout capabilities. This is important as the use of graphene in MEMS/NEMS is being hurriedly transitioned from the Research space to the marketplace.

Dedication

I dedicate this work to my Lord Jesus Christ, to whom my life belongs and for whom I live.

Acknowledgements

Table of Contents

List of Publications

Unom, F.G., 2022. Theoretical models for the vibrational analyses of micro- and nano-sized graphene sheets. (*Under preparation - to be submitted soon*).

Unom, F.G., Hedley, J. Graphene resonators for mass sensing applications. (*Under preparation.*)

List of Tables

List of Figures

Chapter 1: Introduction

1.1   Background and motivation

In recent times, biosensor technologies have become widely applicable in health diagnostics, biochemical analyses, environmental monitoring, forensics, and food quality control. A boost in the development of a variety of Point of Care (POC) diagnostic devices in the past decade is an indication of the increased interest in biosensor technologies, especially for clinical analysis and diagnosis of diseases, with the integration of molecular diagnostics with POC testing being the fastest growing area[2]. Biosensors, as reported in literature, are classified based on either the device's transduction method, for example as electrochemical, mechanical, piezoelectric, optical or calorimetric biosensors[3]; or the type of bio-recognition element used, for example as enzyme, immuno-, nucleic acid probe sensors, or as cell-, tissue- or organelle-based sensors[4]. These devices have been used for the detection and quantification of various biomolecules of clinical interest, including; prostate specific antigen (PSA)[5-7], carcinoembryonic antigen (CEA)[7, 8], glucose[9, 10], Hepatitis B surface antigen (HBsAg)[11, 12], and Cardiac troponin T & I[13, 14], among others. Critical to the success of any biosensor are issues bordering around the intrinsic device performance as well as the performance of the overall system. These issues include; the complexity of their fabrication and system integration, ease of biofunctionalization and potential for multiplexing, the balance between sensitivity and the frequency of false positives, device robustness, shelf life and adaptability for mass production[15].

As biosensor devices scale down in physical size, the prospects of improving the intrinsic device performance scale up. Recent advances in micro- and nanofabrication technologies have greatly aided the development of micro- and nanoelectromechanical biosensors with nano-sized moving parts. The exploitation of nanomaterials in the development of these technologies provides a path towards achieving rapid and accurate results, higher sensitivities, portability, ease of use, and affordability; and the possibility of simultaneous multiplex detection of biomolecules/biomarkers. Gold nanoparticles, magnetic nanoparticles, carbon nanotubes and graphene lead the chart of nanomaterials being used in biosensor technologies today. Graphene's emergence as a nanomaterial[16], opened up a whole new world of possibilities in the use of

nanomaterials in biosensors, because of its exceptional physical, electrical, chemical and mechanical properties. However, these exciting properties are greatly inhibited by the presence of strong impurity, and other factors such as, interactions with the underlying substrates used to support it, especially SiO_2, surface charge traps, interfacial phonons, substrate stabilized ripples, and fabrication residues on or under the graphene sheet[17-19].

Synthesis of graphene by mechanical exfoliation so far yields the best graphene quality there is. This technique, which was first used to isolate graphene in 2004, involves peeling off fragments from highly-ordered pyrolytic graphite (HOPG) repeatedly until graphene is isolated[16]. Though simple and straightforward, the technique requires utmost care where monolayer graphene is to be produced and is unsuitable for high throughput and large volume fabrication of graphene. Currently, graphene is mostly produced commercially by Chemical Vapour Deposition (CVD), which yields a relatively high quality of graphene, and involves growing large scale graphene films by passing a hydrocarbon gas over a metallic substrate (usually Ni or Cu) heated to about 1000 ^0C[20, 21]. Other methods used in the production of graphene include; reduction of graphene oxide[22], the epitaxial growth of graphene on heated silicon carbide[23], and the chemical synthesis from reactive precursor compounds[24].

Since its debut as a nanomaterial, graphene and its derivatives have been used in the design of a number of micro- and nanoelectromechanical systems (MEMS/NEMS) devices, including cantilever beams for nano switches[25], FETs that detect pH and protein adsorption[26], radio frequency switches[27], pressure sensors[28], hall sensors[29], gas detectors[30-34], DNA sequencers/biosensors[35-38], and sensors that detect biomarkers employed for various diseases[39-43]. Owing to its exceptional mechanical properties and low mass density, graphene promises to be an excellent material for resonance-based NEMS devices used for mass and force sensing. In current mass and force sensing technology, the accreted mass of the target biomolecule represents only a small portion of the effective mass of the system. With graphene's low mass density, and the possibility of nanoscale sizing, the accreted biological mass significantly contributes to the effective system mass, and presents the possibility of achieving attogram sensitivity.

1.2   Aim

This project will aim to utilise the unique mechanical properties of graphene towards the development of ultra-sensitive mass biosensors.

1.3   Objectives

The project is defined by three (3) key objectives;

- Determine appropriate fabrication routes for the manufacture of rectangular graphene resonators.
- Establish analytical and/or numerical methods for the vibration analysis of graphene micro-resonators.
- Fabricate, characterise and calibrate rectangular graphene micro-resonators to ensure fitness of use in mass sensing applications.

1.4   Outline of thesis

Chapter 1 provides the background and motivation for the work and outlines the objectives the study aims to achieve. Chapter 2 presents a survey of the relevant literature related to graphene, graphene-based devices and nanoelectromechanical devices. The mathematical and numerical models that represent the vibration of rectangular suspended structures are developed and presented in Chapter 3, whilst Chapter 4 presents the FEA modal analysis of rectangular graphene resonators. Chapter 5 details the work done in the design and fabrication of the graphene resonators and the mass sensing platform used in this study. Whilst in Chapter 6, the techniques used in characterizing the various aspects of the fabricated sensor are presented. Finally, Chapter 7 hosts general discussions and overview of the study, along with suggestions for future work and the conclusion.

Chapter 2: Literature Survey

2.1   Introduction

This section explores relevant literature on graphene as a nanomaterial and its modification and/or manipulation for use in biosensor applications. Graphene is first presented as a nanomaterial with discussions focusing on its lattice structure and phonon dispersion. Then some characterization techniques for graphene layers ranging from monolayer graphene up to few-layer graphene are presented. A few techniques for achieving free-standing graphene structures are explored with emphasis on transfer of CVD grown graphene onto pre-patterned substrates. Finally, some actuation and detection methods used in nanoelectromechanical (NEMS) systems are discussed.

2.2   Biosensor technologies

Thévenot et al.[3] adopting the International Union of Pure and Applied Chemistry (IUPAC) definition of an electrochemical biosensor, define a biosensor as "an integrated receptor-transducer device, which is capable of providing selective quantitative or semi-quantitative analytical information using a biological recognition element" retained in direct spatial contact with the transduction element. Simply put, biosensors measure the physicochemical changes that occur in a biological recognition layer attached to a solid transducer when it interacts with the targeted biomolecules called the target analyte. Biosensors should be clearly distinguished from bioanalytical systems, which require additional processing steps, such as reagent addition, or additional hardware.

Biosensors are generically divided into 2 parts: a biological recognition system and a transduction system (Figure 2-1). The biological recognition system interacts directly with the test sample, and its main purpose is to identify or interact selectively with the analyte of interest. It converts information from the biochemical domain into a chemical or physical output signal by the changes in its physicochemical properties. The transduction system converts the output of the biological recognition system mostly to the electrical domain. Usually, a read-out system or user interface is named as a third part of biosensors or as an indispensable addendum. This system converts the electrical signal from the transducer into analytical data, which is appropriately displayed.
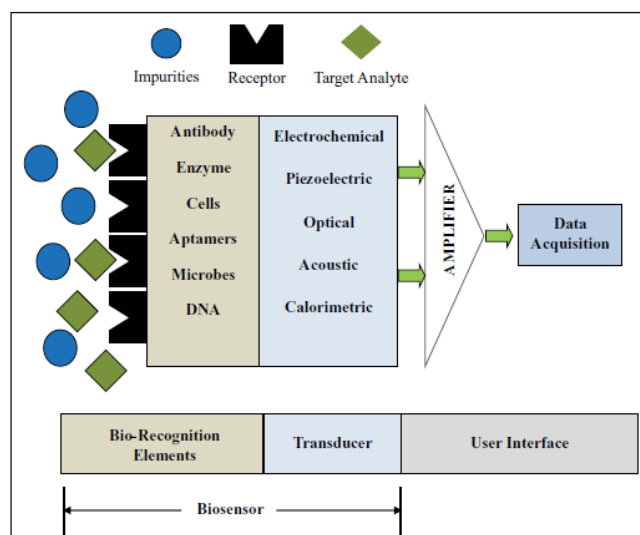
Figure 2-1: Schematic representation of a biosensor[4]

There are many different criteria used to categorize biosensors, viz.: size, transducer type, type of bio-recognition element, possibility of re-use, or the type of analytes or reactions they monitor. Most commonly, biosensors are broadly categorized based on their transducer type or type of bio-recognition element. Based on the transducer type, biosensors can be classified as electrochemical, mass sensitive (piezoelectric), optical and calorimetric (thermal) biosensors[44]. Based on the type of bio-recognition element, biosensors can broadly be classified as affinity-based or catalytic biosensors. The former includes immunosensors (antibody-based sensors), nucleic acid probe sensors, or biosensors based on molecularly imprinted polymers; the latter includes enzyme sensors, or cell-, tissue- or organelle-based biosensors[45].

2.2.1 Electrochemical Biosensors

Electrochemical biosensors are biosensors that employ electrochemical transduction methods in the detection or quantification of the analyte of interest. Their principle of detection is based on the changes in the electrical properties of the transducer element as it interacts with the analyte of interest via the biological recognition element. These changes are expected to be proportional to the concentration of the analyte and are interpreted by the calibrated read-out system to indicate the presence or the amount of the analyte. Based on the electrical properties being measured, electrochemical biosensors can be classified into amperometric, potentiometric, and impedimetric or conductomeric biosensors.

Amperometric Biosensors

Amperometric biosensors measure the change in electrical current resulting from the oxidation or reduction of an electroactive species. This is achieved by maintaining the potential of a working electrode at a fixed value relative to a reference electrode and monitoring the current flow as a function of time. The applied potential drives the electron transfer reaction of the electroactive species with the resulting current indicating the rate of the recognition reaction and is therefore proportional to the concentration of the target analyte. The working electrode used is critical to the success and sensitivity of the biosensor; working electrodes have a variety of shapes, for example, disk, fibre, microband, arrays, and interdigitated microbands[44], and some of the materials commonly used include, glassy carbon, carbon paste, platinum and gold[46]. Amperometric biosensors have been used to measure glucose, sialic acid; and detect *Bacillus cereus* and *Mycobacterium smegmatis*[47], and hepatitis B surface antibody (HBsAb)[12], among others.

Potentiometric Biosensors

The principle of detection of potentiometric biosensors is based on the difference in potential caused by the accumulation of ions resulting from an enzyme reaction between two electrodes of an electrochemical cell, with no significant current flowing between them. In most cases, the first electrode is a reference electrode whose potential is known and maintained at a constant value and is made insensitive to the target analyte. While the second electrode is an indicator electrode, whose potential is dependent on the concentration of the target analyte, as it rapidly responds to changes in the activity of the target analyte ions. The potential difference between these two electrodes is proportional to the logarithm of the analyte ion activity[44] or gas fugacity[3]. In other cases, both electrodes are reference electrodes separated by an ion-selective membrane, and they measure the difference in potential across the membrane. The electrodes used in potentiometric biosensors are either ion-selective electrodes (ISEs) or field-effect transistors (FETs) modified with layers containing ionophores to become ion-selective field-effect transistors (ISFETs). ISFETs could have layers modified by enzymes and are called enzyme field-effect transistors (ENFETs), or antibodies which would then be called immunological field-effect transistors (IMFETs). Examples of potentiometric biosensors include a

potentiometric sensor array for investigating the cytotoxicity of hydroquinone to cultured mammalian V79 cells[48], and a creatinine-sensitive pH-ISFET[49].

Impedimetric biosensors

Impedimetric biosensors are based on the change in the resistive/conductive or capacitive properties of the sensing element in response to a small amplitude sinusoidal excitation signal. They detect the change in impedance or conductance of electrodes caused by the adsorption of the target analyte by receptors immobilized on the electrode surface. Guan et al.[50] in their review of impedimetric biosensors, discussed these biosensors in groups categorized by the type of bio-recognition element used. Some examples of impedimetric biosensors from their review include: an enzyme based impedimetric biosensor for the detection of collagenase; an immune-binding based impedimetric biosensor for human mammary tumour associated glycoprotein; a nucleic acid-based impedimetric biosensor for the monitoring of the hybridization reaction of a hepatitis B virus DNA; and a cell- and microorganism-based impedimetric biosensor for the detection of microorganisms in milk and dairy products.

2.2.2 Optical Biosensors

In optical biosensors, the principle of detection is based on changes in the optical characteristics (mostly optical absorption, reflection or luminescence) of the sensing element as a result of the presence of the target analyte. There are two main categories of optical biosensors: those that exploit the changes in the intrinsic optical properties of the bio-recognition element called label-free optical biosensors, and those that employ optical labels and probes of various kinds whose optical properties change as the bio-recognition element interacts with the target analyte. Optical biosensors can be grouped further into surface plasmon resonance (SPR), fluorescence, luminescence, absorption and reflection, and optical fibre biosensors; with SPR and fluorescence optical sensors being the most popular of the cohort. In SPR biosensors, a light wave excites a special mode of electromagnetic field or evanescent field and generates a surface plasma wave, which propagates along a thin metal film, between the film and a semi-infinite dielectric. A change in the refractive index in the vicinity of the metal surface due to bio-specific interactions occurring there results in a change in the velocity of the surface plasmon[51]. This change in velocity is detected by an

optical reader, usually by the variations in the intensity of a light wave reflected from the back of the metal film. The change in intensity of the reflected light wave, velocity of the surface plasmon wave or refractive index of the sensing surface is proportional to the mass of the target analyte adsorbed by the bio-recognition element. SPR biosensors for detecting cardiac troponin T[13] and β-galactosidase[52], among others have been reported. Fluorescence biosensors employ fluorescent labels or probes for signal generation; the parameters that are usually measured include the intensity, decay time, anisotropy, quenching efficiency, and luminescence energy transfer of the signal.

2.2.3 Calorimetric Biosensors

Calorimetric biosensors are designed to measure the heat of the biochemical reaction between the target analyte and the bio-recognition molecules on the sensing surface. Many enzyme reactions with oxidases or hydrolytic enzymes result in significant enthalpy changes. These enthalpy changes are utilized in the detection or quantification of analytes. Calorimetric biosensors consist basically of temperature sensors (mostly thermistors) with bio-recognition molecules immobilized on them. The heat of the biochemical reaction, which is proportional to the molar enthalpy and the total number of molecules in the reaction[4], is absorbed by the temperature sensor and results in a corresponding change in its temperature; and in the case of thermistors, the electrical resistance. The change in temperature, and consequently the resistance of the thermistor, is thus proportional to the analyte concentration. A major disadvantage with calorimetric biosensors is that all enthalpy changes, including those not initiated by the target biochemical reaction, contribute to the final output of the measurement process. The use of calorimetry in the analysis of food and cosmetics has been demonstrated by Antonelli et al.[53] in the determination of L-malic acid concentration in some foods and cosmetic products. The concentration of ascorbic acid (vitamin C) has also been determined using calorimetric biosensors[54].

2.2.4 Mass Sensitive Biosensors

Mass sensitive biosensors encompass the family of mechanical systems (macro-, micro- and nanomechanical systems) that are capable of detecting the forces, motion, mechanical properties and masses that result from the biological

interactions between target analytes and bio-recognition systems. Mass sensitive biosensors can be broadly grouped into surface-stress biosensors and dynamic-mode sensors. Surface-stress biosensors are based on the surface stress developed when the target biomolecules bind to the biorecognition molecules immobilized on the transducer surface, while dynamic-mode biosensors are based on the change in resonance frequency of the transducer when the target biomolecules bind.

Surface-stress Biosensors

Surface-stress biosensors measure the quasistatic deflection of the transducer, usually a cantilever, caused by the binding of the target analyte to the bio-recognition molecules immobilized on the surface of the transducer. Due to electrostatic repulsion or attraction, steric interactions, hydration and entropic effects involved in the binding event[15], surface stress is developed which induces a deflection in the cantilever. The surface stress developed could either be positive or negative; when negative, it is referred to as compressive surface stress and induces surface expansion; when positive, it is referred to as tensile surface stress and induces surface contraction. Only one side of the cantilever surface is immobilized with the recognition molecules and is called the active side. The opposite side, called the passive side, must be made inert to the target biomolecule, and possibly blocked to avoid non-specific binding. The biological recognition event generates small amounts of surface stress, usually between $0.001 - 0.01$ Nm^{-1}, which give rise to deflections measuring from a few nanometers to tens of nanometers. These deflections can be measured optically by reflecting a laser beam off the cantilever or electrically by employing piezoresistive detection methods. Optical detection methods are bulky but leave room for flexibility in the fabrication of the biosensors. With electrical methods, on the other hand, miniaturization of the device becomes achievable, though the complexities in fabrication are higher, with the imposition of major restrictions on the size, geometry and materials of the sensors. In operational modes, minute changes in refractive index, temperature and fluidic disturbances could cause false deflections in the cantilevers. These can be circumvented by employing differential measurements between cantilevers that have been functionalized and those that have been passivated, such that both sets are susceptible to the false

deflections, but only the functionalized cantilever deflects due to the binding of the target biomolecule.

Dynamic-mode Biosensors

Dynamic-mode biosensors are based on the shift in resonance frequency of a resonator when its mass changes. The biosensor transducer or resonator is made to oscillate at a resonance frequency, and this frequency changes as the target biomolecules bind to the biorecognition molecules. Key to the success of dynamic-mode biosensors is the type of resonator used. Janshoff et al.[55] describes four major classes of piezoelectric resonators used in dynamic-mode sensors, based on their shapes and the propagation mode of the acoustic wave excited in them, viz. Thickness-Shear-Mode (TSM), Flexural-Plate-Wave (FPW), Surface-Acoustic-Wave (SAW), and Shear-Horizontal-Acoustic-Plate-Mode (SH-APM) resonators (Figure 2-2).
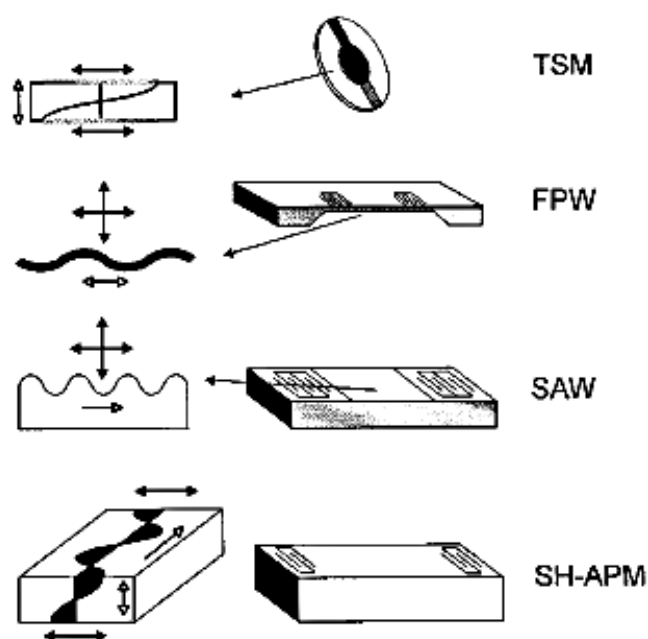
Figure 2-2: Schematic sketches of the four types of acoustic resonators (particle displacement - black arrow; wave propagation direction - open arrow)[55]

Thickness-Shear-Mode (TSM) resonators or Quartz-Crystal Microbalances (QCM) are one of the most established techniques used in piezoelectric biosensors[56]. QCM devices consist of a thin disk of single piezoelectric quartz crystal, cut at an angle of 35.25^0 from the mother crystal (AT-cut)[55]. Metal electrodes deposited on each side of the disk, excite it to oscillate in shear mode.

Resonance is achieved when a sufficient AC voltage with a frequency close to the resonance frequency of the crystal is applied to the electrodes. Adsorption of a thin layer of the target analyte onto the crystal surface, changes its mass and consequently its resonance frequency. Typical QCMs have resonance frequencies in the order of MHz, which vary with the thickness of the crystal; the thinner the crystal, the higher the resonance frequency. Crystals with resonance frequencies of 5 MHz have corresponding thicknesses of ~330 μm[56]. QCM biosensors have been used to detect *Bacillus anthracis*[57], *Pseudomonas aeruginosa*[58], human α-thrombin protein[59], and measure Immunoglobulin E (IgE) in human serum[60], among others.

SAW devices operate based on the Rayleigh wave propagation principle at solid thin-film boundaries. Rayleigh waves are surface-confined acoustic waves, resulting from the stress-free boundary of a solid, that propagate as coupled longitudinal and transversal waves. SAW devices generate and detect these waves using two interdigital transducers (IDTs) deposited on the surface of a piezoelectric crystal, one of which functions as the transmitter and the other as the receiver. This helps strongly confine the acoustic energy at the surface of the crystal in the range of the wavelength, irrespective of the thickness of the complete substrate[61]. Due to the confinement of the wave to the surface of the crystal, changes on the crystal surface, such as mass loading, viscosity and conductivity changes easily affect the wave. Frequencies of SAW resonators usually range from ~50 MHz to a few GHz[62]. SAW biosensors for detection of hepatocyte growth factor/scatter factor in serum[63], *Escherichia coli*[64], and for detecting antigen-antibody reactions[65] have been reported.

In APM devices, the acoustic wave is confined by multiple reflections between the upper and lower surfaces of the crystal, as it propagates between the transmitter and the receiver. Shear-Horizontal APM resonators are driven by horizontal shear waves to reduce their attenuation in liquid; the particles of the plate exhibit displacement components that are parallel to the surfaces and direction of propagation of the wave. Particle displacements that are perpendicular to the surfaces and direction of propagation interact more with the environment, leading to a higher loss of acoustic energy. APM devices for detecting antigen-antibody reactions[66] have been reported.

FPW resonators are thin, rectangular membranes or plates which are only a few micrometres thick, most commonly made of silicon nitride embedded in a frame of silicon. These resonators can be excited by IDTs, electrostatically or by using magnetic transducers. When excited, a series of symmetric and antisymmetric plate waves can be generated, called Lamb waves. The velocity of which depends on the material of the plate and its thickness. With sufficiently thin plates, only the lowest modes of these two plate waves occur, with the phase velocity of the antisymmetric wave decreasing as the plate thickness decreases. This translates to FPW sensors having comparatively low resonance frequencies, in the range of 5 – 20 MHz[67], an attractive feature for designing associated electronics. FPW biosensors have been used for the detection of human Immunoglobulin E antigen[68] and *Escherichia coli*[69] have been reported.

In recent times, microcantilevers, and their slightly less popular doubly-clamped beam counterpart, have increasingly become central in dynamic mode biosensing. This is due to the high sensitivity, fast response and versatility of application they offer. Advancements in micro- and nanofabrication technologies have enabled the fabrication of these structures up to nanoscales, giving rise to the proliferation of micro- and nanomechanical biosensors with micron- or nanoscale cantilevers and doubly-clamped beams as resonators.

To achieve ultrahigh mass sensitivity, two factors are important: the dimensions of the resonator and its quality factor, Q. Resonators with high resonance frequencies are highly sought after in the quest to achieve higher sensor sensitivities. Achieving these frequencies with micron-scale resonators is only possible with foreshortened aspect ratios (l/w or l/t) of order unity. But with such aspect ratios, very high dynamic stiffnesses or spring constants are developed which could adversely affect: the attainable dynamic range, the ability to tune the devices with applied mechanical forces, the attainment of the highest quality factor, and the excitation levels required to induce nonlinear response from the resonator[70]. To optimize these characteristics, large aspect ratio resonators (achieved by reducing all dimensions to nanoscale) need to be used. As mentioned earlier, advances in micro- and nanofabrication technologies and techniques have made the fabrication of nanoscale structures relatively easy. Thus, achieving and maintaining a high Q becomes the major performance

limiting factor in many applications. Because biological interactions and processes occur in fluids, operating biosensors in situ, within the fluid, is simpler and immediate. However, Q is reduced due to viscous damping and consequently, the device sensitivity and mass resolution are adversely affected. Other sources of energy dissipation and reduction of Q include: clamping losses at the resonator supports and coupling losses mediated through the transducers[70]. To tackle the Q reduction problem, some detection techniques operate biosensors ex situ; with measurements taken in air or vacuum. In most of these methods, the detector is removed from the fluid, desiccated before measurements are taken in the desired media. The major limitation with this approach is that the sensor is highly susceptible to non-specific binding and contamination during and after the desiccation process. However, measurements in vacuum have achieved exquisite mass resolutions; attogram, zeptogram and yoctogram mass resolutions have been reported[71-75]. Some novel techniques for tackling the Q reduction problem include suspended microchannel resonators (SMRs) and micropillar resonators. In SMRs, the sample aliquot is constrained in microchannels embedded in the cantilevers. The inside walls of the microchannels are functionalized to specifically interact with the target analyte. Antibody-antigen reactions with a sensitivity of 100 ng mL^{-1} has been reported[76].

2.3   Graphene

Graphene is a thermodynamically stable 2D crystal with an exceptionally high crystal and electronic quality[77]. It consists of a hexagonal network of sp^2-hybridized carbon atoms held together by strong covalent bonds in a single layer. Each carbon atom forms three strong sigma-(σ) covalent bonds with three neighbouring carbon atoms in the basal plane. The covalent bonds are formed with the 3 electrons in the sp^2 hybrid orbital, the fourth valence electron located in the P_z orbital forms a pi-(π) bond with the neighbouring atoms. This π electron is delocalized and can move freely between all the bonded atoms.

Graphene has been called the mother of all graphitic forms[78], as it can be wrapped up to form 0-dimensional (0D) fullerenes, rolled into one-dimensional (1D) nanotubes or stacked up in layers to form three-dimensional (3D) graphite. The layers of graphene in graphite are weakly bond to each other by van der Waals forces with a lattice spacing of $c = 6.71\text{Å}$ between the layers[79]; two layer

stacking configurations are possible: ABAB also called Bernal stacking and ABCABC stacking.
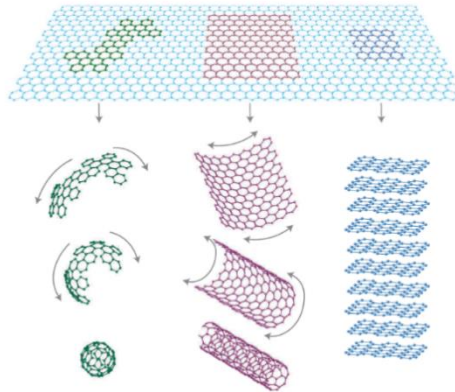
Figure 2-3: Graphene's honeycomb lattice structure. The building block for 0D fullerenes, 1D nanotubes and 3D graphite.[78]

2.3.1 Graphene's lattice structure

Graphene's crystal structure is a spatially periodic repetition of a unit cell that contains the lattice points where the atoms sit. Graphene's unit cell is a hexagonal Bravais lattice (*Figure 2-4*a), with six atoms arranged at the vertices of a hexagon and a seventh atom at the centre, and has lattice vectors, a_1 and a_2. A repetitive translational operation of the unit cell by the lattice vectors will yield all the lattice points in the crystal structure. There are two types of carbon atoms in graphene's lattice, atoms A and B (*Figure 2-4*b). Each A atom has 3 B atoms surrounding it: one to the right of the atom, one at the upper left and another at the lower left. Conversely, each B atom has 3 A atoms surrounding it: one to the left of the atom, one at the upper right and one at the lower right. For every atom, the three nearest-neighbour vectors are defined as δ_1, δ_2 and δ_3.
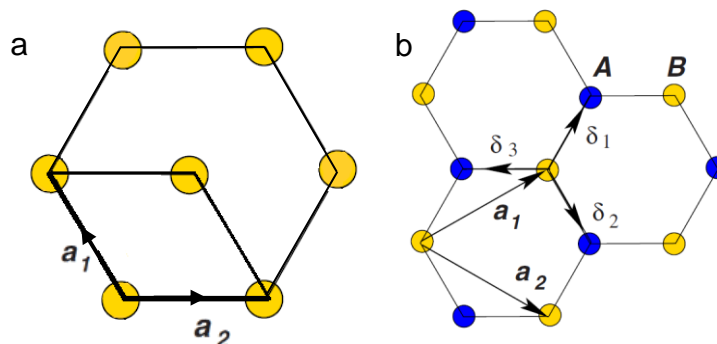
Figure 2-4: a) Bravais hexagonal lattice   b) Type A and Type B atoms[80]

When the hexagonal network of atoms A and B in graphene is looked at, the hexagonal Bravais unit cell is not immediately seen, however, consideration of

only one type of atom does show the hexagonal Bravais unit cell with six lattice points at the corners of the hexagon and one in the middle (Figure 2-5a). A parallelogram-shaped primitive unit cell can also be defined with the lattice vectors a_1 and a_2 (Figure 2-5b and c) and contains two atoms, one each of atom types A and B. This primitive unit cell is commonly used as graphene's unit cell instead of the hexagonal Bravais unit cell.
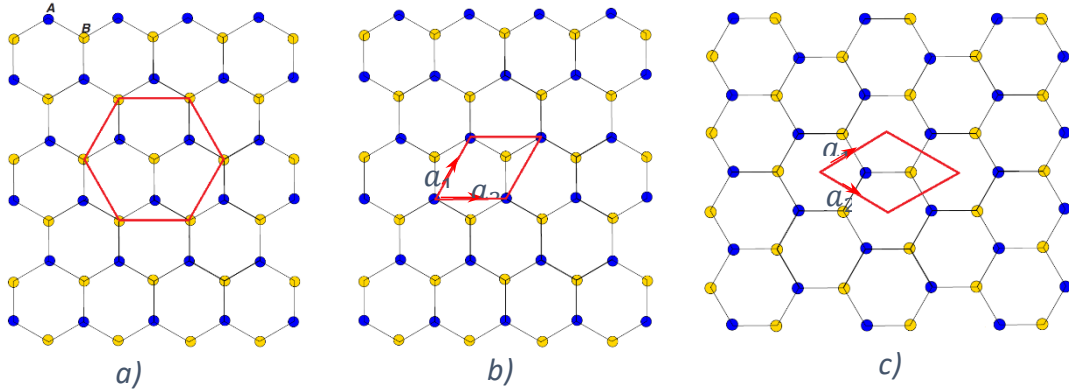
Figure 2-5: a) Hexagonal Bravais lattice in graphene b) & c) Primitive unit cell in graphene (modified from[80])

Graphene's k-space or reciprocal space is gotten by taking the Fourier transform of the real space, which results in a set of periodically arranged points called the reciprocal lattice points. The reciprocal lattice is simply a rotation of the Bravais lattice by 90 degrees. The primitive unit cell in the k-space is defined by the lattice vectors b_1 and b_2. The hexagon in Figure 2-6b defines the Brillouin zone and shows some of the high symmetry points: the zone centre, Γ, the M point in the middle of the hexagonal side, and the K and K' points at the corners of the hexagon. The K and K' points are inequivalent since they are not connected by the lattice vectors of the reciprocal lattice, so a K point cannot be translated along the lattice vector to a K' point. The six corners of the Brillouin zone are called the Dirac points, at which points, graphene exhibits an unusual linear dispersion of the π–band. Figure 2-6c shows graphene's electronic band structure, with the Dirac points.

a)   b)
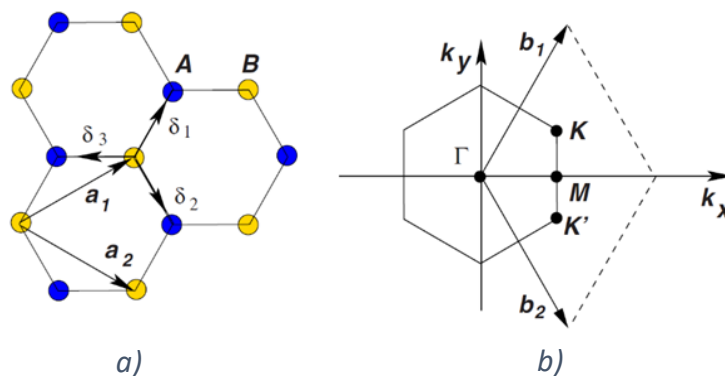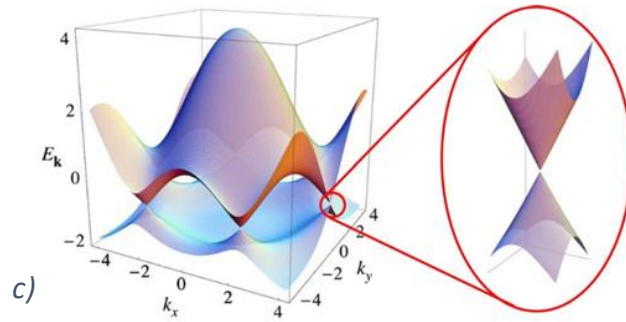
Figure 2-6: Graphene's a) real space b) reciprocal or k-space c) electronic band structure; insert - Dirac point[80]

2.3.2 Phonon dispersion of graphene

Since graphene's primitive unit cell contains two atoms, there are six phonon dispersion bands that describe its phonon dispersion: iLO, iTO, oTO, iLA, iTA and oTA phonon branches (Figure 2-7). Three of these branches are acoustic branches (denoted by the letter A) and three are optic branches (denoted by the letter O). For two acoustic and two optic phonon branches, the vibrations of the atoms are parallel to the graphene plane, so they are the in-plane modes (denoted by the letter i). For the remaining one acoustic and one optic phonon branch, the atomic vibrations are perpendicular to the graphene plane, and are the out-of-plane modes (denoted by the letter o). The phonon branches are also classified as longitudinal (denoted by the letter L) or transverse (T) depending on whether the direction of the vibrations are parallel with or perpendicular to the A-B carbon-carbon directions, respectively. The iLO and iTO optic modes are degenerate at the zone-center (Γ point) and are Raman active modes[81].
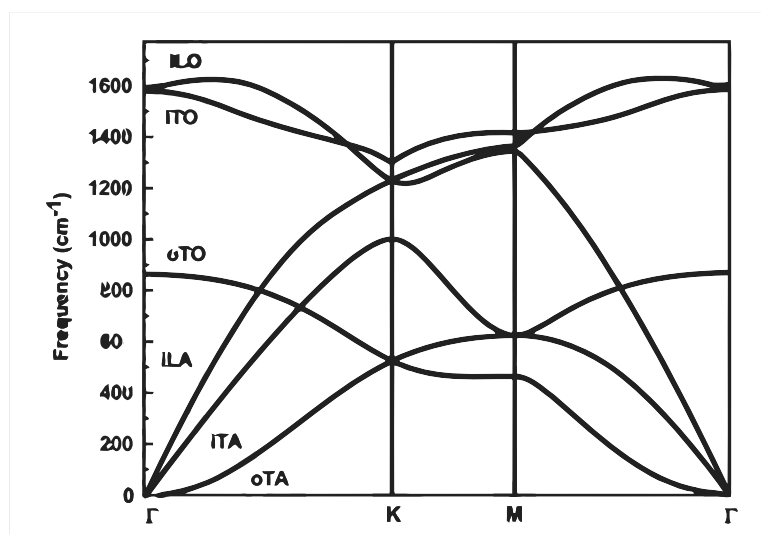
Figure 2-7: Phonon dispersion of graphene[81]

16

2.3.3 Summary of graphene's properties

Graphene is probably the highest trending material of the decade with the amazing properties it possesses. These properties include extremely high charge mobility, excellent electrical and thermal conductivity, exceptional mechanical properties such as its very high strength and mechanical compliance. Table 2-1 gives a summary of the properties of graphene.

Physical		Dimension	Appearance	State @ Room Temperature	Density[82]
		2D Thickness: ~0.335 nm[83]	Transparent for monolayer graphene. Absorbs 2.3% of incident white light[84].	Solid	$\rho \approx 2200\ kg/m^3$
Mechanical		Young's Modulus	Strength	Poisson's ratio[85, 86]	Specific surface area[87]
	Monolayer	$E = 1 \pm 0.1\ TPa^{86}$;		$v = 0.165$	$2600\ m^2/g$
	Bilayer	$E = 1.04\ \textbf{TPa}^{83}$	$\sigma = 126\ GPa^{83}$		
	Trilayer	$E = 0.98\ TPa^{83}$	$\sigma = 101\ GPa^{83}$		
Electrical/Electronic		Charge mobilities[88]	Dirac Fermions	Quantum Hall Effect	Minimum Hall conductivity[87]
		200,000 cm^2/Vs at carrier density of 2×10^{11} cm^{-2}	✓	✓	$\sim 4e^2/h$
Thermal		Thermal conductivity			
		$\sim 4840 \pm 440$ to 5300 ± 480 W/mK^{89}			

Table 2-1: Summary of graphene's properties

2.4   Characterization of graphene structures

2.4.1 Optical imaging of graphene

Images of monolayer, bilayer, trilayer, and few layer graphene can be obtained using a number of techniques/equipment, including optical microscopes, scanning electron microscopy (SEM), atomic force microscopy (AFM), transmission electron microscopy (TEM), and helium ion microscopy (HIM). The resolution of these techniques varies significantly and play a major role in the success of the imaging process. Though optical microscopes have the lowest resolution, they were widely used after the discovery of graphene to image multilayer graphene since they are cheap and readily available in laboratories. Monolayer graphene being a transparent material is usually difficult to image,

even with very good resolution techniques like the SEM. Over the years, substrates have been designed to enhance the visibility of thin sheets for good contrast imaging. SiO_2 is commonly overlaid on silicon to enhance the contrast of graphene layers for imaging, alternatively, Si_3N_4 is used.

Other factors that influence the contrast of graphene images are the wavelength of the incident light and the thickness of the SiO_2 layer. It has been shown that on 300 *nm* SiO_2, thick and thin sheets of graphene are visible under green light illumination, and invisible under blue light. On 200 *nm* SiO_2 under blue light graphene sheets are visible but are invisible under green light. Under normal white light on a 200 *nm* SiO_2, graphene sheets are invisible and are barely visible on 300 *nm* SiO_2[90]. Figure 2-8 shows a colour plot for the expected contrast of graphene on SiO_2/Si wafers as a function of SiO_2 thickness and the wavelength of the incident light. For very high contrast imaging of graphene sheets, SiO_2 with thicknesses ~90 *nm* and ~280 *nm* used under green light are most appropriate. Green light is the preferred illumination light since it is the most comfortable for the eyes.
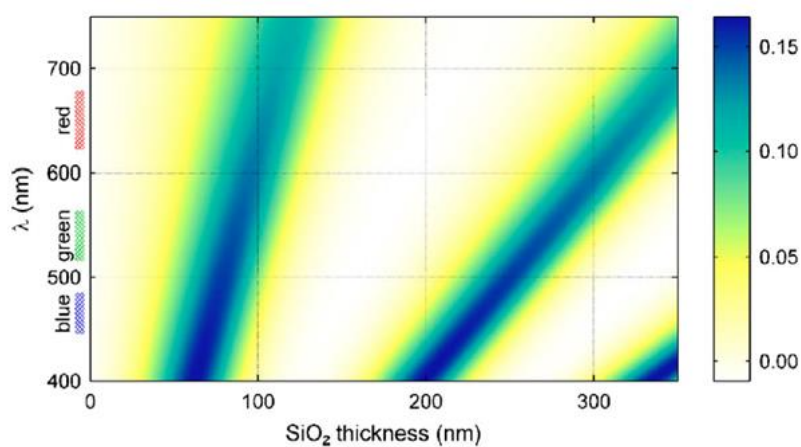
Figure 2-8: Colour plot of contrast as function of wavelength and SiO2 thickness. Colour scale on right shows the expected contrast[90].

Scanning electron microscopy (SEM)

Scanning electron microscopy (SEM) is a non-destructive characterization technique that uses a focused beam of high-energy electrons to generate information about the external morphology, chemical composition, and crystalline structure of a solid sample. The accelerated electrons upon collision with the sample, decelerate and dissipate energy in form of secondary electrons, backscattered electrons, diffracted backscattered electrons, photons, visible light

and heat[91]. The secondary electrons and backscattered electrons are used to produce high resolution images; the diffracted backscattered electrons are used to determine the crystal structure and orientations of minerals; and the photons are used for elemental analysis to determine the elements present in the sample.

Scanning electron microscopes are made up of the following components: an electron source or gun, electron lenses, sample stage, detectors for all signals of interest, display/data output devices and other infrastructure requirements, such as power supply, a vacuum system, cooling system, vibration free floor, and a room free of ambient magnetic and electric fields[91].

Atomic force microscopy (AFM)

Atomic force microscopy (AFM) is a nanolevel imaging technique that generates images almost at an atomic resolution level by measuring the contour of the sample. Atomic force microscopes have an ultra-small probe tip (about $100 - 200$ μm long and $20 - 60$ nm radius of curvature)[92] at the end of a cantilever-type spring, with which they measure the contour of the sample by measuring the forces or the interactions between the probe tip and the sample surface. The cantilever deflects in response to the force between the probe tip and the sample and thus quantifies the force. Images are created by scanning the sample relative to the probing tip, with the force value varying with the difference in surface height of the sample. A laser beam reflects off the top of the cantilever towards a position sensitive photodetector, which detects the bend and calculates the actual position of the cantilever. Typical forces between the probing tip and the sample range from 10^{-11} to 10^{-6} N, with atomic interactions between two covalently bonded atoms at an order of 10^{-9} N non-destructive imaging is possible[93].

AFM can be operated in three modes: contact, non-contact and tapping modes. The contact mode involves a sideways scanning by the probe tip over the sample surface, in such a way that the distance between the tip and the sample surface is less than a few angstroms (Å). The tip contacts the sample surface softly and is traced across the sample. The non-contact mode is operated with the probe tip several tens to hundreds of angstroms away from the sample surface, thereby experiencing an attractive van der Waals force. The cantilever oscillates above the sample surface at a frequency larger than its resonance frequency and with a small amplitude during the scanning process and results in a more sensitive

imaging mode. In the tapping or intermittent contact mode, the cantilever oscillates vertically at or slightly below its resonance frequency, so that its tip alternately contacts and lifts off the sample surface, with an amplitude ranging from 20 nm to 100 nm. This mode is most preferred for high resolution imaging of subcellular structures[92].

AFM imaging can be used to determine the layer thickness of graphene, but this can be a cumbersome process for imaging large areas of graphene.

Transmission electron microscopy (TEM)

Transmission electron microscopy (TEM) is an atomic scale resolution imaging technique that uses high energy electrons, accelerated to nearly the speed of light. When the transmitted electron beam is made to pass through an ultra-thin sample, electrons get scattered. And are focused via a sophisticated system of electromagnetic lenses into an image, a diffraction pattern, or a nano-anlytical spectrum, depending on the mode of operation. TEM imaging generates images with highly magnified views of the micro and nanostructure of the sample, and can provide a direct map of the atomic arrangements in the sample when used in the high resolution mode. Figure 2-9 shows TEM images of monolayer and bilayer graphene which show the atomic arrangement of the carbon atoms. In the diffraction mode, TEM displays accurate information about the local crystal structure of the sample. And the nano-analytical mode provides information about the elements present in the volume of the sample.
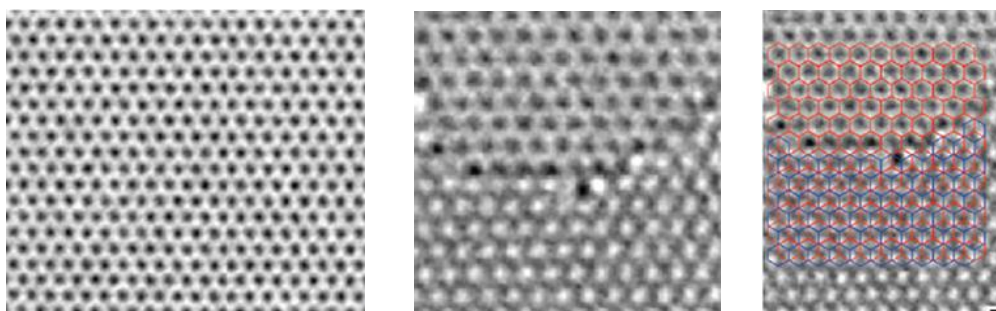
*Figure 2-9: TEM images of **a)** monolayer graphene **b)** bilayer graphene **c)** monolayer and bilayer graphene with superimposed hexagonal lattice structure[87]*

2.4.2 Raman spectroscopy of graphene

Raman spectroscopy is a very powerful non-contact technique for the characterization of materials. It provides useful information about the material

through the inelastic scattering of monochromatic light, as the light interacts with the molecular vibrations or phonons in the material. When monochromatic light is incident upon a sample, it may be reflected, absorbed or scattered. The atoms or molecules of the sample absorb the energy of the incident photons and get excited to virtual energy states. When this happens, the excited molecules can relax back to lower energy states and emit photons in three possible ways. First, the molecules get excited from the ground state to a virtual state and relax back to the ground state in an elastic process, releasing a photon of equal energy and wavelength as the incident photon. This is called Rayleigh scattering and accounts for majority of the scattered light. Second, the molecules get excited from the ground state, but relax back to a real phonon state in an inelastic process, emitting a photon with less energy and longer wavelength than the incident photon. This is one of the Raman scattering called a Stokes scatter. The third scatter possibility occurs with molecules that are already in an excited real phonon state, they get excited to a higher virtual energy state and then relax back to the ground state, releasing a photon with more energy and shorter wavelength than the incident photon. This is the second type of Raman scattering called an Anti-Stokes scatter. Jablonski's diagram in Figure 2-10 shows these scatterings.
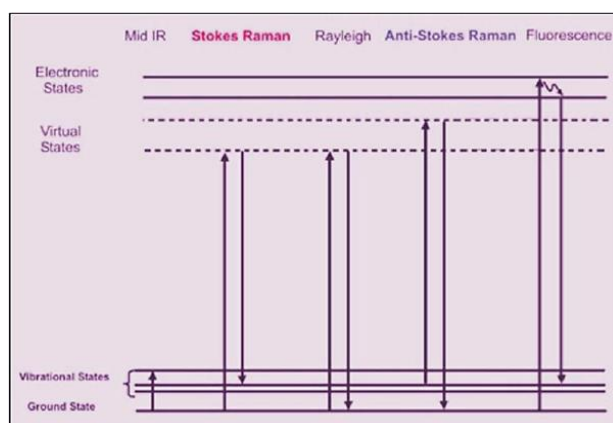
Figure 2-10: Jablonski energy diagram showing Rayleigh and Raman scattering [94]

At room temperature, most molecules will be found in the ground state, as a result, Stokes scattering has been found to be the stronger of the two Raman scattering; with Raman scattering accounting for only a very small fraction, about 1×10^{-7}, of all the scattered light [94]. The change in wavelength of the scattered light is what provides information on the chemical and structural nature of the material.

Raman spectroscopy has been shown to be one of the most powerful and most important characterization techniques for carbon materials, including graphene. It has been used to estimate compressive and tensile strain in graphene[95], determine its thermal conductivity[89], provide detailed information about its band structure[96, 97], and identify the number of layers it has[98].

Single layer graphene

The two most prominent features in the Raman spectra of defect-free graphite and monolayer graphene are the G band at ~1580 cm^{-1} and the G' or 2D band at ~2700 cm^{-1}. Another feature, the D band at ~1350 cm^{-1}, is also seen in defected graphite and graphene. The G band is as a result of the doubly degenerate (iTO and iLO) E_{2g} phonon modes at the Brillouin zone center. It is the only band in the Raman spectra of graphene that results from a normal first order Raman scattering process. The D and 2D bands, on the other hand, are second order Raman scattering processes, with two in-elastic scatterings involving two iTO phonons near the K point for the 2D band, while the D band consists of one elastic defect-induced and one in-elastic iTO phonon scattering. These processes are double resonance processes as the wave-vectors $\boldsymbol{q}$ of the phonons involved with the D and 2D bands couple preferentially to electronic states with wave-vectors $\boldsymbol{k}$, in such a way that $\boldsymbol{q} \simeq 2k$. This double resonance process accounts for the dispersive behaviour exhibited by the D and 2D bands, where their frequencies in the Raman spectra change as the energy of the laser E_{laser} changes. The D band and 2D band frequencies upshift linearly with increasing E_{laser} with dispersions of 53 $cm^{-1}eV^{-1}$ and 106 $cm^{-1}eV^{-1}$ respectively[99].
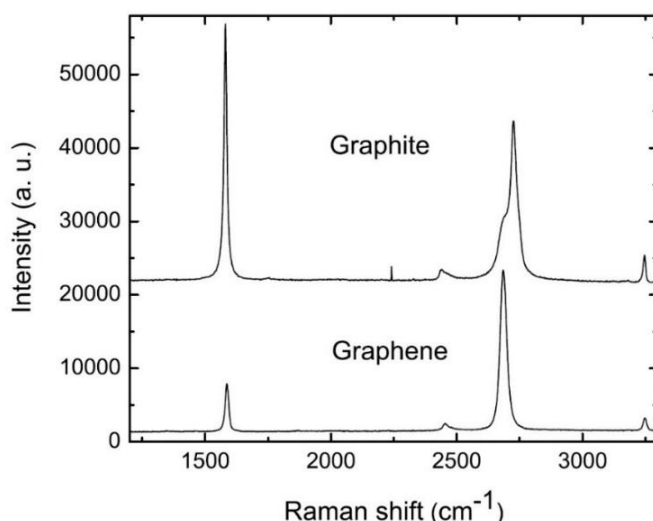
Figure 2-11: Comparison of Raman spectra for graphene and graphite @ 514 nm[98]

Figure 2-11 compares the Raman spectra of bulk graphite and graphene. The shape and intensity of the 2D band for monolayer graphene is significantly different from graphite's. The 2D band for monolayer graphene exhibits a single sharp peak, which can be described as a Lorentzian feature with a full width at half maximum (FWHM) of ~24 cm^{-1} [81], while the 2D band for highly oriented pyrolitic graphite (HOPG) is made up of two peaks, $2D_1$ and $2D_2$, which are ~1/4 and ~1/2 the intensity of HOPG's G band[98]. Graphene's 2D band position is red shifted by ~5 cm^{-1} and ~35 cm^{-1} with respect to graphite's $2D_1$ and $2D_2$ positions which appear at 2690 cm^{-1} and 2720 cm^{-1} respectively[100]. The G bands for graphene and HOPG are very similar in shape, with graphene's G band position blue shifted by $3 - 10$ cm^{-1} from graphite's G position[98, 100]. For monolayer graphene, the 2D band intensity, I(2D), is larger than the G band intensity, I(G); which is the converse case for graphite. The I(G)/I(2D) intensity ratio is ~0.24 for monolayer graphene and ~ 3.2 for HOPG[100]. The large intensity of the 2D band in monolayer graphene can be explained by a triple resonance process[81].

Second-order double resonance Raman Scattering

The defect-induced or two-phonon double resonance process consists of four steps (Figure 2-12): (1) a laser-induced excitation of an electron-hole pair, where an electron in the valence band around K with a wave-vector $\boldsymbol{k}$ is excited to the conduction band by absorbing a photon of energy E_{laser}, (2) an electron-phonon scattering, where the excited electron is then in-elastically scattered by a phonon or elastically scattered by a defect of wave-vector $\boldsymbol{q}$ to a point on a contour, with wave-vector $\boldsymbol{k} + \boldsymbol{q}$, in the conduction band around the K' point, (3) an electron-phonon scattering, where the electron is in-elastically scattered by a phonon with wave-vector $-\boldsymbol{q}$ back to a $\boldsymbol{k}$ state in the conduction band around K, and (4) an electron-hole recombination, where the excited electron is recombined with a hole in the valence band and emits a photon. The double resonance condition is only achieved when the two electron-phonon scatterings satisfy energy-momentum conservation for the two intermediate states. Two resonance conditions for the three scattering events need to be satisfied: the intermediate $\boldsymbol{k} + \boldsymbol{q}$ state is always a real electronic state, and either the initial or the final $\boldsymbol{k}$ state is a real electronic state.
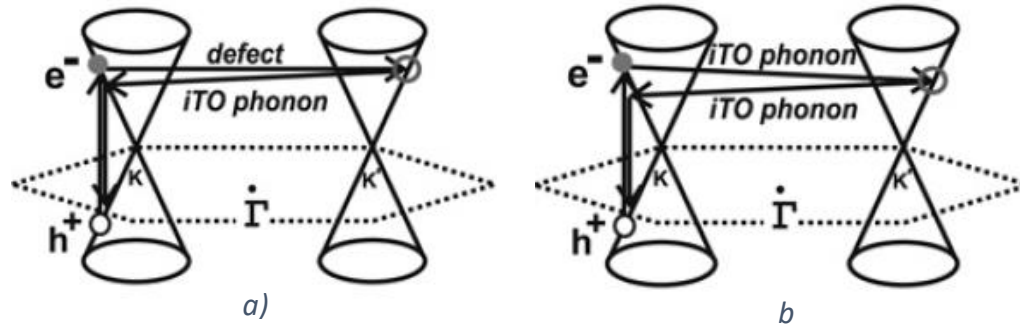
Figure 2-12: Double resonance processes a) defect-induced scattering b) two-phonon scattering[81]

The electronic structure of graphene is linear in wave vector k near the Dirac points. When E_{laser} increases, the resonance k vector for the electron moves away from the K point, correspondingly, the q vector associated with the resonance k vector in the double resonance process increases with increasing k, measured from the K point[99]. This effect is what gives rise to the dispersive behaviour of the D and 2D bands.

Triple resonance Raman scattering

The triple resonance process, like the double resonance process, involves four steps. However, in the third step, instead of the electron being scattered back by a phonon with wave-vector $-q$, the hole in the valence band near K is scattered by a phonon with wave vector $+q$ (Figure 2-13). And the electron recombines with the hole in the conduction band near K' in the fourth step. In the triple resonance process, the electron-hole generation is a resonant process, in which both the electron and hole scattering processes are resonant, and the electron-hole recombination is between an electron and a hole in resonance states. Meaning that all steps in the usual double resonance process become resonant in the triple resonance process. This triple resonance condition might explain why the intensity of the 2D band in monolayer graphene is larger than the G band[81].
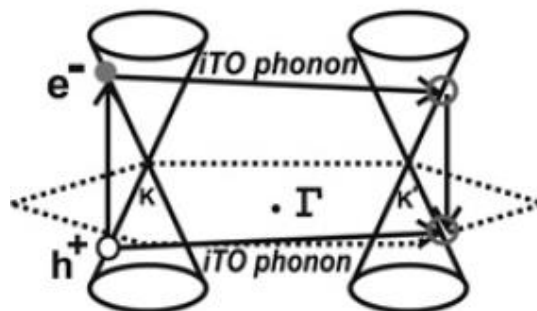
Figure 2-13: Triple resonance process[81]

Bilayer and trilayer graphene

The electronic band structures for bilayer and trilayer graphene with AB layer stacking have the electronic bands near the Fermi level split into two and three energy bands respectively. The electronic band structure for bilayer graphene has two split parabolic bands in the valence and conduction bands with a degeneracy at the K and K' point, while that for trilayer graphene has two linear k bands between the two convex parabolic conduction bands and the two concave parabolic valence bands (Figure 2-14). Generally, for any multi-layer graphene, the electronic band structure near the Fermi level depends on the number of layers n: if n is odd, the band structure will have two linear bands between $n-1$ convex parabolic conduction bands and $n-1$ concave parabolic valence bands; and if n is even, the electronic band structure will have $2n$ parabolic bands[101]. Because of the split energy bands, for a given E_{laser}, there will be different q wave-vectors, since the k states for the optical transitions are different for the different energy bands.
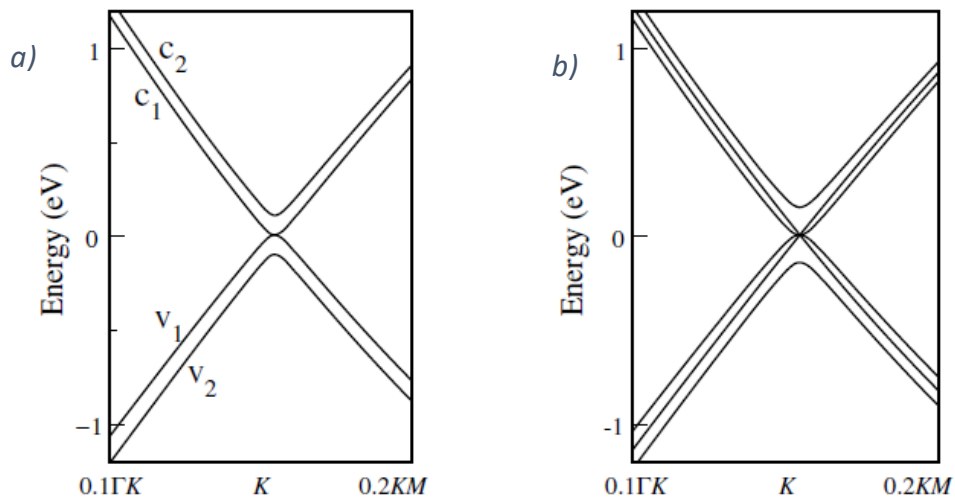
Figure 2-14: Electronic band structure for a) bilayer graphene b) trilayer graphene[101]

Due to the split bands, there are two and three energy contours in the conduction band near the K and K' points for bilayer and trilayer graphene respectively. As a result, there are four and nine possible electron-phonon scattering processes for bilayer and trilayer graphene respectively. For bilayer graphene, these four different processes contribute to the 2D band shape and intensity, and are represented by four Lorentzian features. Figure 2-15 shows the 2D Raman band for bilayer graphene fitted with four Lorentzians. Theoretically, with the valence and conductance bands being mirror images of each another, two of the four

processes are degenerate and the 2D band would be fitted with three Lorentzian features. However, four Lorentzian features give a better fit experimentally, which is an indication of the asymmetries between the valence and conductance bands in bilayer graphene[81].
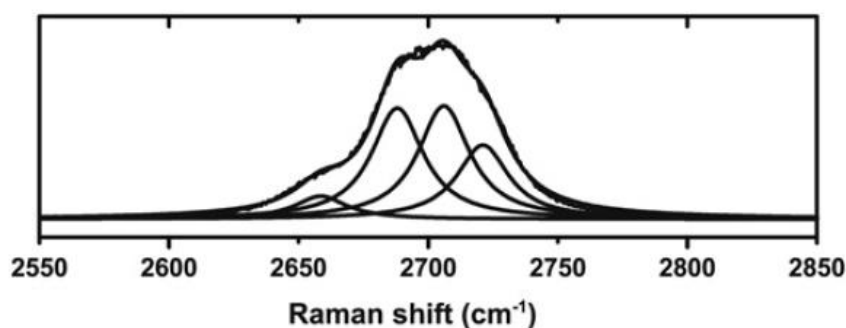
Figure 2-15: 2D Raman band spectra for bilayer graphene fitted with four Lorentzians[81]

For trilayer graphene, the nine optical processes contribute to the 2D band shape, however, with four of the processes being degenerate, only five Lorentzians are fitted to the 2D band shape[101]. Experimentally, a minimum of six Lorentzians with a FWHM of ~24 cm^{-1} are needed to ensure a good fit for trilayer graphene[81]. Figure 2-16 shows the 2D Raman spectra for trilayer graphene fitted with six Lorentzians.
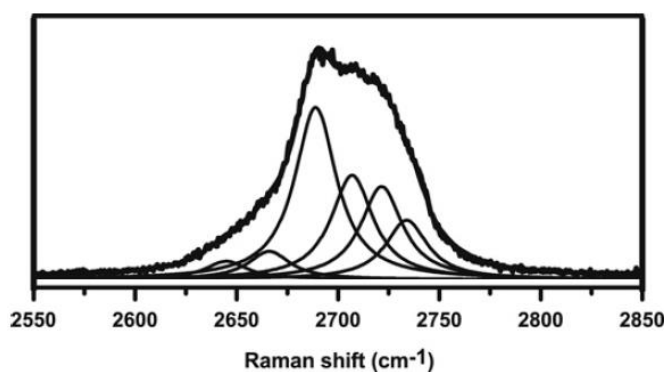
Figure 2-16: 2D Raman spectra for trilayer graphene[81]

The 2D band continues to evolve with increasing graphene layers, its band shape and position can be used as good fingerprints to identify monolayer and bilayer graphene from other multi-layered graphene[100]. With monolayer graphene having a single Lorentzian fit to its 2D band, bilayer graphene having four Lorentzian features, up to graphite having two Lorentzian features.
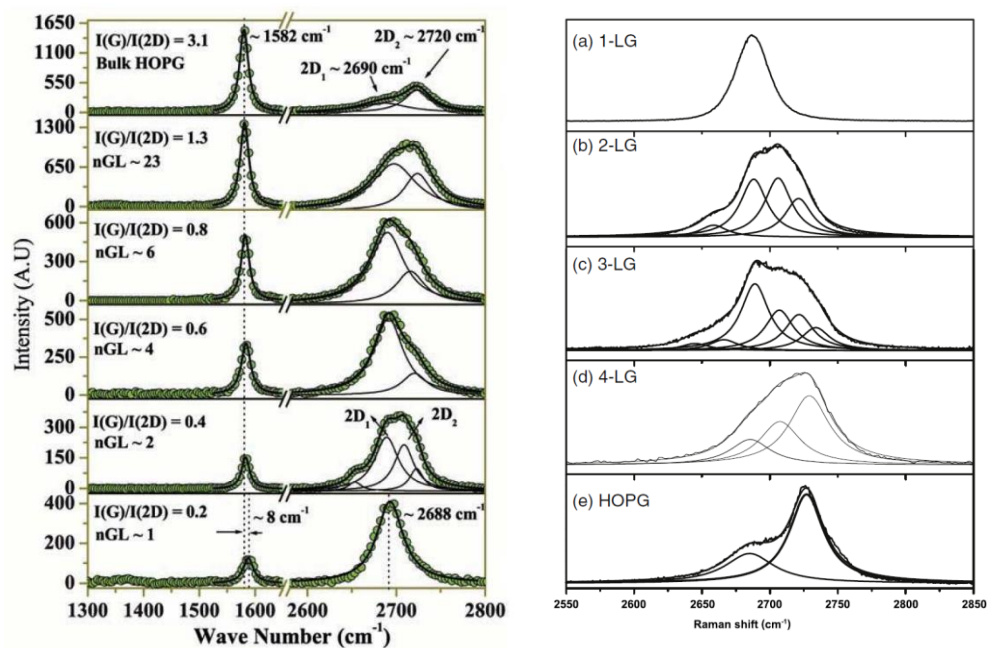
Figure 2-17: Evolution of 2D band with number of graphene layers[81, 100]

Raman Spectra of graphene on different substrates

A huge percentage of the work done with graphene is carried out on SiO$_2$/Si substrates. Charge impurities on SiO$_2$/Si substrates with defects influence the position of the G band of monolayer graphene. This influence is shown in the finite blue shift of the G band by ~5 – 7 cm^{-1} with respect to bulk graphite. In contrast to this blue shift on SiO$_2$/Si substrates, there is a red shift of the G band of monolayer and few layer graphene on indium tin oxide (ITO) by ~6 cm^{-1} with respect to bulk graphite. A large softening of about 20 cm^{-1} in the 2D band of monolayer and few layer graphene on ITO as compared to SiO$_2$ is also reported. Even though the origin of the red shift is yet to be fully understood, the lowering of the frequencies imply that the unit cell constant of the graphene layer is enlarged when deposited on the ITO substrate[100].

2.5   Suspended graphene structures

Apart from the disadvantage that graphene's interaction with an underlying supporting substrate decreases its high mobility due to scattering and negatively affects other properties, the principles of operation of micro- and nanomechanical graphene-based devices (as surface-stress or resonance devices) require graphene to be suspended. A freely suspended graphene layer without contact to any supporting substrate remains the ultimate truly two-dimensional system.

2.5.1 Suspending Graphene

Suspension of graphene is achieved in two ways: etching away of the underlying substrate after graphene transfer or transfer of graphene to pre-patterned substrates. The former requires the transfer of graphene to, and in many cases the pre-patterning of the graphene on, an unpatterned substrate before etching away the underlying substrate. Though very successful, this method exposes graphene to harsh etching chemicals, which potentially damage the graphene.

The methods utilized in transferring graphene to substrates heavily depend on how graphene was synthesized. With mechanically exfoliated graphene, transferring graphene to the substrate of choice is part of the synthesis process. Commercially available graphene are CVD graphene grown on copper (Cu). To transfer graphene to the desired substrate, the copper has to be separated from it. This is done in a number of ways, including wet etching[102], electrochemical delamination[103], soak and peel[104], transfer printing (PDMS stamp)[105], thermal release tape[1] and wet transfer methods[1].

Wet etching

To transfer graphene from copper to a desired substrate using the wet etching method, a protective polymeric coating of Polydimethylsiloxane (PDMS) or Polymethylmethacrylate (PMMA) is first deposited on the graphene/Cu sample. Then the underlying copper is etched in an etching bath with iron chloride ($FeCl_3$ in HCl/H_2O ($1M - 5M$)) by immersing the PMMA/graphene/Cu or PDMS/graphene/Cu in the iron chloride, until a free-standing PMMA/graphene or PDMS/graphene membrane is seen floating in the solution. The polymer/graphene can then be fished out and placed on the desired substrate, with graphene contacting the substrate. After the transfer process is completed, the polymer is then removed by etching with acetone.

Other chemicals that can be used to etch copper include; HCl, HNO_3, $Fe(NO_3)_3$ in H_2O and $(NH_4)_2SO_8$. $FeCl_3$ is the widely preferred option because it slowly and effectively etches away the copper without forming gaseous products or precipitates. Etching with HCl releases corrosive vapour and the etching rate is very slow. HNO_3 forms H_2 bubbles which cause cracking in the graphene sheet, and the HNO_3 itself degrades the carbon sp^2 network.

Electrochemical delamination

The electrochemical delamination transfer process is a non-destructive and highly efficient way of transferring graphene from copper to the desired substrate. In this method, PMMA is first spin-coated onto the graphene/Cu sample, as is done in the wet etching method. Then a direct current voltage is applied to the PMMA/graphene/Cu cathode and a glassy carbon anode in an electrolytic cell with a solution of $K_2S_2O_8$ (0.05 mM) as the electrolyte (Figure 2-18). With the graphene/Cu electrode polarized, reduction of water begins to take place at the graphene/Cu interface, and H_2 gas is produced. The force from the H_2 bubbles gently detaches the graphene film from the Cu foil beginning at its edges. As graphene gets detached from the Cu foil, the hydroxyl ions produced from the water reduction process precipitate CuO and Cu_2O on the Cu foil, thereby passivating the Cu from further chemical etching.
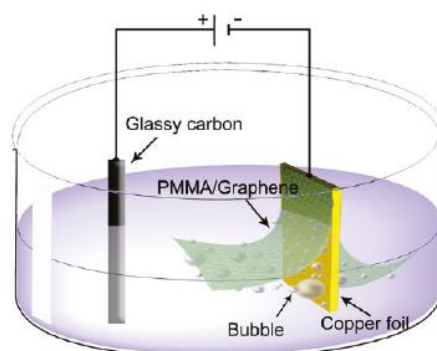
Figure 2-18: Electrochemical delamination of graphene from Cu foil[103].

The PMMA/graphene can then be transferred to the desired substrate and the PMMA dissolved with acetone.

Soak and Peel

The soak and peel method takes advantage of the capability of deionized water to penetrate nanoscale hydrophobic-hydrophilic interfaces and separate them to delaminate graphene from metal substrates. With chemical etchants phased out, cleaner graphene with improved properties is obtained. In this method also, the graphene film is first coated with PMMA, kapton tape is additionally stuck on the PMMA to avoid crumpling of the PMMA after delamination. The kapton/PMMA/graphene/Cu is then immersed in deionized water maintained at 90^0C for 2 hours. The kapton tape (together with the PMMA and graphene) is

then peeled off from the Cu foil and transferred to the desired substrate. To aid adhesion between graphene and the substrate, the kapton/PMMA/graphene/substrate is heated for 40 minutes at 140^0C and allowed to cool for 20 minutes. The kapton tape is removed and from the stack and PMMA dissolved in acetone.
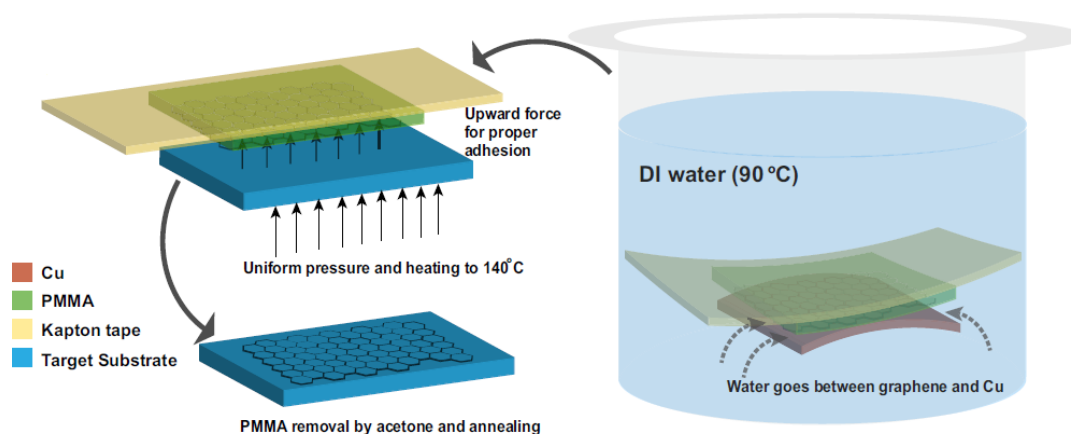
Figure 2-19: Soak and peel delamination method[104].

Transfer printing

Transfer printing is a dry graphene transfer technique suitable for transferring large areas of graphene to pre-patterned substrates. To avoid wet processing of graphene after transfer to the substrate, the graphene is patterned to the desired shapes and sizes while still on the Cu. The etched graphene is stripped from the Cu with the polymer N-methyl-2-pyrrolidone (NMP), with ammonium persulfate (APS) etchant and cellulose nitrate, and transferred to a 3 mm thick PDMS stamp. The cellulose nitrate is then removed by immersing in acetonitrile for 2 hours and air drying. The stamp with graphene is placed on the desired substrate and the stamp peeled off in a controlled low speed peeling process. This leaves the graphene suspended over the pre-patterned substrate.

Thermal release tape

In this method, 200 nm of PMMA is first spin-coated onto graphene/Cu sample, and thermal release tape is pressed onto the stack. The Cu is then etched in $0.25M$ solution of sodium persulfate, and the release-tape/PMMA/graphene cleaned with HCl solution for 30 minutes and dried in N_2 gas. Next the release-tape/PMMA/graphene stack is pressed onto the pre-patterned substrate with graphene contacting it and heated to aid adhesion of the graphene to the

substrate. The whole stack is then heated to a temperature above the release temperature of the thermal release tape, and the tape is easily peeled off. Finally, the PMMA is dissolved in acetone for 2 hours.

Wet transfer method

With the wet transfer method, as with the other methods, PMMA is spin-coated on the graphene/Cu as a supporting layer for the graphene. The Cu is etched away as in previous methods, and the PMMA/graphene stack is cleaned and left floating in deionized water. The desired substrate is then used to fish the PMMA/graphene directly out of the water with the graphene side of the stack contacting the substrate. The PMMA/graphene/substrate is then heated to dry the stack and aid the adhesion of the graphene to the substrate. The PMMA is removed using acetone as with previous methods leaving graphene on the substrate.

Three of the six methods described here have been analysed and compared in terms of the yield and quality of free-standing graphene produced on a large scale[1]. The thermal release tape, transfer printing and wet transfer methods were used to transfer CVD grown graphene unto SiO_2/Si substrates. The SiO_2/Si substrates were pre-patterned with cavity arrays which had holes with diameters between 2 μm and 10 μm. A total of 120 cavities on at least two different SiO_2/Si wafers were analysed per method, to evaluate if the suspended graphene membranes were intact, partly intact, or completely damaged (Figure 2-20).

For monolayer graphene, only the print transfer method produced intact free-standing graphene membranes with a 2.7% yield. For bilayer graphene, the thermal release tape and wet transfer methods had intact graphene membranes with 5% and 16% yields respectively.
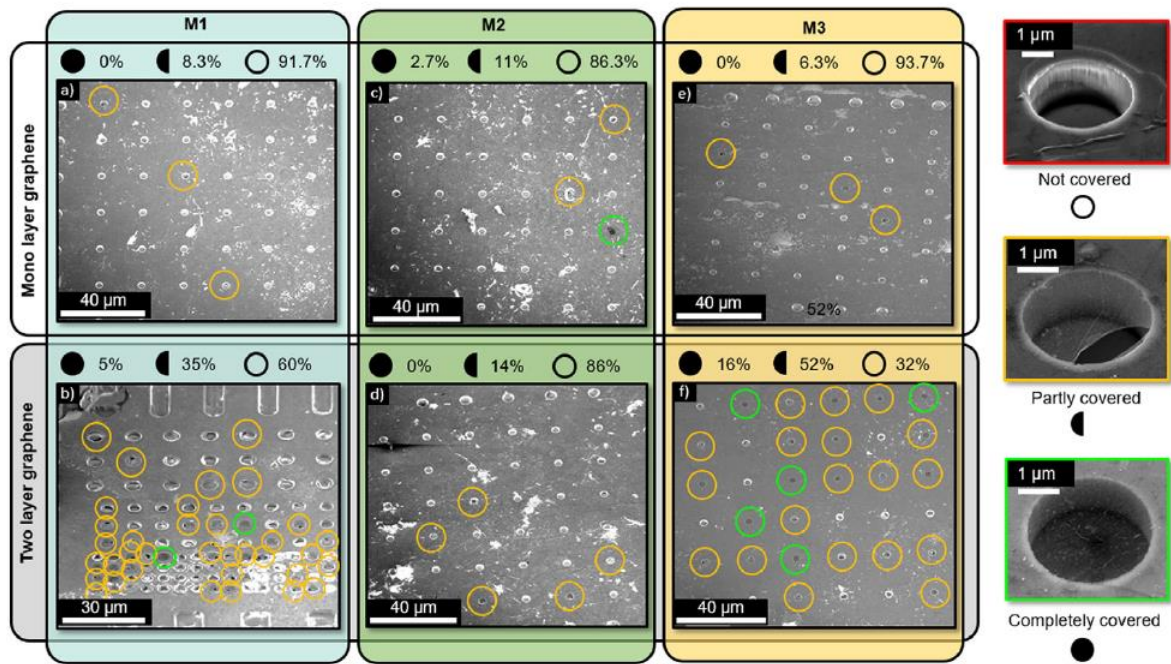
Figure 2-20: Yield comparison of three transfer methods for monolayer and bilayer graphene a) - b) Thermal release tape method   c) - d) Print transfer method   e) - f) Wet transfer method[1]

2.5.2 Micro- and Nanoscale Micromachining of Graphene

Different graphene shapes and geometries are required in micro- and nano-devices. Successful patterning of graphene is therefore key to the success of graphene-based micro- and nano-devices. Several patterning and structuring methods have been developed for micron- and nanoscale patterning of a wide range of materials, which are also applicable to graphene. Ultimately, a minimally invasive patterning method that ensures an intact graphene lattice structure after patterning needs to be identified or developed.

Photolithography or UV lithography and focused ion beam (FIB) micromachining are among the most used methods for micro-patterning, from patterning of parts of a thin film to the bulk of substrates. Photolithography involves the use of a light sensitive material called a photoresist to selectively etch out portions of a solid sample or substrate. The photoresist covers the entire surface of the sample, and is selectively exposed to an intense beam of UV light. Depending on the type of resist used, the exposed or unexposed portions get dissolved in a developer, exposing portions of the sample that need to be etched away. After etching, the resist is removed leaving the patterned sample/substrate. FIB micromachining techniques involve the impingement of energized ions on the surface of the

sample. The ions lose their energy to the electrons and atoms of the substrate, causing sputtering of the neutral and ionized substrate atoms.
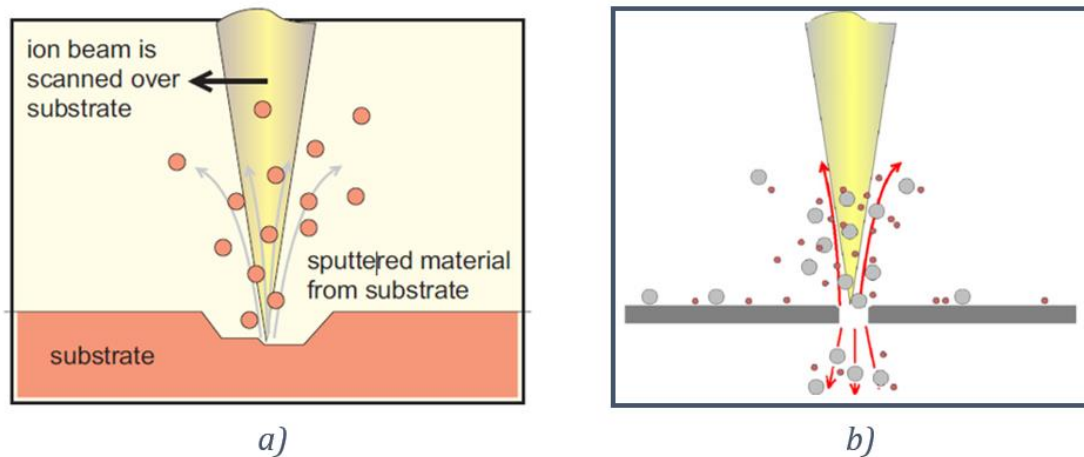
Figure 2-21: Focused Ion Beam Milling a) bulk substrate[106] b) ultra-thin film[107]

Micro- and nanoscale patterning has been achieved for supported and suspended graphene. With nanoscale patterning being the most challenging of the two. Electron-beam lithography (EBL) followed by reactive ion etching is the most common technique for nanoscale patterning of supported graphene. EBL patterned graphene structures like Hall bars[108], nanoribbons[109] and quantum dots[110] have been reported. Patterning of suspended graphene, on the other hand, requires the use of resistless patterning techniques, such as FIB methods, as the resist could damage the suspended graphene structure. FIB provides an easy and fast method for patterning suspended graphene, with resolutions comparable to EBL. However, due to the very high energies of the ions, structural damages are induced in the graphene structures[111]. Other techniques developed for the patterning of graphene are atomic layer etching (ALET)[112], Gas-assisted Focused electron beam (FEB)[113], and scanning tunnel microscope (STM) lithography, among others[114].

2.6 Theoretical modelling of the mechanical behaviour of suspended graphene sheets (GSs)

Suspended structures, depending on the ratio of their length, width and thickness, could be classified as beams, thick flat plates, thin flat plates or as membranes. Assuming the structures are of one material type, their vibrational response is greatly influenced by their spatial dimension, and consequently their classification. A more acceptable criteria for the classification of suspended structures into beams, thick flat plates, thin flat plates and membranes is their

response to static compressive stresses – whether they buckle or become wrinkled – or whether they possess a transverse compressive degree of freedom. Suspended graphene structures being only one atom thick with lengths and widths in the micron and nano scales, qualify with respect to spatial dimensions as very thin plates or as membranes, with their ratio of thickness to width (aspect ratios) being significantly smaller than $1/20$[115]. Due to the cost and level of complexity in running micro- and nano-scaled experimental vibrational analyses, almost all analyses of the vibrations of graphene sheets (GSs) reported in literature are analytical, numerical or semi-analytical; and are mostly based on nano-scaled graphene sheets. This is most likely because nano scaled GSs have aspect ratios that correspond to plates and beams, thereby justifying the application of established plate or beam theories, mostly with the introduction of a small-scale parameter to account for the miniscule sizes. No work has so far shown clearly what theories/analyses are best suited for the vibration analysis of different sized GSs, even though Arash and Wang[116] have shown that for GSs with lengths less than 8 nm the small scale effect must be incorporated to achieve accurate estimates of the resonant frequency.

Theoretical studies have gradually become the predominant approach to studying the mechanical behaviour of mostly nanostructured GSs. Theoretical modelling approaches can be classified into three categories: atomistic modelling, continuum mechanics and a combination of atomistic modelling and continuum mechanics[116, 117].

2.6.1 Atomistic and atomistic-continuum modelling

Atomistic modelling involves the representation and analysis of the behaviour of a system based on the interactions between the molecules or atoms of the system. Because of the number of atoms involved in the interactions and the resulting number of model equations, the help of computing software is needed to carry out these analyses. Macroscopic and microscopic quantities of interest can be derived from such analyses. Atomistic modelling includes techniques such as classical molecular dynamics (MD), Monte Carlo (MC), *ab initio*, molecular mechanics simulations, tight-binding molecular dynamics (TBMD) and density functional theory (DFT).

The MD technique is one of the most widely used numerical methods for studying the interactions between atoms or molecules of a system. It is basically built on the Newtonian equations of motion governing the interactions of the atoms or molecules in the system. Each atom or molecule in the system is treated as a point mass and Newton's equations are integrated to compute their motion. MD uses many-body interatomic potential functions to calculate the total energy of the system, from which the individual force equations of each atom is derived. The behaviour and properties of the system can be extracted from the computed motion of all the atoms/molecules in the system. The accuracy of the results from MD simulations largely depends on the choice of potential function for the system in question and the computing power used. Several potential functions have been developed and improved on to cater to the modelling of various material types and conditions, e.g. TIPS[118], UNICEPP[119], MM1 – MM2 – MM3 – MM4[120-123], AMBER – AMBER/OPLS[124, 125], Cornell[126], MMFF94[127, 128], CHARMM[129], COMPASS[130], Weiner[131], Morse[132], Tersoff – REBO – AIREBO[133-136], etc. Some of the methods employed in MD simulations include the Verlet, velocity Verlet and leapfrog methods.

The MC technique is based on the variation in states of the molecules of a system under a certain stochastic law. It does not use the equations of motion hence it cannot be used to determine the dynamic properties of the system, but is best suited for thermodynamic problems. However, MC techniques are still based on the interatomic potential functions. The *ab initio* techniques are potential-free techniques based on accurate solutions of the Schrödinger equation. Here the atomic forces are not derived from the potential functions but from the electronic structure and state of the atoms as defined by the Schrödinger equation. The molecular structural mechanics technique uses computational molecular mechanics terms in a structural mechanics framework to study the behaviour of the system. Here the covalent bond between two atoms is modelled as a structural beam element and the atoms at the ends of the bond modelled as point masses which form the joint with other bonds. The whole system is viewed as a space frame structure, and hence governed by structural mechanics theories/laws. According to structural mechanics theories, only three sectional stiffness parameters are needed for the analysis of the mechanical behaviour of a frame structure, viz. tensile/stretching, flexural and torsional stiffness parameters.

Therefore, the total steric potential energy, which omits interactions resulting from electrostatic forces, is used to describe the energy of the system, but with the potential energy due to van der Waals forces also neglected so that only the potential energy terms from stretching, bending and twisting are reflected. By imposing equivalency on the molecular potential energies and the elemental strain energy of the frame structure, the sectional stiffness parameters can be expressed in terms of the molecular mechanics force field constants. With the force field constants known, the sectional stiffness parameters can be obtained, and by employing the stiffness matrix solution procedure for frame structures the deformation, vibration and other related elastic behaviour of the system can be simulated.

In atomistic-continuum modelling, the molecular potential energies are also employed but rather than dealing with individual atoms and tracking the interactions between each atom, the interatomic potential is incorporated into the continuum model. This is done by equating the collective molecular potential energies of the atoms with the mechanical strain energies of the representative volume element of the continuum model.

Simulations based on MD and other atomistic modelling techniques including atomistic-continuum techniques have contributed greatly to the understanding of the mechanical behaviour of nanostructured materials. MD and continuum mechanics models have been used to comparatively study the transverse deformation of an SLGS[137]. The generalized tight-binding molecular dynamics (GTBMD) and *ab initio* techniques were used to investigate the nanoplasticity of SWCNT under uniaxial compression[138]. MD and GTBMD were used together to study the buckling behaviour of single and multiwalled carbon nanotubes[139]. Molecular structural mechanics method was implemented to study the vibrational behaviour of SLGSs[140]. TBMD and MD with the AIREBO potentials have been used to investigate the dependency of mechanical strength and properties of graphene under uniaxial tensile test on size and chirality[141]. Nonlocal continuum theory has also been used with MD simulations to study the free vibration of SLGSs and BLGSs[116]. Several other uses of molecular structural mechanics and MD in the study of carbon nanotubes and graphene are reported in literature[142-145]. Rafiee and Moghadam[146] extensively discussed the use of atomistic,

continuum and nano-scale continuum models to study the mechanical, vibrational, buckling and thermal properties of isolated carbon nanotubes.

Although atomistic modelling techniques yield accurate results, the size of the atomic systems they can analyse is limited. Because the length scale for coordinates in atomic systems is angstroms (Å), systems approaching even the sub-micron scale in dimension would be made up of several thousands or millions of atoms which must be simulated. Also, to accurately track the vibrational motion of the atoms, the timesteps used in the simulation is limited to the femtosecond (**fs**) scale. Which means that to even simulate picoseconds of the system's motion tens or hundreds of thousands of timesteps will be required. Therefore, due to the large number of atoms and timesteps needed, the atomistic modelling of the behaviour of GSs in the micron scale becomes prohibitively computationally expensive. Though several improved algorithms and new software have been developed to optimize MD calculations, and with current advances in hardware capacities and capabilities, atomistic modelling of relatively large systems remains computationally expensive. Which might explain why all atomistic modelling techniques used for GSs or CNTs in literature deal with nanostructures with sizes in tens of nanometers.

2.6.2 Continuum mechanics

Continuum mechanics has recently become the predominant tool for modelling nanomechanical structures. This explosion in interest and usage of continuum mechanics for the vibrational analyses of nano- and micro-mechanical structures can be attributed to the very high computational expenses of using atomistic and atomistic-continuum modelling and the complexity and cost of experimental methods. Several works have been published on the application of continuum mechanics theories to the study of the vibrations of GSs. These works can be classified based on several possible classification indices, including the method of formulation of the governing equations, linearity of the governing equations, consideration of the small scale effect in form of nonlocal elasticity theory and/or modified strain gradient elasticity, anisotropy of the material properties, number of GS layers, the solution method used, etc.

Chronological survey of the use of continuum mechanics for the vibrational analysis of graphene-based structures

In 2003, Peddieson et al.[147] first proposed and demonstrated the use of nonlocal continuum mechanics in nanomechanical systems. They formulated a nonlocal Bernoulli/Euler beam model to study the static response of nanobeams. The following year, a large-deflection model to study the static and dynamic responses of thin elastically isotropic films with nanoscale thickness based on von Karman's geometrically nonlinear theory for thin elastic plates and Kirchhoff's kinetic hypothesis was proposed[148]. In 2005, an explicit formula was derived to predict the vdW pressures between any two sheets of a MLGS and was used to develop the first continuum-plate model for the vibration of MLGSs[149, 150]. In the same year, the nanoscale vibration of MLGSs with anisotropic properties embedded in an elastic medium was analysed, in which Hamilton's principle was used to derive the governing equations of motion for the plate. The interactions between the graphene layers were modelled as carbon-carbon vdW pressure and those between the graphene and surrounding medium as polymer-carbon vdW pressure[151]. By 2006, the number of works on the vibration analyses of graphene structures had increased greatly but with a lot of emphasis on CNTs. The vibration of a double walled CNT with the interlayer vdW forces expressed as nonlinear functions of displacement was studied[152]. The nonlinear free vibration of multi-walled CNTs (MWCNTs) was modelled based on continuum mechanics and multiple-elastic beam model, and solved using the incremental harmonic balance method[153]. An elastic, multiple shell model was used to study the vibration of MWCNTs, in which vdW forces were modelled as a radius-dependent function and the effect of the vdW interaction modelling on the vibration characteristics of the tubes was determined[154]. A continuum-based plate model was used to derive the natural frequencies and corresponding modes of MLGSs embedded in an elastic matrix[155].

In the years that followed up to 2011, there was an explosion in the number of works published on the application of continuum mechanics to study the vibration of GSs, with an emphasis on nonlocal models. The nonlocal elasticity theory was used to study the vibration response of SLGSs embedded in an elastic medium[156]. Nonlinear free vibrations of embedded double walled CNTs were investigated based on Eringen's nonlocal elasticity theory and the von Karman

geometric nonlinearity within the framework of the Timoshenko beam model. The governing equations were derived using Hamilton's principle and solved with the differential quadrature (DQ) method[157]. The CLPT and first-order shear deformation theory (FSDT) were used for the vibration analysis of nanoplates, with the small-scale effect accounted for using Eringen's nonlocal theories and the model solved using Navier's solution. The same authors used nonlocal continuum mechanics to study the vibration analysis of MLGSs embedded in a polymer matrix, and investigated the effects of the nonlocal theories on the vibration of the sheets [158, 159]. The bending and stretching of a circular graphene sheet was characterized using von Karman plate theory[160]. A finite element nonlocal plate model was developed to study the vibrational characteristics of MLGSs with different boundary conditions embedded in an elastic medium[161]. The nonlinear free vibration of SWCNTs based on the von Karman geometric nonlinearity and Eringen's nonlocal elasticity theory for different boundary conditions was studied. The SWCNTs were modelled as nanobeams within the framework of the Timoshenko beam theory[162]. An investigation of the nonlinear vibration behaviour of a simply supported, rectangular SLGS in thermal environments modelled as a nonlocal orthotropic plate with von Karman's geometric nonlinearities was carried out. Where the nonlocal parameter value was estimated by matching the natural frequencies of the graphene sheets obtained from the numerical results with those from MD simulation results[163]. The nonlocal 3-D Navier equations of motion were reformulated and decoupled to study the vibration behaviour of nanoplates[164]. The large amplitude vibration of orthotropic MLGSs and the effect of the small-scale parameter on the vibration of the MLGSs were investigated using linear vdW interactions between any two layers. The vdW interactions were modelled as linear vdW pressures using the L-J potential with the coupled nonlinear equations of motion formulated using Hamilton's principle based on the von Karman nonlinear geometric model and Eringen's nonlocal theory, and solved with the harmonic balance (HB) method[165]. A nonlinear membrane model for the study of the vibrational properties of SLGSs was proposed and the finite difference method (FDM) used to solve the model[166]. The effects of nonlinear van der Waals interaction forces from a surrounding medium and adjacent nanotubes on the nonlinear vibration of an embedded DWCNT were investigated[167]. The effect of the small scale parameter on the buckling analysis of circular GSs under uniform radial compression was

investigated[168]. The small-scale effect on the vibration analysis of orthotropic SLGSs embedded in an elastic medium was investigated. Winkler- and Pasternak-type foundation models were used to model the interaction between the GS and the surrounding medium[169]. The nonlocal continuum theory was employed to study the free vibration of SLGSs and DLGSs. The dependence of the vibrational characteristics on small scale effects, sizes of sheets, boundary conditions and number of layers of the GSs was investigated. And MD simulations were used to verify the resonant frequencies obtained from the model[116]. The vibrational analysis of MLGSs with different boundary conditions amongst the sheets using an elastic multi-plate model with vdW forces modelling the interlayer forces was studied. A new GDQ method was used to obtain explicit formulas for the frequencies of a DLGS with all edges simply supported[170]. A nonlinear continuum model for studying the nonlinear vibration analysis of isotropic MLGSs with vdW interactions between any two layers was developed. The small-scale parameter was not incorporated in this model and the model was solved using the HB method[171]. In 2012, the nonlinear free and forced vibration of a BLGS embedded in a polymer medium was studied based on the nonlocal elasticity theory. With a refined pressure expression for the vdW forces between the GSs and the polymer medium, the in-phase and out-of-phase nonlinear and linear natural frequencies for both zigzag and armchair configurations were obtained[172].

In the last five years, the volume of works published on the vibration analysis of GSs have seemed to drop from what it was in the preceding five years. An exact solution for the vibration of DLGSs coupled by a viscoelastic medium simulated as a Visco-Pasternak layer was presented[173]. The nonlinear vibration of GSs using the CLPT and the nonlocal elasticity theory was modelled and solved numerically using the element-free kp-Ritz method[174]. In a separate paper[175], the same authors apply the kp-Ritz method to a nonlocal continuum model to obtain the solutions to the vibration analysis of quadrilateral-shaped GSs subjected to an in-plane magnetic field. The geometrically nonlinear vibration behaviour of DLGSs was studied using the von Karman plate model and the nonlocal elasticity theory. The element-free kp-Ritz method was used to solve the model[176].

2.7   Motion actuation, frequency tracking and sensitivity in mass sensors

Mass sensors as electromechanical systems have mechanical elements coupled to electronic circuits via electromechanical transducers which convert electrical energy into mechanical energy and vice versa in the actuation and sensing operations of the sensor. Critical to the success of a mass sensor is the ease of actuation of its resonator and sensing of the corresponding response, which could be motion or displacement. As the mechanical elements and systems of mass sensors shrink in size, the challenges of actuation and sensing increases. Thus, the actuation and detection of the displacements of micro- and nano resonators in mass sensor devices are among the most challenging aspects of the development of such technologies. A few established techniques for the actuation of dynamic mode mass sensors and their frequency tracking are presented in the ensuing subsections.

2.7.1 Motion actuation techniques in mass sensors

Three common techniques for motion actuation in resonant sensors are the electrostatic, piezoelectric and magnetomotive techniques.

Electrostatic or capacitive actuation technique

In the electrostatic technique, the attractive force developed between the plates of a capacitor when the plates are charged is used to drive the resonator. To achieve electrostatic actuation in MEMS/NEMS, a gate electrode is usually fabricated in the vicinity of the MEMS/NEMS device as shown in Figure 2-22, or the electrostatic potential is applied through the substrate. In electrostatic actuation, the capacitance of the actuation gate is usually in parallel with the parasitic capacitance, which is larger than the gate capacitance by many orders of magnitude. The effect of this is the reduction of the efficiency of actuation at high frequencies. A demonstration of electrostatic actuation in NEMS at frequencies as high as 700 MHz has been reported[177].
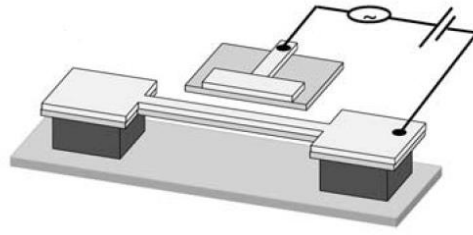
Figure 2-22: Electrostatic actuation in NEMS[178]

Piezoelectric actuation technique

Piezoelectric transducers generate electrical energy when strained and vice versa. When an ac voltage is applied across piezo-transducers, they are strained alternatingly and consequently actuated into vibration. Piezoelectric transducers have been employed as sensing elements in many applications because they are rugged, have extremely high natural frequencies and exhibit excellent linearity over a wide amplitude range. Ideally, in mass sensing applications, the resonator should be fabricated from piezoelectric materials such that the direct application of voltage to the resonator actuates it directly. However, in cases where fabricating resonators from piezoelectric materials is impracticable, piezoelectric shakers can be used to excite the whole unit.

Magnetomotive actuation technique

The magnetomotive technique employs Lorentz force, which is generated when a current-carrying conductor is placed in a static magnetic field, for motion actuation. In this technique, an ac current at frequency ω is driven through the micro- or nanomechanical beam element in the presence of a strong magnetic field (Figure 2-23). The force acting on the beam is

$$F(\omega) = lBI(\omega) \tag{2-1}$$

expressed in the frequency domain, where $I(\omega)$ is the harmonic drive current, l is the length of the beam and B is the magnetic field strength.
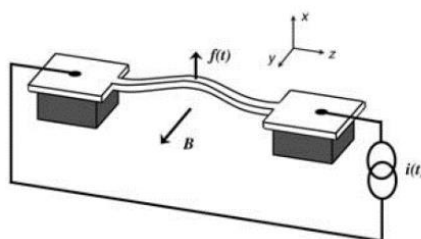
Figure 2-23: Magnetomotive actuation scheme (Lorentz force used to drive mechanical element)[178]

42

The actuation force can be applied in the in-plane or out-of-plane direction depending on the orientation of the nanomechanical beam element with respect to the magnetic field. The harmonic displacement of the centre of the beam is expressed as

$$X(\omega) = \frac{lBI(\omega)}{m_{eff}\left(\omega_0^2 - \omega^2 + \frac{i\omega\omega_0}{Q}\right)}$$

(2-2)

Magnetomotive actuation of MEMS/NEMS has proven to be an excellent actuation technique especially that it is not impeded by parasitic capacitances. The major drawback being the very strong magnetic fields needed to generate Lorentz force.

2.7.2 *Detection techniques and frequency tracking in mass sensors*

Dynamic-mode mass sensors detect the mass of an accreted molecule by detecting the change in frequency of the sensing resonator. The mass effect of the accreted molecule on the resonance frequency of the sensing resonator depends on the accretion position and the vibration mode of the resonator. To be able to detect any change in frequency, the frequency of the resonator must be tracked. The problem of tracking the resonator's frequency is the problem of continuously detecting its minuscule displacement amplitudes. This is a more daunting task than the actuation of the resonators. Some frequency tracking techniques are discussed in this subsection.

Magnetomotive detection technique

The magnetomotive detection technique is complimentary to the magnetomotive actuation technique. Here, a uniform magnetic field is provided, through which the conducting resonator moves. The time-varying flux that results from the movement of the resonator through the magnetic field generates an induced electromotive force in the electrical loop, which is detected in the detection circuit. With the minuscule displacements typical of MEMS/NEMS devices, the induced emf is extremely small and will need to be boosted with a low-noise amplifier. Figure 2-24 shows a schematic representation of a magnetomotive transducer coupled to an amplifier represented by a standard amplifier model with uncorrelated voltage and current noise sources.
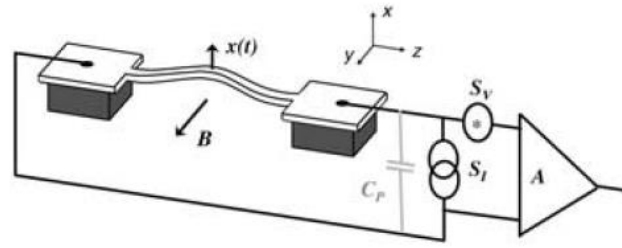
Figure 2-24: Magnetomotive displacement detection technique[178]

For a doubly clamped beam, the emf generated is given by

$$v_0(t) = \xi lB\dot{x}(t) \tag{2-3}$$

Where B is the magnetic field strength, l is the length of the beam $x(t)$ the displacement at the centre of the beam and ξ is a geometric factor whose value for a doubly clamped beam is ~0.885.

The noise power generated in the amplifier determines the displacement sensitivity, which is expressed as[178]

$$[S_X(\omega)]^{1/2} = \left(\frac{S_V(\omega)}{(\xi lB\omega)^2} + \frac{S_I(\omega)l^2B^2}{m_{eff}^2(\omega_0^2 - \omega^2)^2 + \frac{\omega^2\omega_0^2}{Q^2}} \right)^{1/2} \tag{2-4}$$

Implementing the magnetomotive detection method with NEMS devices that are actuated electrically (magnetomotive or electrostatic) poses major challenges. First, the detection bandwidth will most likely be affected by parasitic capacitances in the detection circuit. Secondly, the parasitic coupling between the input and the output reduces the degree of orthogonality of the actuation and detection transducers, which means that the actuation process will generate huge noise signals in the detection process.

Capacitive detection technique

The capacitive detection technique is based on the change in capacitance of a capacitor as the distance between the plates change. The motion of the resonator effectively modulates the capacitance between the element and a fixed gate (Figure 2-25). The method of detection uses a bias voltage or current across the capacitor that monitors for a change in the current or voltage respectively of the capacitor. Consequently, a capacitance change at constant voltage will

generate a current flow across the capacitor. This is easily seen from the definition of capacitance:

$$dQ = VdC + CdV \qquad\qquad (2\text{-}5)$$
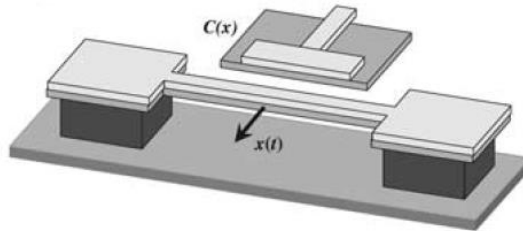
Figure 2-25: Capacitive detection technique[178]

On a MEMS scale, the dynamic capacitance changes due to the motion of the mechanical element are usually in the $10^{-9} - 10^{-12}$ F range, which can readily be detected given the typically low operation frequency range of MEMS devices. In contrast, NEMS devices have typical capacitance modulations in the $10^{-16} - 10^{-18}$ F range, while parasitic capacitances of the chip and the circuitry may be many orders of magnitude larger[178].

Optical detection technique

When a beam of light is incident on a vibrating resonator, the reflected beam is modulated by its motion. Optical detection techniques focus a laser beam on a resonator in motion and detect the motion by sensing the modulated reflected beam using photodetectors. The setup includes a laser source which generates the laser beam, a focusing lens to focus the beam on the vibrating resonator, prisms and mirrors to reflect the beams, and a photodetector that converts the incident beam to voltage or current. A schematic representation of an optical detection technique arrangement for a Laser Doppler Vibrometer.
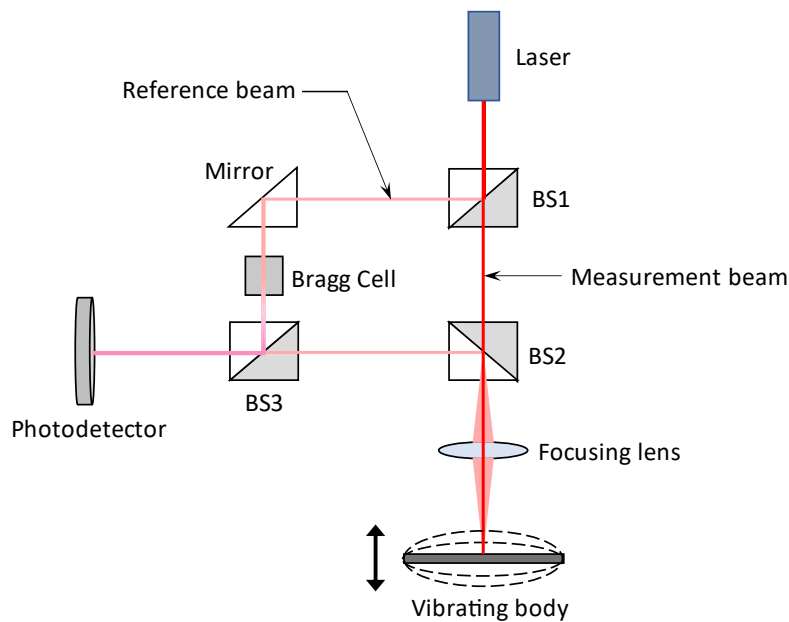
Figure 2-26: Schematic representation of an optical detection technique arrangement

Frequency tracking using Phase Locked Loops (PLLs)

Phase locked loops (PLLs) are one of the commonly used frequency tracking techniques in mass sensing applications. A schematic representation of a PLL setup is shown in Figure 2-27. A basic setup would include a phase detector or comparator, a voltage-controlled oscillator (VCO), and a low pass filter hooked up with the source of the reference signal. PLLs are designed to generate an output signal that matches the reference signal by detecting the phase difference between the two signals. The phase detector evaluates the phase difference between the reference and VCO signals connected to its input ports, and outputs an error voltage corresponding to the phase difference. The low pass filter connected between the phase detector and the VCO removes any high frequency noise elements from the error voltage and governs the stability and lock speed of the PLL. The VCO generates the output signal and the phase detector input signal using the error voltage as its tuning voltage.
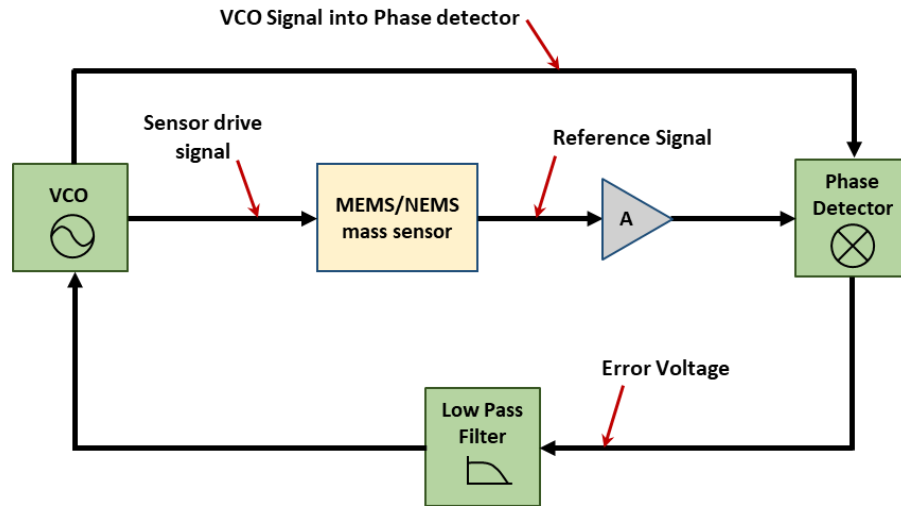
Figure 2-27: Phase-locked loop (PLL) diagram with basic components

At the initial stages of operating the loop, the reference signal and the VCO signal are not locked, meaning they are at different frequencies with a phase difference. The error voltage tunes the VCO to match or 'lock' its signal with the reference signal. With a locked reference and VCO signal, if there are changes in the reference signal frequency, the error voltage is modified to drive the VCO signal frequency to match the new reference signal frequency.

2.7.3 Responsivity and mass resolution

Ultrasensitive sensors are vital in various fields and are thus the focus of recent research works in sensing and instrumentation. The definition and meaning of a sensor's responsivity and resolution depends on the type of sensor and the transduction method employed in the sensor. The responsivity and resolution for mass sensors are briefly discussed in this subsection.

The responsivity of a mass sensor is the ratio of the shift in the frequency of its resonator to the mass accreted on it; this is a measure of how responsive the sensor is to mass accretion. On a calibration curve for a mass sensor, where the frequency shifts of the sensor are plotted against the accreted masses, the responsivity is the slope of the curve – Figure 2-28 illustrates this schematically. To calibrate a mass sensor and hence determine its responsivity, the resonance frequency ω_0 of the functionalized resonator is first determined, then the frequency shifts in steady state $\Delta\omega_0$ when masses Δm are accreted on the resonator are monitored recorded.
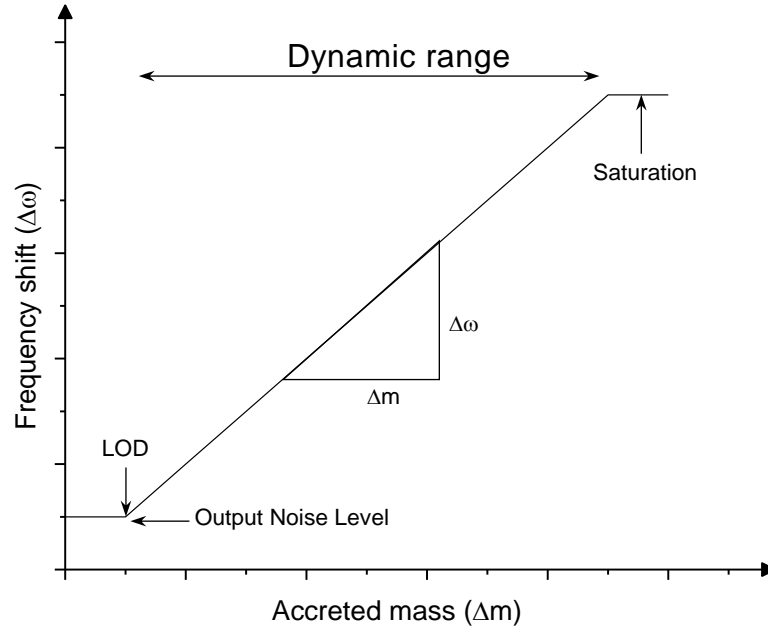
Figure 2-28: Schematic representation of a calibration curve for a mass sensor

Assuming Δm is much smaller than the effective mass m_{eff} of the resonator, the responsivity is given as,

$$\mathcal{R} = \frac{1}{2\pi}\frac{\partial \omega_0}{\partial m_{eff}} = -\frac{\omega_0}{4\pi\, m_{eff}} \tag{2-6}$$

The resolution or sensitivity of a mass sensor is the smallest mass it can detect. As has been assumed for equation (2-6), when $\Delta m \ll m_{eff}$ the mass resolution is given as in equations (2-7) and (2-8)[179, 180]. This minimum detectable mass critically depends on the minimum measurable frequency shift of the resonator and the inverse responsivity of the sensor, as is shown in equation (2-7).

$$\Delta m \approx \frac{\partial m_{eff}}{\partial \omega_0}\,\Delta \omega_0 = \mathcal{R}^{-1}\Delta \omega_0 \tag{2-7}$$

$$\Delta m \approx -4\pi\frac{m_{eff}}{\omega_0}\Delta \omega_0 \tag{2-8}$$

The quality factor of a resonator at a resonance frequency is a measure of how quickly the oscillations of the resonator will die out. Typically expressed as $Q = \omega_0/\delta\omega$, where $\delta\omega$ is the full width at half maximum (FWHM) of the resonance. The resonance frequency expressed in terms of Q when substituted in equation (2-8) results to

$$\Delta m \approx -4\pi \frac{m_{eff}}{Q\delta\omega}\Delta\omega_0 \qquad\qquad (2\text{-}9)$$

If Q remains constant, the mass sensitivity of the sensor is directly proportional to the effective mass of the resonator and the minimum measurable frequency shift, which implies that a bigger m_{eff} and $\Delta\omega_0$ will yield a higher sensitivity. The effective mass of the resonator in measurement mode comprises the mass of the resonator and the accreted mass. The amount of the accreted mass is however the determining factor for the frequency shift, and for the minimum measurable frequency shift in a noiseless system. Therefore, the higher the component of the accreted mass in m_{eff}, the bigger the frequency shift and consequently, the higher the sensitivity of the sensor. When graphene is used as the sensor resonator, it promises to improve the sensitivity of the sensor because being an ultra-low mass material with thickness tending to zero, any accreted mass will make up a huge portion of m_{eff} and in turn generate a big $\Delta\omega_0$. In addition, its high Elastic modulus makes it possible to carry such disproportionately large masses without breaking.

In a damped and noisy system, the minimum measurable frequency shift $\Delta\omega_0$ depends on the noise profiles in the system and the readout technique. An estimate of $\Delta\omega_0$ is given as[179]

$$\Delta\omega_0 \approx \left[\int_{\omega_0-1/2\tau}^{\omega_0+1/2\tau} S_\omega(\omega)\,d\omega\right]^{1/2} \qquad\qquad (2\text{-}10)$$

$S_\omega(\omega)$ is the weighted effective spectral density of the frequency fluctuations in $(rad/s)^2/(rad/s)$. It depends heavily on the physical noise processes operative in the sensor system as well as the readout process employed. Noise in the sensor system could originate from several sources, the principal sources for MEMS resonant structures being: the thermally driven random motion of the resonator (thermo-mechanical), large temperature fluctuations, and adsorption-desorption processes[181]. Such noises attenuate the sensitivity of the sensor. Ultra-high mass sensitivities such as yocto-, and zepto-gram mass sensitivities reported in literature are achieved in vacuum and usually under cryogenic conditions, in which damping and noise are greatly reduced. However, in several real-life situations where mass sensing is applied, measurements are generally

made in dissipative media and under room temperature conditions. As such, it is critical that considerations of noise and damping for such systems be made in the analysis and prediction of their sensitivity and performance.

Thermo-mechanical noise

Thermomechanical noise is a consequence of the interaction of the resonator with the surrounding fluid, the resonator is driven into random motion by imbalances in the surrounding fluid's thermal energy. The spectral density of these random displacements is given as

$$S_x(\omega) = \frac{1}{m_{eff}} \frac{4\omega_0 k_B T}{Q \left[(\omega^2 - \omega_0^2)^2 + \omega^2 \omega_0^2 \big/ Q^2 \right]}$$

(2-11)

Where k_B is Boltzmann's constant, T the resonator temperature, and Q the resonator's quality factor. For a phase locked loop (PLL) readout scheme driven by a constant-amplitude voltage-controlled oscillator (VCO) assumed to be noiseless, the thermally induced random displacements give rise to frequency fluctuations in the sensor output, which have an effective spectral density given by[179]

$$S_\omega(\omega) \approx \frac{\omega_0^5}{Q^3} \frac{k_B T}{E_c} \frac{1}{(\omega^2 - \omega_0^2)^2 + \omega^2 \omega_0^2 \big/ Q^2}$$

(2-12)

Here, $E_c = m_{eff} \omega_0^2 \langle x_c^2 \rangle$ is a representation of the maximum drive energy delivered by the VCO to the resonator, where $\langle x_c^2 \rangle$ is the mean square amplitude of the resonator. The minimum measurable frequency shift $\Delta\omega_0$ for the noisy system is obtained by evaluating the integral in equation (2-10) using equation (2-12). Subsequently, the mass sensitivity is determined using equation (2-8). For a resonator with $Q \gg 1$ and $2\pi\Delta f \ll \omega_0/Q$ (where Δf is the measurement bandwidth), the minimum measurable frequency shift and mass sensitivity are evaluated as[179]

$$\Delta\omega_0 \approx \left[\frac{k_B T}{E_c} \frac{\omega_0 \Delta f}{Q} \right]^{1/2}$$

(2-13)

and

$$\Delta m \approx 2m_{eff} \left(\frac{k_B T}{E_c}\right)^{1/2} \left(\frac{\Delta f}{Q\omega_0}\right)^{1/2} \tag{2-14}$$

Large temperature fluctuations

Large temperature fluctuations can induce frequency fluctuations in a mass sensor's output, due to the size of the resonators. The degree of susceptibility to such fluctuations depends on the thermal contact of the resonator to the environment. For a materially isotropic doubly-clamped resonator of constant cross section with a uniformly distributed thermal transport model, where such large temperature fluctuations exist, the spectral density of the induced frequency fluctuations can be expressed as[179, 182]

$$S_\omega(\omega) = \left(-\frac{22.4 c_s^2}{\omega_0^2 l^2}\alpha_T + \frac{2}{c_s}\frac{\partial c_s}{\partial T}\right)^2 \frac{\omega_0^2 k_B T^2}{\pi g[1 + (\omega - \omega_0)^2 \tau_T^2]} \tag{2-15}$$

Where $c_s = \sqrt{E/\rho}$ is the temperature dependent speed of sound; $\alpha_T = (1/l)\,\partial l/\partial T$ is the linear thermal expansion coefficient, g the thermal conductance, and τ_T the thermal time constant of the resonator. Evaluating the integral in equation (2-10) using equation (2-15), the minimum measurable frequency shift can be expressed as

$$\Delta\omega_0 = \left[\frac{1}{2\pi^2}\left(-\frac{22.4 c_s^2}{\omega_0^2 l^2}\alpha_T + \frac{2}{c_s}\frac{\partial c_s}{\partial T}\right)^2 \times \frac{\omega_0^2 k_B T^2}{g}\frac{arctan\,(2\pi\Delta f\tau_T)}{\tau_T}\right]^{1/2} \tag{2-16}$$

and the mass sensitivity as

$$\Delta m = \frac{2}{\pi^{1/2}} 2m_{eff}\left(-\frac{22.4 c_s^2}{\omega_0^2 l^2}\alpha_T + \frac{2}{c_s}\frac{\partial c_s}{\partial T}\right) \times \left[\frac{k_B T^2\,arctan\,(2\pi\Delta f\tau_T)}{g\tau_T}\right]^{1/2} \tag{2-17}$$

Adsorption-desorption noise

Gas molecules in the surrounding medium of a resonator can be adsorbed on the resonator surface, mass loading it and consequently changing its resonant frequency. Thermally induced random adsorption and desorption of molecules will therefore cause frequency fluctuations in the sensor output. A cycle of adsorption-desorption can be modelled by a flux-dependent adsorption rate and a thermally activated desorption rate. The adsorption rate is expressed as

$$r_a = \frac{2}{5}\frac{p}{\sqrt{mk_BT}}s \qquad\qquad (2\text{-}18)$$

and the desorption rate as

$$r_d = v_d\, exp\left(-\frac{E_b}{k_BT}\right) \qquad\qquad (2\text{-}19)$$

Where m is the mass of one gas molecule, p and T are the gas pressure and temperature respectively, E_b is the binding energy between the resonator surface and the gas molecule. s is the sticking coefficient with values $0 < s < 1$ and v_d the desorption attempt rate, $v_d \sim 10^{13}Hz$. The adsorption and desorption rates depend on the resonator and surrounding medium temperature, the nature of the resonator surface and its treatment, the adsorption gas species, among other factors. The spectral density of the frequency fluctuations caused by adsorption and desorption is given as[179, 182]

$$S_\omega(\omega) = \frac{2\pi\omega_0^2 N_a\sigma_{occ}^2\tau_r}{(1 + (\omega - \omega_0)^2\tau_r^2)}\left(\frac{m}{m_{eff}}\right)^2 \qquad\qquad (2\text{-}20)$$

Where N_a is the number of compromising sites for adsorption, σ_{occ}^2 is the variance in the probability of occupying a site, estimated as $\sigma_{occ}^2 = r_ar_d/(r_a + r_d)^2$, and τ_r is the correlation time for an adsorption-desorption cycle, expressed as $\tau_r = 1/(r_a + r_d)$.

The minimum measurable frequency shift upon evaluating equation (2-10) with equation (2-20) is given as

$$\Delta\omega_0 = \frac{1}{2\pi}\frac{m\omega_0\sigma_{occ}}{m_{eff}}[N_a arctan\,(2\pi\Delta f\tau_r)]^{1/2} \qquad\qquad (2\text{-}21)$$

and the mass sensitivity as

$$\Delta m \approx \frac{1}{2\pi}\,m\sigma_{occ}[N_a arctan\,(2\pi\Delta f\tau_r)]^{1/2} \qquad\qquad (2\text{-}22)$$

2.8   Conclusion

An extensive review of various aspects of graphene as a material has been presented and discussed in this chapter. With a strong interest in using graphene

for biosensing applications, a general overview of biosensors and biosensing applications has been presented. Different types of biosensors have been discussed, including mass biosensors for which graphene resonators have a huge potential. The world of graphene was briefly explored: its properties, production, microfabrication, and characterization. The theory of Raman spectroscopy was presented and its use as a powerful tool for identifying graphene as a material with its characteristic G and 2D bands. The evolution of the bands, especially the 2D band, with increasing layers of graphene was also discussed and highlighted as a means of differentiating layered graphene membranes. An introduction to the theoretical vibration analysis of graphene was made, in-depth discussions are however presented in Chapter 3. A few actuation and sensing techniques for resonators in MEMS/NEMS were presented; brief discussions were made on the use of PLLs to track the resonator's frequency. Finally, the responsivity and mass sensitivity of mass sensors were discussed for both noiseless and noisy systems. Ultra-high mass sensitivities of atto-, zepto-, and even yoctograms have been reported in literature – these have mostly been achieved with nanosized CNTs or graphene operating at ultra-high resonant frequencies. Using equation (2-8), the devices developed from the micro-sized resonators studied in this work should have femtogram mass sensitivities or in the least should have LODs in the $10^{-13} - 10^{-14}$ range to be considered successful.

Chapter 3: Vibration analysis of rectangular-shaped graphene resonators

3.1   Introduction

In this chapter, the vibration analysis of single layer graphene sheets (SLGSs) and multi-layer graphene sheets (MLGSs) with a focus on double layer graphene sheets (DLGSs) is explored. The derivation of governing equations and solution methods, and their application to SLGSs or DLGSs with various boundary conditions are looked at in detail. The limit of the applicability of various continuum-based analytical models to different sizes of GSs is determined. And numerical solutions are adopted and adapted for the modal analysis of micro-scaled DLGSs to be compared with experimental solutions.

3.2   Continuum mechanics models for graphene sheets

This work further explores the continuum models used for the vibration analysis of graphene sheets. As mentioned in section 2.6, these models can be classified based on a number of classification indices, including the approach used to formulate the governing equations, linearity of the governing equations, consideration of the size effect in form of the nonlocal elastic theory or modified strain gradient elasticity, anisotropy of the material properties, and number of layers.

When considering the formulation approach, the governing equations of a continuum model can be formulated by following 1) the dynamic equilibrium approach, through which the classical plate theory (CLPT) or Kirchhoff plate model and the Mindlin plate model which is based on a first order shear deformation theory (FSDT) are derived; 2) the variational method; and 3) the integral equation formulation method. These approaches are built around the maxima or minima or the equilibrium of forces or energy – which yields the equations of motion by considering the balance of forces acting on or the energy distribution in the model.

Based on linearity of the governing equations, the governing equations can be classified as 1) Linear – where all the basic components of the vibration of the sheets (mass, spring and damper components) behave linearly, and 2) Nonlinear – where the vibration is not linear. Practically, the vibration of most structures in

mechanics are linear up to displacements in the order of their thicknesses. With graphene being one atom layer thick and MLGSs a few nanometers thick, the vibrations of GSs are generally considered to be nonlinear. To model nonlinearity in these sheets, geometric nonlinearity is mostly considered rather than material nonlinearity.

Continuum models when applied to micro/nano-systems have been found to overestimate the properties of the systems[116]. This may be because the assumptions made in the formulation of the models only hold true for macro-systems. To account for this size or small-scale effect several new continuum theories have been reported in literature which modify the existing models to predict the properties and behaviour of micro/nano-systems more accurately. Two of such theories are considered here: 1) nonlocal elasticity theory – which is based on the dependence of the stresses in the sheets on nonlocal strain components and is the most widely used small scale effect theory for vibration of nanostructures. 2) strain gradient elasticity – which accounts for the effects of higher order stress gradients and strain gradient nonlocality.

Based on the directionality of the properties of materials, the GSs can be modelled as being 1) Isotropic – with the material properties, e.g. Young's modulus, being same in every direction. And 2) Anisotropic – the material properties varying with change in direction. For GSs, because of the hexagonal layout of the carbon atoms, material properties like the Young's modulus are orthotropic.

In modelling the vibration of GSs, the sheets can be 1) Single-layered – referred to as SLGSs and is simply one sheet of graphene modelled as a single thin plate, beam, or membrane. Or 2) Multi-layered – referred to as MLGSs, which could be 2 layers (DLGSs) or more modelled as composite plates. For MLGSs, the interaction between the layers is widely modelled as van der Waal's (vdW) pressure using the Lennard-Jones (L-J) potential, or less widely as Winkler-type strings. It is also possible to estimate the equivalent properties of the MLGSs using the standard rule of mixture for unidirectional composite plates.

The solution methods that have been employed in solving nonlinear systems can be broadly classified into analytical and semi-analytical methods. Some of such

solution methods that have been used for nonlinear systems include: 1) Perturbation methods 2) Harmonic Balance (HB) method 3) Differential Quadrature Method (DQM) and its modifications 4) Element-free kp-Ritz method 5) Finite Difference Methods (FDM).

3.2.1 Theories accounting for size effect

As the sizes of plates decrease into micro/nano scales, the plate transits from being a true continuum to a matrix of atoms acting as discrete mass points interconnected by the atomic bonds. This might explain why, as earlier mentioned, the direct application of continuum models to nano-systems have been found to overestimate the properties of the systems[116]. Furthermore, experiments on metals and polymers have shown that the size-dependency of mechanical properties and physical responses of materials on a microscale or microsystems are tangible and should not be overlooked[183-185]. To account for the size effect on the properties and responses of micro- and nano- structures, new continuum theories have been proposed such as the plastic strain gradient theory[183, 186, 187], modified couple stress theory[188], nonlocal elasticity theory[189], and strain gradient theory[184], among others.

The scope of this work allows for a focus on the size effects in elasticity, which manifest in a stiffness softening or hardening response when the structure is loaded. Hence, the most used theories for size effects in elasticity: the nonlocal elasticity and strain gradient theory are briefly discussed.

Nonlocal Elasticity theory

To account for the long-range interaction between atoms in a discretized mass system, Eringen, "in accordance with atomic theory of lattice dynamics and experimental observations on phonon dispersion" proposed the nonlocal elasticity theory[189]. The nonlocal elasticity theory states that the stress at a reference point x in an elastic continuum is not just a function of the strain field at that point but a function of the strain field at every point x' in the continuum. For homogenous and isotropic elastic solids, the nonlocal stress tensor σ at point x is expressed as[189]

$$\sigma = \int_V \alpha(|x' - x|, \tau)\, \sigma'(x') dv(x') \qquad (3\text{-}1)$$

$$\alpha(|x|, \tau) = (2\pi l^2 \tau^2)^{-1} K_0 \left(\frac{\sqrt{x.x}}{l\tau} \right) \tag{3-2}$$

$$\tau = {e_0 a}/{l} \tag{3-3}$$

Where $\alpha(|x' - x|, \tau)$ is the nonlocal modulus, $\sigma'(x')$ is the macroscopic stress tensor at x' which is related to the strain tensor at any point x' in the continuum at time t, and $\int_V$ is the volume integral over the region V occupied by the continuum body. K_0 is the modified Bessel function, a is an internal characteristic length such as bond length or granular distance, l is an external characteristic length, and e_0 is a constant appropriately selected for each material to calibrate the model to match experimental results.

The macroscopic stress tensor is related to strain by the generalized Hooke's law as[190]

$$\sigma'(x') = C_{kl} \varepsilon_{kl}(x') \tag{3-4}$$

Where C_{kl} is the fourth-order elasticity tensor and ε_{kl} is the strain tensor.

The integral constitutive relation in equation (3-1) can be rewritten in a differential form as[162, 191]

$$(1 - \tau^2 l^2 \nabla^2)\sigma = \sigma' \tag{3-5}$$

Which reduces to the form most commonly used in literature

$$\boxed{(1 - \mu\nabla^2)\sigma = \sigma'} \tag{3-6}$$

Where $\mu = (e_0 a)^2$ is the small scale or nonlocal parameter and ∇^2 is the Laplacian operator ($\nabla^2 = \frac{\partial^2}{\partial x^2} + \frac{\partial^2}{\partial y^2}$ for two dimensional models).

In the limit that the effects of the strain field at the points x' are ignored in the consideration of the stress at the reference point x i.e. $\mu = 0$, the classical (local) elasticity theory is recovered. Arash and Wang[192] provide a good review of the nonlocal elasticity theory and its application in the modelling of CNTs and graphene.

Nonlocal strain gradient elasticity theory

It has been argued that Eringen's nonlocal elasticity theory does not adequately capture the size effect in the analysis of nanostructures as its use of only the nonlocal parameter only introduces stiffness-softening effects but neglects the stiffness-hardening effect reported by the strain gradient theory[193]. Therefore, Eringen's nonlocal elasticity theory is generalized to include the strain gradient effect by considering higher-order stress gradients and strain gradient nonlocality[194]. The stress function is expressed in the nonlocal strain gradient elasticity theory as

$$\sigma_{ij} = \sigma_{ij0} - \frac{d\sigma_{ij1}}{dx} \tag{3-7}$$

where σ_{ij0} and σ_{ij1} are the stresses related to the strain ε_{ij} and strain gradient $d\varepsilon_{ij}/dx$ respectively, and are given as

$$\sigma_{ij0} = \int_0^L C_{ijkl}\alpha_0(x,x',e_0a)\,\varepsilon'_{kl}(x')dx'$$

$$\tag{3-8}$$

$$\sigma_{ij1} = l^2 \int_0^L C_{ijkl}\alpha_1(x,x',e_1a)\frac{d\varepsilon'_{kl}}{dx}(x')dx'$$

where C_{ijkl} are the elastic constants, e_0a and e_1a are the nonlocal parameters accounting for the nonlocal stress field, l is the length scale parameter and $\alpha_m(x,x',e_0a); m = 1,2$ is the nonlocal modulus given in equation (3-2). Equation (3-7) is multiplied by the linear nonlocal differential operator, $(1-\mu\nabla^2)$, to derive the constitutive relation for the nonlocal strain gradient elasticity theory as[193]

$$(1-(e_0a)^2\nabla^2)(1-(e_0a)^2\nabla^2)\sigma_{ij}$$
$$= \boldsymbol{C_{ijkl}}(1-(e_1a)^2\nabla^2)\varepsilon_{kl} - \boldsymbol{C_{ijkl}}l^2(1-(e_1a)^2\nabla^2)\nabla^2\varepsilon_{kl} \tag{3-9}$$

Which reduces, with the assumption that $e_0 = e_1 = e$ and $(ea)^2 = \mu$, to

$$(1-\mu\nabla^2)\sigma_{xx} = C(1-l^2\nabla^2)\varepsilon_{xx} \tag{3-10}$$

Equation (3-10) is the generalized constitutive relation for the nonlocal strain gradient elasticity theory.

3.2.2 Modelling inter-layer interactions

The interaction between layers of GSs and other materials deposited on them or the surrounding medium in which they vibrate, e.g. in liquids, have an impact on the vibrations of the sheets and should be considered in their vibration analysis. Two considerations for modelling these interactions will be discussed in this subsection: van der Waals interaction model and the Pasternak foundation model.

Van der Waal's (vdW) interaction between graphene sheets

The interaction between any two GS layers is a non-bonded interaction that can be an attraction or a repulsion force. This interaction is ubiquitously attributed to van der Waal's (vdW) forces, which are derived from the Lennard-Jones (LJ) pair potential.

The Lennard-Jones potential also called the Lennard-Jones 6-12 model is given as

$$V_{LJ}(\bar{d}) = 4\varepsilon \left[\left(\frac{\sigma}{\bar{d}}\right)^{12} - \left(\frac{\sigma}{\bar{d}}\right)^{6} \right] \tag{3-11}$$

Where $\bar{d}$ is the distance between the interacting atoms, ε is the depth of potential, and σ is a parameter that is determined by the equilibrium distance.

Rappe et al.[195] in presenting a universal force field for molecular mechanics and molecular dynamics simulations express the Lennard-Jones potential between any two atoms of any given element as

$$E_{vdW} = D_{IJ} \left[\left(\frac{x_{IJ}}{x}\right)^{12} - 2\left(\frac{x_{IJ}}{x}\right)^{6} \right] \tag{3-12}$$

Where D_{IJ} is the well depth or the depth of potential in kcal/mol and x_{IJ} is the van der Waals bond length in Å. D_{IJ} and x_{IJ} for any pair of atoms I and J are found by using a geometric mean combination rule for distance.

$$D_{IJ} = \left(D_I D_J\right)^{1/2} \tag{3-13}$$

$$x_{IJ} = \sqrt{x_I \times x_J} \tag{3-14}$$

Where x_I is the van der Waals distances and D_I the atomic van der Waals energy. Values for x_I and D_I for atoms of different elements have been published[195].

The vdW force, F, is obtained from the Lennard-Jones pair potential by taking the derivative of same with respect to the distance between the interacting atoms. For the LJ pair potential in equation (3-11), the vdW force is derived as

$$F(\bar{d}) = -\frac{dV_{LJ}}{d\bar{d}} = \frac{24\varepsilon}{\sigma}\left[2\left(\frac{\sigma}{\bar{d}}\right)^{13} - \left(\frac{\sigma}{\bar{d}}\right)^{7}\right] \qquad (3\text{-}15)$$

The vdW force can be estimated by the Taylor expansion around the equilibrium position $\bar{d}$ with the odd functions of $\bar{d}$ ignored. Since the initial vdW pressure is negligible at the equilibrium distance, the first term in the expansion is always set to zero. The vdW force can be modelled as a linear function by truncating the Taylor expansion to the first order. In that case, the vdW force becomes

$$F(\bar{d}) = -\frac{24\varepsilon}{\sigma^2}\left[26\left(\frac{\sigma}{\bar{d}_0}\right)^{14} - 7\left(\frac{\sigma}{\bar{d}_0}\right)^{8}\right](\bar{d} - \bar{d}_0) \qquad (3\text{-}16)$$

Where $\bar{d}_0$ is the initial distance between atoms of the different graphene layers, given as[171]

$$\bar{d}_0 = \sqrt{\left(x_j - x_i\right)^2 + \left(y_j - y_i\right)^2 + \left(z_j - z_i\right)^2} \qquad (3\text{-}17)$$

When only infinitesimal vibrations are being modelled, it suffices to assume that the vdW interaction is linearly proportional to the transverse displacements of the GSs[150, 155]. However, Jomehzadeh et al.[172] argues that since the vdW force as expressed in equation (3-15) is a highly nonlinear function of distance, it is not reasonable to model it as a linear function. In other works[171], the vdW force is also modelled as a nonlinear function to develop a geometrically nonlinear continuum mechanics model. To model a nonlinear vdW force, the Taylor expansion is truncated to the third order and the vdW force becomes

$$\begin{aligned}F(\bar{d}) = &-\frac{24\varepsilon}{\sigma^2}\left[26\left(\frac{\sigma}{\bar{d}_0}\right)^{14} - 7\left(\frac{\sigma}{\bar{d}_0}\right)^{8}\right](\bar{d} - \bar{d}_0)\\ &-\frac{336\varepsilon}{\sigma^4}\left[65\left(\frac{\sigma}{\bar{d}_0}\right)^{16} - 6\left(\frac{\sigma}{\bar{d}_0}\right)^{10}\right](\bar{d} - \bar{d}_0)^3\end{aligned} \qquad (3\text{-}18)$$

Any two layers in an MLGS can be AA- or AB- stacked, depending on the positions of the atoms in the top layer relative to those in the layer immediately beneath it. In an AA-stacking, the carbon atoms in one layer are stacked directly on top of those in the layer beneath it, while in an AB-stacking the atoms in one layer are located directly above the center of the Brillouin zone of the layer beneath it (see Figure 3-1). Since the vdW force acts along the atoms' direction, for AA-stacked layers the force acts in the z direction but this is not the case for AB-stacked layers. Therefore, to find the vdW interaction pressure between any two layers in the z direction, the vdW force needs to be projected along the z direction, divided by the area occupied by one atom, and then integrated over the entire sheet.

a)   b)
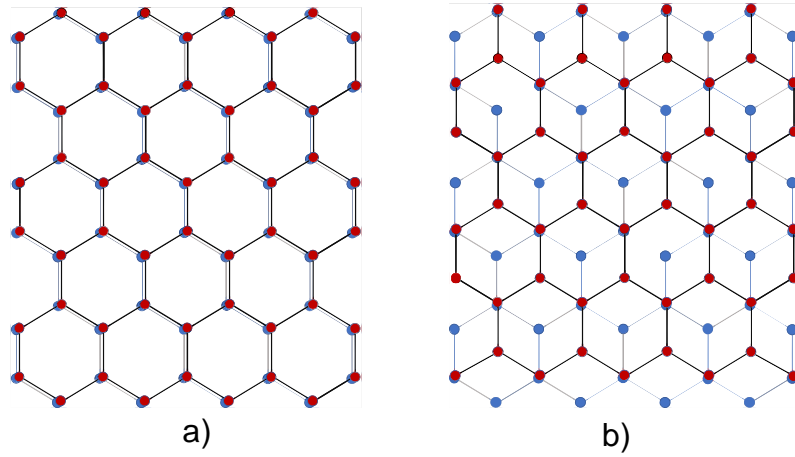
*Figure 3-1: Graphene **a)** AA-stacking **b)** AB-stacking*

As shown in Figure 3-2, the projection of $F(\bar{d})$ along the z direction and the relation between the distance difference of the two atoms and the transverse displacements of the graphene layers are given as

$$F(\bar{d})_z = F(\bar{d}) \cos \theta \qquad (3\text{-}19)$$

$$\cos \theta = \frac{z}{\bar{d}} \qquad (3\text{-}20)$$

$$\therefore F(\bar{d})_z = F(\bar{d}) \frac{z}{\bar{d}} \qquad (3\text{-}21)$$

$$Also, \quad \frac{w_i - w_j}{\bar{d} - \bar{d}_0} = \frac{z}{\bar{d}} \qquad (3\text{-}22)$$

$$\Rightarrow \quad w_i - w_j = (\bar{d} - \bar{d}_0) \frac{z}{\bar{d}} \qquad (3\text{-}23)$$

Equations (3-21) and (3-23) hold true for both AA- and AB-stacked layers, with $z = \bar{d}$ for the AA-stacked layers. Therefore, for both AA- and AB-stacked layers, assuming that each carbon atom occupies an area of $9a^2/4\sqrt{3}$ [196] and the GSs are continuum plates, the linear vdW pressure is derived using equation (3-16) as[171]

$$q_{ij} = -\left(\frac{4\sqrt{3}}{9a^2}\right)^2 \frac{24\varepsilon}{\sigma^2} \int_{-a/2}^{a/2} \int_{-b/2}^{b/2} \left[26\left(\frac{\sigma}{\bar{d}_0}\right)^{14} - 7\left(\frac{\sigma}{\bar{d}_0}\right)^{8} \right] \times (\bar{d} - \bar{d}_0)\frac{z}{\bar{d}} dx dy \qquad (3\text{-}24)$$

$$q_{ij_L} = \left(\frac{4\sqrt{3}}{9a^2}\right)^2 \frac{24\varepsilon}{\sigma^2} \left[\frac{13\pi}{3}\left(\frac{\sigma}{a}\right)^{14} \frac{1}{(\bar{z}_j - \bar{z}_i)^{12}} - \frac{7\pi}{3}\left(\frac{\sigma}{a}\right)^{8} \frac{1}{(\bar{z}_j - \bar{z}_i)^{6}} \right] (w_i - w_j) \qquad (3\text{-}25)$$
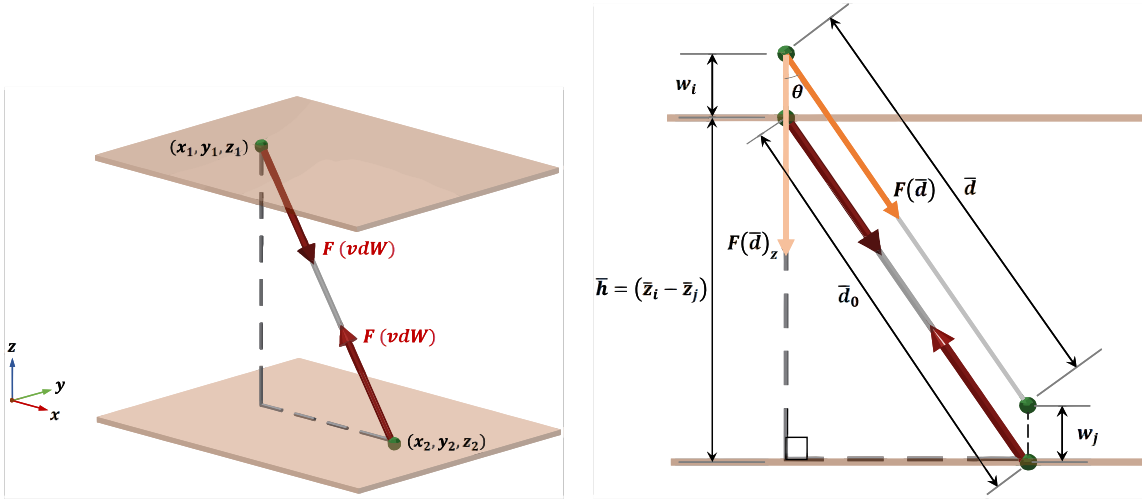
Figure 3-2: Atoms in any two adjacent GS layers and the vdW force acting between them.

Similarly, the nonlinear vdW pressure is derived for both AA- and AB-stacked layers using equation (3-18) as

$$q_{ij} = -\left(\frac{4\sqrt{3}}{9a^2}\right)^2 \frac{24\varepsilon}{\sigma^2} \int_{-a/2}^{a/2} \int_{-b/2}^{b/2} \left[26\left(\frac{\sigma}{\bar{d}}\right)^{14} - 7\left(\frac{\sigma}{\bar{d}}\right)^{8} \right] \times (\bar{d} - \bar{d}_0)\frac{z}{\bar{d}} dx dy$$
$$-\left(\frac{4\sqrt{3}}{9a^2}\right)^2 \frac{336\varepsilon}{\sigma^4} \int_{-a/2}^{a/2} \int_{-b/2}^{b/2} \left[65\left(\frac{\sigma}{\bar{d}}\right)^{16} - 6\left(\frac{\sigma}{\bar{d}}\right)^{10} \right] \times (\bar{d} - \bar{d}_0)^{3}\frac{z}{\bar{d}^3} dx dy \qquad (3\text{-}26)$$

$$q_{ij_{NL}} = -\left(\frac{4\sqrt{3}}{9a^2}\right)^2 \frac{24\varepsilon}{\sigma^2} \left[\frac{13\pi}{3}\left(\frac{\sigma}{a}\right)^{14} \frac{1}{(\bar{z}_j - \bar{z}_i)^{12}} - \frac{7\pi}{3}\left(\frac{\sigma}{a}\right)^{8} \frac{1}{(\bar{z}_j - \bar{z}_i)^{6}} \right] (w_i - w_j)$$
$$-\left(\frac{4\sqrt{3}}{9a^2}\right)^2 \frac{168\varepsilon}{\sigma^4} \left[\frac{130\pi}{7}\left(\frac{\sigma}{a}\right)^{16} \frac{1}{(\bar{z}_j - \bar{z}_i)^{14}} \right.$$
$$\left. - 3\pi\left(\frac{\sigma}{a}\right)^{10} \frac{1}{(\bar{z}_j - \bar{z}_i)^{8}} \right] (w_i - w_j)^{3} \qquad (3\text{-}27)$$

The net pressure caused by the vdW interactions on a layer i by all the other layers $j = 1,2,\dots,N$ with $i \neq j$ when modelled as a linear pressure can be expressed as

$$q_{i_L} = \sum_{j=1}^{N} c_{ij} \left(w_i - w_j \right) \qquad \text{(3-28)}$$

Where N is the number of layers in the MLGS, w_i and w_j are the transverse deflections of the ith layer and the other layers respectively, with c_{ij} given as

$$c_{ij} = -\left(\frac{4\sqrt{3}}{9a^2}\right)^2 \frac{24\varepsilon}{\sigma^2} \left[\frac{13\pi}{3} \left(\frac{\sigma}{a}\right)^{14} \frac{1}{\left(\bar{z}_j - \bar{z}_i\right)^{12}} - \frac{7\pi}{3} \left(\frac{\sigma}{a}\right)^8 \frac{1}{\left(\bar{z}_j - \bar{z}_i\right)^6} \right] \qquad \text{(3-29)}$$

When the vdW pressure is modelled as a nonlinear function, the net pressure is given as

$$q_{i_{NL}} = \sum_{j=1}^{N} c_{ij} \left(w_i - w_j \right) + \sum_{j=1}^{N} e_{ij} \left(w_i - w_j \right)^3 \qquad \text{(3-30)}$$

with

$$e_{ij} = -\left(\frac{4\sqrt{3}}{9a^2}\right)^2 \frac{168\varepsilon}{\sigma^4} \left[\frac{130\pi}{7} \left(\frac{\sigma}{a}\right)^{16} \frac{1}{\left(\bar{z}_j - \bar{z}_i\right)^{14}} - 3\pi \left(\frac{\sigma}{a}\right)^{10} \frac{1}{\left(\bar{z}_j - \bar{z}_i\right)^8} \right] \qquad \text{(3-31)}$$

It is worthy to note that the same procedure followed to derive the vdW pressure between GSs can be used to derive the pressure resulting from the non-bonded vdW interactions between a GS and any layer/sheet of a different material. One example is the interactions between graphene and a polymer matrix, polyethylene[172]. Here, equations (3-28) - (3-31) are thought to suffice for the vdW interaction between GSs and any other layer of different material type. For the interactions between GSs and other layers of a different material type, ε in equations (3-28) - (3-31) becomes ε_{g_m}, σ becomes σ_{g_m}, and $\left(4\sqrt{3}/9a^2\right)^2$ becomes $\rho_m\left(4\sqrt{3}/9a^2\right)$, where the subscripts **g** and **m** refer to graphene and the other

material type respectively. These new quantities can be obtained using equations specified in the universal force field periodic table[195].

Pasternak foundation model

Unlike the vdW interaction model, the Pasternak foundation model assumes that chemical bonds are formed between the GS and the elastic medium in which it is embedded. The Pasternak foundation model[190, 197, 198] is improved from the Winkler model to include the shear deformation G_b of the elastic medium. The Winkler model approximates the normal pressure from the elastic medium as a series of mutually independent, closely spaced, vertical elastic springs whose stiffness K_W represents the medium's modulus (Figure 3-3).
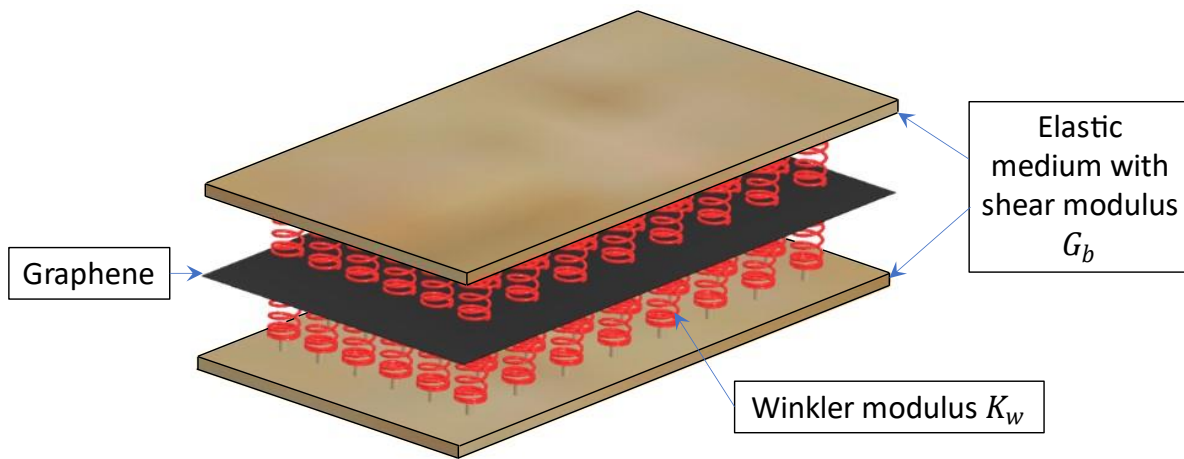
Figure 3-3: GS embedded in an Pasternak foundation medium with Winkler modulus K_W and Pasternak shear modulus G_b

Where the Winkler model is used, the interactions of surrounding elastic media with the GSs are modelled as

$$q_W = K_W w_i \qquad (3\text{-}32)$$

Where w_i is the transverse deflection of the topmost or bottom-most layers in direct contact with the elastic medium. For the Pasternak model, the interactions are modelled as

$$q_P = -K_W w_i + G_b \nabla^2 w_i \qquad (3\text{-}33)$$

3.2.3 Derivation of plate models using the equilibrium approach

In this sub-section, the formulation of the governing equations for various continuum models using variational and equilibrium methods is presented, including plate and membrane models. Beam models are not considered in this work because even though relatively easy and established solution pathways exist for them, they do not adequately represent the vibration problem of GSs (except where $a/b \to \infty$).

Classical plate theory (CLPT)

A plate can be considered as a two-dimensional analogue of a beam – which means that both bending moments and transverse shear forces will be active. The basic kinematics of the classical theory of thin plates is therefore the same as that of the Bernoulli-Euler beam.

Isotropic graphene sheets

Consider a graphene sheet modelled as an isotropic thin plate of uniform thickness, h, with dimension $a \times b$ and with its undeflected surface in the x-y plane as shown in Figure 3-4.
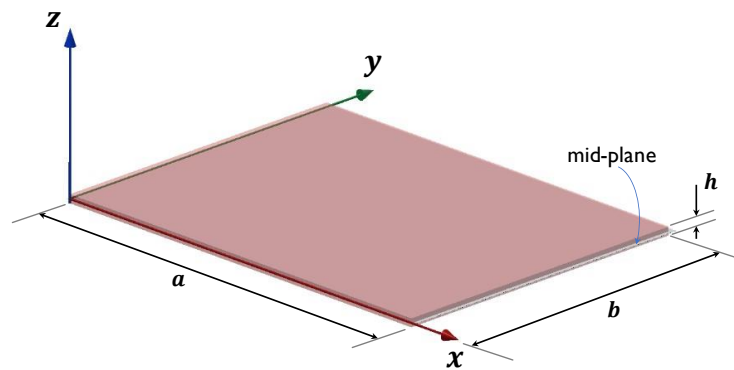
Figure 3-4: Isometric plate model

Based on the CLPT, the displacement components of an arbitrary point in the GS are expressed as

$$u(x,y,z,t) = u_0(x,y,t) - z\frac{\partial w_0(x,y,t)}{\partial x} \tag{3-34}$$

$$v(x,y,z,t) = v_0(x,y,t) - z\frac{\partial w_0(x,y,t)}{\partial y}$$

$$w(x, y, z, t) = w_0(x, y, t)$$

Where u_0, v_0 and w_0 are the displacement components of the corresponding mid-plane point $(x, y, 0)$ along the x, y and z directions respectively and t is the time.

For nonlinear vibrations, geometric nonlinearity is modelled by using the nonlinear von Karman type strain-displacement relations given as

$$\varepsilon_{xx} = (\varepsilon_{xxL} + \varepsilon_{xxNL}) + z\kappa_{xx}$$

$$\varepsilon_{yy} = (\varepsilon_{yyL} + \varepsilon_{yyNL}) + z\kappa_{yy} \qquad (3\text{-}35)$$

$$\gamma_{xy} = (\gamma_{xyL} + \gamma_{xyNL}) + z\kappa_{xy}$$

where the subscripts L and NL refer to the linear and nonlinear terms respectively, and the in-plane strains and curvature parameters are defined as

$$\begin{Bmatrix} \varepsilon_{xxL} \\ \varepsilon_{yyL} \\ \gamma_{xyL} \end{Bmatrix} = \begin{Bmatrix} \dfrac{\partial u_0}{\partial x} \\ \dfrac{\partial v_0}{\partial y} \\ \dfrac{\partial u_0}{\partial y} + \dfrac{\partial v_0}{\partial x} \end{Bmatrix}, \qquad \begin{Bmatrix} \varepsilon_{xxNL} \\ \varepsilon_{yyNL} \\ \gamma_{xyNL} \end{Bmatrix} = \begin{Bmatrix} \dfrac{1}{2}\left(\dfrac{\partial w_0}{\partial x}\right)^2 \\ \dfrac{1}{2}\left(\dfrac{\partial w_0}{\partial y}\right)^2 \\ \dfrac{\partial w_0}{\partial x}\dfrac{\partial w_0}{\partial y} \end{Bmatrix} \qquad (3\text{-}36)$$

$$\begin{Bmatrix} \kappa_{xx} \\ \kappa_{yy} \\ \kappa_{xy} \end{Bmatrix} = \begin{Bmatrix} -\dfrac{\partial^2 w_0}{\partial x^2} \\ -\dfrac{\partial^2 w_0}{\partial y^2} \\ -2\dfrac{\partial^2 w_0}{\partial x \partial y} \end{Bmatrix} \qquad (3\text{-}37)$$

Note that when only material rather than geometric nonlinearity is considered the nonlinear terms in equation (3-35) are ignored to give the linear kinematic relations.

Based on equation (3-6), the plane stress constitutive relation for the GS when considering the small-scale effect is given as

$$(1 - \mu\nabla^2)\begin{Bmatrix} \sigma_{xx} \\ \sigma_{yy} \\ \sigma_{xy} \end{Bmatrix} = \begin{bmatrix} \dfrac{E}{1-v^2} & \dfrac{vE}{1-v^2} & 0 \\ \dfrac{vE}{1-v^2} & \dfrac{E}{1-v^2} & 0 \\ 0 & 0 & G \end{bmatrix} \begin{Bmatrix} \varepsilon_{xx} \\ \varepsilon_{yy} \\ \gamma_{xy} \end{Bmatrix} \qquad (3\text{-}38)$$

Where E, G and υ are the elastic modulus, shear modulus and Poisson's ratio respectively, with $G = \frac{E}{2(1+\upsilon)}$. The local plane stress constitutive relation is recovered when the small-scale parameter, μ, is set to zero.

The governing equations for the nonlinear vibrations of the GS are derived using Hamilton's principle, which states that[172]

$$\int_0^t (\delta T - \delta U + \delta V)dt = 0 \tag{3-39}$$

where T, U and V are the kinetic energy, strain energy of the GS and potential energy of the external loads, respectively. The equilibrium equations are given as[174]

$$\frac{\partial N_{xx}}{\partial x} + \frac{\partial N_{xy}}{\partial y} = I_0 \frac{\partial^2 u_0}{\partial t^2} - I_1 \frac{\partial^2}{\partial t^2}\left(\frac{\partial w_0}{\partial x}\right) \tag{3-40}$$

$$\frac{\partial N_{xy}}{\partial x} + \frac{\partial N_{yy}}{\partial y} = I_0 \frac{\partial^2 v_0}{\partial t^2} - I_1 \frac{\partial^2}{\partial t^2}\left(\frac{\partial w_0}{\partial y}\right) \tag{3-41}$$

$$\frac{\partial^2 M_{xx}}{\partial x^2} + 2\frac{\partial^2 M_{xy}}{\partial x \partial y} + \frac{\partial^2 M_{yy}}{\partial y^2} + N_{NL} + p$$
$$= I_0 \frac{\partial^2 w_0}{\partial t^2} + I_1 \frac{\partial^2}{\partial t^2}\left(\frac{\partial u_0}{\partial x} + \frac{\partial v_0}{\partial y}\right) - I_2\left(\frac{\partial^4 w_0}{\partial x^2 \partial t^2} + \frac{\partial^4 w_0}{\partial y^2 \partial t^2}\right) \tag{3-42}$$

Where N_{xx}, N_{yy}, and N_{xy} are the in-plane force resultants, M_{xx}, M_{yy}, and M_{xy} are the moment resultants. p is the external load due to vdW pressure and the applied force in forced vibration analysis. I_0, I_1 and I_2 are the inertia parameters expressed in terms of the mass density, ρ, of the GSs as

$$I_0 = \int_{-h/2}^{h/2} \rho dz$$

$$I_1 = \int_{-h/2}^{h/2} \rho z dz \tag{3-43}$$

$$I_2 = \int_{-h/2}^{h/2} \rho z^2 dz$$

N_{NL} is the term arising from the geometrical nonlinearity introduced via the von Karman strain-displacement relations and is given as[199]

$$N_{NL} = \frac{\partial}{\partial x}\left(N_{xx}\frac{\partial w_0}{\partial x} + N_{xy}\frac{\partial w_0}{\partial y}\right) + \frac{\partial}{\partial y}\left(N_{xy}\frac{\partial w_0}{\partial x} + N_{yy}\frac{\partial w_0}{\partial y}\right) \qquad (3\text{-}44)$$

And simplifies to

$$N_{NL} = N_{xx}\frac{\partial^2 w_0}{\partial x^2} + 2N_{xy}\frac{\partial^2 w_0}{\partial x \partial y} + N_{yy}\frac{\partial^2 w_0}{\partial y^2} \qquad (3\text{-}45)$$

In equation

(3-42), N_{NL} is absent when the nonlinearity being considered is not geometric, and where the rotary inertia term is ignored the term $I_2\left(\frac{\partial^4 w_0}{\partial x^2 \partial t^2} + \frac{\partial^4 w_0}{\partial y^2 \partial t^2}\right)$ disappears.

The force and moment resultants are given as

$$\begin{bmatrix} N_{xx} & N_{yy} & N_{xy} \end{bmatrix}^T = \int_{-h/2}^{h/2}\begin{pmatrix} \sigma_{xx} & \sigma_{yy} & \sigma_{xy} \end{pmatrix}^T dz \qquad (3\text{-}46)$$

$$\begin{bmatrix} M_{xx} & M_{yy} & M_{xy} \end{bmatrix}^T = \int_{-h/2}^{h/2}\begin{pmatrix} \sigma_{xx} & \sigma_{yy} & \sigma_{xy} \end{pmatrix}^T z dz \qquad (3\text{-}47)$$

According to the stress constitutive relation in equation (3-38), the force and moment resultants satisfy the following equations

$$(1 - \mu\nabla^2)\begin{bmatrix} N_{xx} \\ N_{yy} \\ N_{xy} \end{bmatrix} = h\begin{bmatrix} \frac{E}{1-v^2} & \frac{vE}{1-v^2} & 0 \\ \frac{vE}{1-v^2} & \frac{E}{1-v^2} & 0 \\ 0 & 0 & G \end{bmatrix}\begin{Bmatrix} \frac{\partial u_0}{\partial x} + \frac{1}{2}\left(\frac{\partial w_0}{\partial x}\right)^2 \\ \frac{\partial v_0}{\partial y} + \frac{1}{2}\left(\frac{\partial w_0}{\partial y}\right)^2 \\ \frac{\partial u_0}{\partial y} + \frac{\partial v_0}{\partial x} + \frac{\partial w_0}{\partial x}\frac{\partial w_0}{\partial y} \end{Bmatrix} \qquad (3\text{-}48)$$

$$(1 - \mu\nabla^2)\begin{bmatrix} M_{xx} \\ M_{yy} \\ M_{xy} \end{bmatrix} = \frac{h^3}{12}\begin{bmatrix} \frac{E}{1-v^2} & \frac{vE}{1-v^2} & 0 \\ \frac{vE}{1-v^2} & \frac{E}{1-v^2} & 0 \\ 0 & 0 & G \end{bmatrix}\begin{Bmatrix} -\frac{\partial^2 w_0}{\partial x^2} \\ -\frac{\partial^2 w_0}{\partial y^2} \\ -2\frac{\partial^2 w_0}{\partial x \partial y} \end{Bmatrix} \qquad (3\text{-}49)$$

It has been shown that the effect of in-plane inertia on large amplitude vibration of thin-walled structures is neglible[200], therefore neglecting the in-plane inertia terms in equations (3-40) - (3-42), and multiplying the equations by $(1 - \mu\nabla^2)$, with I_1 being zero for sheets that are symmetric with respect to the z-axis, we have

$$(1 - \mu\nabla^2)\left(\frac{\partial N_{xx}}{\partial x} + \frac{\partial N_{xy}}{\partial y}\right) = 0 \tag{3-50}$$

$$(1 - \mu\nabla^2)\left(\frac{\partial N_{xy}}{\partial x} + \frac{\partial N_{yy}}{\partial y}\right) = 0 \tag{3-51}$$

$$
\begin{aligned}
(1 - \mu\nabla^2)&\left(\frac{\partial^2 M_{xx}}{\partial x^2} + 2\frac{\partial^2 M_{xy}}{\partial x \partial y} + \frac{\partial^2 M_{yy}}{\partial y^2}\right) \\
&+ (1 - \mu\nabla^2)\left(N_{xx}\frac{\partial^2 w_0}{\partial x^2} + 2N_{xy}\frac{\partial^2 w_0}{\partial x \partial y} + N_{yy}\frac{\partial^2 w_0}{\partial y^2} + p\right) \\
&= (1 - \mu\nabla^2)\left(I_0 \frac{\partial^2 w_0}{\partial t^2} - I_2\left(\frac{\partial^4 w_0}{\partial x^2 \partial t^2} + \frac{\partial^4 w_0}{\partial y^2 \partial t^2}\right)\right)
\end{aligned} \tag{3-52}
$$

To satisfy equations (3-50) - (3-52), the stress function is defined as Airy's stress function, φ

$$N_{xx} = \frac{\partial^2 \varphi}{\partial y^2}$$

$$N_{yy} = \frac{\partial^2 \varphi}{\partial x^2} \tag{3-53}$$

$$N_{xy} = -\frac{\partial^2 \varphi}{\partial x \partial y}$$

Now substituting equations (3-49) and (3-53) in equation (3-52) and simplifying, we have

$$
\begin{aligned}
-D&\left(\frac{\partial^4 w_{0i}}{\partial x^4} + 2\frac{\partial^4 w_{0i}}{\partial x^2 \partial y^2} + \frac{\partial^4 w_{0i}}{\partial y^4}\right) \\
&+ (1 - \mu\nabla^2)\left(\frac{\partial^2 w_{0i}}{\partial x^2}\frac{\partial^2 \varphi}{\partial y^2} - 2\frac{\partial^2 w_{0i}}{\partial x \partial y}\frac{\partial^2 \varphi}{\partial x \partial y} + \frac{\partial^2 w_{0i}}{\partial y^2}\frac{\partial^2 \varphi}{\partial x^2} + p_i\right) \\
&= (1 - \mu\nabla^2)\left(I_0 \frac{\partial^2 w_{0i}}{\partial t^2} - I_2\left(\frac{\partial^4 w_{0i}}{\partial x^2 \partial t^2} + \frac{\partial^4 w_{0i}}{\partial y^2 \partial t^2}\right)\right)
\end{aligned} \tag{3-54}
$$

Or

$$
\begin{aligned}
-D\nabla^4 w_{0i} &+ (1 - \mu\nabla^2)\left(\frac{\partial^2 w_{0i}}{\partial x^2}\frac{\partial^2 \varphi}{\partial y^2} - 2\frac{\partial^2 w_{0i}}{\partial x \partial y}\frac{\partial^2 \varphi}{\partial x \partial y} + \frac{\partial^2 w_{0i}}{\partial y^2}\frac{\partial^2 \varphi}{\partial x^2} + p_i\right) \\
&= (1 - \mu\nabla^2)\left(I_0 \frac{\partial^2 w_{0i}}{\partial t^2} - I_2\left(\frac{\partial^4 w_{0i}}{\partial x^2 \partial t^2} + \frac{\partial^4 w_{0i}}{\partial y^2 \partial t^2}\right)\right)
\end{aligned} \tag{3-55}
$$

where $\nabla^4 = \frac{\partial^4}{\partial x^4} + 2\frac{\partial^4}{\partial x^2 \partial y^2} + \frac{\partial^4}{\partial y^4}$, and D is the bending rigidity given as

$$D = \frac{Eh^3}{12(1-v^2)} \tag{3-56}$$

Equation (3-54) or (3-55) is the nonlinear, nonlocal fourth order partial differential equation of motion for an isotropic GS being analysed as part of a MLGS-composite in terms of the transverse displacement of the sheet and Airy's stress function. The subscript i denotes the layer number.

Since equation (3-54) or (3-55) are functions of two unknowns, a compatibility equation is needed to augment either of them before solutions can be obtained. The compatibility equation is obtained by eliminating the in-plane displacement functions, u and v, from equations (3-35) - (3-37) and expressing the in-plane strain components in terms of the stress function. The compatibility equation starts off with the form[199]

$$\frac{\partial^2 \varepsilon_{0xx}}{\partial y^2} - 2\frac{\partial^2 \varepsilon_{0xy}}{\partial x \partial y} + \frac{\partial^2 \varepsilon_{0yy}}{\partial x^2} = \left(\frac{\partial^2 w_{0i}}{\partial x \partial y}\right)^2 - \frac{\partial^2 w_0}{\partial x^2}\frac{\partial^2 w_0}{\partial y^2} \tag{3-57}$$

The in-plane strain components are obtained from equation (3-48) as

$$\begin{Bmatrix} \varepsilon_{0xx} \\ \varepsilon_{0yy} \\ \gamma_{0xy} \end{Bmatrix} = \begin{bmatrix} A_{11} & A_{12} & 0 \\ A_{21} & A_{22} & 0 \\ 0 & 0 & A_{33} \end{bmatrix} \left(\begin{Bmatrix} N_{xx} \\ N_{yy} \\ N_{xy} \end{Bmatrix} - \mu\nabla^2 \begin{Bmatrix} N_{xx} \\ N_{yy} \\ N_{xy} \end{Bmatrix} \right) \tag{3-58}$$

where $\begin{bmatrix} A_{11} & A_{12} & 0 \\ A_{21} & A_{22} & 0 \\ 0 & 0 & A_{33} \end{bmatrix}$ is the inverse of the stretching stiffness matrix $\begin{bmatrix} \frac{Eh}{1-v^2} & \frac{vEh}{1-v^2} & 0 \\ \frac{vEh}{1-v^2} & \frac{Eh}{1-v^2} & 0 \\ 0 & 0 & Gh \end{bmatrix}$

in equation (3-48). Equation (3-57) then becomes

$$(1 - \mu\nabla^2)\left[A_{11}\frac{\partial^2 N_{xx}}{\partial y^2} + A_{12}\left(\frac{\partial^2 N_{yy}}{\partial y^2} + \frac{\partial^2 N_{xx}}{\partial x^2}\right) + A_{22}\frac{\partial^2 N_{yy}}{\partial x^2} - 2A_{33}\frac{\partial^2 N_{xy}}{\partial x \partial y} \right]$$
$$= \left(\frac{\partial^2 w_{0i}}{\partial x \partial y}\right)^2 - \frac{\partial^2 w_0}{\partial x^2}\frac{\partial^2 w_0}{\partial y^2} \tag{3-59}$$

Substituting equation (3-53) in (3-59) and simplifying, we have

$$(1 - \mu\nabla^2)\left[A_{11}\frac{\partial^4\varphi}{\partial y^4} + (A_{12} + 2A_{33})\frac{\partial^4\varphi}{\partial x^2\partial y^2} + A_{22}\frac{\partial^4\varphi}{\partial x^4}\right] = \left(\frac{\partial^2 w_{0i}}{\partial x\partial y}\right)^2 - \frac{\partial^2 w_0}{\partial x^2}\frac{\partial^2 w_0}{\partial y^2} \quad (3\text{-}60)$$

with the inverse of the stretching stiffness matrix given as

$$\begin{bmatrix} A_{11} & A_{12} & 0 \\ A_{21} & A_{22} & 0 \\ 0 & 0 & A_{33} \end{bmatrix} = \begin{bmatrix} \dfrac{1}{Eh} & \dfrac{-v}{Eh} & 0 \\ \dfrac{-v}{Eh} & \dfrac{1}{Eh} & 0 \\ 0 & 0 & \dfrac{2(1+v)}{Eh} \end{bmatrix} \quad (3\text{-}61)$$

Equation (3-60) is the nonlocal compatibility equation that complements equation (3-54). In some works, the nonlocal effects are not included in the compatibility equation. Equations (3-54) and (3-60) form the **nonlinear**, **nonlocal** equations of motion needed for the vibration analysis of an **isotropic** GS in **a MLGS composite**. Together they are

$$\begin{aligned}
&-D\left(\frac{\partial^4 w_{0i}}{\partial x^4} + 2\frac{\partial^4 w_{0i}}{\partial x^2\partial y^2} + \frac{\partial^4 w_{0i}}{\partial y^4}\right) \\
&\qquad + (1-\mu\nabla^2)\left(\frac{\partial^2 w_{0i}}{\partial x^2}\frac{\partial^2\varphi_i}{\partial y^2} - 2\frac{\partial^2 w_{0i}}{\partial x\partial y}\frac{\partial^2\varphi_i}{\partial x\partial y} + \frac{\partial^2 w_{0i}}{\partial y^2}\frac{\partial^2\varphi_i}{\partial x^2}\right) \\
&\qquad + (1-\mu\nabla^2)p_i = (1-\mu\nabla^2)\left(I_0\frac{\partial^2 w_{0i}}{\partial t^2} - I_2\left(\frac{\partial^4 w_{0i}}{\partial x^2\partial t^2} + \frac{\partial^4 w_{0i}}{\partial y^2\partial t^2}\right)\right) \\[1em]
&(1-\mu\nabla^2)\left[A_{11}\frac{\partial^4\varphi_i}{\partial y^4} + (A_{12}+2A_{33})\frac{\partial^4\varphi_i}{\partial x^2\partial y^2} + A_{22}\frac{\partial^4\varphi_i}{\partial x^4}\right] = \left(\frac{\partial^2 w_{0i}}{\partial x\partial y}\right)^2 - \frac{\partial^2 w_{0i}}{\partial x^2}\frac{\partial^2 w_{0i}}{\partial y^2}
\end{aligned} \quad (3\text{-}62)$$

Equation (3-62) can be appropriately tailored for a few cases of vibrating isotropic GSs. For an **isotropic MLGS**, the **nonlinear** equations of motion **without considering the nonlocal effects** are

$$\begin{aligned}
&-D\left(\frac{\partial^4 w_{0i}}{\partial x^4} + 2\frac{\partial^4 w_{0i}}{\partial x^2\partial y^2} + \frac{\partial^4 w_{0i}}{\partial y^4}\right) + \frac{\partial^2 w_{0i}}{\partial x^2}\frac{\partial^2\varphi_i}{\partial y^2} - 2\frac{\partial^2 w_{0i}}{\partial x\partial y}\frac{\partial^2\varphi_i}{\partial x\partial y} + \frac{\partial^2 w_{0i}}{\partial y^2}\frac{\partial^2\varphi_i}{\partial x^2} + p_i \\
&\qquad = I_0\frac{\partial^2 w_{0i}}{\partial t^2} - I_2\left(\frac{\partial^4 w_{0i}}{\partial x^2\partial t^2} + \frac{\partial^4 w_{0i}}{\partial y^2\partial t^2}\right) \\[1em]
&A_{11}\frac{\partial^4\varphi_i}{\partial y^4} + (A_{12}+2A_{33})\frac{\partial^4\varphi_i}{\partial x^2\partial y^2} + A_{22}\frac{\partial^4\varphi_i}{\partial x^4} = \left(\frac{\partial^2 w_{0i}}{\partial x\partial y}\right)^2 - \frac{\partial^2 w_{0i}}{\partial x^2}\frac{\partial^2 w_{0i}}{\partial y^2}
\end{aligned} \quad (3\text{-}63)$$

For an **isotropic MLGS**, the **linear**, **nonlocal** equation of motion is deduced as

$$
\begin{aligned}
-D\left(\frac{\partial^4 w_{0i}}{\partial x^4} + 2\frac{\partial^4 w_{0i}}{\partial x^2 \partial y^2} + \frac{\partial^4 w_{0i}}{\partial y^4}\right) + p_i \\
= (1 - \mu \nabla^2)\left(I_0 \frac{\partial^2 w_{0i}}{\partial t^2} - I_2\left(\frac{\partial^4 w_{0i}}{\partial x^2 \partial t^2} + \frac{\partial^4 w_{0i}}{\partial y^2 \partial t^2}\right)\right)
\end{aligned}
$$

(3-64)

Without considering nonlocal effects, the **linear** equation of motion for an **isotropic MLGS** becomes

$$
-D\left(\frac{\partial^4 w_{0i}}{\partial x^4} + 2\frac{\partial^4 w_{0i}}{\partial x^2 \partial y^2} + \frac{\partial^4 w_{0i}}{\partial y^4}\right) + p_i = I_0 \frac{\partial^2 w_{0i}}{\partial t^2} - I_2\left(\frac{\partial^4 w_{0i}}{\partial x^2 \partial t^2} + \frac{\partial^4 w_{0i}}{\partial y^2 \partial t^2}\right)
$$

(3-65)

Equations (3-62) - (3-65) are same for an SLGS under the same assumptions for which they are given for MLGSs, but with the subscript i removed as there is only one layer of graphene in an SLGS. In cases where the rotary inertia terms are ignored, the term $I_2\left(\frac{\partial^4 w_{0i}}{\partial x^2 \partial t^2} + \frac{\partial^4 w_{0i}}{\partial y^2 \partial t^2}\right)$ vanishes in equations (3-62) - (3-65) for MLGSs and their adaptation for SLGSs.

Orthotropic graphene sheets

Graphene has its carbon atoms arranged in a hexagonal lattice structure, with the structural pattern differing depending on the orientation being considered resulting in armchair and zigzag edges in GSs (see Figure 3-5). Because of this peculiar structure the elastic properties of GSs are said to differ in the two perpendicular orientations, consequently the sheets are expected to behave differently depending on the edge the load/boundary condition is applied.

a)

b)
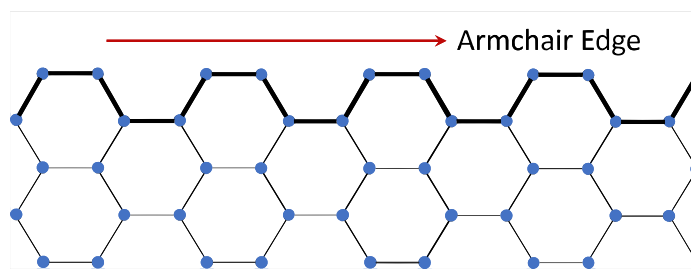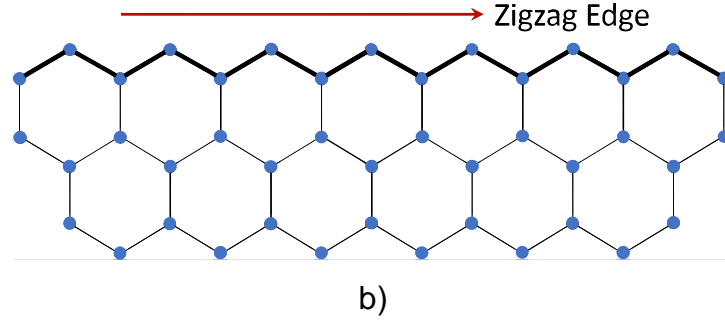
Figure 3-5: a) Armchair and b) Zigzag graphene edges

The governing equations for the vibration analysis of orthotropic plates are derived in the same way the equations for iso*tropic* plates are derived and are in fact same except for the bending stiffnesses and the inverse of the stretching stiffnesses. Therefore, for an orthotropic plate of uniform thickness h, with dimension $a \times b$, the equivalent of equations (3-62) - (3-65) with the corresponding assumptions are given in the next few paragraphs.

The **nonlinear**, **nonlocal** equations of motion for an **orthotropic MLGS** are given as

$$
\begin{aligned}
& D_{11}\frac{\partial^4 w_{0i}}{\partial x^4} + 2(D_{12} + 2D_{33})\frac{\partial^4 w_{0i}}{\partial x^2 \partial y^2} + D_{22}\frac{\partial^4 w_{0i}}{\partial y^4} \\
& \quad - (1 - \mu\nabla^2)\left(\frac{\partial^2 w_{0i}}{\partial x^2}\frac{\partial^2 \varphi_i}{\partial y^2} - 2\frac{\partial^2 w_{0i}}{\partial x \partial y}\frac{\partial^2 \varphi_i}{\partial x \partial y} + \frac{\partial^2 w_{0i}}{\partial y^2}\frac{\partial^2 \varphi_i}{\partial x^2}\right) - p_i \\
& \quad = -(1 - \mu\nabla^2)\left(I_0\frac{\partial^2 w_{0i}}{\partial t^2} - I_2\left(\frac{\partial^4 w_{0i}}{\partial x^2 \partial t^2} + \frac{\partial^4 w_{0i}}{\partial y^2 \partial t^2}\right)\right) \\[10pt]
& (1 - \mu\nabla^2)\left[A_{11}\frac{\partial^4 \varphi_i}{\partial y^4} + (A_{12} + 2A_{33})\frac{\partial^4 \varphi_i}{\partial x^2 \partial y^2} + A_{22}\frac{\partial^4 \varphi_i}{\partial x^4}\right] = \left(\frac{\partial^2 w_{0i}}{\partial x \partial y}\right)^2 - \frac{\partial^2 w_{0i}}{\partial x^2}\frac{\partial^2 w_{0i}}{\partial y^2}
\end{aligned}
\tag{3-66}
$$

The **nonlinear** equations of motion for an **orthotropic MLGS without considering the nonlocal effects** are

$$
\begin{aligned}
& D_{11}\frac{\partial^4 w_{0i}}{\partial x^4} + 2(D_{12} + 2D_{33})\frac{\partial^4 w_{0i}}{\partial x^2 \partial y^2} + D_{22}\frac{\partial^4 w_{0i}}{\partial y^4} - \frac{\partial^2 w_{0i}}{\partial x^2}\frac{\partial^2 \varphi_i}{\partial y^2} + 2\frac{\partial^2 w_{0i}}{\partial x \partial y}\frac{\partial^2 \varphi_i}{\partial x \partial y} \\
& \quad - \frac{\partial^2 w_{0i}}{\partial y^2}\frac{\partial^2 \varphi_i}{\partial x^2} - p_i = -\left(I_0\frac{\partial^2 w_{0i}}{\partial t^2} - I_2\left(\frac{\partial^4 w_{0i}}{\partial x^2 \partial t^2} + \frac{\partial^4 w_{0i}}{\partial y^2 \partial t^2}\right)\right) \\[10pt]
& A_{11}\frac{\partial^4 \varphi_i}{\partial y^4} + (A_{12} + 2A_{33})\frac{\partial^4 \varphi_i}{\partial x^2 \partial y^2} + A_{22}\frac{\partial^4 \varphi_i}{\partial x^4} = \left(\frac{\partial^2 w_{0i}}{\partial x \partial y}\right)^2 - \frac{\partial^2 w_{0i}}{\partial x^2}\frac{\partial^2 w_{0i}}{\partial y^2}
\end{aligned}
\tag{3-67}
$$

The **linear**, **nonlocal** equation of motion for an **orthotropic MLGS** is

$$
\begin{aligned}
D_{11} \frac{\partial^4 w_{0i}}{\partial x^4} + 2(D_{12} + 2D_{33}) \frac{\partial^4 w_{0i}}{\partial x^2 \partial y^2} + D_{22} \frac{\partial^4 w_{0i}}{\partial y^4} - p_i \\
= -(1 - \mu\nabla^2) \left(I_0 \frac{\partial^2 w_{0i}}{\partial t^2} - I_2 \left(\frac{\partial^4 w_{0i}}{\partial x^2 \partial t^2} + \frac{\partial^4 w_{0i}}{\partial y^2 \partial t^2} \right) \right)
\end{aligned}
\tag{3-68}
$$

The **linear** equation of motion for an **orthotropic MLGS without considering nonlocal effects** is

$$
\begin{aligned}
D_{11} \frac{\partial^4 w_{0i}}{\partial x^4} + 2(D_{12} + 2D_{33}) \frac{\partial^4 w_{0i}}{\partial x^2 \partial y^2} + D_{22} \frac{\partial^4 w_{0i}}{\partial y^4} - p_i \\
= - \left(I_0 \frac{\partial^2 w_{0i}}{\partial t^2} - I_2 \left(\frac{\partial^4 w_{0i}}{\partial x^2 \partial t^2} + \frac{\partial^4 w_{0i}}{\partial y^2 \partial t^2} \right) \right)
\end{aligned}
\tag{3-69}
$$

The stretching and bending stiffness matrices for an armchair configuration are given as

$$
\begin{bmatrix}
S_{11} & S_{12} & 0 \\
S_{21} & S_{22} & 0 \\
0 & 0 & S_{33}
\end{bmatrix}
=
\begin{bmatrix}
\dfrac{E_1 h}{(1 - v_{12} v_{21})} & \dfrac{E_2 h}{(1 - v_{12} v_{21})} & 0 \\
\dfrac{E_2 h}{(1 - v_{12} v_{21})} & \dfrac{v_{21} E_1 h}{(1 - v_{12} v_{21})} & 0 \\
0 & 0 & \dfrac{E_1 h}{2(1 + v_{12})}
\end{bmatrix}
\tag{3-70}
$$

$$
\begin{bmatrix}
D_{11} & D_{12} & 0 \\
D_{21} & D_{22} & 0 \\
0 & 0 & D_{33}
\end{bmatrix}
=
\begin{bmatrix}
\dfrac{E_1 h^3}{12(1 - v_{12} v_{21})} & \dfrac{E_2 h^3}{12(1 - v_{12} v_{21})} & 0 \\
\dfrac{E_2 h^3}{12(1 - v_{12} v_{21})} & \dfrac{v_{21} E_1 h^3}{12(1 - v_{12} v_{21})} & 0 \\
0 & 0 & \dfrac{E_1 h^3}{24(1 + v_{12})}
\end{bmatrix}
\tag{3-71}
$$

The inverse of the stretching stiffness matrix is deduced from equation (3-70) as

$$\begin{bmatrix} A_{11} & A_{12} & 0 \\ A_{21} & A_{22} & 0 \\ 0 & 0 & A_{33} \end{bmatrix} = \begin{bmatrix} \dfrac{v_{21}E_1(1 - v_{12}v_{21})}{h(v_{21}E_1^2 - E_2^2)} & \dfrac{-E_2(1 - v_{12}v_{21})}{h(v_{21}E_1^2 - E_2^2)} & 0 \\ \dfrac{-E_2(1 - v_{12}v_{21})}{h(v_{21}E_1^2 - E_2^2)} & \dfrac{E_1(1 - v_{12}v_{21})}{h(v_{21}E_1^2 - E_2^2)} & 0 \\ 0 & 0 & \dfrac{2(1 + v_{12})}{E_1 h} \end{bmatrix} \tag{3-72}$$

For the zigzag configuration, the stretching and bending stiffness matrices are given as

$$\begin{bmatrix} S_{11} & S_{12} & 0 \\ S_{21} & S_{22} & 0 \\ 0 & 0 & S_{33} \end{bmatrix} = \begin{bmatrix} \dfrac{v_{21}E_1 h}{(1 - v_{12}v_{21})} & \dfrac{E_2 h}{(1 - v_{12}v_{21})} & 0 \\ \dfrac{E_2 h}{(1 - v_{12}v_{21})} & \dfrac{E_1 h}{(1 - v_{12}v_{21})} & 0 \\ 0 & 0 & \dfrac{E_1 h}{2(1 + v_{12})} \end{bmatrix} \tag{3-73}$$

$$\begin{bmatrix} D_{11} & D_{12} & 0 \\ D_{21} & D_{22} & 0 \\ 0 & 0 & D_{33} \end{bmatrix} = \begin{bmatrix} \dfrac{v_{21}E_1 h^3}{12(1 - v_{12}v_{21})} & \dfrac{E_2 h^3}{12(1 - v_{12}v_{21})} & 0 \\ \dfrac{E_2 h^3}{12(1 - v_{12}v_{21})} & \dfrac{E_1 h^3}{12(1 - v_{12}v_{21})} & 0 \\ 0 & 0 & \dfrac{E_1 h^3}{24(1 + v_{12})} \end{bmatrix} \tag{3-74}$$

And the inverse of the stretching stiffness matrix for the zigzag configuration is

$$\begin{bmatrix} A_{11} & A_{12} & 0 \\ A_{21} & A_{22} & 0 \\ 0 & 0 & A_{33} \end{bmatrix} = \begin{bmatrix} \dfrac{E_1(1 - v_{12}v_{21})}{h(v_{21}E_1^2 - E_2^2)} & \dfrac{-E_2(1 - v_{12}v_{21})}{h(v_{21}E_1^2 - E_2^2)} & 0 \\ \dfrac{-E_2(1 - v_{12}v_{21})}{h(v_{21}E_1^2 - E_2^2)} & \dfrac{v_{21}E_1(1 - v_{12}v_{21})}{h(v_{21}E_1^2 - E_2^2)} & 0 \\ 0 & 0 & \dfrac{2(1 + v_{12})}{E_1 h} \end{bmatrix} \tag{3-75}$$

As with the iso*tropic* equations, equations (3-66) - (3-69) are same for the orthotropic SLGS under the same assumptions for which they are given for MLGSs, but with the subscript i removed. Also, in cases where the rotary inertia terms are ignored, the term $I_2 \left(\dfrac{\partial^4 w_{0i}}{\partial x^2 \partial t^2} + \dfrac{\partial^4 w_{0i}}{\partial y^2 \partial t^2} \right)$ vanishes in equations (3-66) - (3-69) for MLGSs and their adaptation for SLGSs. The effect of the anisotropy of graphene on the natural frequency of GSs has been found to be negligible at higher lengths $(a, b > 20\,nm)$[201]. So, we conclude that the orthotropic CLPT models

should only really be applied to nanoplates, with dimensions in the tens of nanometers.

Although equations (3-62), (3-63), (3-66) and (3-67) include geometric nonlinearities, by incorporating small strain and moderate rotation relations and thereby including bending-stretching coupling effects, the transverse deflections are still limited to the order of the plate's thickness. This therefore means that if the transverse deflections of vibrating GSs are large and not in the order of the sheet's thickness, stress stiffening effects set in and all equations derived in accordance with the CLPT including the nonlinear equations may be erroneous representations of the behaviour of the vibrating sheets.

First-order shear deformation theory (FSDT)

The first-order shear deformation theory (FSDT) is an extension of the CLPT but with transverse shear deformations considered. The FSDT is sometimes erroneously called the Reissner-Mindlin plate theory[170], which is meant to be an amalgamation of Reissner and Mindlin plate theories. However, the Mindlin plate theory is slightly different from the Reissner plate theory as is elucidated by Wang et al[202]. They point out that although both theories were proposed for analysing thick plates, it is erroneous to associate them as the 'Reissner-Mindlin' plate theory or to use one of them in an analysis and then compare the results with those obtained by using the other. In fact, the assumptions upon which the Reissner plate theory was derived do not allow for it to be classified as a FSDT which implies a linear displacement variation through the plate thickness.

Isotropic graphene sheets

Consider a graphene sheet modelled as the plate shown in Figure 3-4 but with thickness in the range of one-tenth to one-fiftieth of the planar dimensions. According to FSDT, the displacement components for an arbitrary point in the sheet are given as

$$u(x, y, z, t) = u_0(x, y, t) - z\psi_x(x, y, t)$$

$$v(x, y, z, t) = v_0(x, y, t) - z\psi_y(x, y, t) \qquad (3\text{-}76)$$

$$w(x, y, z, t) = w_0(x, y, t)$$

Where u_0, v_0 and w_0 are the displacement components of the corresponding mid-plane point $(x, y, 0)$ along the x, y and z directions respectively, t is the time, and ψ_x and ψ_y are the rotations of a normal to the midplane about the x- and y-axis respectively (Figure 3-6). When the plates being considered are thin, the rotations can be approximated as $\psi_x = \frac{\partial w_0}{\partial x}$ and $\psi_y = \frac{\partial w_0}{\partial y}$, which reverts equation (3-76) to the CLPT case in equation (3-34).

The strain-displacement relations are given as

$$
\begin{Bmatrix} \varepsilon_{xx} \\ \varepsilon_{yy} \\ \gamma_{xy} \\ \gamma_{yz} \\ \gamma_{xz} \end{Bmatrix} = \begin{Bmatrix} \dfrac{\partial u}{\partial x} \\ \dfrac{\partial v}{\partial y} \\ \dfrac{\partial v}{\partial x} + \dfrac{\partial u}{\partial y} \\ \dfrac{\partial w}{\partial y} + \psi_y \\ \dfrac{\partial w}{\partial x} + \psi_x \end{Bmatrix} + z \begin{Bmatrix} \dfrac{\partial \psi_x}{\partial x} \\ \dfrac{\partial \psi_y}{\partial y} \\ \dfrac{\partial \psi_y}{\partial x} + \dfrac{\partial \psi_x}{\partial y} \\ 0 \\ 0 \end{Bmatrix} \tag{3-77}
$$

where ε_{xx} and ε_{yy} are the normal strains, and γ_{xy}, γ_{yz} and γ_{xz} are the shear strains
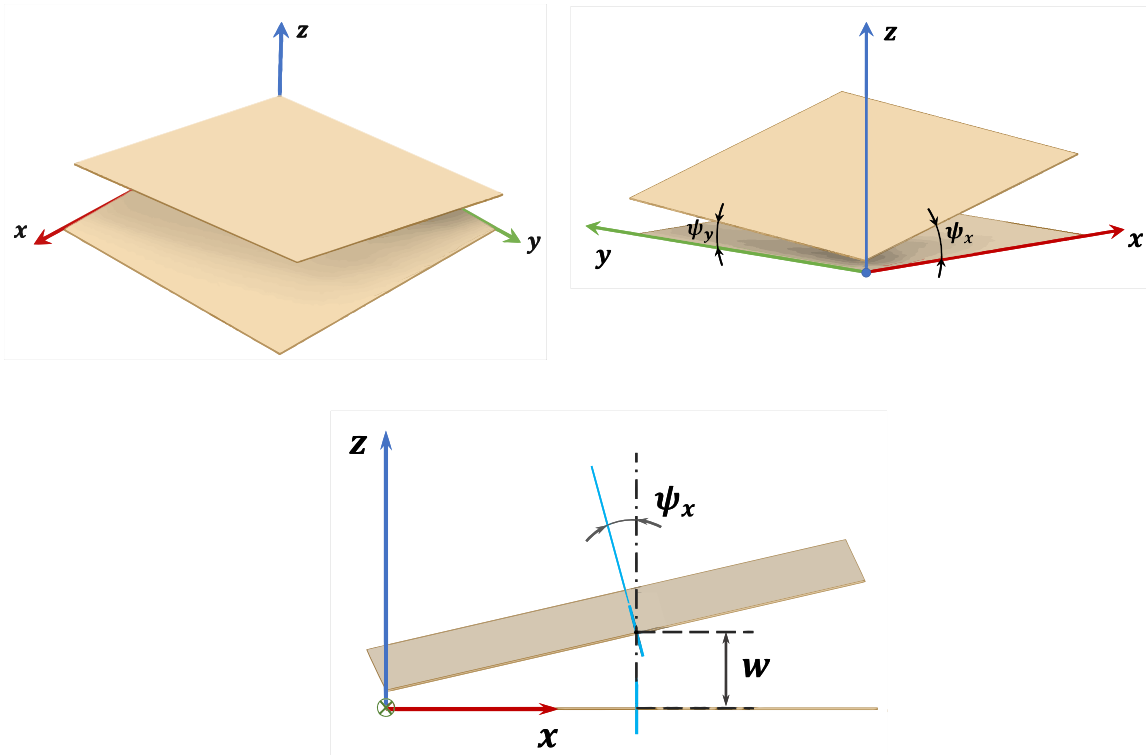
Figure 3-6: Plate rotational components

The stress-strain constitutive relation based on the nonlocal elasticity theory is expressed as

$$
\begin{Bmatrix} \sigma_{xx} \\ \sigma_{yy} \\ \sigma_{xy} \\ \sigma_{yz} \\ \sigma_{xz} \end{Bmatrix} - \mu \nabla^2 \begin{Bmatrix} \sigma_{xx} \\ \sigma_{yy} \\ \sigma_{xy} \\ \sigma_{yz} \\ \sigma_{xz} \end{Bmatrix} = \begin{bmatrix} \dfrac{E}{1-v^2} & \dfrac{vE}{1-v^2} & 0 & 0 & 0 \\ \dfrac{vE}{1-v^2} & \dfrac{E}{1-v^2} & 0 & 0 & 0 \\ 0 & 0 & 2G & 0 & 0 \\ 0 & 0 & 0 & G & 0 \\ 0 & 0 & 0 & 0 & G \end{bmatrix} \begin{Bmatrix} \varepsilon_{xx} \\ \varepsilon_{yy} \\ \gamma_{xy} \\ \gamma_{yz} \\ \gamma_{xz} \end{Bmatrix}
\tag{3-78}
$$

The force and moment resultants are expressed as has been given for CLPT in equations (3-46) and (3-47). Substituting equations (3-77) and (3-78) in those equations, the force and moment resultants for FSDT become[158, 203]

$$
(1 - \mu\nabla^2)\begin{bmatrix} N_{xx} \\ N_{yy} \\ N_{xy} \end{bmatrix} = h \begin{bmatrix} \dfrac{E}{1-v^2} & \dfrac{vE}{1-v^2} & 0 \\ \dfrac{vE}{1-v^2} & \dfrac{E}{1-v^2} & 0 \\ 0 & 0 & G \end{bmatrix} \begin{Bmatrix} \dfrac{\partial u_0}{\partial x} \\ \dfrac{\partial v_0}{\partial y} \\ \dfrac{\partial u_0}{\partial y} + \dfrac{\partial v_0}{\partial x} \end{Bmatrix}
\tag{3-79}
$$

$$
(1 - \mu\nabla^2)\begin{bmatrix} M_{xx} \\ M_{yy} \\ M_{xy} \\ Q_{xx} \\ Q_{yy} \end{bmatrix} = \begin{bmatrix} D & vD & 0 & 0 & 0 \\ vD & D & 0 & 0 & 0 \\ 0 & 0 & \dfrac{D(1-v)}{2} & 0 & 0 \\ 0 & 0 & 0 & k^2Gh & 0 \\ 0 & 0 & 0 & 0 & k^2Gh \end{bmatrix} \begin{Bmatrix} \dfrac{\partial \psi_x}{\partial x} \\ \dfrac{\partial \psi_y}{\partial y} \\ \dfrac{\partial \psi_y}{\partial x} + \dfrac{\partial \psi_x}{\partial y} \\ \dfrac{\partial w_0}{\partial x} + \psi_x \\ \dfrac{\partial w_0}{\partial y} + \psi_y \end{Bmatrix}
\tag{3-80}
$$

where k^2 is the shear correction factor, and D and G are the bending rigidity and shear modulus, respectively, as have already been defined.

The equilibrium equations for the Mindlin plate theory as restated by Ansari et al.[170] are

$$
\frac{\partial N_{xx}}{\partial x} + \frac{\partial N_{xy}}{\partial y} = I_0 \frac{\partial^2 u_0}{\partial t^2} + I_1 \frac{\partial^2 \psi_x}{\partial t^2}
$$

$$
\frac{\partial N_{xy}}{\partial x} + \frac{\partial N_{yy}}{\partial y} = I_0 \frac{\partial^2 v_0}{\partial t^2} + I_1 \frac{\partial^2 \psi_y}{\partial t^2}
$$

$$
\tag{3-81}
$$

$$\frac{\partial Q_{xx}}{\partial x} + \frac{\partial Q_{yy}}{\partial y} + p = I_0 \frac{\partial^2 w_0}{\partial t^2}$$

$$\frac{\partial M_{xx}}{\partial x} + \frac{\partial M_{xy}}{\partial y} - Q_{xx} = I_1 \frac{\partial^2 u_0}{\partial t^2} + I_2 \frac{\partial^2 \psi_x}{\partial t^2}$$

$$\frac{\partial M_{xy}}{\partial x} + \frac{\partial M_{yy}}{\partial y} - Q_{yy} = I_1 \frac{\partial^2 v_0}{\partial t^2} + I_2 \frac{\partial^2 \psi_y}{\partial t^2}$$

where I_0, I_1 and I_2 are mass moments of inertia as given in equation (3-43). I_1 is zero for sheets that are symmetric about the z axis.

Equation (3-81) is multiplied by $(1 - \mu \nabla^2)$ and equations (3-78) to (3-80) are substituted and simplified to yield the governing equations in terms of the five unknowns u_0, v_0, w_0, ψ_x and ψ_y.

$$\frac{Eh}{1-v^2}\frac{\partial^2 u_{0i}}{\partial x^2} + Gh\frac{\partial^2 u_{0i}}{\partial y^2} + \left(\frac{vEh}{1-v^2} + Gh\right)\frac{\partial^2 v_{0i}}{\partial x \partial y} = I_0\left(\frac{\partial^2 u_{0i}}{\partial t^2} - \mu\nabla^2\frac{\partial^2 u_{0i}}{\partial t^2}\right)$$

$$\left(\frac{vEh}{1-v^2} + Gh\right)\frac{\partial^2 u_{0i}}{\partial x \partial y} + Gh\frac{\partial^2 v_{0i}}{\partial x^2} + \frac{Eh}{1-v^2}\frac{\partial^2 v_{0i}}{\partial y^2} = I_0\left(\frac{\partial^2 v_{0i}}{\partial t^2} - \mu\nabla^2\frac{\partial^2 v_{0i}}{\partial t^2}\right)$$

$$k^2Gh\frac{\partial^2 w_{0i}}{\partial x^2} + k^2Gh\frac{\partial^2 w_{0i}}{\partial y^2} + k^2Gh\frac{\partial \psi_{xi}}{\partial x} + k^2Gh\frac{\partial \psi_{yi}}{\partial y} + (1 - \mu\nabla^2)p_i$$

$$= I_0\left(\frac{\partial^2 w_{0i}}{\partial t^2} - \mu\nabla^2\frac{\partial^2 w_{0i}}{\partial t^2}\right) \qquad (3\text{-}82)$$

$$-k^2Gh\frac{\partial w_{0i}}{\partial x} + D\frac{\partial^2 \psi_{xi}}{\partial x^2} - k^2Gh\psi_{xi} + \frac{D(1-v)}{2}\frac{\partial^2 \psi_{xi}}{\partial y^2} + \frac{D(1+v)}{2}\frac{\partial^2 \psi_{yi}}{\partial x \partial y}$$

$$= I_2\left(\frac{\partial^2 \psi_{xi}}{\partial t^2} - \mu\nabla^2\frac{\partial^2 \psi_{xi}}{\partial t^2}\right)$$

$$-k^2Gh\frac{\partial w_{0i}}{\partial y} + \frac{D(1+v)}{2}\frac{\partial^2 \psi_{xi}}{\partial x \partial y} + D\frac{\partial^2 \psi_{yi}}{\partial y^2} + \frac{D(1-v)}{2}\frac{\partial^2 \psi_{yi}}{\partial x^2} - k^2Gh\psi_{yi}$$

$$= I_2\left(\frac{\partial^2 \psi_{yi}}{\partial t^2} - \mu\nabla^2\frac{\partial^2 \psi_{yi}}{\partial t^2}\right)$$

Equation (3-82) is the nonlocal FSDT equations of motion for isotropic GSs in an MLGS composite in terms of u_0, v_0, w_0, ψ_x and ψ_y. Since I_1 is zero the first two equations of equation (3-82) are not coupled to the last three and can be ignored

to reduce the number of unknowns to be found and consequently the amount of computations to be carried out. Therefore, the **nonlocal** equations of motion for **isotropic** GSs in an **MLGSs** composite in terms of the transverse displacements and the rotations, w_0, ψ_x and ψ_y are given as

$$k^2 Gh \frac{\partial^2 w_{0i}}{\partial x^2} + k^2 Gh \frac{\partial^2 w_{0i}}{\partial y^2} + k^2 Gh \frac{\partial \psi_{xi}}{\partial x} + k^2 Gh \frac{\partial \psi_{yi}}{\partial y} + (1 - \mu \nabla^2) p_i$$

$$= I_0 \left(\frac{\partial^2 w_{0i}}{\partial t^2} - \mu \nabla^2 \frac{\partial^2 w_{0i}}{\partial t^2} \right)$$

$$-k^2 Gh \frac{\partial w_{0i}}{\partial x} + D \frac{\partial^2 \psi_{xi}}{\partial x^2} - k^2 Gh \psi_{xi} + \frac{D(1-v)}{2} \frac{\partial^2 \psi_{xi}}{\partial y^2} + \frac{D(1+v)}{2} \frac{\partial^2 \psi_{yi}}{\partial x \partial y}$$

$$= I_2 \left(\frac{\partial^2 \psi_{xi}}{\partial t^2} - \mu \nabla^2 \frac{\partial^2 \psi_{xi}}{\partial t^2} \right) \qquad (3\text{-}83)$$

$$-k^2 Gh \frac{\partial w_{0i}}{\partial y} + \frac{D(1+v)}{2} \frac{\partial^2 \psi_{xi}}{\partial x \partial y} + D \frac{\partial^2 \psi_{yi}}{\partial y^2} + \frac{D(1-v)}{2} \frac{\partial^2 \psi_{yi}}{\partial x^2} - k^2 Gh \psi_{yi}$$

$$= I_2 \left(\frac{\partial^2 \psi_{yi}}{\partial t^2} - \mu \nabla^2 \frac{\partial^2 \psi_{yi}}{\partial t^2} \right)$$

For the local equations of motion, μ is set to zero in equation (3-83).

Some works[204, 205] have proposed a new FSDT that also reduces the five unknowns in the classical FSDT to four and eliminates the use of the shear correction factor.

Membrane theory

Various continuum models and approaches based on plate models have been predominant in the vibrational analysis of GSs and some of them have been discussed here. However, very little attention has been given to the use of membrane models for such analyses. Membranes are two dimensional structures that cannot resist compressive stresses and bending moments, with restoring forces arising exclusively from the in-plane tensile forces. An easily observable distinction between membranes and thin plates is the length to thickness aspect ratio. Generally, based on length to thickness ratio, classification of structures could be made as Table 3-1 presents.

a/h	2	5	$10-20$	$20-100$ $(20-80)$	≥ 80
Structural classification	Very thick plates	Thick plates	Moderately thick plates	Thin plates	Membranes?

Table 3-1: Classification of structures based on a/h ratio

The mechanical behaviour of a structure depends on its material type and spatial dimension. To classify a structure as a membrane, the question that begs therefore is whether with a ratio $a/h \geq 80$ the structure has negligible resistance to compressive stresses and bending moments and as such behaves as a membrane. The next section derives the equation of motion for the nonlinear vibration of an SLGS modelled as a membrane structure.

Consider an orthotropic SLGS modelled as a taut membrane under in-plane tensile force T and consider a rectangular element of the membrane in a deflected configuration as shown in Figure 3-7.
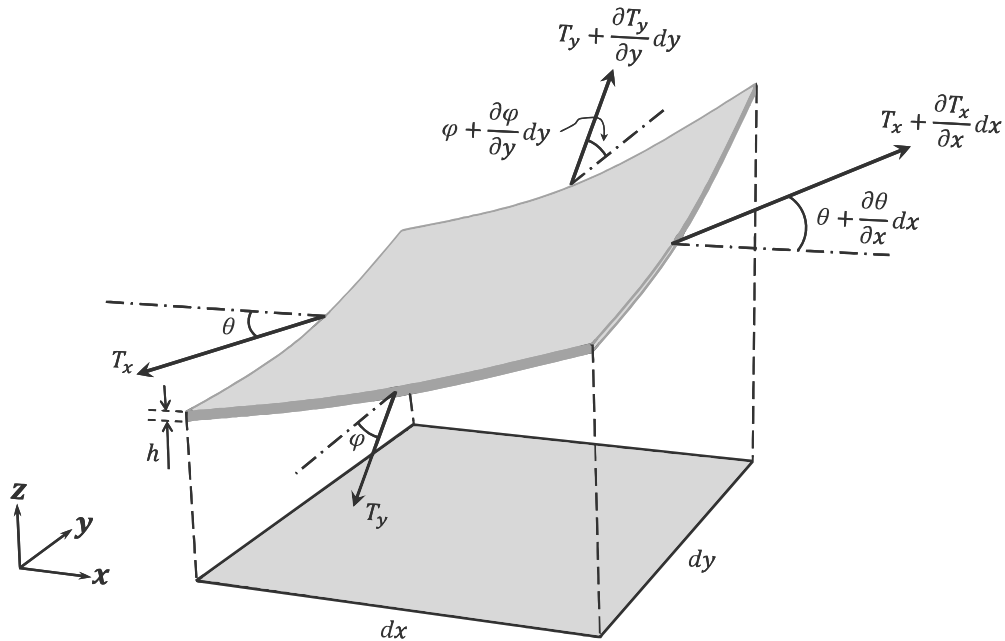
Figure 3-7: Tensile forces on a deflected rectangular membrane element

T_x and T_y are the intensity per unit length of the tensile forces acting along the x- and y-axes and p is the pressure acting on the membrane element. The resultant force acting on the element in the z-direction is given as

$$\sum F_z = \left(T_x + \frac{\partial T_x}{\partial x} dx\right) \sin\left(\theta_x + \frac{\partial \theta_x}{\partial x} dx\right) dy - T_x \sin\theta_x \, dy$$
$$+ \left(T_y + \frac{\partial T_y}{\partial y} dy\right) \sin\left(\theta_y + \frac{\partial \theta_y}{\partial y} dy\right) dx - T_y \sin\theta_y \, dx + p dx dy \tag{3-84}$$

Expanding brackets and collecting like terms, equation (3-84) becomes

$$\sum F_z = T_x \left[\sin\left(\theta_x + \frac{\partial \theta_x}{\partial x} dx\right) - \sin\theta_x\right] dy + \frac{\partial T_x}{\partial x} \sin\left(\theta_x + \frac{\partial \theta_x}{\partial x} dx\right) dx dy$$
$$+ T_y \left[\sin\left(\theta_y + \frac{\partial \theta_y}{\partial y} dy\right) - \sin\theta_y\right] dx + \frac{\partial T_y}{\partial y} \sin\left(\theta_y + \frac{\partial \theta_y}{\partial y} dy\right) dx dy \tag{3-85}$$
$$+ p dx dy$$

Replacing the triangular parts with the first two terms of their Taylor's expansion and neglecting higher order terms and terms with trivial parts like $\frac{\partial T_x}{\partial x} \frac{\partial \theta_x}{\partial x}$, we have

$$\sum F_z = \frac{\partial T_x}{\partial x} \sin\theta_x \, dx dy + T_x \cos\theta_x \frac{\partial \theta_x}{\partial x} dx dy + \frac{\partial T_y}{\partial y} \sin\theta_y \, dx dy + T_y \cos\theta_y \frac{\partial \theta_y}{\partial y} dx dy$$
$$+ p dx dy \tag{3-86}$$

Applying Newton's second law in the z-direction, we have

$$\sum F_z = \rho h \left(\frac{dx dy}{\cos\theta_x \cos\theta_y}\right) \frac{\partial^2 w}{\partial t^2} \tag{3-87}$$

 Where w is the deflection of the membrane in the z direction, ρ the mass per unit area of the membrane and t the time. Equating equation (3-86) to (3-87) and simplifying, the general form of the equation of motion for the vibrating SLGS membrane is given as

$$\frac{\partial^2 w}{\partial t^2} = \frac{1}{\rho h}\left(\frac{\partial T_x}{\partial x} \sin\theta_x \cos\theta_x \cos\theta_y + T_x \cos^2\theta_x \cos\theta_y \frac{\partial \theta_x}{\partial x} + \frac{\partial T_y}{\partial y} \sin\theta_y \cos\theta_x \cos\theta_y\right.$$
$$\left. + T_y \cos\theta_x \cos^2\theta_y \frac{\partial \theta_y}{\partial y} + p\right) \tag{3-88}$$

From Figure 3-7 , the following geometric relations can be deduced

$$\tan\theta_x = \frac{\partial w}{\partial x} \tag{3-89}$$

Which means

$$\frac{\partial \theta_x}{\partial x} = \cos^2\theta_x \frac{\partial^2 w}{\partial x^2} \cong \frac{\partial^2 w}{\partial x^2} \tag{3-90}$$

Similarly,

82

$$\tan \theta_y = \frac{\partial w}{\partial y} \tag{3-91}$$

and,

$$\frac{\partial \theta_y}{\partial y} = \cos^2 \theta_y \frac{\partial^2 w}{\partial y^2} \cong \frac{\partial^2 w}{\partial y^2} \tag{3-92}$$

Substituting equations (3-90) and (3-92) in (3-88), the general form of the equation of motion for a SLGS membrane with large amplitude and large rotation is given by

$$\frac{\partial^2 w}{\partial t^2} = \frac{1}{\rho h} \left(\frac{\partial T_x}{\partial x} \sin \theta_x \cos \theta_x \cos \theta_y + T_x \cos^2 \theta_x \cos \theta_y \frac{\partial^2 w}{\partial x^2} + \frac{\partial T_y}{\partial y} \sin \theta_y \cos \theta_x \cos \theta_y \right.$$
$$\left. + T_y \cos \theta_x \cos^2 \theta_y \frac{\partial^2 w}{\partial y^2} + p \right) \tag{3-93}$$

For very small rotations, $\cos \theta_x \cong 1$, $\cos \theta_y \cong 1$, $\sin \theta_x \cong 0$ and $\sin \theta_y \cong 0$, equation (3-93) becomes

$$\frac{\partial^2 w}{\partial t^2} = \frac{1}{\rho h} \left(T_x \frac{\partial^2 w}{\partial y^2} + T_y \frac{\partial^2 w}{\partial y^2} + p \right) \tag{3-94}$$

The tensile forces per unit length, T_x and T_y are given as[166]

$$T_x = T_{x,0} + h E_x \left(\frac{\int_0^a \sqrt{1 + \left(\frac{\partial w}{\partial x} \right)^2} \, dx - a}{a} \right)$$
$$\tag{3-95}$$
$$T_y = T_{y,0} + h E_y \left(\frac{\int_0^b \sqrt{1 + \left(\frac{\partial w}{\partial y} \right)^2} \, dy - b}{b} \right)$$

where a and b are the length and width of the SLG membrane in the equilibrium position, E_x and E_y are the Young's modulus of the membrane in the x and y directions, $T_{x,0}$ and $T_{y,0}$ are the pretensions per unit length in the x and y directions, respectively. Equation (3-95) is substituted in (3-94) to give the equation of motion for the **large amplitude** vibration of an **SLGS** with **small rotations** as

$$\frac{\partial^2 w}{\partial t^2} = \frac{1}{\rho h}\left[\left(T_{x,0} + hE_x\left(\frac{\int_0^a \sqrt{1+\left(\frac{\partial w}{\partial x}\right)^2}\,dx - a}{a}\right)\right)\frac{\partial^2 w}{\partial x^2}\right.$$
$$\left. + \left(T_{y,0} + hE_y\left(\frac{\int_0^b \sqrt{1+\left(\frac{\partial w}{\partial y}\right)^2}\,dy - b}{b}\right)\right)\frac{\partial^2 w}{\partial y^2} + p\right]$$

(3-96)

When the amplitude of the vibration is small, $\int_0^a \sqrt{1+\left(\frac{\partial w}{\partial x}\right)^2}\,dx \cong a$, and

$\int_0^b \sqrt{1+\left(\frac{\partial w}{\partial y}\right)^2}\,dy \cong b$. Equation (3-96) becomes

$$\frac{\partial^2 w}{\partial t^2} = \frac{1}{\rho h}\left(T_{x,0}\frac{\partial^2 w}{\partial x^2} + T_{y,0}\frac{\partial^2 w}{\partial y^2} + p\right)$$

(3-97)

Equation (3-97) is the equation of motion for the **small amplitude** vibration of an **SLGS** with **small rotations**. In the language of this chapter, equation (3-96) is the *nonlinear* equation of motion for the vibration analysis of *orthotropic SLGSs*, while equation (3-97) is the *linear* equation of motion for the *orthotropic SLGS*.

3.2.4 Boundary conditions

The boundary conditions (BCs) of a vibrating structure are pertinent in its vibration analysis because they influence the resonant frequencies and mode shapes of the vibration. To solve any of the plate models presented in Section 3.2.3, appropriate boundary conditions must be applied to the model. Boundary conditions are conditions/equations that hold true at each point on the periphery of the structure. Generally, when solving a mathematical model in a domain, the BCs define the constraints existing at the extremes (maximum and minimum states) of the domain. When the BCs are the major determining conditions in the solution of a problem, such problems are described as Boundary Value Problems (BVPs). A similar set of problems called the Initial Value Problems (IVPs) use initial conditions (ICs) as the constraints in the solution of the problem. Where the

initial conditions are the values of the independent variable at the lowest domain point; for time domain, the ICs are usually the values of the independent variables when $time = 0$. Because vibrating problems involve both spatial and time domains, the ICs also have to be defined.

The BCs applied to a given problem depend on the physical condition and meaning of the problem being modelled. Classically, there are three basic BCs that can be applied to a classic vibration problem in any combination that represents the physical boundaries of the problem. These are the simply supported (SS), clamped (C), and free (F) boundary conditions.

Simply Supported

Physically, when an edge of a structure is prevented from deflecting transversely but can rotate freely as though hinged at that edge, the edge is said to be simply supported. Consequently, the value of the transverse displacement variable and the bending moments along any edge that is simply supported will have a value of zero, as shown mathematically in equation (3-98). The specific expression for the bending moments will however depend on the plate model being used.

$$w(x, y, t)|_{x,y\,=\,min\,and\,max} = 0$$

$$M_{xx}|_{x,y\,=\,min\,and\,max} = M_{yy}|_{x,y\,=\,min\,and\,max} = 0$$

(3-98)

Clamped

For the clamped case, the edges of the structure are prevented from deflecting transversely and from rotating. On such edges, the value of the transverse displacement variable and the rotation angles along the edges being clamped are zero (equation (3-99)).

$$w(x, y, t)|_{x,y\,=\,min\,and\,max} = 0$$

$$\varphi_x(x, y, t)|_{x,y\,=\,min\,and\,max} = \varphi_y(x, y, t)\big|_{x,y\,=\,min\,and\,max} = 0$$

(3-99)

Free

When the edges are free, they can deflect transversely and rotate. Consequently, the effective transverse shear force and the bending moments along those edges must be zero, as shown in equation (3-100).

$$Q_{xx}|_{x,y\,=\,min\,and\,max} = \; Q_{yy}|_{x,y\,=\,min\,and\,max} \; = \; 0$$

(3-100)

$$M_{xx}|_{x,y\,=\,min\,and\,max} = \; M_{yy}|_{x,y\,=\,min\,and\,max} \; = \; 0$$

3.3   Solution methods

The derived partial differential equations (PDEs) of motion for the vibration of GSs, particularly nonlinear vibrations, are appreciably complex and difficult to solve. A few different solution methods have been employed by different researchers in the search for accurate solutions to the PDEs derived in the preceding subsections. Most of these solutions are numerical solutions that have been developed for problems in engineering and physical sciences. Some of these solution methods applied to the vibration problem of GSs include the Differential Quadrature method (DQM), the Generalized Differential Quadrature Rule (GDQR), Navier's solution method, Harmonic Balance Method (HBM), Finite Difference Method (FDM), the Element-free kp-Ritz Method, etc. Of all these methods, only the GDQR has been demonstrated to be robust enough to handle any combination of the classic simply supported, clamped and free boundary conditions. This work therefore used the GDQR methods to solve the derived PDEs of motion for the GSs. Since a huge chunk of the literature on vibration of GSs deal with the fully simply supported (SSSS) or fully clamped GS, the focus in this work and the presentation here is for a simply supported-free-simply supported-free (SSFSSF) and a clamped-free-clamped-free resonator (CFCF). To validate the GDQR, the basic CLPT model (linear local Kirchhoff plate model for a SLGS) was solved and compared with results from exact solutions.

A few works[206-210] have outlined the DQM and GDQR in detail, but a few loopholes still exist that make their application a bit difficult to understand. Therefore, step by step processes in using the DQM and GDQR are outlined in this work.

Differential Quadrature Method (DQM)

The DQM is a numerical method for solving initial- and/or boundary-value problems, initially proposed as a general numerical method for solving nonlinear PDEs[211]. After it was first applied in structural mechanics[212, 213], it became one of the widely used numerical methods in solving structural mechanics problems. Detailed reviews on its chronological development have been published[207, 214], as such this work will not delve into that. However, a generalised form of the classical DQM that has been proposed to particularly ease handling problems with multiple initial or boundary conditions will be reviewed in detail.

The Differential Quadrature Rule (DQR)

The basic idea of the DQM is that the partial derivative of a function with respect to a spatial variable at a discrete sample point can be approximated as a weighted linear sum of the values of the function at all sample points in a certain spatial direction in the domain. Because this work focuses on two dimensional structural problems, the DQM rule for two dimensional problems is presented. Consider a function $f = f(x, y)$ with its field in a rectangular domain $0 \leq x \leq a, 0 \leq y \leq b$. Let the grid of discrete sampling points with n_x and n_y points in the x- and y-directions, respectively, be as shown in Figure 3-8. An rth-order partial derivative with respect to x at a discrete point $x = x_p$ along any line $y = y_q$ parallel to the x-axis can be approximated as[207]

$$\left. \frac{\partial^r f(x,y)}{\partial x^r} \right|_{x=x_p} = \sum_{k=1}^{n_x} A_{pk}^{(r)} f_{kq}; \quad p = 1, 2, 3, \dots, \boldsymbol{n_x} \tag{3-101}$$

where n_x is the total number of grid points in the x-direction, $A_{pk}^{(r)}$ are the weighting coefficients, and f_{kq} are the function values at the point (k, q) *i.e.* $f_{kq} = f(k, q)$. Similarly, an sth-order partial derivative with respect to y at a discrete point $y = y_q$ along any line $x = x_p$ parallel to the y-axis can be approximated as[207]

$$\left. \frac{\partial^s f(x,y)}{\partial y^s} \right|_{y=y_q} = \sum_{m=1}^{n_y} B_{qm}^{(s)} f_{qm}; \quad q = 1, 2, 3, \dots, n_y \tag{3-102}$$

here, n_y is the total number of grid points in the y-direction, $B_{qm}^{(s)}$ are the corresponding weighting coefficients. For a mixed derivative, the quadrature rule is

$$\frac{\partial^{(r+s)} f(x,y)}{\partial x^r \partial y^s}\bigg|_{x_p, y_q} = \sum_{k=1}^{n_x} \sum_{m=1}^{n_y} A_{pk}^{(r)} B_{qm}^{(s)} f_{km}; \quad p = 1, 2, \dots, n_x; \, q = 1, 2, \dots, n_y \qquad (3\text{-}103)$$
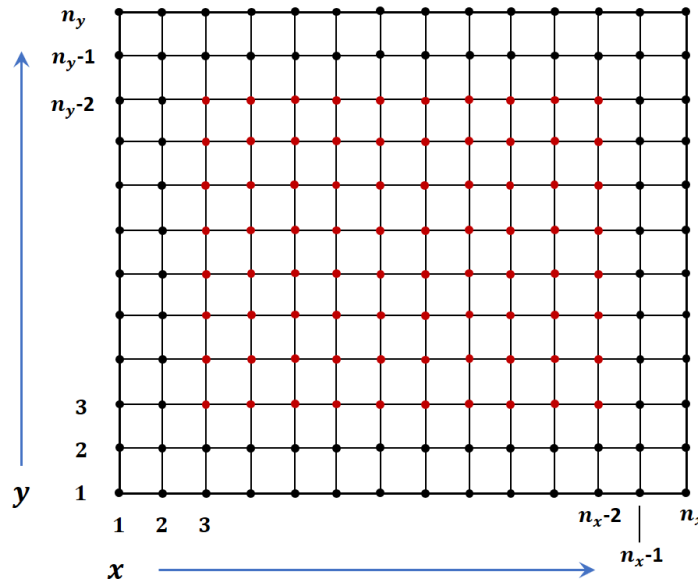
Figure 3-8: DQM grid distribution of solution domain

With the quadrature rules in equations (3-101) - (3-103), the quadrature analogue for a given differential equation can be written for every point in its solution domain. Thereby, reducing the differential equation to a set of algebraic equations, the number of which depends on the number of sample points selected. The accuracy of the solution depends heavily on the accuracy of the weighting coefficients and the choice of sampling points[207].

Weighting coefficients

The weighting coefficients of the DQR can be determined by some appropriate functional approximations, with the approximate functions called test functions. Using the Langrangian interpolation shape functions as the test functions, the weighting coefficients for the first derivative when $p \neq k$ and $q \neq m$ are given as

$$A_{pk}^{(1)} = \frac{M(x_p)}{(x_p - x_k)M(x_k)}; \qquad p, k = 1, 2, \dots, n_x; p \neq k$$

(3-104)

$$B_{qm}^{(1)} = \frac{M(y_q)}{(y_q - y_m)M(y_m)}; \qquad q, m = 1, 2, \dots, n_y; q \neq m$$

where $M(\beta_i)$ is defined as

$$M(\beta_i) = \prod_{j=1;\ j \neq i}^{n} (\beta_i - \beta_j) \qquad\qquad (3\text{-}105)$$

When $p = k$ and $q = m$, the weighting coefficients for the first derivative are given as[198]

$$A_{pp}^{(1)} = -\sum_{i=1;\ i \neq p}^{n_x} A_{pi}^{(1)}; \qquad p = 1, 2, \dots, n_x$$

(3-106)

$$B_{qq}^{(1)} = -\sum_{j=1;\ j \neq p}^{n_y} B_{qj}^{(1)}; \qquad q = 1, 2, \dots, n_y$$

And the weighting coefficients for the second and higher order derivatives are given as[207]

$$A_{pk}^{(r)} = \begin{cases} r\left(A_{pp}^{(r-1)}A_{pk}^{(1)} - \dfrac{A_{pk}^{(r-1)}}{x_p - x_k}\right), & p \neq k \\[2ex] -\displaystyle\sum_{i=1;}^{n_x} A_{pi}^{(r)}, & p = k \end{cases} \qquad p, k = 1, 2, \dots, n_x; 2 \leq r \leq (n_x - 1)$$

(3-107)

$$B_{qm}^{(r)} = \begin{cases} r\left(B_{qq}^{(r-1)}B_{qm}^{(1)} - \dfrac{B_{qm}^{(r-1)}}{y_q - y_m}\right), & q \neq m \\[2ex] -\displaystyle\sum_{j=1;}^{n_y} B_{qj}^{(r)}, & q = m \end{cases} \qquad q, m = 1, 2, \dots, n_y; 2 \leq r$$

$$\leq (n_y - 1)$$

Distribution of sampling points

The choice of grid distribution for a solution domain, as earlier mentioned, impacts the accuracy of DQM solutions. Six typical grid distributions commonly used in literature are[209, 215]

1. Equally spaced grid points

$$X_i = \frac{i-1}{N-1}, \quad i = 1, 2, \dots, N \tag{3-108}$$

2. Roots of Chebyshev polynomials of the first kind

$$X_i = \frac{r_i - r_1}{r_N - r_1}, \quad i = 1, 2, \dots, N$$

$$r_i = \cos\left(\frac{(2i-1)\pi}{2N}\right) \tag{3-109}$$

3. Roots of Chebyshev polynomials of the second kind

$$X_i = \frac{r_i - r_1}{r_N - r_1}, \quad i = 1, 2, \dots, N$$

$$r_i = \cos\left(\frac{i\pi}{N-1}\right) \tag{3-110}$$

4. Roots of Legendre polynomials

$$X_i = \frac{r_i - r_1}{r_N - r_1}, \quad i = 1, 2, \dots, N$$

$$r_i = \left(1 - \frac{1}{8N^2} + \frac{1}{8N^3}\right)\cos\left(\frac{(4i-1)\pi}{4N+2}\right) \tag{3-111}$$

5. Quadratic grid points

$$X_i = \begin{cases} 2\left(\dfrac{i-1}{N-1}\right)^2, & i = 1, 2, \dots, \dfrac{N+1}{2} \\[2ex] -2\left(\dfrac{i-1}{N-1}\right)^2 + 4\left(\dfrac{i-1}{N-1}\right) - 1, & i = \left(\dfrac{N+1}{2}\right) + 1, \dots, N \end{cases} \tag{3-112}$$

6. Chebyshev-Gauss-Lobatto grid points

$$X_i = \frac{1}{2}\left[1 - \cos\left(\frac{i-1}{N-1}\pi\right)\right], \quad i = 1, 2, \dots, N \tag{3-113}$$

Where $X_i = {x_i}/{a}$ is the normalized sample point ($Y_i = {y_i}/{b}$ for sampling points in the y-direction) and N is the number of grid points in the specified direction (n_x and

90

n_y in the x- and y-directions respectively). The number of grid points and choice of grid point distribution for the x- and y-directions do not have to be the same. Ultimately, the choice of grid point distribution will depend on the problem to be solved, however, the Chebyshev-Gauss-Lobatto grid points are recommended for structural mechanics problems[207]. With the DQM, when solving two-dimensional vibration problems in which two boundary equations exist for each boundary, the first boundary equations are applied to the sampling points on the boundary lines and the second boundary equations are applied to sampling points adjacent and very close to the points on the boundary lines. These points adjacent and close to the boundary points are called δ-points and the method called the δ-technique.

Generalized Differential Quadrature (GDQ) Method

One major challenge with the DQR presented in equation (3-101) is the difficulty in handling multiple BCs, even with the δ-technique. The δ-points used in the δ-technique no matter how close they are to the BPs are still inner domain points and as such are mathematically unsound and are bound to cause ill-conditioned problems in the DQM solution[206]. Consequently, a new DQR called the generalized differential quadrature rule (GDQR) was developed that accurately and efficiently handles multiple BCs[206].

Consider a one-dimensional field variable $f(x)$ prescribed by a differential equation in a field domain $x_1 \leq x \leq x_N$ which may also be constrained by a set of given conditions at any point(s) in the domain. The solution domain is divided into N parts by points x_i $(i = 1, 2, \ldots, N)$ that include all points in the domain whether they are constrained by conditions or not. Let $f_i^{(r)} = f^{(r)}(x_i)$ $(r = 0, 1, 2, \ldots)$ be the rth-order derivative of the field variable $f(x)$, with $f_i^{(0)} = f_i$ being the function value at point x_i. If the number of equations applicable at point x_i is denoted by n_i, the highest value of r is $(n_i - 1)$ and the independent variables at that point which are chosen as the function value and its derivatives of possible lowest order wherever necessary, are $f_i^{(r)}$ $(r = 0, 1, 2, \ldots, n_i - 1)$.

The test function used here is the Hermite interpolation shape function, the field function's interpolation expression is therefore given as

$$f(x) = \sum_{j=1}^{N} \left(h_{j0}(x) f_j^{(0)} + h_{j1}(x) f_j^{(1)} + \cdots + h_{j(n_j-1)}(x) f_j^{(n_j-1)} \right)$$

$$= \left\{ h_{10}(x), h_{11}(x), \ldots, h_{1(n_1-1)}(x), \ldots, h_{N0}(x), h_{N1}(x), \ldots, h_{N(n_N-1)}(x) \right\}^T$$

$$\times \left\{ f_1^{(0)}, f_1^{(1)}, \ldots, f_1^{(n_1-1)}, \ldots, f_N^{(0)}, f_N^{(1)}, \ldots, f_N^{(n_N-1)} \right\}$$

(3-114)

$$f(x) = \sum_{k=1}^{M} h_k(x) \, U_k$$

where M is the total number of independent variables in the domain, U_k the independent variable at x_k, and h_k the Hermite interpolation shape function which are given as

$$M = \sum_{j=1}^{N} n_j$$

$$\{U_k\} = \{U_1, U_2, \ldots, U_M\}$$

$$= \left\{ f_1^{(0)}, f_1^{(1)}, \ldots, f_1^{(n_1-1)}, \ldots, f_N^{(0)}, f_N^{(1)}, \ldots, f_N^{(n_N-1)} \right\}$$

(3-115)

$$\{h_k\} = \{h_1, h_2, \ldots, h_M\}^T$$

$$= \left\{ h_{10}(x), h_{11}(x), \ldots, h_{1(n_1-1)}(x), \ldots, h_{N0}(x), h_{N1}(x), \ldots, h_{N(n_N-1)}(x) \right\}^T$$

The Hermite interpolation shape functions have the following properties[210]

$$h_{jl}^{(r)} = \begin{cases} 1 & if\ i = j\ and\ l = r \\ 0 & otherwise \end{cases}$$

(3-116)

Taking the rth derivative of equation (3-114), we have

$$\frac{d^r f(x_i)}{dx^r} = \sum_{j=1}^{N} \left(h_{j0}^{(r)}(x_i) f_j^{(0)} + h_{j1}^{(r)}(x_i) f_j^{(1)} + \cdots + h_{j(n_j-1)}^{(r)}(x_i) f_j^{(n_j-1)} \right)$$

$$= \left\{ h_{10}^{(r)}(x_i), h_{11}^{(r)}(x_i), \ldots, h_{1(n_1-1)}^{(r)}(x_i), \ldots, h_{N0}^{(r)}(x_i), h_{N1}^{(r)}(x_i), \ldots, h_{N(n_N-1)}^{(r)}(x_i) \right\}^T$$

$$\times \left\{ f_1^{(0)}, f_1^{(1)}, \ldots, f_1^{(n_1-1)}, \ldots, f_N^{(0)}, f_N^{(1)}, \ldots, f_N^{(n_N-1)} \right\}$$

(3-117)

$$\frac{d^r f(x_i)}{dx^r} = \sum_{k=1}^{M} E_{ik}^{(r)} U_k$$

where $E_{ik}^{(r)}$ are the weighting coefficients of the rth-order derivative of the function at point x_i. Therefore, the GDQR is

$$\frac{d^r f(x_i)}{dx^r} = \sum_{k=1}^{M} E_{ik}^{(r)} U_k \qquad (3\text{-}118)$$

And the weighting coefficients

$$E_{ik}^{(r)} = \frac{d^r h_k(x_i)}{dx^r} \qquad (3\text{-}119)$$

By rule, the number of independent variables at a sampling point in the solution domain must equal the number of equations that point must satisfy.

GDQR and explicit weighting coefficients for rectangular plates

For vibrating rectangular plates, the GDQR for x-, y- and xy-partial derivatives is

$$\frac{\partial^r f(x_i, y_j)}{\partial x^r} = \sum_{k=1}^{M_x} E_{ik}^{(r)} U_{kj}$$

$$\frac{\partial^s f(x_i, y_j)}{\partial y^s} = \sum_{m=1}^{M_y} E_{jm}^{(s)} U_{im}$$

$$\qquad (3\text{-}120)$$

$$\frac{\partial^{(r+s)} f(x_i, y_j)}{\partial x^r \partial y^s} = \sum_{k=2}^{M_x-1} \sum_{m=2}^{M_y-1} E_{ik}^{(r)} E_{jm}^{(s)} U_{km} + \sum_{m=1}^{n_y} B_{jm}^{(s)} \left(E_{i1}^{(r)} U_{1(m+1)} + E_{in_x}^{(r)} U_{n_x(m+1)} \right)$$
$$+ \sum_{k=1}^{n_x} A_{ik}^{(r)} \left(E_{j1}^{(s)} U_{(k+1)1} + E_{jn_y}^{(s)} U_{(k+1)n_y} \right)$$

where $i = 1, 2, \ldots, n_x$; $j = 1, 2, \ldots, n_y$; $M_x = n_x + 2$; $M_y = n_y + 2$; and $A_{ik}^{(r)}$ and $B_{jm}^{(s)}$ are the Langrangian interpolation shape functions given in equations (3-104), (3-106) and (3-107). For convenience in the application of the Hermite interpolation functions as derived by Wu and Liu[210], equation (3-120) is rewritten in the form

$$\frac{\partial^r f(x_i, y_j)}{\partial x^r} = \sum_{k=1}^{n_x} E_{ik0}^{(r)} h_j(y_j) f_{kj} + l_j(y_j) \left(E_{i11}^{(r)} f_{1j}^{(1)} + E_{in_x1}^{(r)} f_{n_xj}^{(1)} \right)$$

$$\qquad (3\text{-}121)$$

$$\frac{\partial^s f(x_i, y_j)}{\partial y^s} = \sum_{m=1}^{n_y} h_i(x_i) E_{jm0}^{(s)} f_{im} + l_i(x_i) \left(E_{j11}^{(s)} f_{i1}^{(1)} + E_{jn_y1}^{(s)} f_{in_y}^{(1)} \right)$$

$$\frac{\partial^{(r+s)} f(x_i, y_j)}{\partial x^r \partial y^s} = \sum_{k=1}^{n_x} \sum_{m=1}^{n_y} E_{ik0}^{(r)} E_{jm0}^{(s)} f_{km} + \sum_{m=1}^{n_y} B_{jm}^{(s)} \left(E_{i11}^{(r)} f_{1m}^{(1)} + E_{in_x1}^{(r)} f_{n_xm}^{(1)} \right)$$

$$+ \sum_{k=1}^{n_x} A_{ik}^{(r)} \left(E_{j11}^{(s)} f_{k1}^{(1)} + E_{jn_y1}^{(s)} f_{kn_y}^{(1)} \right)$$

Where $l_i(x_i)$ and $l_j(y_j)$ are the Lagrange functions at points x and y respectively, and

$$E_{ikp}^{(r)} = \frac{\partial^r h_{kp}(x_i)}{\partial x^r}$$

$$\text{(3-122)}$$

$$E_{jmq}^{(s)} = \frac{\partial^s h_{mq}(y_j)}{\partial y^s}$$

and the derived Hermite interpolation shape functions[210] $h_{kp}(x_i)$ are given in Table 3-2.

$h_{10}(x_i) = (a_{10} x_i^2 + b_{10} x_i + c_{10}) l_1(x_i)$	$a_{10} = \dfrac{-1}{(x_1 - x_N)^2} + \dfrac{l_1^{(1)}(x_1)}{x_1 - x_N}$ $b_{10} = \dfrac{1}{x_1 - x_N} - a_{10}(x_1 + x_N)$ $c_{10} = 1 - a_{10} x_1^2 - b_{10} x_1$
$h_{11}(x_i) = (a_{11} x_i^2 + b_{11} x_i + c_{11}) l_1(x_i)$	$a_{11} = \dfrac{1}{x_1 - x_N}$ $b_{11} = \dfrac{-(x_1 + x_N)}{x_1 - x_N}$ $c_{11} = \dfrac{x_1 x_N}{x_1 - x_N}$
$h_{Nj}(x_i) = (a_{Nj} x_i^2 + b_{Nj} x_i + c_{Nj}) l_N(x_i)$ $j = 0,1$	$a_{N0} = \dfrac{-1}{(x_1 - x_N)^2} + \dfrac{l_N^{(1)}(x_N)}{x_1 - x_N}$ $b_{N0} = \dfrac{-1}{x_1 - x_N} - a_{N0}(x_1 + x_N)$ $c_{N0} = 1 - a_{N0} x_N^2 - b_{N0} x_N$ $a_{N1} = \dfrac{-1}{x_1 - x_N}$ $b_{N1} = \dfrac{(x_1 + x_N)}{x_1 - x_N}$ $c_{N1} = \dfrac{-x_1 x_N}{x_1 - x_N}$
$h_{j0}(x_i) = \dfrac{(x_i - x_1)(x_i - x_N)}{(x_j - x_1)(x_j - x_N)} l_j(x_i)$ $j = 2, 3, \ldots, N - 1$	

Table 3-2: Hermite interpolation shape functions for rectangular plate vibration problem given for the x-direction ($N = n_x$) but also applicable in the y-direction

GDQR application to rectangular plate vibration problems

As with the DQM, the GDQR is applied to discretize the governing equation and BCs and the resulting set of linear equations are solved.

Step one

The governing equation(s) of motion are expressed as a function of the transverse deflection (w) and vibration frequency (ω) and the BC equations for the boundary conditions are specified according to the desired continuum model.

Step two

The number of grid points n_x and n_y in the x- and y-directions, respectively, and the grid point distribution to be used are specified. Although the authors of the GDQR claim it does not require solution domain decomposition, the deduction of the eigenvalue form of the model (described in step five) requires the solution domain to be decomposed. Figure 3-9 shows the grid points and the solution domain decomposition for the GDQR. The solution domain decomposition is different to that of the DQM in that the boundary domain does not include δ-points but only the points on the boundary lines $X = 0, a$ and $Y = 0, b$. The number of sampling points in the inner domain is $(n_x - 2)(n_y - 2)$ and in the boundary domain is $2(n_x + n_y) - 4$. At each of these sampling points the independent variable(s) is/are defined. If n_i is the number of equations satisfied in the inner domain, then the total number of independent variables in the inner domain is $n_i(n_x - 2)(n_y - 2)$; similarly, if n_b is the number of equations satisfied on each point in the boundary domain, the total number of independent variables in the boundary domain is $2n_b(n_x + n_y - 2)$.
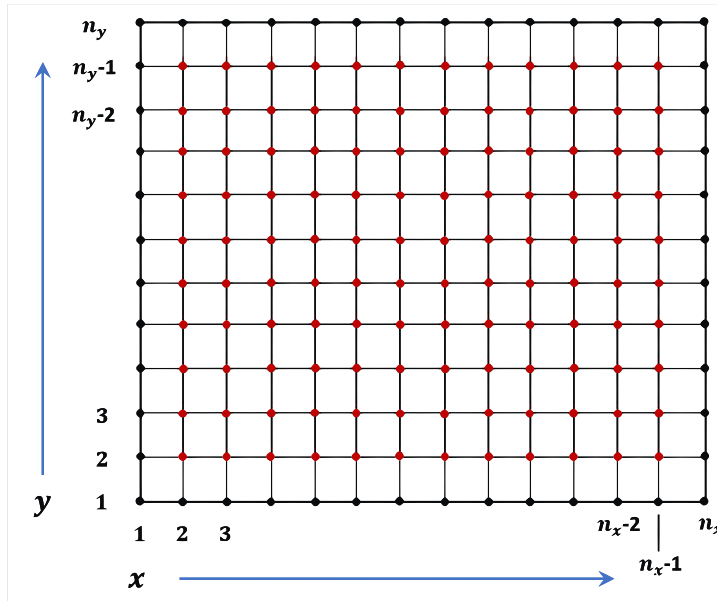
Figure 3-9: GDQR grid distribution of solution domain

Step three

The quadrature analogues of the equation(s) of motion and BCs are written using the GDQR with respect to the domains in which they are satisfied. Since the number of independent variables in a system of linear equations must equal the number of equations in the system to be solvable, the total number of equations in the inner domain must equal the total number of independent variables, therefore the number of equations required for the inner domain is $n_i(n_x - 2)(n_y - 2)$. Similarly, the number of equations required for the boundary domain is $2n_b(n_x + n_y - 2)$.

Step four

Assemble, rearrange and express in matrix format the quadrature analogues of the equation(s) of motion and BC equations within the framework of a generalized eigenvalue problem. The assembled matrix equation is of the form

$$\begin{bmatrix} [K_{ii}] & [K_{ib}] \\ [K_{bi}] & [K_{bb}] \end{bmatrix} \begin{Bmatrix} \{\mathcal{g}_i\} \\ \{\mathcal{g}_b\} \end{Bmatrix} = \omega^2 \begin{Bmatrix} [M]\{\mathcal{g}_i\} \\ \{0\} \end{Bmatrix} \tag{3-123}$$

where $[K]$ is the stiffness matrix with its elements being functions of the elastic and geometric properties of the GS. The subscripts b and i denote the boundary and inner domains, respectively. Therefore, $[K_{ii}]$ is an $n_i(n_x - 2)(n_y - 2) \times n_i(n_x - 2)(n_y - 2)$ matrix, $[K_{bb}]$ is a $2n_b(n_x + n_y - 2) \times 2n_b(n_x + n_y - 2)$ matrix, $[K_{ib}]$ is an $(n_x - 2n_{BC})(n_y - 2n_{BC}) \times (2n_{BC}(n_x + n_y) - 4n_{BC}^2)$ matrix, and $[K_{bi}]$ is a

$\left(2n_{BC}(n_x + n_y) - 4n_{BC}^2\right) \times (n_x - 2n_{BC})(n_y - 2n_{BC})$ matrix. $[M]$ is the equivalent mass matrix whose elements are functions of the mass moments of inertia. And $\{\mathcal{G}_i\}$ and $\{\mathcal{G}_b\}$ are the displacement vectors of the points in the inner and boundary domains, respectively.

Step five
Equation (3-123) from step four is re-written into the standard form of the eigenvalue equation using the condensation technique as

$$([K_{ii}] - [K_{ib}][K_{bb}^{-1}][K_{bi}])\{\mathcal{G}_i\} - \omega^2[M]\{\mathcal{G}_i\} = 0 \qquad (3\text{-}124)$$

Equation (3-124) is solved to obtain the eigenvalues and eigenvectors of the vibrating plate.

3.4　Results and Discussions

3.4.1 Validation of the GDQR

To validate the GDQR method, the classical Kirchhoff plate model was solved for an SSFSSF plate using the GDQR method and compared with results obtained from exact solutions.

The governing equation for the classical Kirchhoff plate model deduced from equation (3-65) by neglecting the rotary inertia terms and the vdW pressure, p_i, from adjacent layers is given as

$$-D\left(\frac{\partial^4 w}{\partial x^4} + 2\frac{\partial^4 w}{\partial x^2 \partial y^2} + \frac{\partial^4 w}{\partial y^4}\right) = I_0 \frac{\partial^2 w}{\partial t^2} \qquad (3\text{-}125)$$

The boundary conditions are given as

$$w = \frac{\partial^2 w}{\partial x^2} = 0 \qquad\qquad x = 0, a; 0 \le y \le b \qquad (3\text{-}126)$$

for the simply supported edges, and

$$\frac{\partial^2 w}{\partial x^2} + v\frac{\partial^2 w}{\partial y^2} = \frac{\partial^3 w}{\partial x^3} + (1-v)\frac{\partial^3 w}{\partial x \partial y^2} = 0 \qquad 1 < x < a; y = 0, b \qquad (3\text{-}127)$$

for the free edges.

Assuming a sinusoidal time response solution to equation (3-125) of

$$w(x,y,t) = W(x,y)e^{i\omega t} \tag{3-128}$$

the corresponding mode shape function $W(x,y)$ is the classical Voigt function

$$W_m = \sin \alpha x \left[A_m \sin\left(\sqrt{k^2 - \alpha^2}\, y\right) + B_m \cos\left(\sqrt{k^2 - \alpha^2}\, y\right) \right.$$
$$\left. + C_m \sinh\left(\sqrt{k^2 + \alpha^2}\, y\right) + D_m \cosh\left(\sqrt{k^2 + \alpha^2}\, y\right) \right] \tag{3-129}$$

where $k^2 = \sqrt{\rho\omega^2/D}$, $\alpha^2 = (m\pi/a)^2$, ω is the frequency of vibration, and m is the number of half waves in the x-direction.

For an SSFSSF plate the frequency equation is given as[216]

$$2\phi_1\phi_2[\lambda^2 - m^4\pi^4(1-v)^2]^2(\cos\phi_1 \cosh\phi_2 - 1)$$
$$+ \{\phi_1^2[\lambda + m^2\pi^2(1-v)]^4$$
$$- \phi_2^2[\lambda - m^2\pi^2(1-v)]^4\}\sin\phi_1 \sinh\phi_2 = 0 \tag{3-130}$$

where $\lambda = \omega a^2\sqrt{\rho/D}$ is the non-dimensional frequency parameter, and

$$\phi_1 = \frac{b}{a}\sqrt{\lambda - m^2\pi^2}$$

$$\phi_2 = \frac{b}{a}\sqrt{\lambda + m^2\pi^2} \tag{3-131}$$

Equation (3-130) assumes that $k^2 > \alpha^2$, however if $k^2 < \alpha^2$ equation (3-130) becomes

$$2\eta_1\eta_2[\lambda^2 - m^4\pi^4(1-v)^2]^2(\cosh\eta_1 \cosh\eta_2 - 1)$$
$$+ \{\eta_1^2[\lambda + m^2\pi^2(1-v)]^4$$
$$- \eta_2^2[\lambda - m^2\pi^2(1-v)]^4\}\sinh\eta_1 \sinh\eta_2 = 0 \tag{3-132}$$

Where

$$\eta_1 = \frac{b}{a}\sqrt{m^2\pi^2 - \lambda}$$

$$\eta_2 = \frac{b}{a}\sqrt{m^2\pi^2 + \lambda} \tag{3-133}$$

The $fzero$ command was utilized in a MATLAB programme to solve the frequency equation (equation (3-130)). The $fzero$ command finds the roots of a nonlinear function by identifying the points at which the sign of the function changes. Table

3-3 gives the normalized natural frequencies of the first few modes for the free vibration of a classical Kirchhoff plate, using a Poisson's ratio $v = 0.3$ with spatial aspect ratios (a/b) of 0.4, 1.0 and 2.5. The fundamental frequencies as shown in the first row of Table 3-3 occur at the points where the value of the frequency function switches from zero to a positive or negative real number. All the values of the frequency function before zero are complex numbers, as such the MATLAB programme was unable to find that first switching point since the $fzero$ command will only accept real and finite inputs. Hence, λ for all $m = 1, 2, 3, ...$ and $n = 1$ could not be extracted and have been taken from the literature[216]. It should be noted that in at least one other place[217], the fundamental frequencies are reported as those in the second row of Table 3-3, for example, $\lambda_{11} = 16.1348$ for a square plate and not $\lambda_{11} = 9.6314$. By comparing the mode shapes of $\lambda = 9.6314$ and $\lambda = 16.1348$ (Figure 3-10), both shapes satisfy $m = 1$ and $n = 1$ the difference being the position of the nodal lines, therefore a labelling of λ_{11} for both frequencies will not be totally wrong. However, since 9.6314 is the lower of the two frequencies, it should be considered as the fundamental frequency.

Mode sequence	a/b		
	0.4	1.0	2.5
1	11	11	11
	9.7600*	9.6314*	9.4841*
2	12	12	12
	11.0368	16.1348	33.6228
3	13	13	21
	15.0626	36.7256	38.3629*
4	14	21	22
		38.9450*	75.2037
5	15	22	31
		46.7381	86.9684*
6	21	23	32
	39.2387*	70.7401	130.3576
7	22	14	41
	40.5035		155.3211*
8	16	31	13
		87.9867*	156.1248
9	23	32	23
	44.9416	96.0405	199.8452

* Values taken from literature[216]

Table 3-3: Non-dimensional frequency parameters $\lambda = \omega a^2 \sqrt{I_0/D}$ for SSFSSF plates deduced from the frequency equation
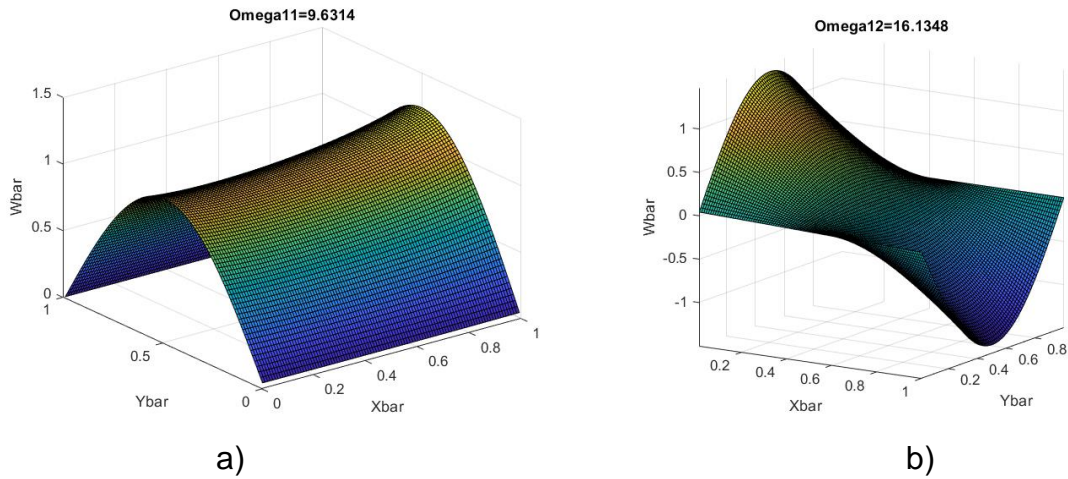
Figure 3-10: Mode shapes for **a)** $\lambda = 9.6314$ **b)** $\lambda = 16.1348$

The GDQR was applied to equation (3-125) and boundary equations (3-126) and (3-127) following the steps outlined in section 3.3. The Chebyshev-Gauss-Lobatto grid distribution was used for the solution domain. Table 3-4 shows the convergence rate of the method for the free vibration of an SSFSSF plate. Unlike the rates in literature[156, 210], the rates achieved here are not fast and even at high sampling points of 39×39 the frequencies do not properly converge.

Grid	SSFSSF (λ_{12}?)
11×11	30.7674
15×15	-
21×21	33.4836
24×24	34.1197
27×27	32.8243
35×35	32.3349
39×39	32.1514
50×50	33.2412

Table 3-4: Convergence of the GDQR applied to vibration problem of an SSFSSF plate.

As a result of poor convergence rates a grid with a large number of sampling points (50×50) was used as the solution domain for the validation of the GDQR method. This was necessary as very accurate mode shapes were required to ensure that the frequencies being compared with those from the exact solution method were for the same resonant mode. Table 3-5 shows the comparison of the frequencies obtained from the GDQR with those from exact solution methods for a SSFSSF square plate. The percentage error is calculated as

$$\% \; error = \frac{GDQR \; method - Exact \; Solution}{Exact \; Solution} \times 100 \qquad (3\text{-}134)$$

Mode label	Exact Solution	GDQR (This work)	% error
14	75.2834	71.3934	-5.167
44	236.2620	223.8526	-5.252

Table 3-5: Comparison of the GDQR frequencies with those from exact solution methods. $a/b = 1, \upsilon = 0.3$

The percentage errors of the GDQ are not too large as to discard the method, however, the ultra-low error percentages of the method as shown in literature for plates with opposite sides simply supported[210], have not been repeated here. It is also noted that the GDQR as used in this work by comparison with exact solution methods did not yield the first few occurring frequencies.

3.4.2 Vibration of micro and nano-sized plates

Although the GDQR did not show very low percentage errors, which might mean it may not be a suitable method for determining the natural frequencies of graphene resonators, it was used to study the effect of the small-scale parameter on the vibration of micro and nanosized rectangular resonators. It is assumed that the error margins for one solution will be roughly the same as another, allowing for both solutions to be reasonably compared.

The value of the small-scale parameter used in literature varies from work to work. Several earlier works used Eringen's value of 0.39 for e_0 in the small-scale parameter relation $\mu = (e_0 a)^2$. However, it has been demonstrated that suitable values of $e_0 a$ can be chosen to constrain the analytical solution to match MD simulations[163], with values in the range $0 - 2.0\ nm$. A few other works have used this range as values of $(e_0 a)^2$ and not $e_0 a$. The effect of the small-scale parameter has been shown for the vibration of different sized nanoplates[156], while a no-effect verdict has been implied for micro-sized plates[116]. The plot in Figure 3-11 shows the change in the first non-dimensional frequency for different $e_0 a$ selected between 0 and 2.0 nm for a linear, nonlocal model. When $e_0 a$ is 0, the local plate model is achieved. It is evident from Figure 3-11 that the frequency parameter when $e_0 a = 0$ is several orders larger than the frequency parameters for all the other values of $e_0 a$, which seemingly agrees with literature that classical plate models overestimate the frequencies of nanoplates. The effect the inclusion of the small-scale parameter has on the frequencies can also be seen;

the pertinent question then becomes, what value of e_0a should be used for different sized plates? With experimental or MD simulation data, an appropriate value of e_0a can be selected for a given resonator size range.
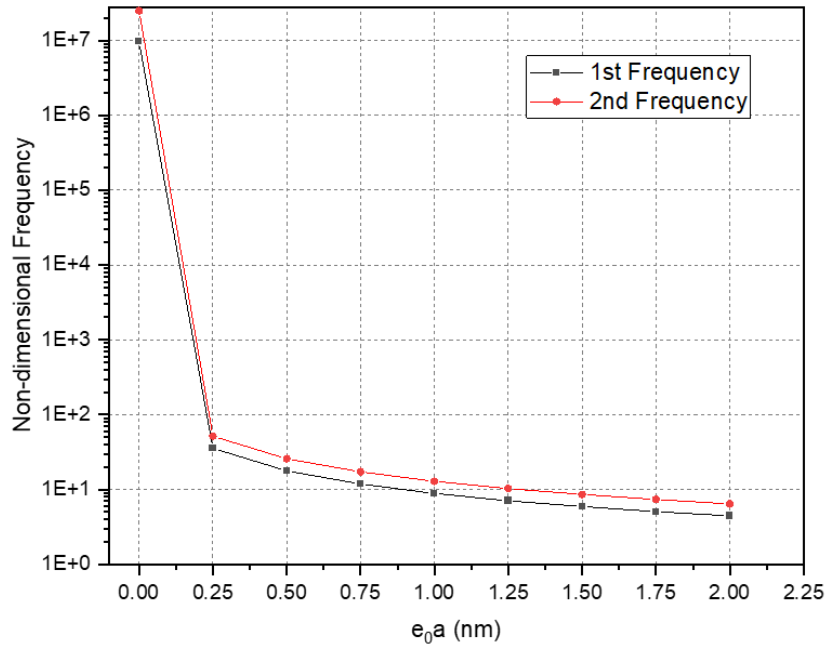
Figure 3-11: The effect of the small scale parameter on the non-dimensional frequency.
$$a/b = 1, v = 0.3, a = 16 \, \mu m$$

Figure 3-12 shows the change in the effect e_0a has on the first frequency of various micro-scaled SSFSSF graphene resonators. It should be noted that frequencies in these plots are referred to as the first non-dimensional frequency or first frequency and not the fundamental frequency of the plate in line with previous discussions on the inability of the GDQR as used in this work to produce the fundamental frequency for the model being solved. Notwithstanding, all values of the small-scale parameter rescale the overestimated frequency of $e_0a = 0$. Most importantly, it can be deduced that for micro-scaled GSs, the choice of e_0a is unimportant as all $0 \leq e_0a \leq 2$ scales the overestimated frequency to the same value for a given resonator length. Figure 3-13 shows the effect of e_0a on the first frequency of nano-scaled SSFSSF graphene resonators which is very much in agreement with literature[158, 161]. The small-scale parameter scales the overestimated frequency, but with nanoplates the choice of e_0a matters as different values scale the overestimated frequency to different frequencies.
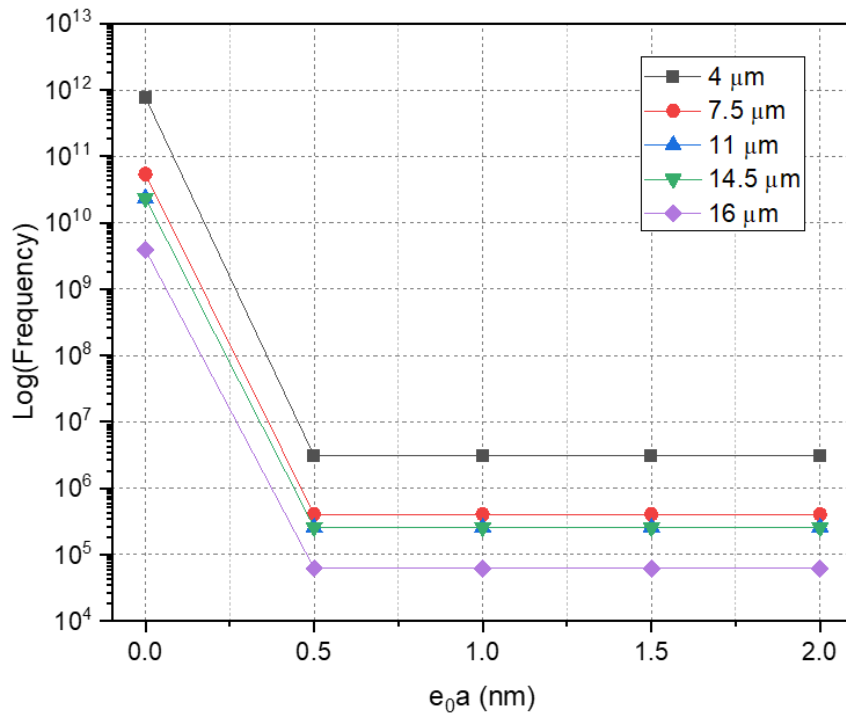
Figure 3-12: The effect of small scale parameter on the frequency of micro-scaled GSs
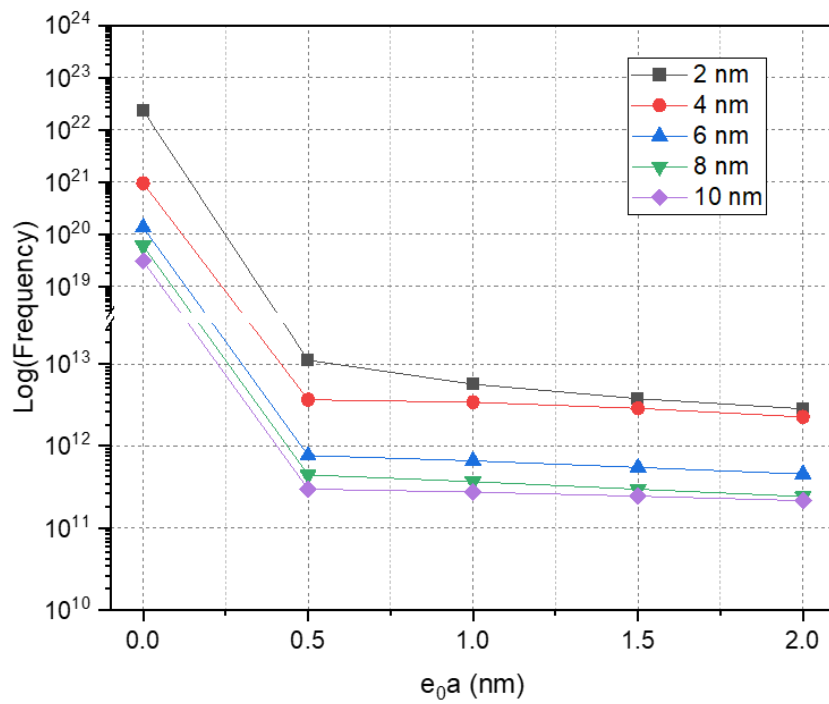
a)
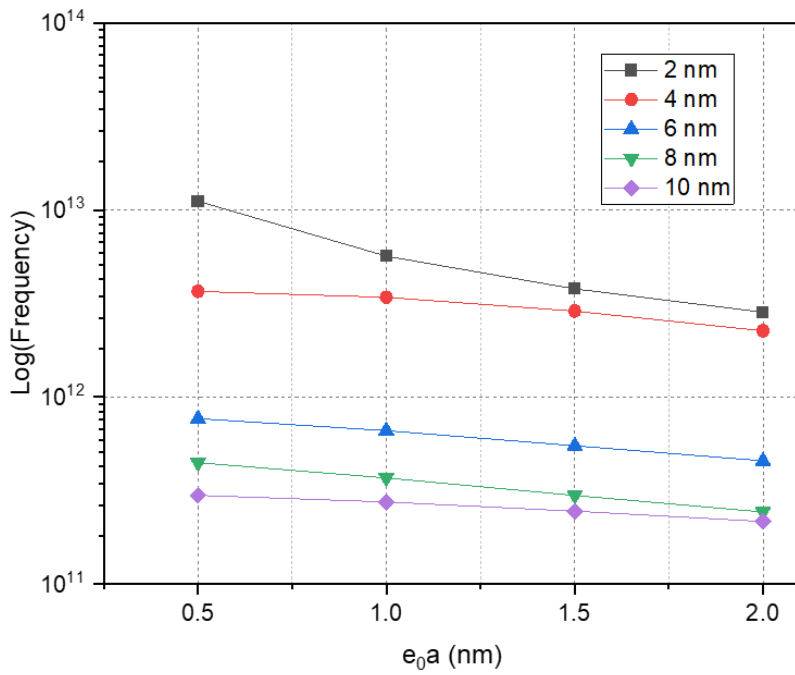
b)

Figure 3-13: The effect of on the first frequency of nanosized GSs

To validate the effect the small-scale parameter has on micro-scaled GSs, comparison is made with experimental results reported in literature. Figure 3-14 shows the plot of the first frequency derived from the nonlocal linear equation of motion for a 1 μm by 2 μm SSFSSF SLGS with fundamental frequency, $f_0 = 70.5$ MHz[82] for different small-scale parameter values.
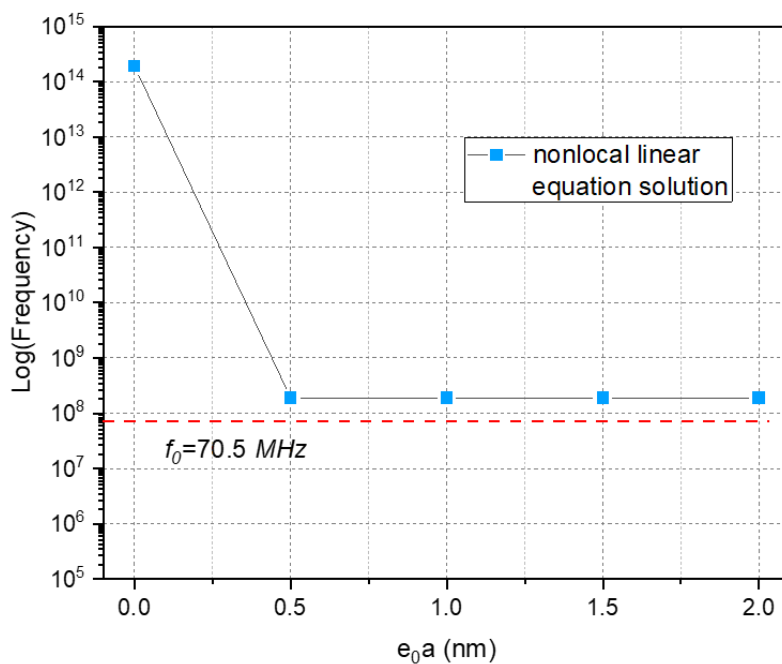
Figure 3-14: Nonlocal linear equation solution compared with experimental results for a 1 μm by 2 μm SLGS resonator.

The local linear plate equations (when $e_0a = 0$) are clearly not suitable for the vibration analysis of micro-sized GSs because they overestimate in no small way the natural frequencies of the sheets. Therefore, the small-scale parameter must be incorporated in the governing equations in the modelling of the vibration of the sheets. Even though the small-scale parameter rescales the overestimated frequency in Figure 3-14, the rescaled frequencies are still about 168% higher than the measured fundamental frequency. This is not completely out of place, as the first frequencies from the GDQR as used in this work are not the fundamental frequencies of the vibration being modelled. The comparison is made to validate the theory that the small-scale parameter is important for the vibration analysis of micro-sized GS.

3.5　Conclusion

This chapter has looked at the theoretical analyses of the vibration of rectangular GSs. The transition from the use of MD simulations to continuum mechanics models in the analyses of the mechanical behaviour of nano-sized structures is discussed. A few different continuum models are looked at in detail and their respective governing equations derived. The theories developed to account for the size effect of the structures, models for the interlayer pressures, consideration of nonlinearities in the models are also discussed. The GDQR method is used to deduce the applicability of some of the discussed continuum models in the vibration analysis of nano- and micro-sized GSs. As has been presented in the literature, the small-scale parameter e_0a was found to resolve the overestimation problem encountered when classical plate models are applied to nano-scaled sheets. This work extends the necessity of a small-scale parameter to micro-sized GSs. It shows that when $e_0a = 0$, the frequencies of micro-sized GSs are overestimated, but at any value of e_0a other than zero, the frequencies are scaled closer to the expected values. Hence, we establish that the choice of value for e_0a is insignificant compared to its incorporation in the governing equations applied to micro-sized GSs.

Chapter 4: Computer Aided FE Analysis of graphene resonators

4.1　Introduction

This chapter presents the modelling and vibration analysis of rectangular graphene resonators using ANSYS Mechanical APDL. Section 4.2 presents the specification and derivation of some parameters used in the FEA simulations and subsequently in the mass sensor design in Chapter 5 - including resonator sizes, actuation forces from piezoelectric shakers and Lorentz force. ANSYS Electronics Desktop is used to model the magnetic fields used in deriving Lorentz force. Section 4.3 presents the modelling of the graphene resonators. The resonators are modelled as thin plates by selecting appropriate element types. A mesh sensitivity analysis is carried out to determine the optimum mesh size for the models. Modal analysis and subsequently harmonic analysis are carried out for the graphene bridges. Monolayer and bilayer GSs are modelled. The accuracy of the models depends on using appropriate element types and mesh size, inputting correct material properties, defining appropriate boundary conditions and loads, and running the appropriate analysis types in the correct order where applicable. Section 4.4 presents a structure-field interaction model for the graphene resonator-air interaction. The damping coefficient and spring force constants are extracted from the analysis and compared with estimated analytical values. An estimate of the mass sensitivity of a mass sensor based on the simulated performance of the resonators is given.

4.2　Parameter specification and derivation

The graphene resonators of interest in this study are GSs with lengths less than $50\ \mu m$. Due to characterization and measurement resolution limits, the lengths of the GSs are however kept above $10\ \mu m$, with widths varying from $2\ \mu m$ to $7\ \mu m$. The modal frequency characteristics of resonators are a function of their spatial dimensions, material properties, and boundary conditions. The specification of these therefore suffices to run a modal analysis for the resonators. To derive the frequency response of the resonators, the forcing function acting on the resonator needs to be specified. And damping can be estimated and included for more accurate results.

4.2.1 Lorentz Force

The use of Lorentz or magnetomotive force for the actuation of mass sensor resonators was briefly discussed in Section 2.7.1. Equation (2-1) describes the relation for Lorentz force. To correctly estimate its magnitude, the magnetic flux density B at the resonator position must be specified. It is good practice to ensure that the current density limits of the resonator are not exceeded, to avoid electrically damaging it, and that the currents flow through the current signal track and resonator and not through the sensor substrate.

Magnetic flux density at resonator surface

Two permanent magnets with strengths $0.5635T$ supply the magnetic field. A magnetic flux keeper is created with Swedish iron as shown schematically in Figure 4-1. The magnetic flux and flux density in the keeper and the surrounding medium are derived using an FEA model in ANSYS Electronics Desktop. The magnetic properties of the magnet and keeper are given in Table 4-1.
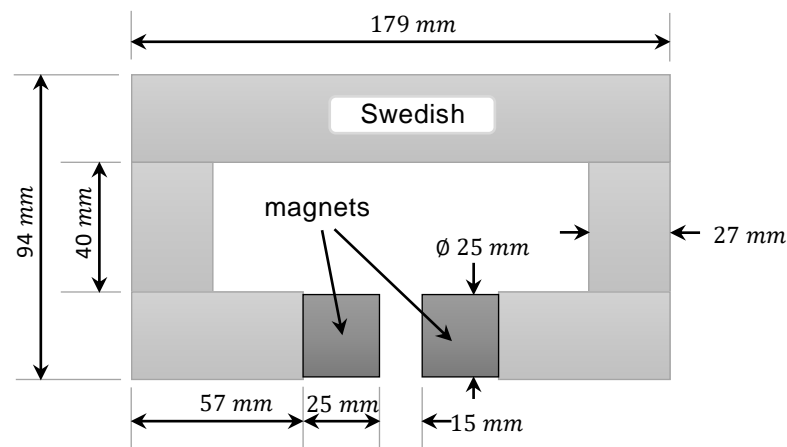
Figure 4-1: Schematic representation of magnets and Swedish iron magnetic flux path

	Material	Relative Permeability	Coercive force	Flux Density at magnet's surface
Magnets	Neodymium	1	836,000 A/m	0.5635T
Flux keeper	Swedish Iron	1000		
Surrounding Medium	Air	1		

Table 4-1: Magnetic properties of magnets, flux keeper and surrounding medium

To model the magnetic field, the geometries of the magnets, iron keeper, and air are first defined as shown in Figure 4-2 Their material properties and the boundary conditions are defined next. The model is then meshed with a level 7 mesh resolution on a resolution scale of 1 to 10 in increasing order of fineness (Figure 4-3), before solving. The magnetic flux vector plot is shown in Figure 4-4 The keeper conserves the magnetic flux and forms a path for it from one magnet to the other. The colour plot of the magnetic flux magnitude in Figure 4-5 indicates that the flux density is approximately zero everywhere except in the keeper and the medium between both magnets. Figure 4-6 shows how the magnetic flux density varies along the line $x = 0$ between both magnets, where the resonator will be located.
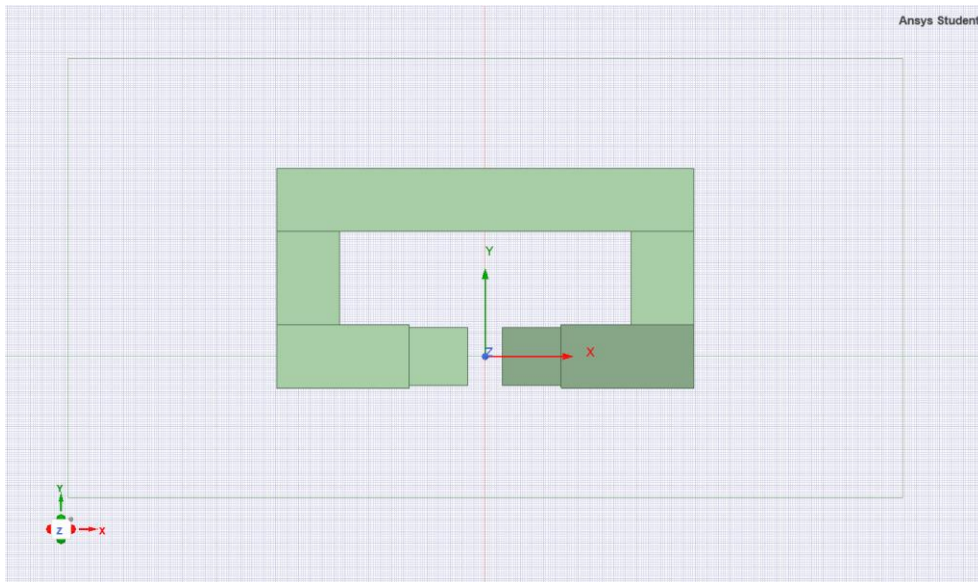
Figure 4-2: Model of magnets and Swedish iron keeper
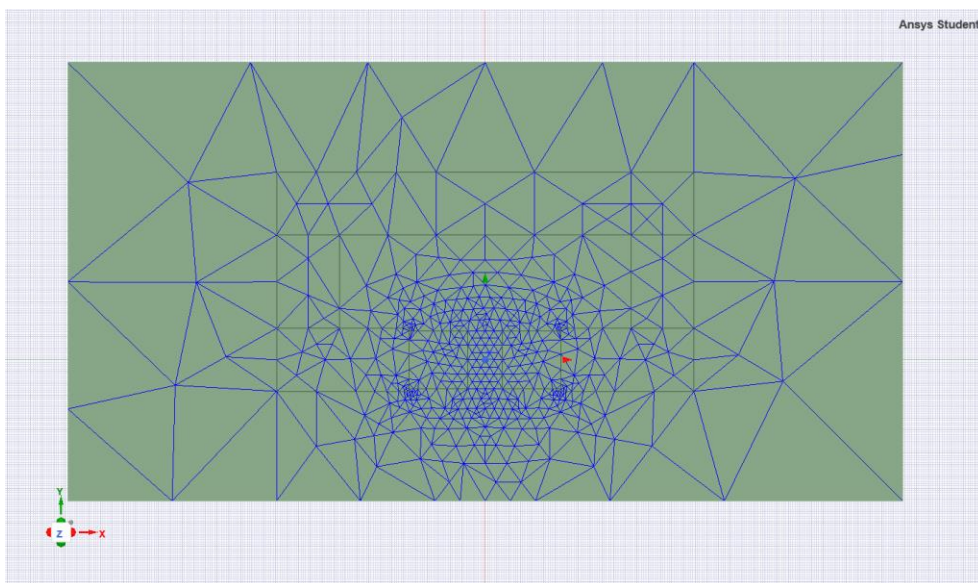
Figure 4-3: Magnet and iron model mesh
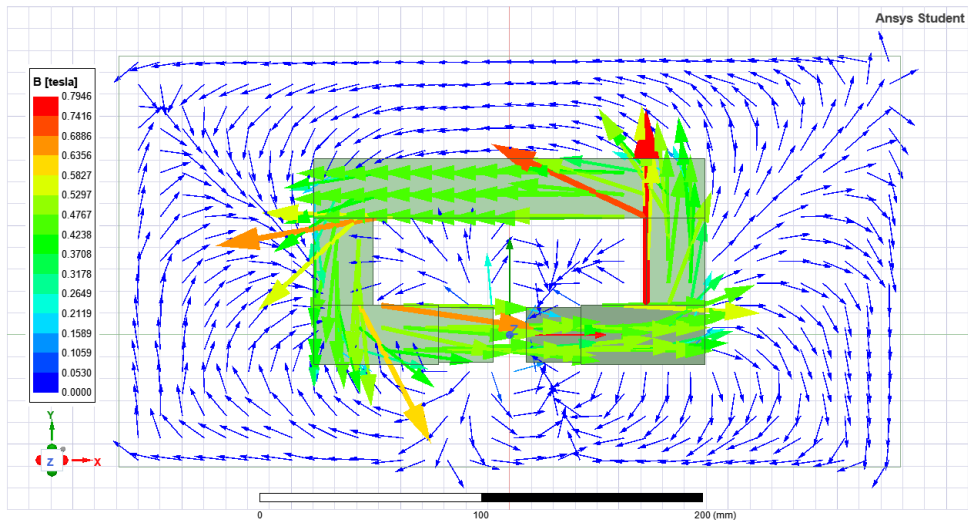
Figure 4-4: Magnetic flux vector plot
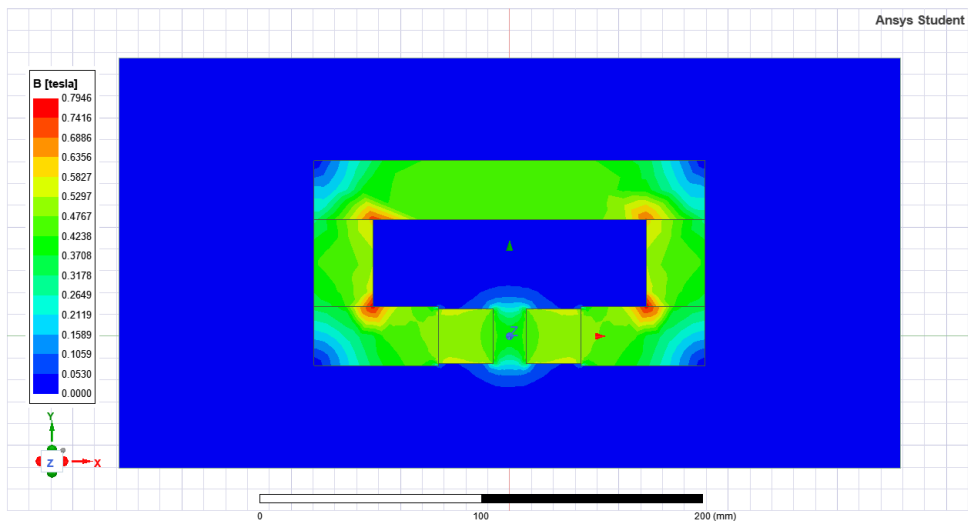
Figure 4-5: Magnetic flux magnitude plot
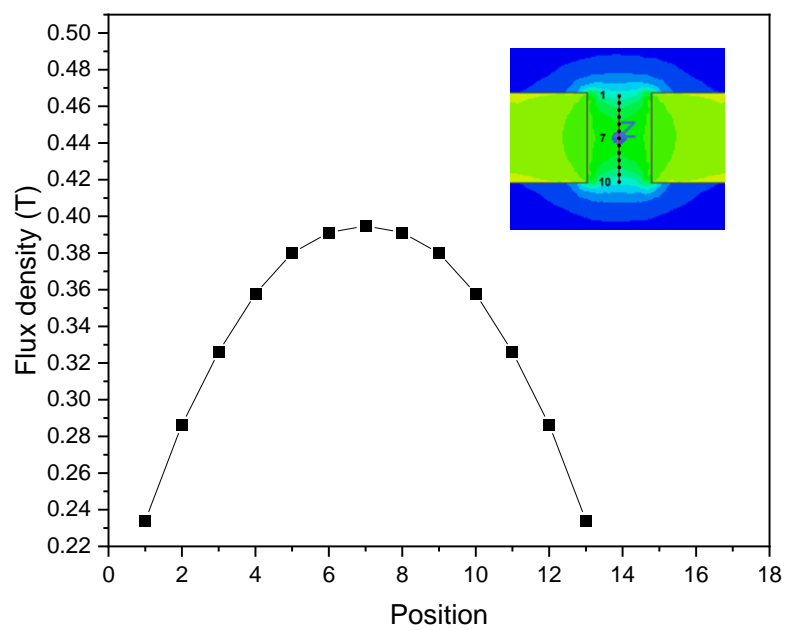
Figure 4-6: Variation of flux density along line $x = 0$

Current density in graphene

The current density of a current carrying conductor is the ratio of the current flowing through it to its cross-sectional area, as is expressed in equation (4-1).

$$I_d = \frac{I}{A}$$

(4-1)

The graphene resonators used in this work were designed to have a minimum width of $4 \, \mu m$. Assuming inaccuracies in the microfabrication process resulted in the resonator widths of $3 \, \mu m$, with an ideal thickness of $0.34 \, nm$ the cross sectional area of a monolayer graphene resonator will be $1.02 \times 10^{-11} cm^2$. Breakdown current densities in graphene have been reported in orders of $10^7 \, A/cm^2$ and $10^8 \, A/cm^2$, e.g. $1.2 \times 10^7 \, A/cm^2$ and $1.18 \times 10^8 \, A/cm^2$ among others[218, 219]. Assuming a maximum current density of an order lesser than reported, the maximum working current in this work will be $10.2 \, \mu A$.

Impedance of signal tracks and substrates

Standard equations have been developed for determining the impedances of a wide range of signal-carrying (transmission) line circuits. These can be found in transmission line design handbooks and guides, one of such resources is recommended and used in this work. The transmission line designs used in this work are best described as nonhomogeneous dielectric embedded coplanar waveguides, for which there are no direct standard equations for the impedance. As such this works merges the equations and principles used for normal coplanar waveguides and nonhomogeneous dielectric embedded microstrip line.

Consider a standard coplanar waveguide as shown in Figure 4-7. For the proposed equations to be applicable, the ground plane must extend greater than $5b$ on each side of the gap. And are recommended to be periodically connected depending on the frequency being used.
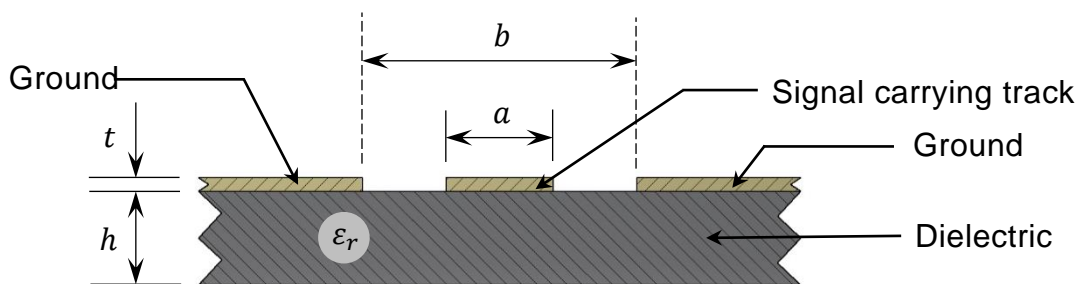
Figure 4-7: Coplanar waveguide

The characteristic impedance of the conducting track, Z_0, is given as

$$Z_0 = \frac{30\,\pi}{\sqrt{\varepsilon_{eff,t}}} \frac{K(k_t')}{K(k_t)} \tag{4-2}$$

where ε_{eff} is the effective dielectric constant, K is the complete elliptic function given in equation (4-13).

$$K(k) = \int_0^{\pi/2} \frac{d\theta}{\sqrt{1 - k^2 \sin^2 \theta}} \tag{4-3}$$

$$\varepsilon_{eff,t} = \varepsilon_{eff} - \frac{\varepsilon_{eff} - 1}{\frac{(b-a)/2}{0.7t} \frac{K(k)}{K(k')} + 1} \tag{4-4}$$

$$\varepsilon_{eff} = 1 + \frac{\varepsilon_r - 1}{2} \frac{K(k')K(k_1)}{K(k)K(k_1')} \tag{4-5}$$

$$k_t = \frac{a_t}{b_t} \qquad k = \frac{a}{b}$$

$$k_t' = \sqrt{1 - k^2} \qquad k' = \sqrt{1 - k^2} \tag{4-6}$$

$$k_1 = \frac{sinh\left(\frac{\pi a_t}{4h}\right)}{sinh\left(\frac{\pi b_t}{4h}\right)} \qquad k_1' = \sqrt{1 - k_1^2}$$

$$a_t = a + \frac{1.25t}{\pi}\left[1 + ln\left(\frac{4\pi a}{t}\right)\right]$$

$$b_t = b - \frac{1.25t}{\pi}\left[1 + ln\left(\frac{4\pi a}{t}\right)\right] \tag{4-7}$$

where ε_r is the relative dielectric constant.

The characteristic impedance for an embedded or buried microstrip line is given as

$$Z_0 = \frac{Z_{0,microstrip}\sqrt{\varepsilon_{eff,microstrip}}}{\sqrt{\varepsilon_{eff,buried}}} \tag{4-8}$$

$$\varepsilon_{eff,buried} = \varepsilon_{eff} \, e^{-\frac{2b}{h}} + \varepsilon_r \left[1 - e^{-\frac{2b}{h}} \right] \qquad (4\text{-}9)$$

For the nonhomogeneous dielectric embedded microstrip line illustrated in Figure 4-8, the equation for its characteristic impedance is same as that of the embedded microstrip line in equation (4-8) but with $\varepsilon_{\text{eff},embedded}$ bound by the relation $\varepsilon_{\text{eff},microstrip} < \varepsilon_{\text{eff,embedded}} < \varepsilon_{\text{eff,2}}$. And $\varepsilon_{eff,2}$ evaluated using the standard ε_{eff} equations but with ε_r replaced with $\varepsilon_{r1}/\varepsilon_{r2}$.
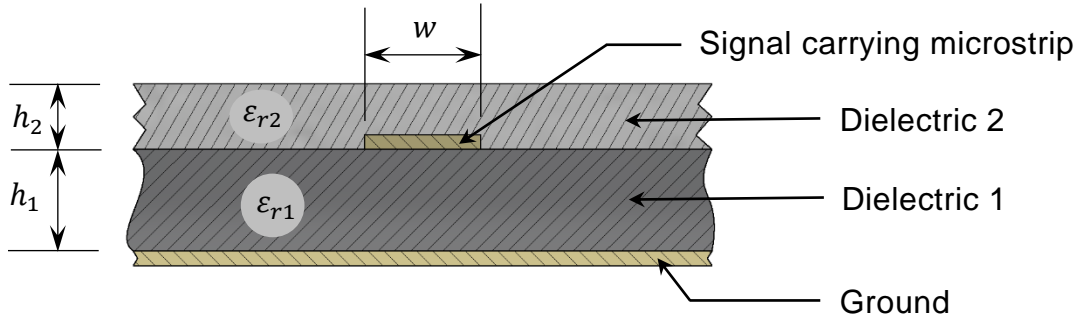
Figure 4-8: Nonhomogeneous dielectric embedded microstrip line

The transmission line designs used for this study are illustrated in Figure 4-9. Using equation (4-8), the characteristic impedance for an embedded coplanar waveguide is expressed as

$$Z_0 = \frac{Z_{0,coplanar} \sqrt{\varepsilon_{eff,coplanar}}}{\sqrt{\varepsilon_{eff,embedded}}} \qquad (4\text{-}10)$$

$$\varepsilon_{eff,coplanar} < \varepsilon_{eff,embedded} < \varepsilon_{eff,2} \qquad (4\text{-}11)$$
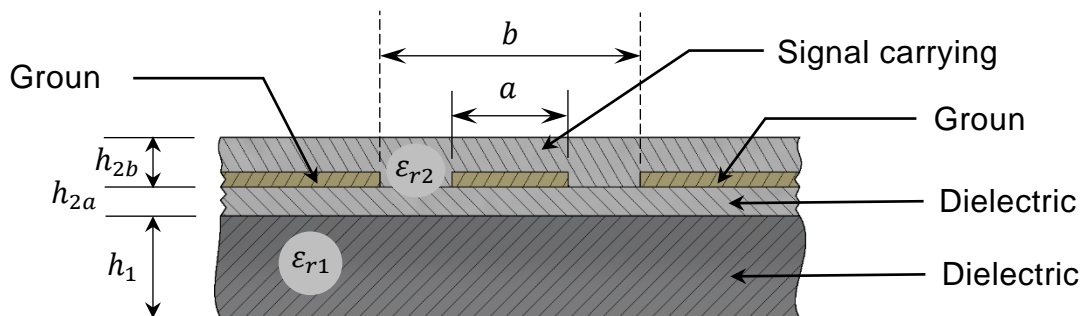
Figure 4-9: Nonhomogeneous dielectric embedded coplaner waveguide

$\varepsilon_{\text{eff},coplanar}$ is equation (4-5), $\varepsilon_{\text{eff,2}}$ is also equation (4-5) but with ε_r replaced by $\varepsilon_{r1}/\varepsilon_{r2}$. $Z_{0,\text{coplanar}}$ is equation (4-2). The parameter values for the nonhomogeneous dielectric embedded waveguide as indicated in Figure 4-9 are:

$h_1 = 300 \, \mu m$, $h_{2a} = 2 \, \mu m$, $h_{2b} = 200 \, nm$, $t = 250 \, nm$, $a = 30 \, \mu m$, $b = 50 \, \mu m$, $\varepsilon_{r,Si} =$ 11.7, and $\varepsilon_{r,SiO2} = 3.9$. Evaluating equation (4-10) for the conducting track in Figure 4-9 gives an impedance of $112.878 \, \Omega$. The silicon substrate (dielectric 1 in Figure 4-9) is insulated from the track by a $2 \, \mu m$ SiO2 layer (dielectric 2). SiO2 has resistivity values between 1×10^{15} and $1 \times 10^{19} \, \Omega m$, considering current flow through the thickness of the layer and using an upper limit of cross-sectional area (area of the whole die), the smallest resistance of the insulating layer will be $ca. \, 3.2 \times 10^{14} \, \Omega$. CVD grown graphene sheets have been shown to have resistances of $770 - 1000 \, \Omega/sq$. For a $16 \, \mu m$ by $4 \, \mu m$ graphene resonator, using the upper limit of $1000 \, \Omega/sq$, its resistance will be in $ca. \, 64 \, k\Omega$. With the resistance of the SiO2 layer being about 11 and 14 orders of magnitude higher than those of the graphene resonators and conducting tracks respectively, the flow of current will be through the tracks and resonator and not through the substrate. Because the conducting tracks are designed as coplanar waveguides, the frequency components of the drive signal have a minimal impact on their impedance.

Lorentz force acting on the graphene resonators

The mass sensor resonator was designed to be located at any point along line $x = 0$ in Figure 4-6. Assuming a $16 \, \mu m$ resonator is located at one of the points with lowest magnetic flux densities, for a current of $10 \, \mu A$ flowing through the resonator, using equation (2-1), the maximum force acting on the resonator will be $37.456 \, pN$. Figure 4-10 to Figure 4-12 present plots of the forces acting on resonators of different lengths for different current values and magnetic flux densities.
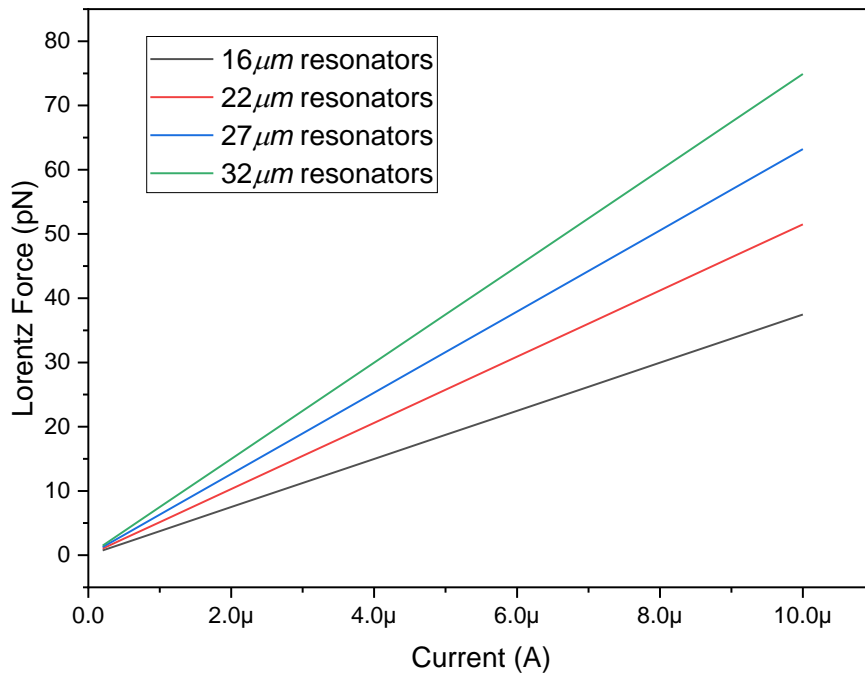
Figure 4-10: Lorentz force for selected resonator lengths in a magnetic field of strength 0.2341 T
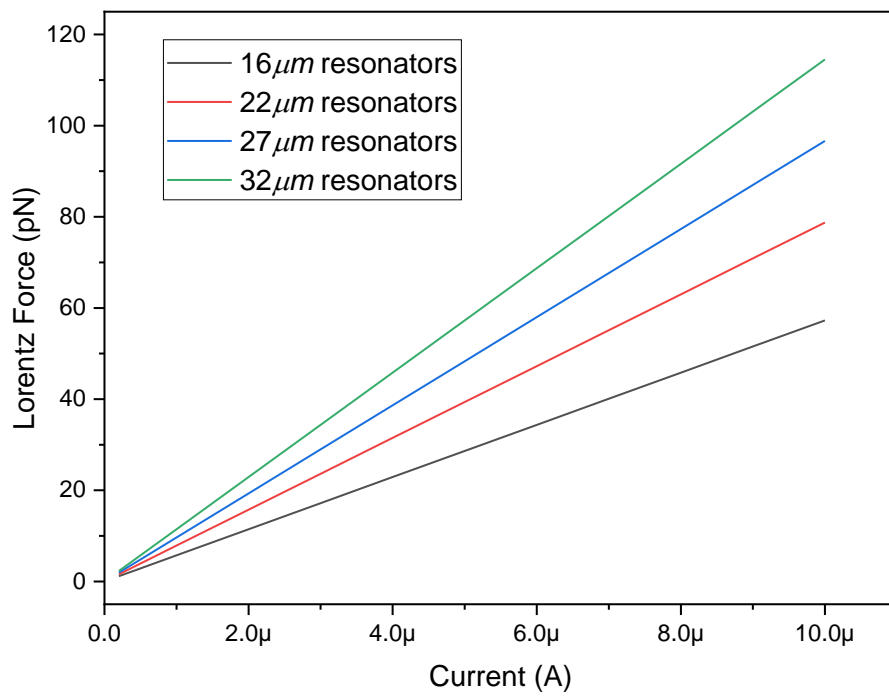
Figure 4-11: Lorentz force for selected resonator lengths in a magnetic field of strength 0.3579 T
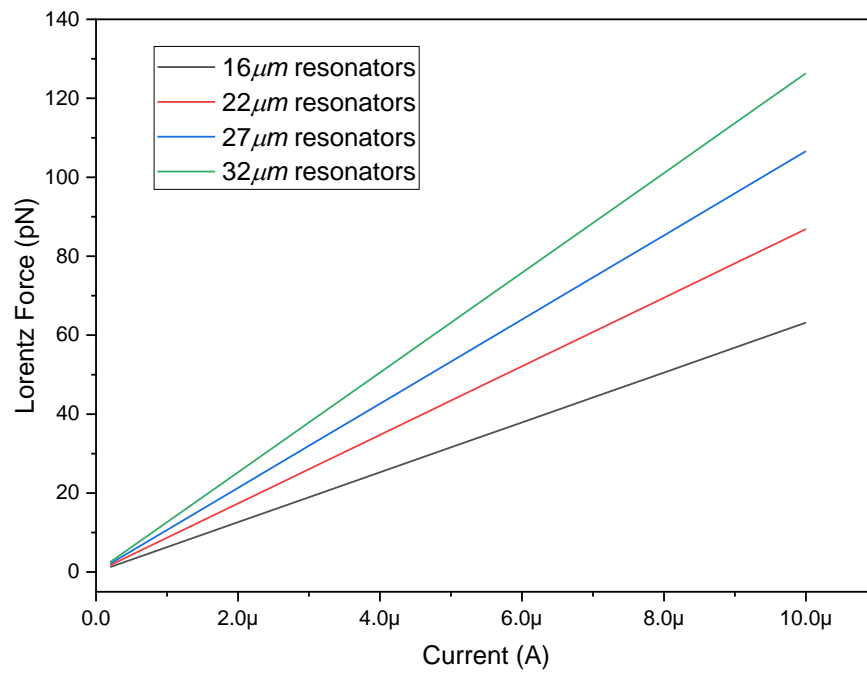
Figure 4-12: Lorentz force for selected resonator lengths in a magnetic field of strength 0.3948 T

4.2.2 Forces from Piezoelectric actuators

Piezoelectric actuators are used in several sensor experimental setups, mostly as actuators. For resonator-based mass sensors, they can be used to shake the whole sensor device and consequently actuate the sensor resonator. A PIC181 piezoelectric actuator is selected for use in this work. It is made from modified lead zirconate titanate (material properties are given in Table 4-2) and boasts a very high mechanical quality factor with good temperature and time stability of its dielectric and elasticity constants.
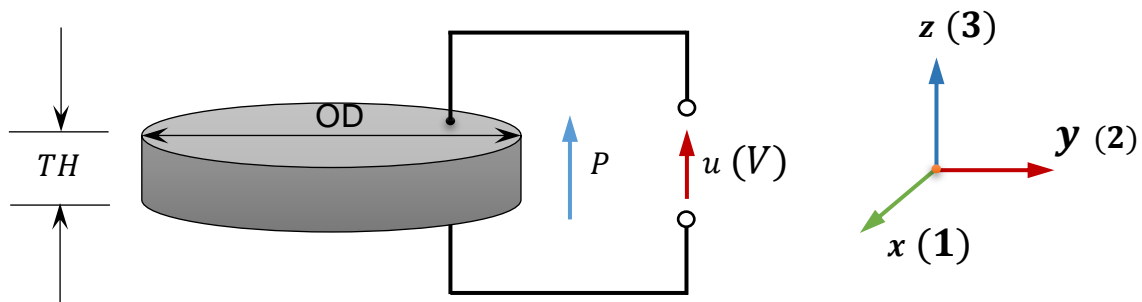
Figure 4-13: Piezoelectric actuator with orthogonal coordinate system (P = poling direction, u = applied drive voltage, TH = thickness, OD = outside diameter)

Physical and dielectric properties	Symbol	Value	Electromechanical properties	Symbol	Value
Density	ρ	$7.80\ g/cm^3$	Coupling factor	k_p	0.56
Poisson's ratio	ν	0.34		k_t	0.46
Specific heat capacity		$\sim 350\ Jkg^{-1}K^{-1}$		k_{31}	0.32
Specific thermal conductivity		$\sim 1.1\ Wm^{-1}K^{-1}$		k_{33}	0.66
Coefficient of thermal expansion	α_3	$ca.-4\ bis -6 \times 10^{-5}K^{-1}$		k_{15}	0.63
	α_1	$ca.\ 4\ bis\ 8 \times 10^{-5}K^{-1}$	Piezoelectric charge coefficient	d_{31}	$-120 \times 10^{-12}CN^{-1}$
Curie temperature	T_c	$330\ ℃$		d_{33}	$265 \times 10^{-12}CN^{-1}$
Relative permittivity in the polarisation direction	$\varepsilon_{33}^T/\varepsilon_0$	1200		d_{15}	$475 \times 10^{-12}CN^{-1}$
Relative permittivity perpendicular to polarity	$\varepsilon_{11}^T/\varepsilon_0$	1500	Piezoelectric voltage coefficient	g_{31}	$-11.2 \times 10^{-3}VmN^{-1}$
Dielectric loss factor	$tan\delta$	3×10^{-3}		g_{33}	$25 \times 10^{-3}VmN^{-1}$
Acousto-mechanical properties					
Frequency coefficients	N_p	$2200\ Hz.m$	Elastic compliance coefficient	S_{11}^E	$11.8 \times 10^{-12}m^2N^{-1}$
	N_1	$1640\ Hz.m$		S_{33}^E	$14.2 \times 10^{-12}m^2N^{-1}$
	N_3	$2010\ Hz.m$	Elastic stiffness coefficient	C_{33}^D	$16.6 \times 10^{-10}Nm^{-2}$
	N_t	$2110\ Hz.m$	Mechanical quality factor	Q_m	2000

Table 4-2: Material properties of a PIC181 piezoelectric actuator

An estimate of the pressure generated in a piezo-transducer when a voltage is applied across it is given as

$$P = \frac{\varepsilon_R \varepsilon_0 V}{k_t d_{33} t} \qquad\qquad (4\text{-}12)$$

Where ε_R is the relative dielectric constant, ε_0 is permittivity of free space, V is the applied voltage, t is the thickness, k_t and d_{33} are as given in Table 4-2. A plot of the estimated pressure against the applied voltage for a PIC 181 piezo-actuator using equation (4-12) is presented in Figure 4-14.
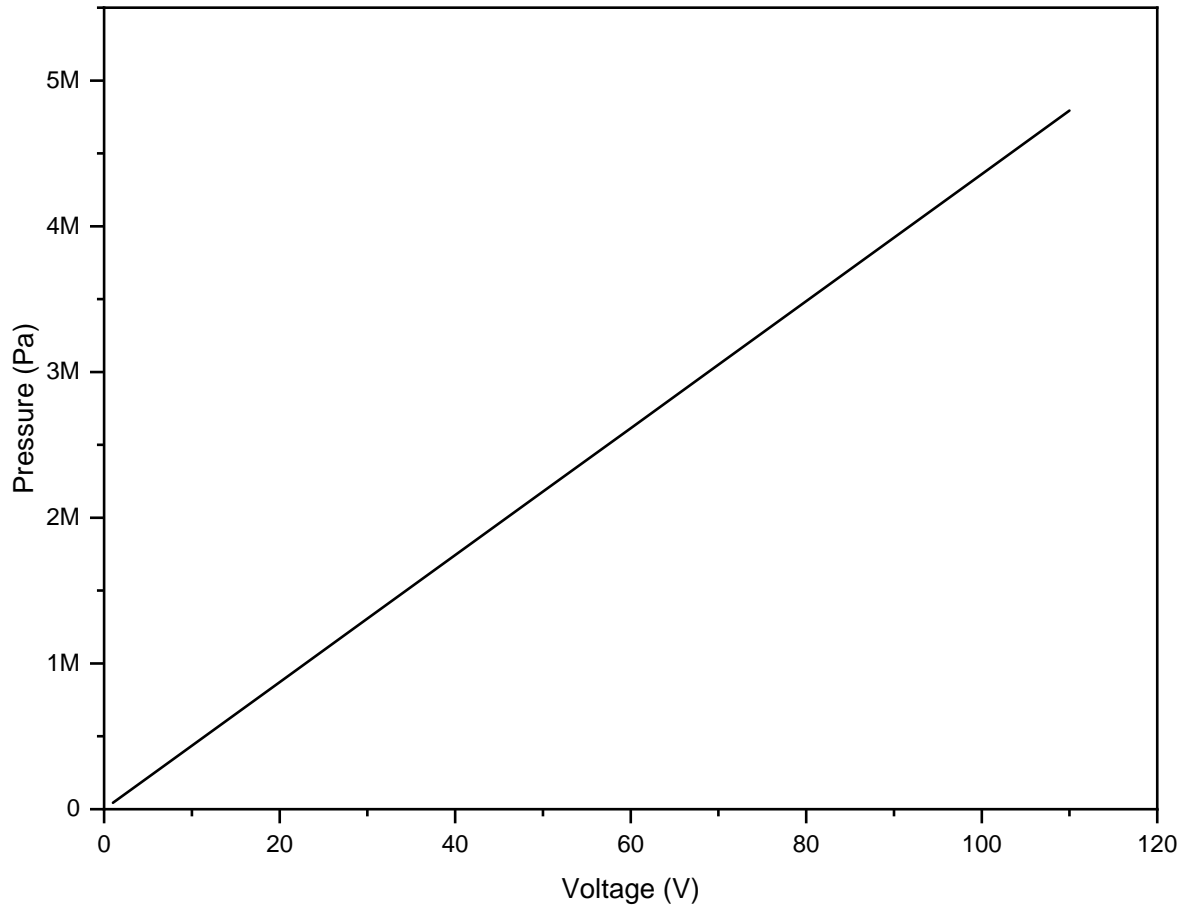
Figure 4-14: Plot of Piezoelectric actuator pressure to applied voltage

Assuming a voltage of 10 V is supplied to the piezo-actuator, for a $16\ \mu m$ by $4\ \mu m$ resonator the force acting on it will be $27.89\ \mu N$. Which is several orders bigger than the estimated Lorentz forces in Section 4.2.1.

4.2.3 Damping coefficient

The energy dissipation in a resonator could be intrinsic but is majorly a result of the 'fluid-structure' interaction between the resonator and the surrounding medium. Consider a microcantilever or bridge with length l, width b and thickness d, assuming a free-molecular-flow regime around the resonator, if the structures vibrate transversely, the drag force per unit length on them is given as

$$f_d = f_1 u(x) = c.w.P_i.u(x) \tag{4-13}$$

Where f_1 is the damping parameter, u the velocity, c is the damping coefficient, and P_i the ambient pressure. The fluid-structure interaction quality factor, Q_f is then estimated as

$$Q_f = \frac{k_n^2}{cP_i}\left(\frac{d}{l}\right)^2 \left(\frac{\rho_s E}{12}\right)^{1/2} \tag{4-14}$$

Here, E is the elastic modulus, ρ_s the density of the structure, and k_n the constant for the nth-order resonance mode, with a first mode value of 1.875 for cantilevers and 4.694 for bridges.

The net drag force on the structure, assuming the structure's velocity is smaller than the thermal velocity c_T, is given as

$$F_D = \frac{bP_i}{c_T}u\left[(2-\sigma_n)\left(\frac{2}{\sqrt{\pi}}+1\right)+\sigma_n\pi^{1/2}\sqrt{\frac{T_w}{T_i}}+2\frac{d}{b}\frac{\sigma_t}{\pi^{1/2}}\right] \tag{4-15}$$

Therefore, the damping coefficient is expressed as

$$c = \left(\frac{m}{2kT_i}\right)^{1/2}\left[(2-\sigma_n)\left(\frac{2}{\sqrt{\pi}}+1\right)+\sigma_n\pi^{1/2}\sqrt{\frac{T_w}{T_i}}+2\frac{d}{b}\frac{\sigma_t}{\pi^{1/2}}\right] \tag{4-16}$$

where m is the mass of the gas molecules ($48.1 \times 10^{-27} kg$ for air), k is the Boltzmann constant ($1.38064852 \times 10^{-23} J/K$), σ_n is the normal accommodation coefficient, σ_t the tangential accommodation coefficient, T_w is the wall temperature and T_i the ambient temperature.

For an isothermal system with a low aspect ratio and full momentum accommodation, c becomes

$$c = \left(\frac{m}{2kT_i}\right)^{1/2}\left(\frac{2}{\sqrt{\pi}}+1+\pi^{1/2}\right) \tag{4-17}$$

For a room temperature of $18\,°C$ ($291.15\,K$), the damping coefficient for the resonators used in this study when operated in air are estimated to be 9.54×10^{-3}.

4.3   Graphene resonator FEA models

4.3.1 Model setup and mesh sensitivity

Graphene resonators are generally considered to be 2 dimensional; here they are modelled as very thin plates. First, they are built geometrically as rectangles.

Then the element type used to discretize the geometric model is specified – shell181, a structural shell element type having six degrees of freedom at each of its four nodes, suitable for modelling thin to moderately thick shells with capability for large strains and nonlinear behaviour, is selected for the models. Next the material properties for the model are defined. Then the model is meshed, boundary conditions are applied, and the appropriate solution type is run.

Before the model is meshed, a mesh sensitivity analysis is carried out to determine the optimum mesh fineness for accurate results. Figure 4-15 represents the mesh sensitivity analysis for a $16 \, \mu m$ by $4 \, \mu m$ resonator. As the element size decreases (the mesh fineness increases), the value of the fundamental resonant frequency converges to about $29.3 \, kHz$. From the plot, a mesh fineness of $2.0 \, \mu m^{-1}$ would suffice in meshing the models. The meshed model is shown in Figure 4-16. The resonators are clamped at opposite ends as shown in Figure 4-17; all values of the six degrees of freedom (displacements in x, y, and z, and rotations about x, y, and z) at those nodes are set to zero.
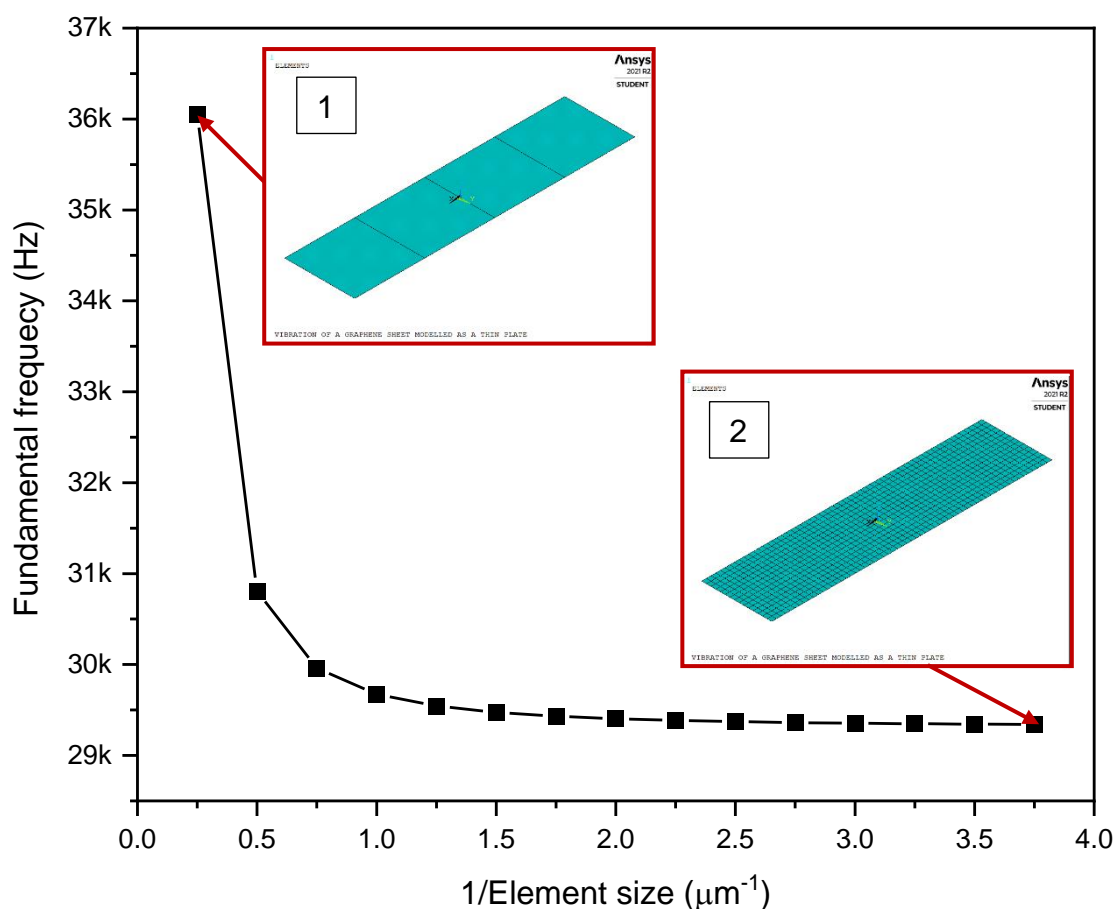
Figure 4-15: Mesh sensitivity analysis for graphene resonator models. Insert 1: Mesh fineness for element size $4 \, \mu m$. Insert 2: Mesh fineness for element size $0.27 \, \mu m$
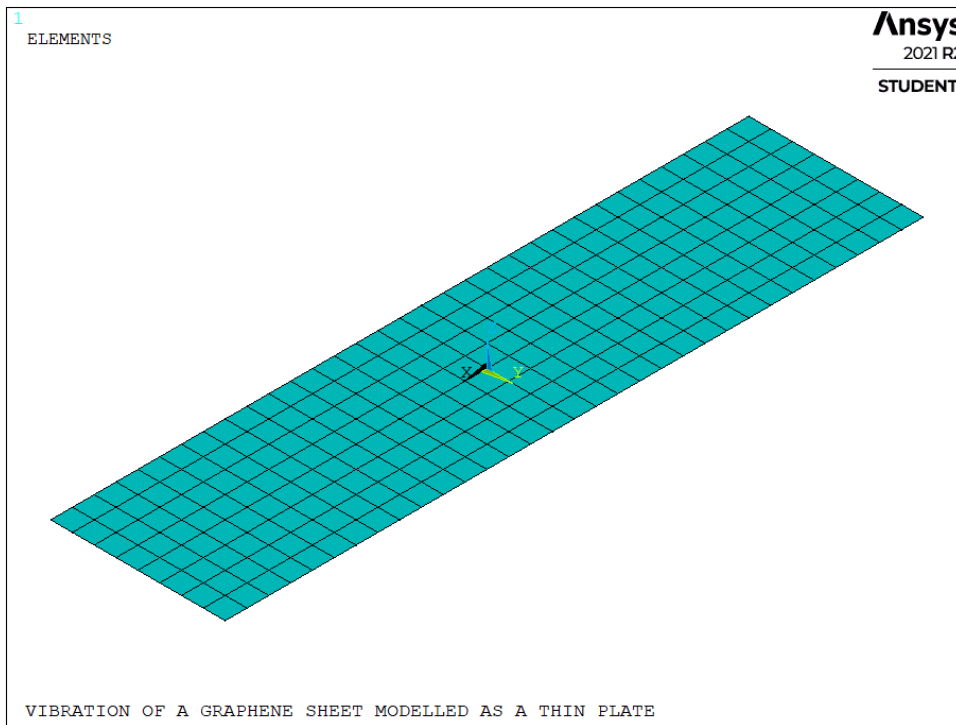
Figure 4-16: Meshed rectangular graphene resonator model with element size 0.5 μm
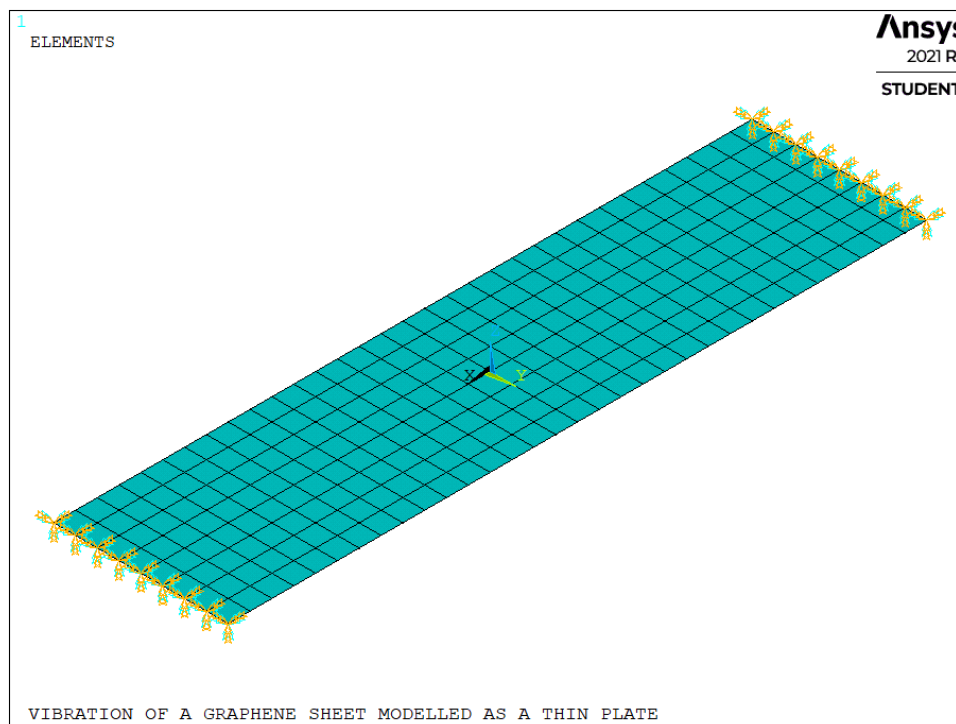
Figure 4-17: Boundary conditions on rectangular graphene model

4.3.2 Modal analysis of rectangular graphene resonators

Four sensing platform types were designed with four different cavity sizes over which graphene was suspended and microfabricated into doubly clamped bridges. The modal analyses for all four resonator sizes were carried out and

120

their fundamental frequencies are presented in Table 4-3 for monolayer and bilayer graphene. The mode shape for the fundamental resonant frequency of a 16 $\mu m \times 4\ \mu m$ graphene resonator is given in Figure 4-18.

Resonator size	Monolayer graphene		Bilayer graphene	
	f_0 (MHz)	Participation factor	f_0 (MHz)	Participation factor
16 $\mu m \times 4\ \mu m$	0.029404	0.35757E-33	0.060539	-0.11702E-32
22 $\mu m \times 5\ \mu m$	0.015537	0.79404E-33	0.031989	0.14277E-32
27 $\mu m \times 7\ \mu m$	0.010329	-0.12147E-33	0.021266	0.23772E-32
32 $\mu m \times 7\ \mu m$	0.0073417	-0.47513E-34	0.015115	-0.85316E-33

Table 4-3: FEA predicted fundamental frequencies for graphene resonators
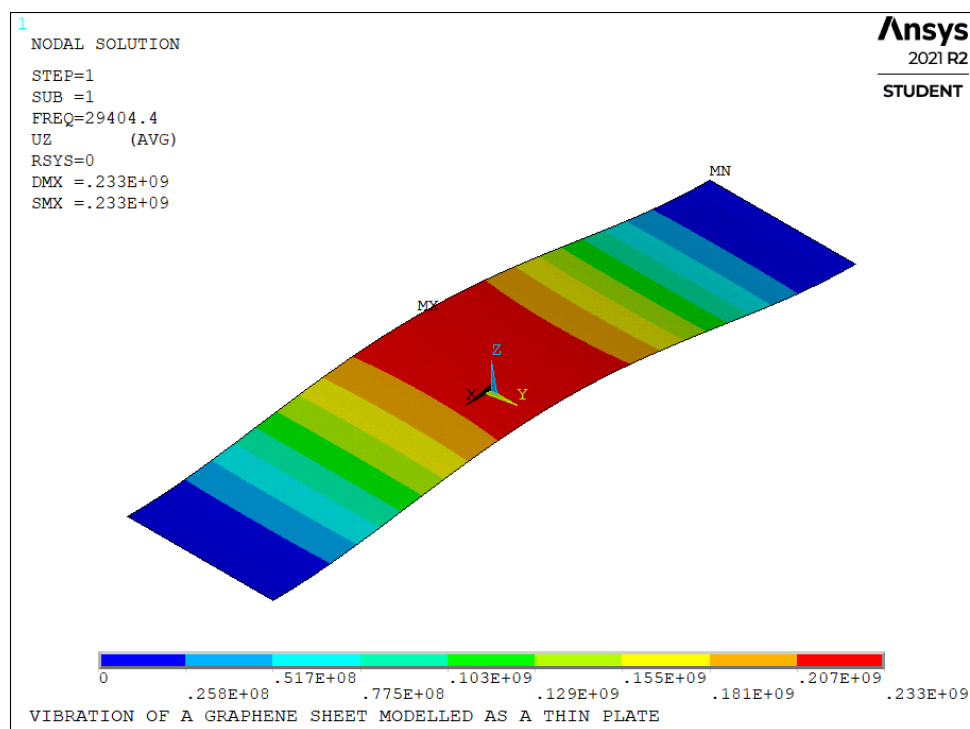
Figure 4-18: Mode shape for fundamental resonant frequency for 16 μm by 4 μm resonator

4.3.3 Frequency response of the resonators

Lorentz force excitation

Harmonic analysis of the graphene resonators is carried out with Lorentz force excitation for a 16 $\mu m \times 4\ \mu m$ bilayer graphene resonator. Lorentz force and damping coefficient as estimated in sections 4.2.1 and 4.2.3 respectively are used for the analysis. The frequency response plot is presented in Figure 4-19.

The response plot does not show the expected peaks at the resonance frequencies predicted by the modal analysis. This could be as a result of the magnitude of the Lorentz force or it could be that the resonance modes for the selected frequencies cannot be excited, given their negligible participation factors.

Piezoelectric shaker excitation

The harmonic analysis for a 16 μm × 4 μm bilayer graphene resonator is run for a piezo excitation with the estimated pressure at 10 V of 0.436 MPa from section 4.2.2. The frequency response plot is presented in Figure 4-20. As with the Lorentz force excitation, the expected peaks are not seen in the frequency response when using a piezoelectric shaker. The values of the displacement are several orders higher than the Lorentz force values, however, the lack of peaks is same. This could also be a non-excitable frequency mode problem.
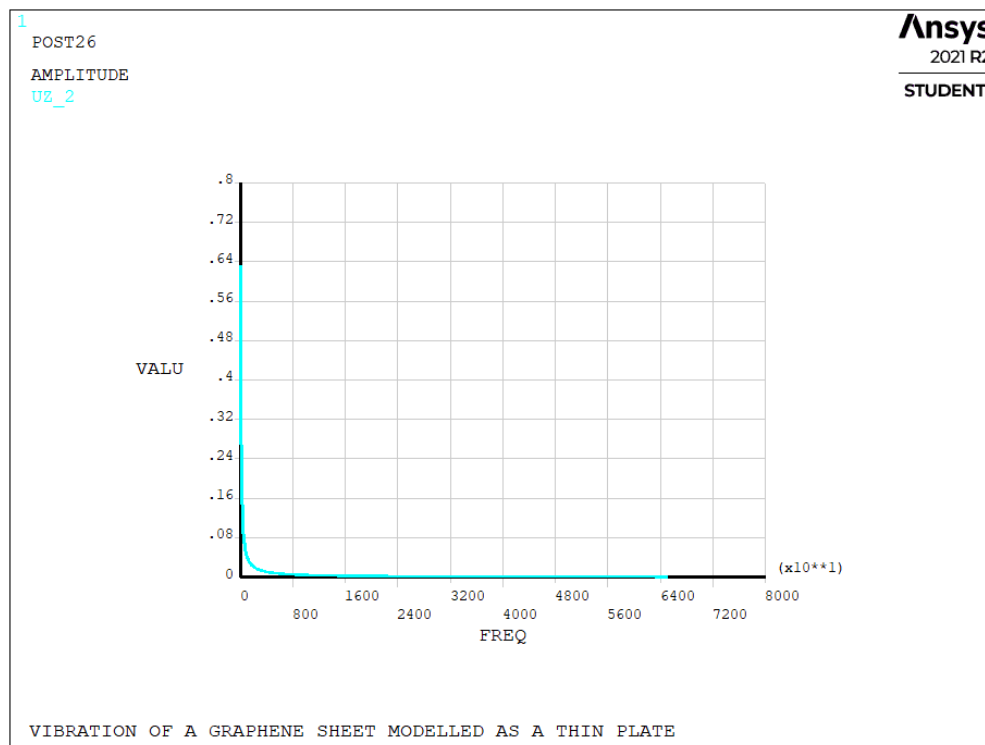
Figure 4-19: Frequency response plot for 16 μm by 4 μm bilayer graphene resonator excited via Lorentz force
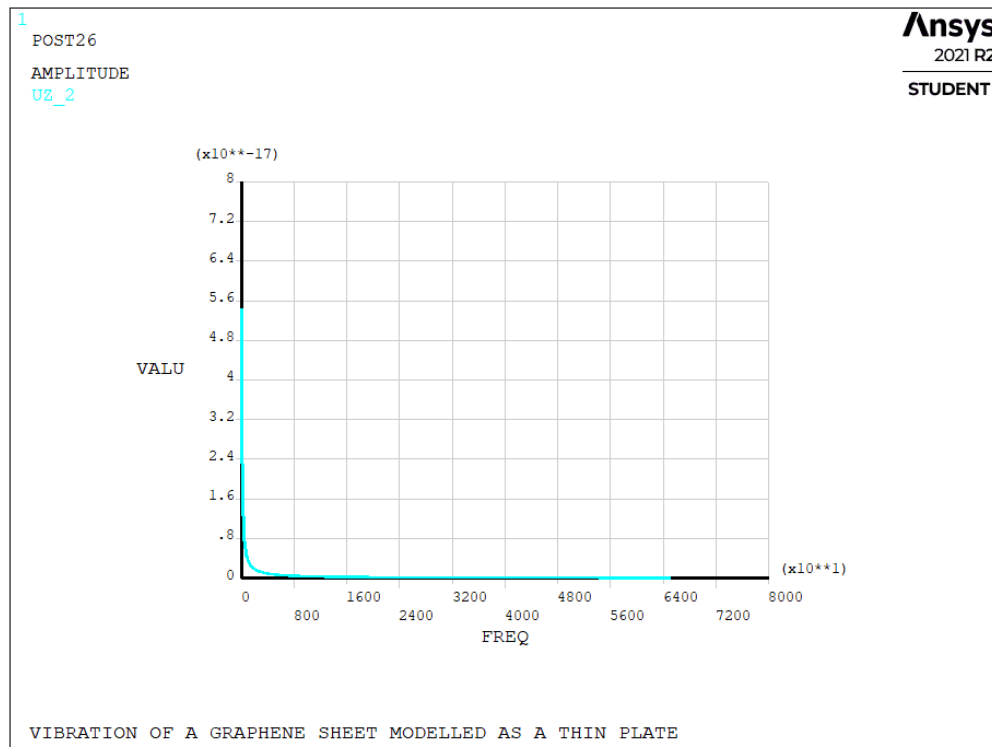
Figure 4-20: Frequency response plot for 16 μm by 4 μm bilayer graphene resonator excited with a piezoelectric shaker

4.4 Conclusion

In this chapter, FEA models of graphene resonators were used to predict their resonant frequencies and frequency response to excitations by Lorentz force and a piezoelectric actuator. The magnetic flux density at the device surface was estimated to be 0.2341 T. With a maximum current of $10.2 \, \mu A$ estimated for the resonators to avoid electrical breakdown, the maximum Lorentz force that would act on the resonators was estimated to be $ca. \, 37.456 \, pN$. The impedances of the conducting tracks and parasitic paths were checked to ensure the current flows through the resonator and not the substrate. The pressures generated in the piezoelectric actuator were estimated for various applied voltages. Viscous damping was assumed to be majorly responsible for energy dissipation in the resonators, and the damping coefficient was estimated to be about 9.54×10^{-3}. The frequency response of the resonators could not be obtained from the FEA harmonic analysis carried out. This could probably be because the modes excited were not active modes – this is supported by the very low participation factors the activated modes had.

Chapter 5: Design of a graphene-based mass sensor

5.1   Introduction

Chapter 2 highlighted several graphene sensor designs reported in literature and reviews the various techniques used in driving and sensing them. This work has focused on the use of graphene as the resonator in a mass sensor design type. Though graphene is one of the strongest contenders for micro- and nano-resonators in mass sensing applications, it does present peculiar challenges in production in research labs, handling and manipulation, and microfabrication. In this chapter, the design of a graphene-based mass sensor and the fabrication routes taken to achieve the design are presented. Subsections include: the sensor design, sensor fabrication, experimental test rig design and setup.

5.1.1 Principle of operation

Mass sensitive sensors, as described in Chapter 2, are a family of mechanical systems that sense the presence of the target analyte by detecting the forces, motion, change in mechanical properties or mass that result from the interaction of the target analyte with the recognition system in place. They can be surface-stress or dynamic-mode sensors; where the dynamic-mode sensors output a change in resonance frequency when the target analyte binds to the resonator. The sensors designed in this study are dynamic-mode mass sensors that utilise doubly clamped rectangular graphene resonators. The resonator is driven at one of its resonance frequencies during operation. The resonance frequency is then tracked to note any shift in frequency which would be an indication of an accreted mass to the resonator, hence detecting the presence of the target molecules.

Various techniques for driving and sensing NEMS and MEMS devices have been discussed in Chapter 2. Due to potential challenges with parasitic capacitances or coupling between the drive and sense capacitances, the magnetomotive driving technique which employs the use of Lorentz force was chosen for this study. Graphene is assumed to behave as any current carrying conductor in the presence of a magnetic field, however, in very strong magnetic fields changes in its electronic configuration, e.g. splitting of its Landau levels, have been shown to occur[225-227]. To actuate the resonator harmonically, a periodic Lorentz force can be generated either by driving an alternating current (ac) through the resonator whilst the magnetic field is static or driving a direct current (dc) through the

resonator in the presence of an alternating magnetic field. As it is easier to achieve a static magnetic field than an alternating one, the former method is preferred. For sensing, a capacitive sensing technique was chosen. This technique monitors the change in capacitance between the resonator and a parallel electrode plate. As the resonator vibrates, its distance to the electrode plate and consequently the capacitance, changes continuously and can be detected as an induced alternating current with a frequency associated with the vibrating frequency of the resonator. A change in the frequency of the induced current would indicate a change in the vibrating frequency of the resonator. Although lateral comb capacitive structures have been shown to offer better sensing performance in terms of generating a change in capacitance that varies linearly with the motional amplitude of the resonator[228, 229], achieving such structures with the graphene resonators were deemed impracticable for this study.

5.2   Graphene transfer trials

Free-standing graphene structures can be achieved via a few routes (see Chapter 2). To avoid exposing graphene to the harsh chemicals used in etching away the underlying substrate after graphene transfer, transfer to prepatterned substrates by the wet transfer method was preferred.

 Transfer trials were carried out on SiO_2/Si wafers prepatterned with trenches of widths ranging from 5 μm to ~35 μm and 10 μm depths. To transfer graphene to the wafers, commercially grown CVD graphene sandwiched between a supporting PMMA layer and hydrophobic polymer layer was gently introduced to deionized water. The PMMA/graphene detached from the hydrophobic polymer film and was left floating in the deionized water. The polymer film was removed and the prepatterned substrate used to fish out the PMMA/graphene at an angle of approximately 45^0. The PMMA/graphene/substrate was dried in air overnight. To remove the PMMA supporting layer, the PMMA/graphene/substrate was left to sit in acetone for 1 hour and subsequently in IPA for another hour and then left to dry in air.

Figure 5-1a shows HIM images of the suspended graphene over 5 μm trenches. Raman spectroscopy of the suspended membrane showed the characteristic G and 2D Raman peaks found in graphene (Figure 5-1b), which was a confirmation

that graphene was suspended. However, by optical imaging, the quality of the suspended membrane was deemed very poor, moreso, the suspension was achieved only on one of several prepatterned substrates used. The collapse or rupture of the graphene membranes across the trenches might have been due to the
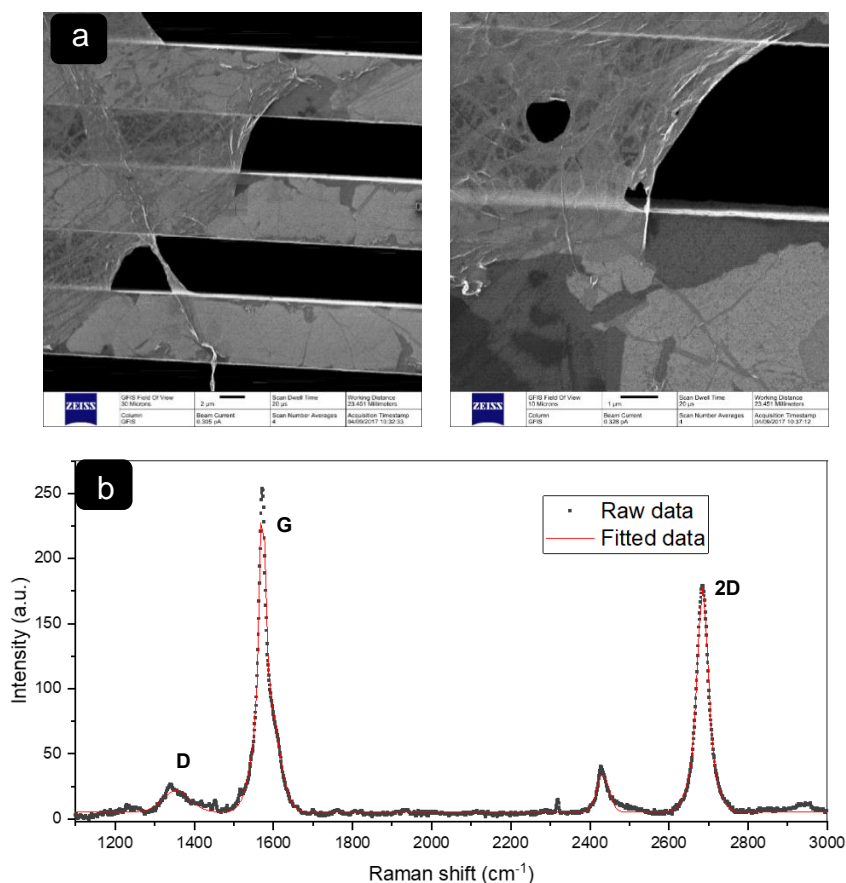
*Figure 5-1: **a)** HIM images of graphene transferred to a 5 µm-trenched SiO2/Si wafer. **b)** Raman spectra of graphene/PMMA/substrate*

size of the width of the trenches, thereby allowing water's surface tension during the drying process or acetone's action during the removal of the PMMA to rupture the membrane. Other factors that could have hampered successful transfers include the environment where the transfer process was carried out (not in a clean room), availability of a vacuum chamber to store the wafers immediately after transfer to avoid detachment of the graphene from the substrate, and availability of a controlled atmosphere oven for a thermal release of the PMMA to avoid using acetone.

5.3   Graphene on 3 μm cavities

After further trials and transfer attempts failed to achieve suspended graphene, the suspension of graphene was outsourced to Graphenea, a world-leading graphene firm in Spain. Monolayer graphene was transferred to SiO$_2$/Si wafers with arrays of 3 μm elliptical cavities; SEM images are shown in Figure 5-2a&b (30 nm of gold was evaporated onto the graphene to aid its visibility in the SEM). A relatively high percentage yield in terms of intact suspended membranes was achieved as compared to the results of monolayer graphene wet transfer by Wagner et al.[1] (Figure 5-2c&d).
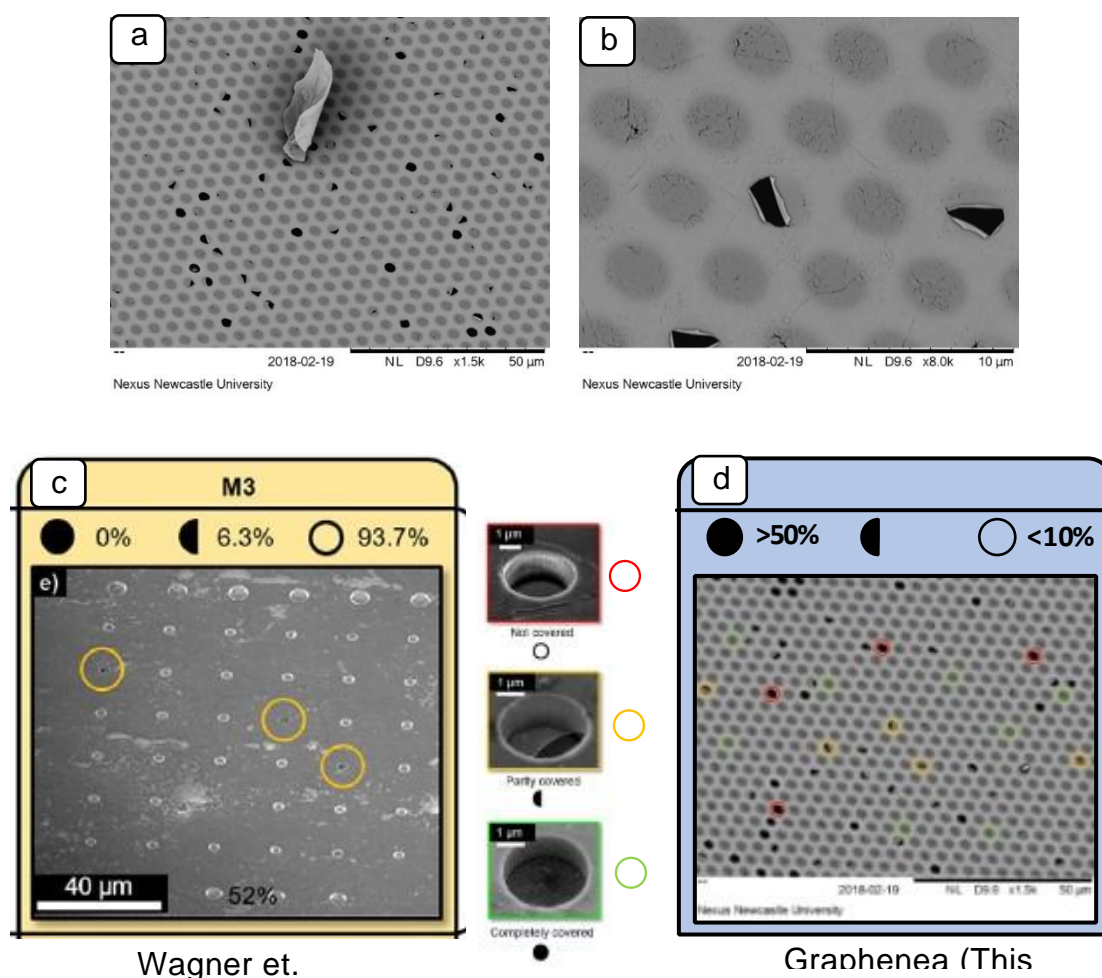
*Figure 5-2: **a) & b)** SEM images of graphene suspended on SiO2/Si with arrays of **3 μm** elliptical cavities **c) & d)** Yield comparison for transfer of monolayer graphene using the wet transfer method.*

The graphene structures suspended over **3 μm** elliptical cavities were microfabricated into doubly-clamped bridges and trampolines using focused ion beam (FIB) at the Research Centre for MicroEngineering and Nanotechnology, University of Birmingham. Images of the structures are shown in Figure 5-3.

Modal testing of the resonators to find their natural frequencies was done using a Polytec UHF-120 vibrometer (a similar optical measurement equipment is discussed in-subsection 6.4). No frequency peaks for the resonators were found except background noise peaks from the piezoelectric actuator. Because the sizes of the resonators were smaller than the focused measurement beam, the reflected beam from which the natural frequencies are extracted could only pick up the vibration properties of the silicon die/piezo actuator and not the resonator itself. Bigger resonators were therefore needed.
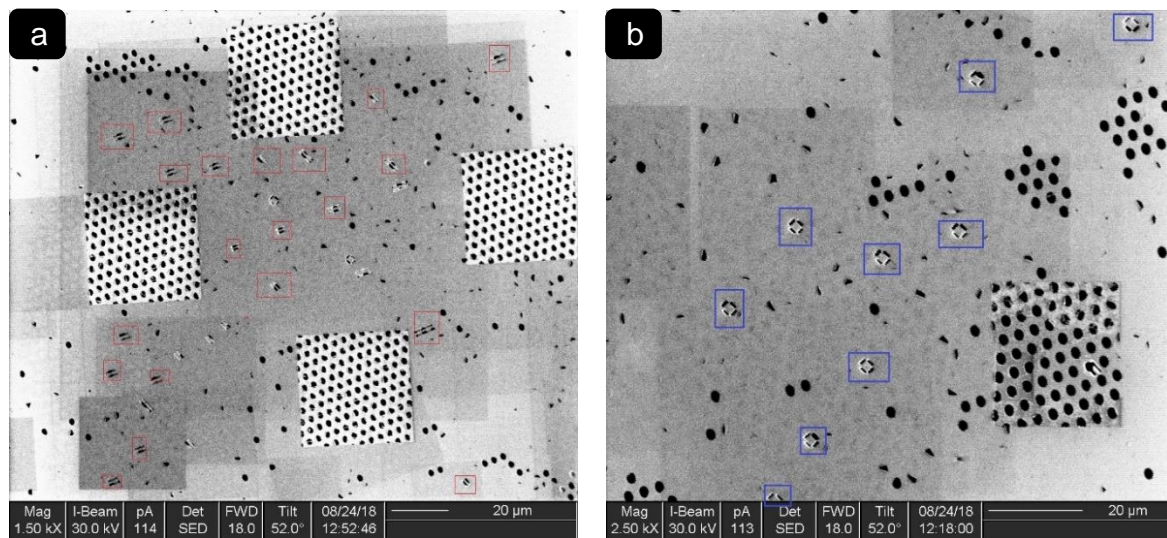
*Figure 5-3: Images of FIB microfabrication of **a)** doubly-clamped bridges **b)** trampolines.*

5.4 Sensor design with larger resonators

5.4.1 Design considerations and design of sensing platform

Most biological and non-biological target molecules exist in liquids, requiring at the least that the sensing element operate in liquid. For resonators vibrating out of plane, this will result in low quality factors due to damping. To offer a better quality factor, the resonators were designed with the option of being driven in-plane in addition to the out-of-plane mode, by changing the position of the external magnetic field such that mutual orthogonality is achieved between the field direction, current flow direction and the desired drive direction. The preferred method for producing suspended graphene structures for this study required that prepatterned substrates with cavities over which graphene would be suspended, electric current paths (tracks) and bond/contact pads be first fabricated before graphene is transferred to them. To have full control of the sizes of substrates to work with in the graphene transfer phase, snap guides were designed along the

edges of the individual sensor substrates to allow any size of the substrate down to one sensing platform to be easily obtained by snapping along the desired edges. With the possibility of in-plane and out-of-plane actuation, provision for sensing in both cases was considered. To achieve in-plane capacitive sensing, two electrodes in form of gold tracks terminating at the edge of the resonator cavity were used with an intended differential current measurement across the resonator. MEMS sensor platforms with multiple signal tracks easily generate crosstalk between the tracks. To avoid this, all tracks were sandwiched by earthed regions which act as shields to the tracks.

2.5 mm by *2.5 mm* sensor platforms were designed to be fabricated on 6-inch silicon wafers, each with provisions for 3 resonators to be driven magnetomotively and 96 others that can be driven with piezoelectric drivers. Only one resonator on each die was designed with capacitive sensing, however, all resonators were designed to be sensed optically with a vibrometer. Four cavity sizing options were designed and labelled as A1, A2, A3 and A4; A1 had rectangular cavities with sizes 16 μm by 6 μm, A2 cavities were 22 μm by 7 μm, A3s were 27 μm by 9 μm and A4s were 32 μm by 9 μm. In Table 5-1 the achievable sizes of bridges for each cavity are given. Figure 5-4 shows an A1 type sensor platform design made in Tanner's L-Edit software (v13.1). These were the substrates onto which graphene was transferred and microfabricated into bridges. The sensor platform size (2.5 mm by 2.5 mm) was chosen so the dies were just big enough to handle manually and small enough to produce a high throughput per wafer processed.

Table 5-1: Achievable graphene bridge sizes with sensor platform cavities

Sensor Platform Label	Cavity size	Length of Bridge	Width of Bridge
A1	16 μm × 6 μm	16 μm	≤ 4 μm
A2	22 μm × 7 μm	22 μm	≤ 5 μm
A3	27 μm × 9 μm	27 μm	≤ 7 μm
A4	32 μm × 9 μm	32 μm	≤ 7 μm
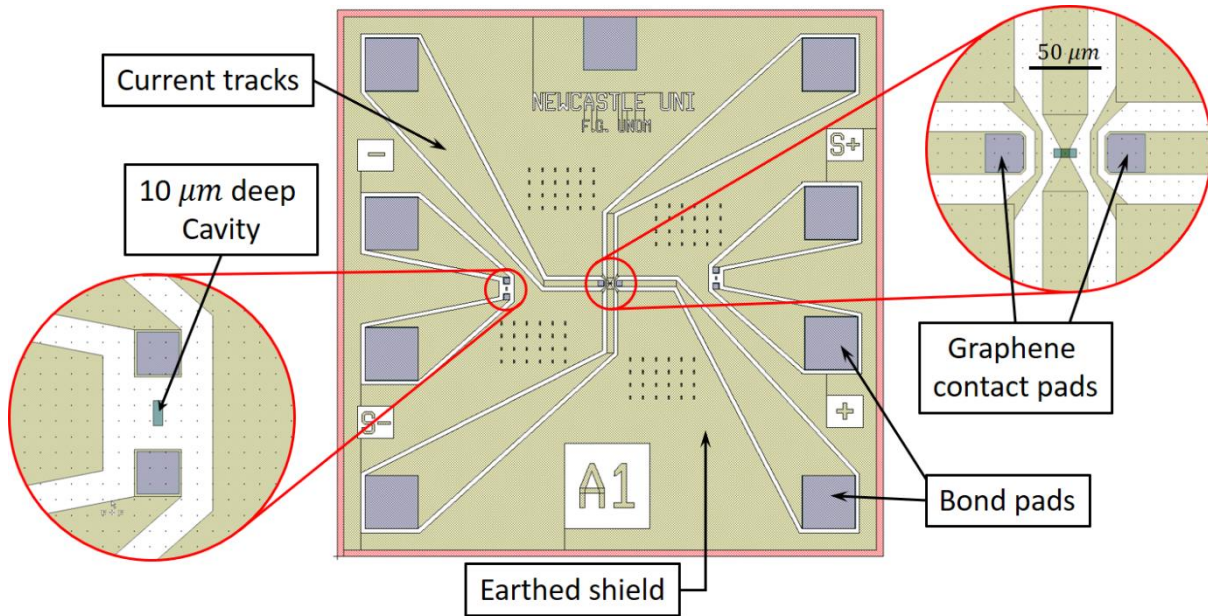
Figure 5-4: Design of sensor with drive and sense contact points. In the right exploded view, the gold under the cavity mask was etched away in the making of the cavity. (Designed with Tanners L-Edit)

5.4.2 Sensor platform fabrication

The sensor platform dies were made from silicon (Si), with layers of silicon oxide (SiO$_2$), chrome and gold added on and selectively etched by lithographic processes carried out at INEXMicro Newcastle University. These processes are discussed in the paragraphs that follow.

Fabrication process

The process flow for the fabrication of the sensor platforms is given in Table 5-2.

Step No	Fabrication Process	Illustration
1	Issue 300 μm 6" silicon wafer	
2	PECVD 2 μm silicon oxide	
3	Spin coat photoresist (LOR 5.0A + S1813 coats) and softbake	
4	Place and align mask 1 (metal mask), expose, develop and descum	

5	Deposit 20/250/20 nm of chrome/gold/ chrome	
6	Lift-off photoresist/chrome/gold/ chrome and clean	
7	PECVD 200 nm silicon oxide	
8	Spin coat photoresist (S1813 coat + wax bond + resist strip + SPR coat) and softbake	
9	Place mask 2 (oxide mask), expose and develop	
10	Etch through the silicon oxide and chrome to reveal the gold for the contacts	
11	Remove photoresist (wax de-bond) and clean	
12	Spin coat photoresist (S1813 coat + wax bond + resist strip + AZ9260 coat) and softbake	
13	Place mask 3 (recess mask), expose and develop	
14	Etch the oxide, (chrome, gold, chrome – on some cavities), oxide and silicon by 10 μm	
15	Remove photoresist (wax de-bond) and clean	
16	Spin coat photoresist (S1813 coat + wax bond + resist strip + AZ9260 coat) and softbake	
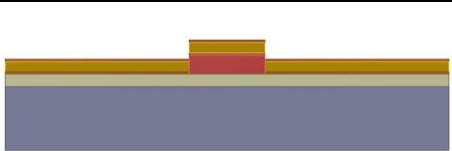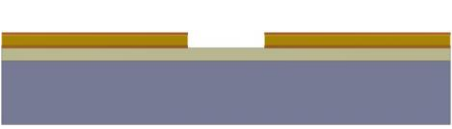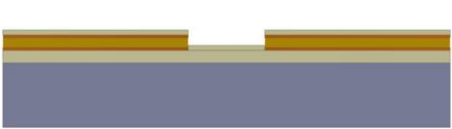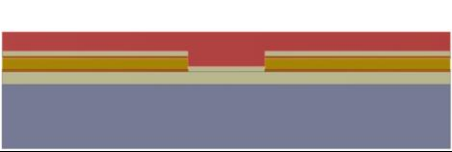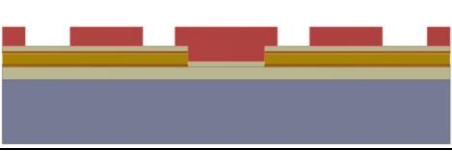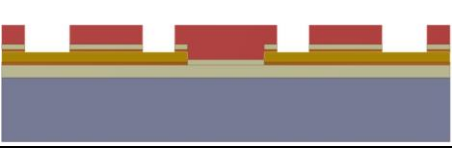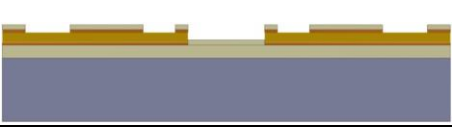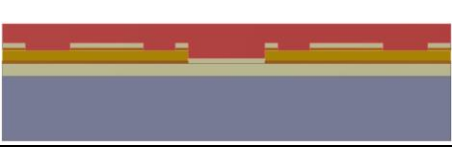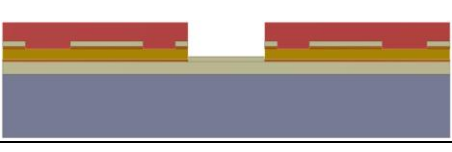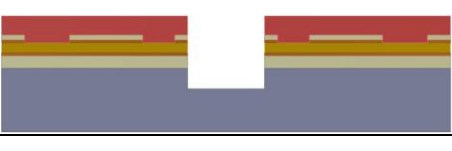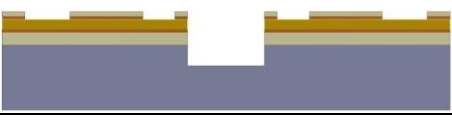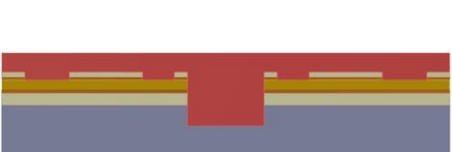
17	Place mask 4 (snap guides), expose and develop	
18	Etch the oxide, chrome, gold, chrome, oxide and silicon by 300 μm	
19	Remove photoresist and clean to have the final die.	
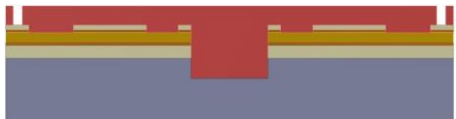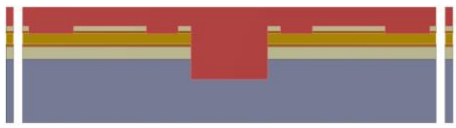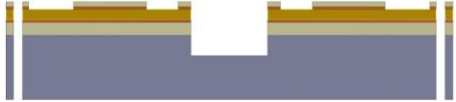
Table 5-2: Process flow diagram for fabrication of devices

A 300 μm thick 6-inch wafer was first cleaned, then 2 μm of silicon oxide (SO₂) was deposited on the wafer using an Oxford PECVD, and the thickness verified with a Filmetrics F20 instrument. The wafer was then prebaked and coated with hexamethyldisilazane (HMDS) in a Labline oven to improve the adhesion of the photoresist to the SO₂ surface. Two layers of photoresist, LOR 5.0A and S1813 were coated and soft baked on the pre-processed wafers one after the other with an EVG 101 spin coater and EMS hotplate. Next, the first mask (metal mask) was set, aligned to the photoresist coated wafer, and exposed to UV light in an EVG 620 contact aligner. After exposure, the wafer was developed in an EVG 102 spin developer and descumed in a Tegal etcher. 20 nm of chromium, 200 nm of gold and 20 nm of chromium respectively (Cr/Au/Cr) were deposited on the wafers in a Balzers BAK 550 evaporator. A lift-off process was then carried out to remove the unwanted regions and leave the electric current paths, earthing-shield regions, and bonding/contact pads.

The next steps in the fabrication process were to provide an insulating layer between the gold tracks and the graphene to be transferred to the sensor platform, with exposed regions as contact points. With the metal layer patterned on the wafer, the wafer was cleaned to remove any leftover particles in a Semitool SRD spin rinse dryer. A 200 nm layer of SiO₂ was deposited directly on the metal and exposed SiO₂ layers (this formed the insulation layer). The remaining steps at this point were etch-back processes for which thin wafer handling was not possible, therefore for each etch phase the wafer was bonded to a 6-inch 575 μm wafer carrier before carrying out the lithography processes. To bond the wafer to the carrier, a protective S1813 resist coat was first applied to

the wafer side to be bonded before the wax bonding was done using a wax bond tool. The S1813 resist was used to protect the wafer and aid removal of the wax used for bonding and other residues. After wax bonding, a resist strip step was done in an EVG 102 Spin Developer to remove any resist residue and other surface contaminants on the surface to be processed. Next, an SPR resist coat was applied and soft baked, the second mask (Oxide + chrome mask) was then set and aligned using an Ultratech Stepper, after which exposure and development were done in the EVG *102* Spin Developer. The exposed SiO_2 and immediate underlying chromium layers ($200\,nm$ and $20\,nm$) were etched in an STS AOE (Advanced Oxide Etcher) and STS Cluster respectively. After the etch processes, the wafer was de-bonded from the carrier on an EMS hotplate. The SPR resist was removed in a Felcon Solvent Bench and the resulting wafer cleaned with the Semitool SRD spin rinse dryer.

With the contact points and bond pads created, the cavities over which the graphene was to be suspended were etched next. As in the previous step, the wafer was bonded to a carrier wafer before being coated with a thick photoresist AZ9260 resist and soft baked. The third mask (Recess mask) was then set and aligned using the Ultratech Stepper, exposure and development was done before the resist was hard baked (post exposure bake - PEB) with a Labline oven. Several layers of material had to be removed to have a $10\,\mu m$ cavity; the first $200\,nm$ of SiO_2 was etched in an STS AOE, then metal etch in the STS cluster to remove the $20/200/20\,nm$ Cr/Au/Cr, next was $2\,\mu m$ oxide deep reactive-ion etch (DRIE) using the STS AOE, and finally 2 steps of silicon DRIE to an overall depth of $10\,\mu m$ from the surface of the first SiO_2 layer in an STS ASE (Advanced Silicon Etcher). The wafer was then de-bonded from the carrier wafer and cleaned to remove all resist and surface residue.

The final batch of processes was to produce the snap guides. As with the previous batch of steps, the processed wafer was wax bonded to a carrier wafer, then coated with AZ9260 resist and soft baked, the fourth mask (Snap guides mask) was set and aligned, the setup was exposed and developed before hard baking the resist. Next at the exposed regions, every layer of material was removed: $200\,nm$ of SiO2, $20\,nm$ of chromium, $200\,nm$ of gold, $20\,nm$ of chromium, $2\,\mu m$ of SiO2 and $300\,\mu m$ of Silicon. The final processed wafer was de-

bonded from carrier wafer and cleaned with oxygen ash using a Tepla 300 Plasma Asher to remove all resist and residue.

5.4.3 Suspension of graphene structures

Graphene was transferred to a 1.5 cm by 1.5 cm substrate comprising 36 pieces of 2.5 mm by 2.5 mm snap-able sensor platforms by Graphenea. This was advantageous because it allowed for cost management and a high through-put. Due to the relatively large cavity sizes (>16 μm by 6 μm), monolayer graphene transfer was not successful. Bilayer graphene (BLG) was therefore transferred to the substrates. Transfers to the bigger sized cavities (sensor platform types A3 and A4) mostly failed even for BLG. Figure 5-5 shows SEM images of fully intact suspended structures and ruptured structures.

5.4.4 Microfabrication of graphene bridges

The FIB microfabrication proved to be an excellent method in achieving the desired microstructures, however, the Research Centre for MicroEngineering and Nanotechnology was temporarily unavailable at the time the next microfabrication had to be done. Hence, electron-beam lithography (EBL) was attempted for the microfabrication of the suspended BLG at INEXMicro Lab, Newcastle University. Clearing doses of 10 $k\,\mu C/cm^2$, 50 $k\,\mu C/cm^2$ and 150 $k\,\mu C/cm^2$ were used, but the beam could not cut through the BLGS. Regions of exposure can be clearly seen in Figure 5-6 with the regions being clearer the higher the e-beam dosage used. Although, doses greater than 4500 $\mu C/cm^2$ have been said to amorphize
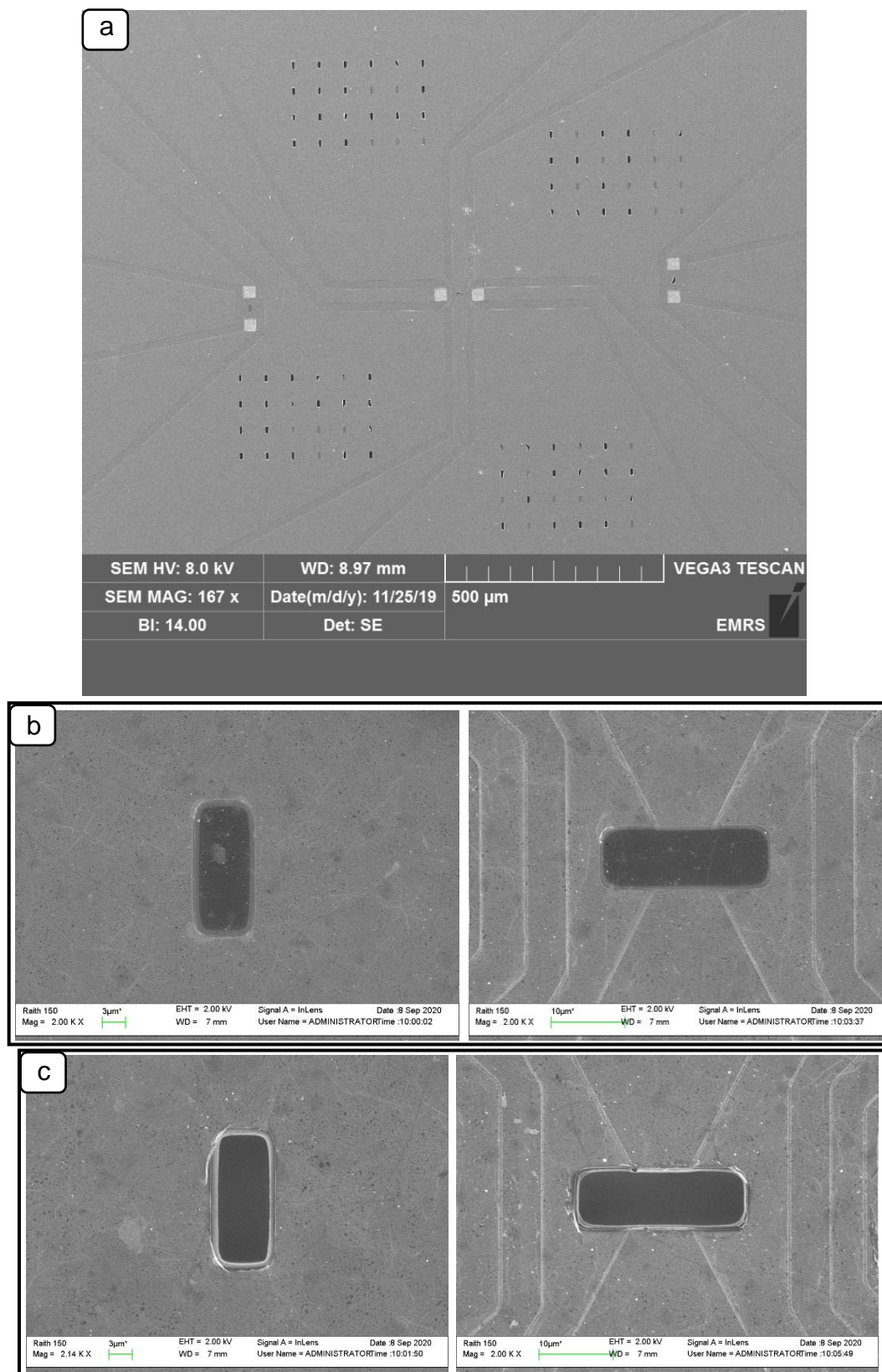
*Figure 5-5: SEM images of **a)** sensor platform showing all cavities and status of suspended graphene with 10 nm deposited gold (10nm-Au) **b)** intact suspended graphene structure (A1 & A2) – no Au **c)** ruptured graphene structure – no Au.*

graphene[230], much higher doses were used in this case firstly because the beam had to cut through not just one but two layers of graphene, and secondly because it was assumed that the amorphization, if it occurred, would not extend much beyond the area of exposure. In any case, the beam was unable to cut through the suspended BLGS, even though it could be assumed by inspection that the properties of the exposed areas were modified.
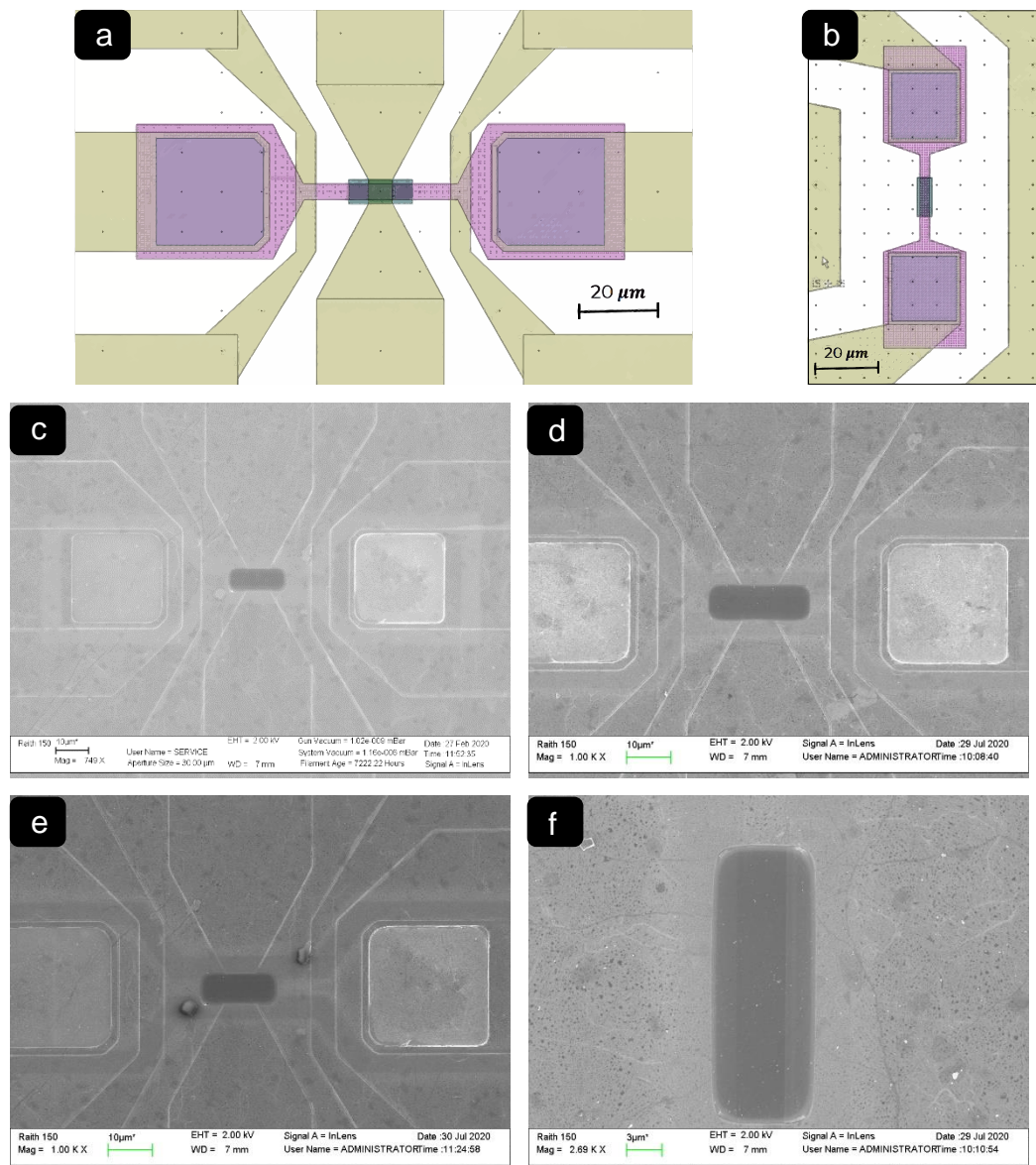
*Figure 5-6: E-beam writing **a) & b)** E-beam masks as drawn in L-Edit software **c)** @ 10k $\mu C/cm^2$ **d)** @ 50k $\mu C/cm^2$ **e)** 150k $\mu C/cm^2$ **f)** close up of 50k $\mu C/cm^2$ dosage.*

Following the inability of the e-beam to microfabricate the BLGS, photolithography was resorted to. To protect the graphene layer from being damaged by the resist, a 50 nm/10 nm layer of titanium/gold (Ti/Au) was deposited on the graphene/sensor-platform. Next resist was spin-coated on the

die, exposed and developed. Then 20 nm of Ti was deposited before lift-off to act as a hard mask for the exposed Ti/Au/Ti/G during the lift-off process and the plasma sputtering to follow. The resist was removed in a lift-off process and the resulting substrate cleaned and descummed using ultrasonics and oxygen ashing. Argon sputtering for about 3 minutes was then done to remove sections not masked by Ti/Au/Ti. The lithography steps are illustrated in Table 5-3. After deposition of Ti/Au on graphene, the suspended BLG appeared to have undulating features on its surface as shown in Figure 5-7(a), possibly induced by thermal stresses. Figure 5-7(b) shows the achieved Ti/Au/Ti/G bridges before removal of the Ti/Au/Ti layers. A yellow tint on the Ti/Au/Ti/G bridge was an indication that the top Ti layer had been considerably removed by the sputtering process leaving a residual Ti layer. This was taken into consideration for the FE model and the top Ti layer was decreasingly varied from 20 nm.

Step No	Fabrication Process	Illustration
1	Start with suspended graphene as transferred to the sensor platform (SP)	
2	Deposit 50/10 nm of Ti/Au on entire surface of graphene/SP	
3	Spin coat photoresist and softbake	
4	Place and align mask, expose, develop and descum	
5	Deposit 20 nm of Ti on entire surface	
6	Lift-off photoresist/Ti/Au/Ti and clean	
7	Carry out argon sputtering in increasing times of 1 minute to cut through Ti/Au/Ti	
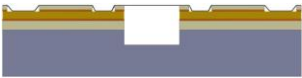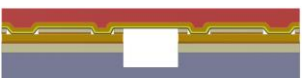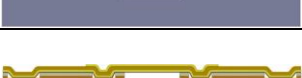
8	Etch or use controlled argon sputtering to remove Ti/Au/Ti to leave suspended graphene bridge	
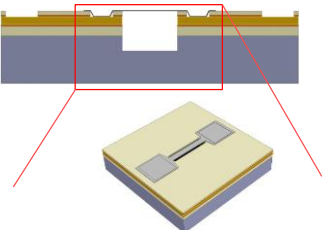
Table 5-3: Lithography for microfabrication of graphene bridges

Step 8 in the flow process though planned was not carried out. The Ti/Au/Ti bridges were sought to be characterized modally before step 8 was attempted.
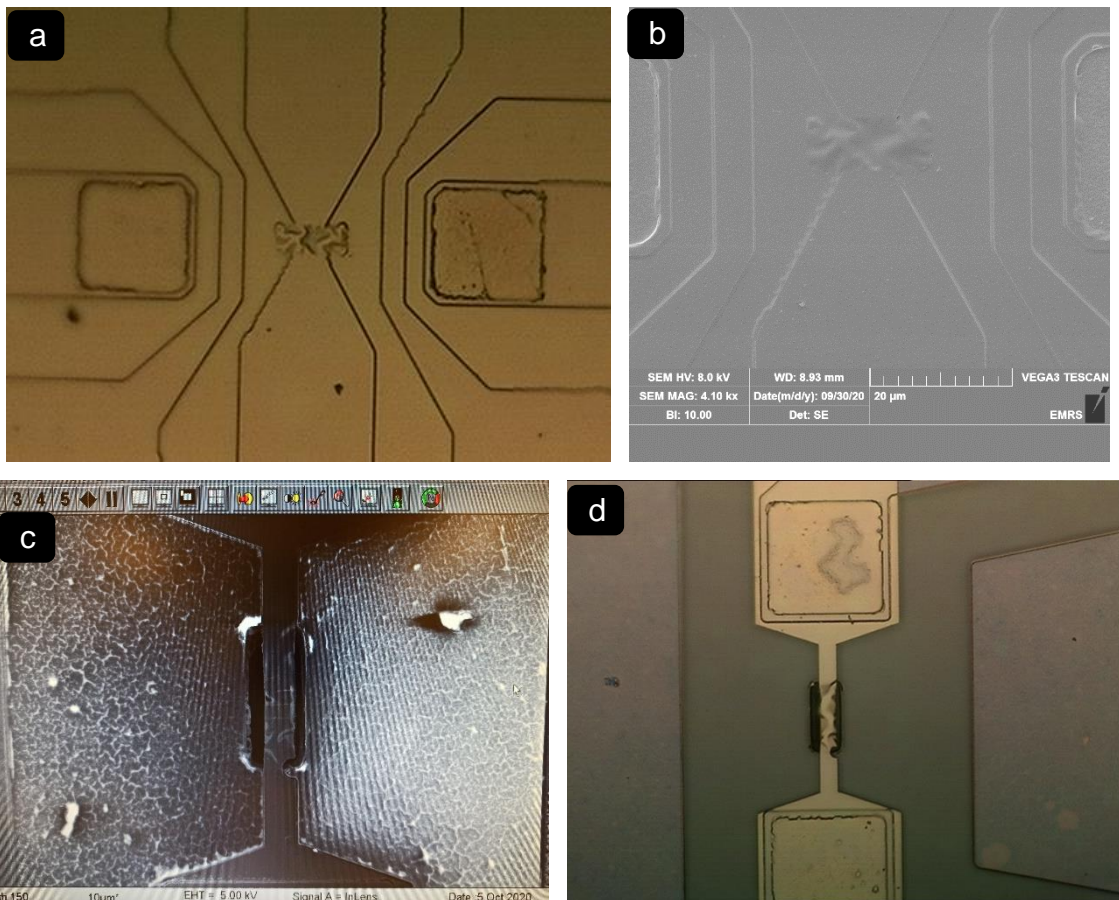
*Figure 5-7: **a) & b)** Images of warped Au/Ti/graphene membrane*
__b) & c)__ Images of microfabricated bridges of Ti/Au/Ti/Graphene

5.5   Experimental test rig design and setup

The resonators fabricated as described in the preceding subsections were designed to be driven magnetomotively or using piezoelectric actuators and be sensed optically or electronically (capacitive sensing). Specific setups are needed for any combination of the driving and sensing methods for the sensors. In this section, the setup for optical sensing using laser vibrometry is presented.

Optical sensing was first chosen to characterize the bridges and ensure their mechanical vibrancy before electronics were designed for capacitive sensing.

5.5.1 Measurement equipment/setup

A bespoke vibrometer setup assembled from component parts of a Polytec MSV 400 vibrometer or similar parts is shown schematically in Figure 5-8. The setup works with a DMS, OFV-073 scanner unit, OFV-072 microscope adapter fitted with a VCT-101 camera, MSA-E-400 junction box, OFV-5000 controller and an OFV-552 interferometer. The system's operation is based on the principle of Doppler vibrometry which is an application of Doppler velocimetry in the measurement of vibrations. This principle is discussed in detail in Chapter 6:.
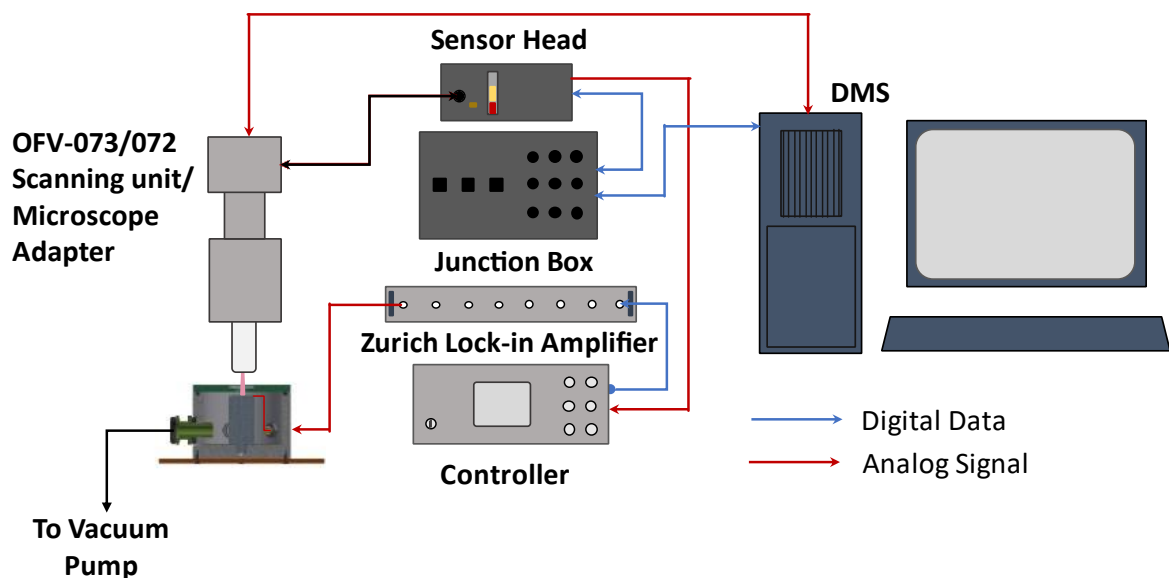
Figure 5-8: Laser Doppler Vibrometer (LDV) setup similar to Polytec MSV-400 vibrometer

The LDV setup included a Zurich HF Lock-In amplifier used to analyse the signal from the vibrometer. The Lock-in amplifier is particularly designed to deal with noisy signals by employing a heterodyne/homodyne mixing technique, in which the input signal is down-mixed with a reference signal generated in the Lock-in or supplied externally before being demodulated to extract the desired signal. The measurement signal from the OFV-5000 controller is fed into the Lock-in and analysed in the Zi-control software. The drive signal and measurement settings, including the data collection were all done in the software. The drive signal from the Lock-in drives a piezoelectric disc upon which the resonator sensing platform was affixed. The piezoelectric disc was affixed to a piezo stand designed and fabricated as part of a vacuum chamber setup for measurements in air and

vacuum. The vacuum chamber was fastened to an xy stage used to accurately position the test structure under the objective lens for measurement.

5.5.2 Optional magnetomotive drive setup

To allow for out-of-plane and in-plane driving modes using the magnetomotive method, a holder was designed to hold an iron core which provided a closed path for the magnetic flux and allowed for the sensing platform to be rotated through 90^0 to achieve orthogonality between the magnetic flux, the current flow and the desired drive direction. The holder was made from plywood by laser cutting the various parts and gluing them together. The magnetic field source was a pair of axially magnetised cylindrical rare earth Neodymium permanent magnets each of strength $0.5\ T$ at the magnet's pole. A simple connection of an AC voltage source (Rohde & Schwarz SMBV100A vector signal generator) in series with a resistor supplies alternating current to the resonator. The sensing platform is fixed to a dual in-line package (DIP) and the bond pads connected to the DIP with $50\ \mu m$ diameter wires using a wire bonder.

5.6   Conclusion

The design and fabrication of a graphene-based mass sensing platform has been presented in this chapter. A 2.5 mm by 2.5 mm silicon/silicon-oxide prepatterned substrate was designed and fabricated with appropriate cavities, bond pads and current tracks onto which CVD grown graphene was transferred and microfabricated into doubly clamped resonators. Over 2000 sensor platforms were fabricated, graphene transfer was made to single units each comprising 36 sensor platforms. Each sensor platform had 3 cavities plus 96 extra cavities from which magnetomotively driven and piezoelectrically driven resonators respectively could be achieved. Several hundreds of suspended graphene structures were achieved during this study; about twenty 3 μm doubly clamped resonators were achieved by FIB microfabrication and three 16 μm by 3.5 μm achieved by lithography. The major challenges faced in this study had to do with achieving suspended graphene and then microfabricating them into bridges. However, the achievement of released graphene resonators establishes a proven fabrication route for the resonators from which future works can start in the pursuit of a compact single unit sensor.

Chapter 6: Sensor resonator characterization

6.1 Introduction

The graphene resonators designed and fabricated in Chapter 5: are characterized in this chapter. Characterization techniques when employed are aimed at determining or verifying the material and structural properties of a structure. Improved designs and usage of products and devices are impossible without proper characterization. Raman spectra as has been extensively discussed in Sub-section 2.4.2 was used to characterize the resonator's materials and verify the number of layers of graphene suspended – this is discussed in Subsection 6.2. Surface profile and modal tests were also carried out and are presented in Subsections 6.3 and 6.4 respectively.

6.2 Raman spectroscopy of the suspended graphene structures

The Raman spectra of the suspended graphene structures were taken using a Horiba Scientific LabRam HR Raman spectrometer. The Horiba had two beam options, an Argon (Ar) laser beam with wavelength 514 nm and a Helium-Neon (HeNe) beam of wavelength 633 nm. The Ar laser beam was used for all the Raman spectra presented in this work.

6.2.1 Monolayer graphene on 3 μm cavities

Point scans were taken at the centre of the suspended drumheads and the Raman data was fitted to a Voight profile (convolution of a Gaussian and Lorentzian profile) where best suited or to Gaussian or Lorentzian profiles using OriginLab statistical application. Figure 6-1 shows the Raman spectroscopy plot for the SLG structure. The G and 2D bands characteristic of graphene materials can be clearly seen, but so is the defect-induced D band. The G band peak appears at 1587.53 cm^{-1}, the 2D band peak at 2680.25 cm^{-1}, and the D band peak at 1349.77 cm^{-1}. The 2D band is the major fingerprint for identifying the number of layers in graphene. A single Lorentz fit for the 2D band (Figure 6-1c) agrees with 2D band fits for single layer graphene in literature (Figure 6-1b), however a much broader width is observed with the suspended SLG in this work. It is worth noting that the spectra for graphene in literature are mostly for graphene on substrates, so comparisons with such data is made with care, even though it has been shown that there is no significant difference in the spectra for

suspended and non-suspended graphene[98, 231]. However, a narrowing of the width of the 2D band is reported for suspended graphene[231], which is very different from the broadening of the 2D band observed with the 3 μm suspended SLG.
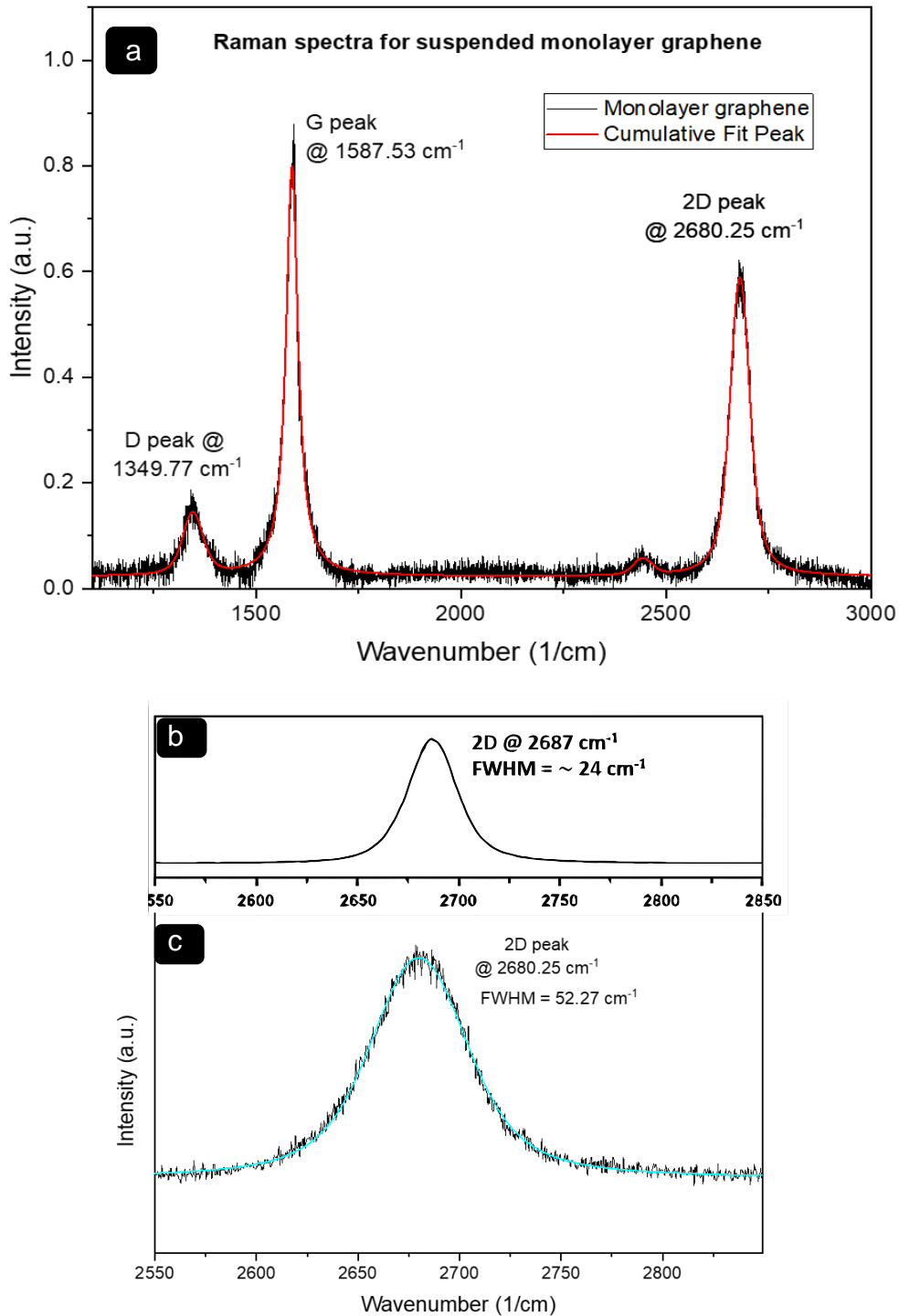
*Figure 6-1: **a)** Raman spectra of suspended monolayer graphene structures*
***b)** Single Lorentz fit for 2D band of SLG[81]*
***c)** Single Lorentz fit for 2D band of SLG over 3 μm cavities*

The presence of the D band indicates that there are defects in the crystal structure of the suspended graphene. Another plausible indication of the presence of defects in the graphene material is the ratio of the 2D band intensity to the G band intensity (I(G)/I(2D)), which should be ~0.24 for monolayer graphene on SiO_2[100] and a value lesser than that for suspended graphene[231]; but I(G)/I(2D) for the suspended single layer graphene in this work was 1.3, indicating strongly that the graphene was doped or there were large amounts of charge impurities in the structure. Albeit it is no doubt that the suspended graphene structures were single layer graphene structures.

6.2.2 Bilayer graphene on 16 *µm*+ rectangular cavities

Raman scans for the bilayer graphene were made on the free-standing graphene structures and on the graphene portions in contact with silicon. The electronic band structures for bilayer graphene as discussed in Chapter 2 are modified from those of SLG, this is the primary cause of the evolution of the 2D band. The interactions of the two graphene planes cause the π and π^* bands to split into four bands, which create the possibility of four optical transitions. Only two of these transitions couple strongly with the incident light from the Raman beam and are shown in Figure 6-2[98]. With these two transitions, there are four processes involving phonons with momenta q_{1B}, q_{1A}, q_{2A}, and q_{2B}, which are directly responsible for the four peaks that fit the 2D band of BLG Raman spectra. For a 514 *nm* beam, the shifts of the four peaks with respect to the average of the two main peaks are approximately[98] -44 cm^{-1}, -10 cm^{-1}, 10 cm^{-1}, and 25 cm^{-1}.
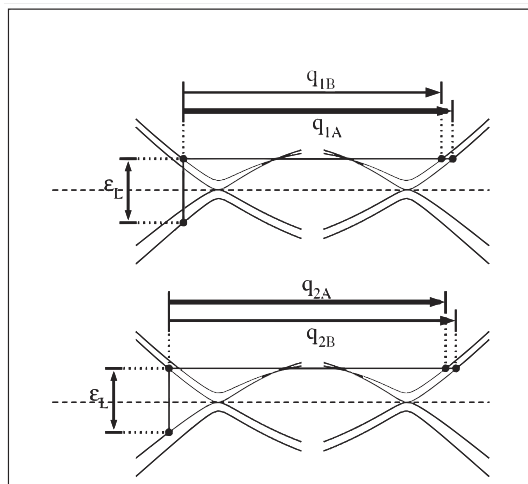
Figure 6-2: Double resonance for 2D peak in bilayer graphene

Figure 6-3 shows the Raman spectra for the suspended BLG. At first glance no difference is seen when compared to the Raman spectra for SLG, its 2D band could get away with a single Lorentzian fit (Figure 6-3-Insert 3), however, the best fit convolutes two Lorentz profiles (Figure 6-3-Insert 2) and not four as is reported in literature[81, 98, 100](Figure 6-3-Insert 1). This might mean that the electronic structure of the BLGs were not changed significantly from that of SLG when produced; that the graphene plane interactions did not split the π and π^* bands into four with the resulting four optical transition possibilities. This could be possible due to the stacking achieved. Turbostratic graphite, which has no AB stacking, has been shown to exhibit a single 2D Raman peak[232], but with a width that is twice that of SLG 2D Raman band. Which suggests that it is indeed possible to have a BLG with a single Lorentz fit 2D Raman band, possessing the rigidity of BLG but with electronic properties very close to SLG's.

The G band occurs at 1580.91 cm^{-1} and is red shifted from the G peak position in SLG. The D and 2D bands occur at 1354.08 cm^{-1} and 2691.79 cm^{-1} respectively and are both blue shifted from the corresponding band peak positions in SLG. I(G)/I(2D) for the suspended BLG is unusually high at 4.94 compared to an estimated range of ~0.24 $\leq$ I(G)/I(2D) $\leq$ ~3.2 when going from SLG to highly ordered pyrolytic graphite (HOPG)[100]. The four Lorentz fits in Figure 6-3-Insert 1 occur at 2658 cm^{-1}, 2688 cm^{-1}, 2706 cm^{-1}, and 2721 cm^{-1}, respectively. The two fits in Insert 2 have their peaks at 2686.94 cm^{-1} and 2694.12 cm^{-1}. For BLG on silicon oxide/silicon, the G, 2D and D peaks occur at about the same wavenumbers, and I(G)/I(2D) is 1.16 which falls within the reported range. In addition, a slight broadening of the 2D band is observed for graphene on SiO_2/Si (Figure 6-4) with a FWHM value of 41.32 cm^{-1}, but like the suspended BLG only 2 Lorentz profiles are sufficient to fit the band. The G and D bands however are fit with 3 profiles and have shapes that are evidently different from the suspended graphene bands, contrary to the findings in literature.
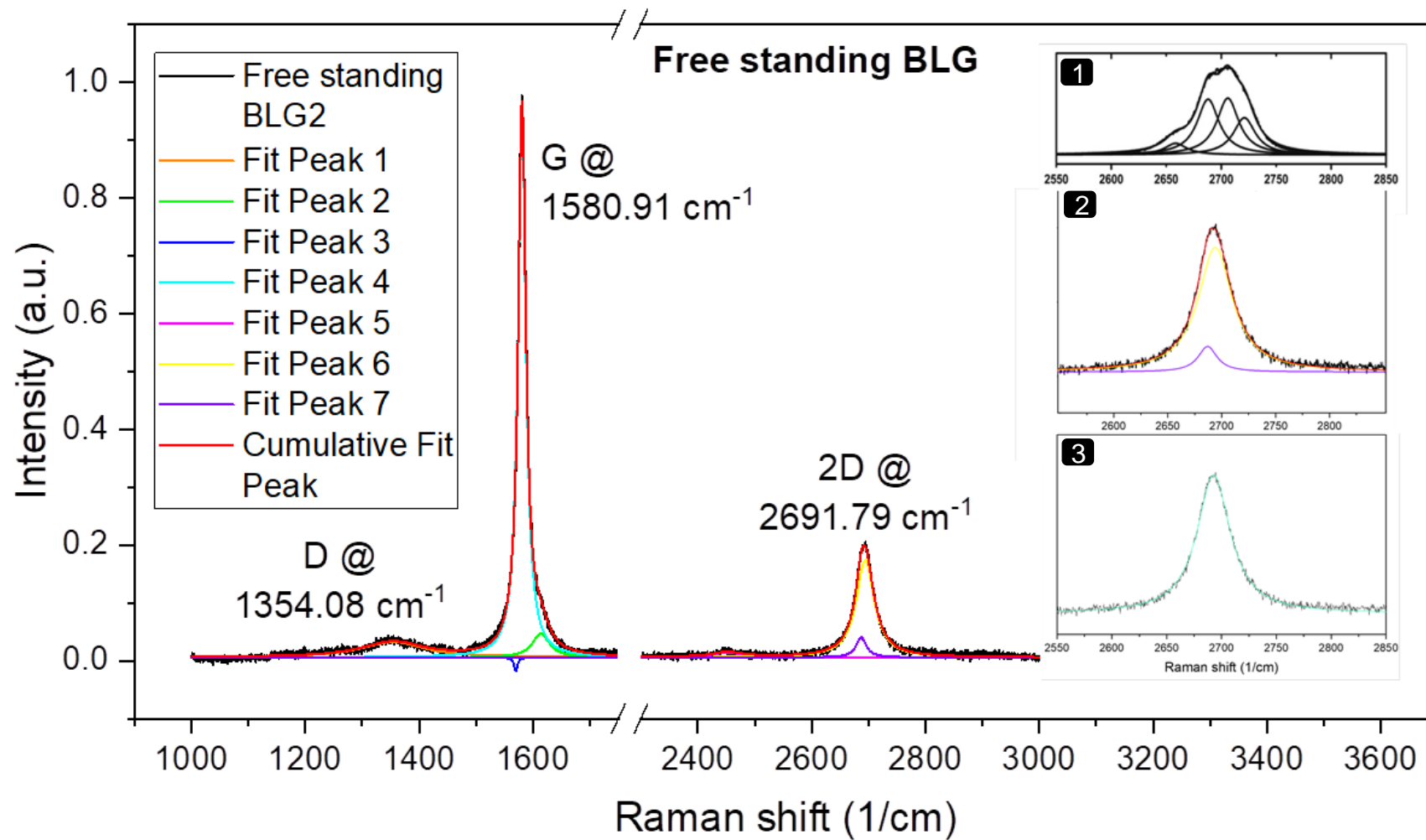
*Figure 6-3: Suspended BLG Raman spectrum with fit Lorentz peaks. **Inserts: 1.** 2D band of BLG from literature[81] **2.** 2D band with two Lorentz fits **3.** 2D band with one Lorentz fit*
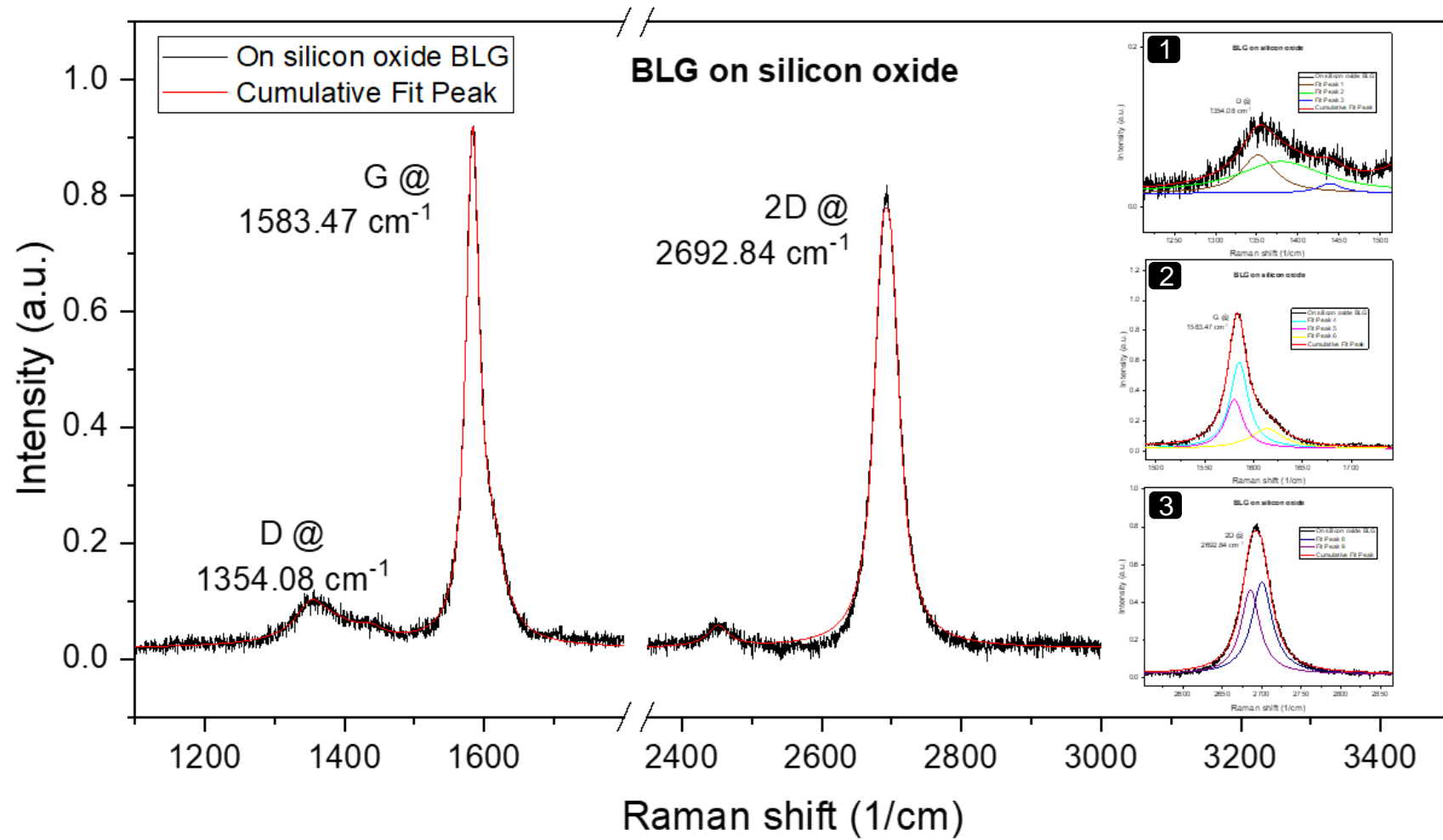
Figure 6-4: Raman spectra of graphene on silicon oxide/silicon. **Inserts: 1.** *D band fit profiles* **2.** *G band fit profiles* **3.** *2D band fit profiles*

6.3   Surface profiles of suspended graphene

The surface profile of graphene at three different stages in the microfabrication process were characterized using a Zygo NewView 5000 surface profiler. The Zygo operates based on the principle of white light interferometry, which involves the analysis of the diffraction pattern of a wavelength of white light generated by the interaction of the light with the surface to be characterized. Because of the various wavelengths in white light, the Zygo can achieve very high measurement resolutions, down to 1 nm, and provide accurate data on the surface topography of the test samples. One major drawback of the Zygo, and other optical non-contact equipment is the requirement of reflectivity of the test sample. Graphene being transparent made it impossible to take direct measurements of its surface topography, consequently thin layers of gold were required to be deposited on it to impart reflectivity to it and ensure measurements with the Zygo were possible. Also, only the flatness of the graphene structures was sought to be determined. Deposition of hot metal on suspended graphene resulted in the rupturing and wrinkling/warping of the suspended structures (See Figure 6-5). Wrinkling and rippling of graphene structures suspended over prepatterned SiO_2/Si surfaces have been observed during annealing processes[233]. This is mainly due to the difference in the thermal expansivities of graphene and SiO_2. When heated this way, graphene experiences biaxial compression which together with the boundary conditions at the graphene/SiO_2 interface results in wrinkling, rippling, buckling or failure of the structures.
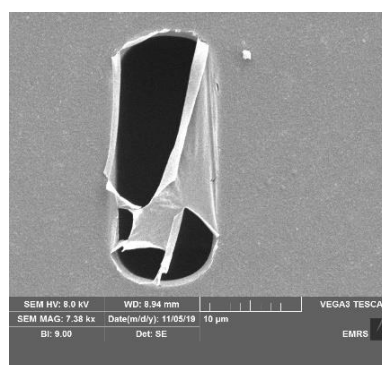
Figure 6-5: Ruptured BLG sheet after deposition of 10 nm gold

To reduce the probability of wrinkling and structure failure, the metal deposition rate was reduced and together with the cooling provided during deposition via a Peltier stage, flat, unwrinkled gold/graphene structures were achieved.

Figure 6-6 shows the profile of a fully clamped (drumhead) graphene structure with 5 nm of gold deposited. The red box in subfigure a) indicates the position of the cavity, which can pretty much be made out in the 3D model and surface map. Subfigure d) plots the surface profile along the line drawn in the surface map. The surface profile shows a fairly flat structure; zooming in on the profile (subfigure e) an average upward deflection is observed with the maximum deflection being ~26 nm in an upward-positive direction. The structure was considered fairly flat despite the deflection because over a 16 μm length with the shape of the profile, the structure will not be wrinkled or rippled, but bulged. This could very much be due to the pressure imbalance across the membrane since the cavity is completely sealed. The spikes in the 3D model around the contact pad and the 3D model itself are measurement noises and can be removed with further data processing to have a more accurate representation of the surface. They however do not impede accurate interpretation of the surface profile and structure. Therefore, by surface profiling and optical imaging,

Figure 6-6 and Figure 5-5 show that the suspended BLG were considered flat and without wrinkles or ripples.

Lithographic processes were used to microfabricate the suspended graphene structures into doubly clamped rectangular bridges as discussed in Chapter 5:. As mentioned in subsection 5.4.4, the deposition of Ti/Au on graphene as a mask for graphene during the microfabrication of the bridges caused graphene to warp (Figure 6-7a). The Ti/Au/Ti/Gr bridges in Figure 6-7b were microfabricated from the warped suspended graphene. Figure 6-8 shows the surface profile of one of the bridges. Subfigure d) shows that the bridge was deformed in the upwards-positive direction with an approximate curvature radius of 1.85 μm. Because the deformation of the bridge resulted from an already warped structure, the curvature is seen to be irregular, and might be responsible for the missing data points on the surface profile plot since the Zygo will only measure surfaces tilted up to 4^0. The missing data points may also be due to the Ti/Au/Ti being removed in some regions of the bridge leaving only graphene which is transparent, however, with the SEM images of the bridge in Figure 6-7b the cause for the missing data is strongly believed to be due to the tilt of the deformed structure.
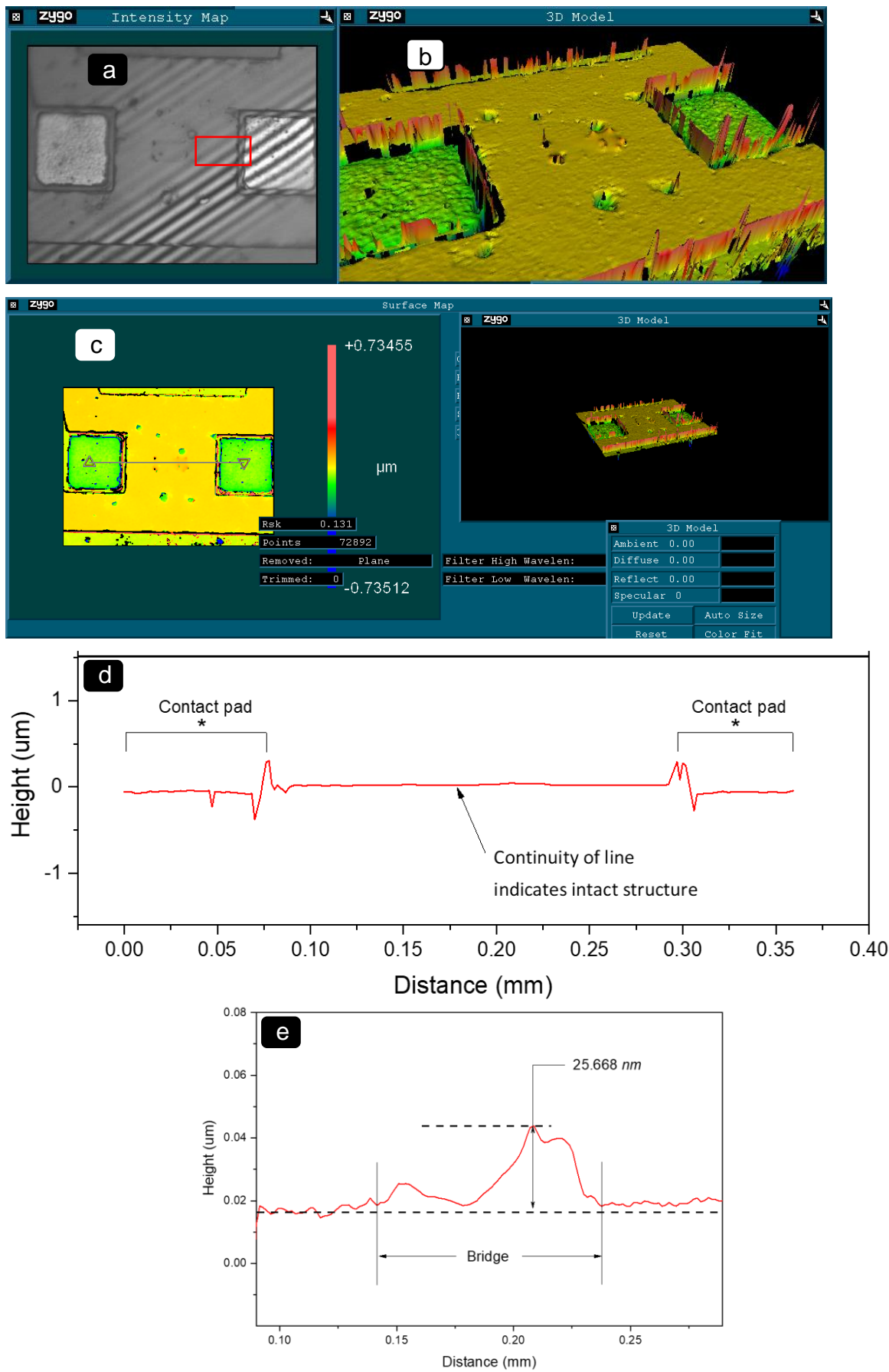
*Figure 6-6: Fully clamped rectangular graphene structure **a)** Intensity map with measurement fringes **b)** 3D plot **c)** Surface map **d)** Surface profile plot **e)** Zoomed in surface profile plot*

Given that the total thickness of the composite bridge is ~75 nm, with a deflection of ~1.85 μm which is about 2400% of the bridge's thickness, it will be expected that stress stiffening effects will be induced in the structure because of the very large deflection. Stress stiffening is advantageous in several engineering designs and scenarios for example where vibration damping and resistance to buckling are needed, but where vibrations are integral to the working success of the design or system, as is the case with this work, stress stiffening becomes a disadvantage. It was assumed that the graphene bridges were stiffened as a result of the very large deflection and the presumed effect of this is discussed in the next subsection.
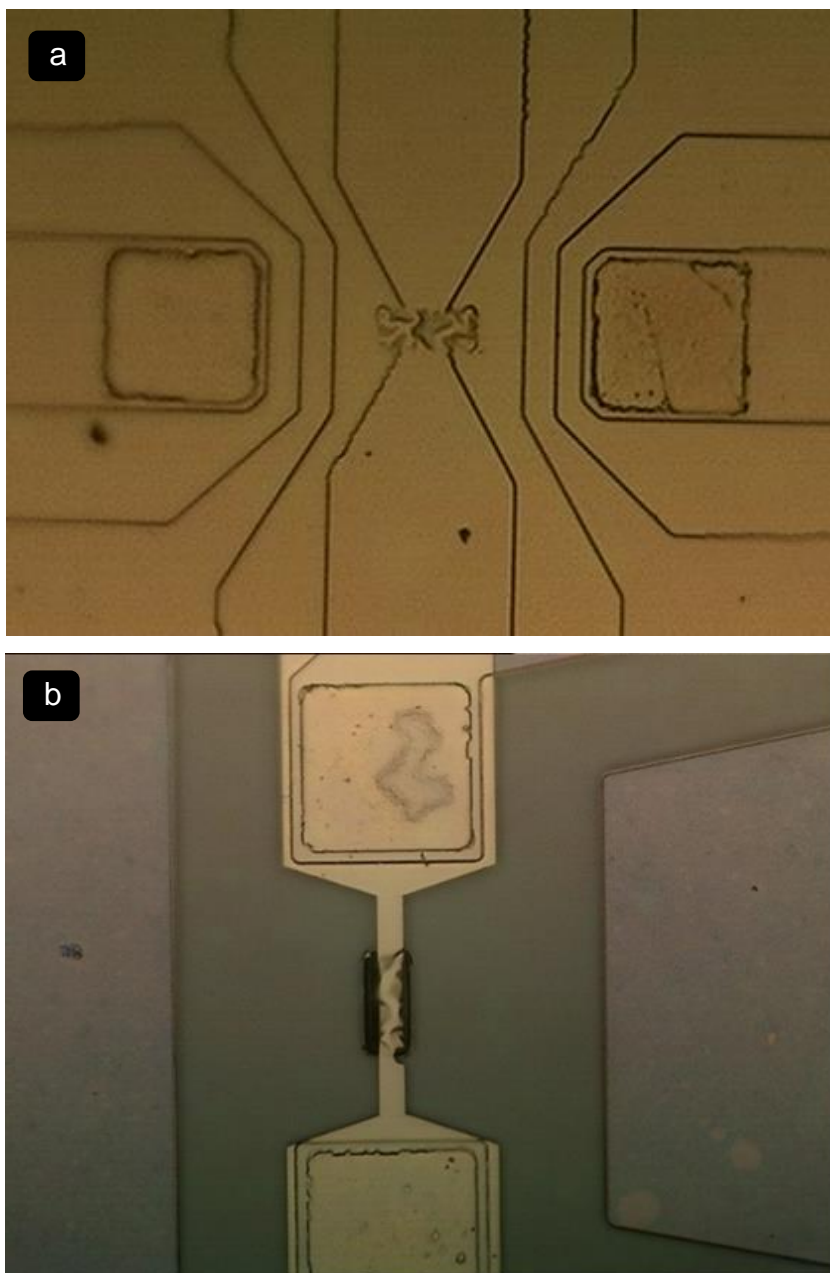
Figure 6-7: a) Image of warped Au/Ti/Gr membranes b) Image of microfabricated bridge
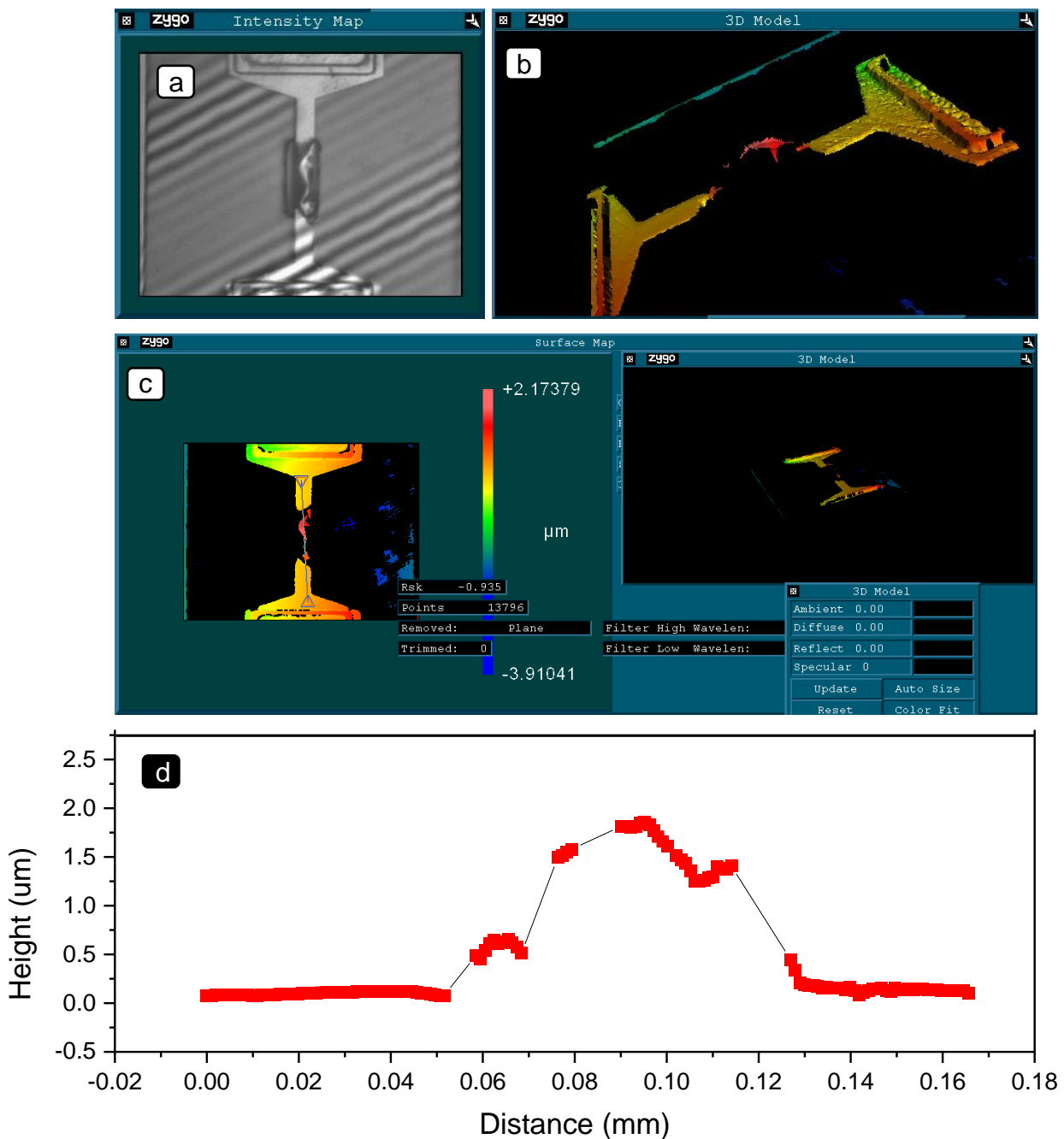
*Figure 6-8: Microfabricated Ti/Au/Ti/Gr Bridge **a)** Intensity map **b)** 3D model **c)** Surface map **d)** Surface profile along line drawn in surface map*

6.4   Doppler laser vibrometry

To characterize the vibrational properties of the suspended graphene structures, the Laser Doppler Vibrometer (LDV) setup described in Chapter 5: was used. Figure 5-8 is repeated in Figure 6-9a for easy reference, the setup details can be found in subsection 5.5.1. The LDV operates by generating a polarized laser beam using a HeNe laser source in the sensor head which is split into a measurement beam and a reference beam by a polarizing beam splitter, labelled BS1 in Figure 6-9 The reference beam is made to pass through a Bragg cell that

shifts its frequency by ω_{Bragg}, while the measurement beam travels through a polarizing beam splitter, BS2, and an objective lens and reflects off the vibrating structure to be analysed. The reflected beam with its frequency modulated by the Doppler effect due to the vibrating structure travels back through the objective lens and is deflected at BS2 to the polarizing beam splitter BS3, where it is recombined with the reference beam to form a superposed Doppler wave. This modulated heterodyne signal is detected by a photodetector and subsequently analysed to yield the vibrational properties of the vibrating structure. Vibrometry measurements provide real time data and frequency spectra from which the resonance frequencies and mode shapes of the vibrating structure can be obtained.
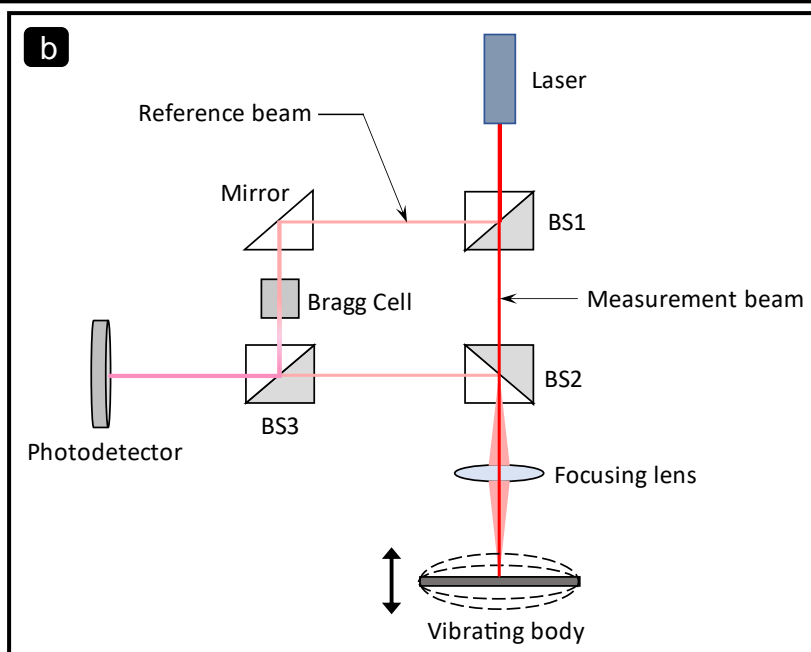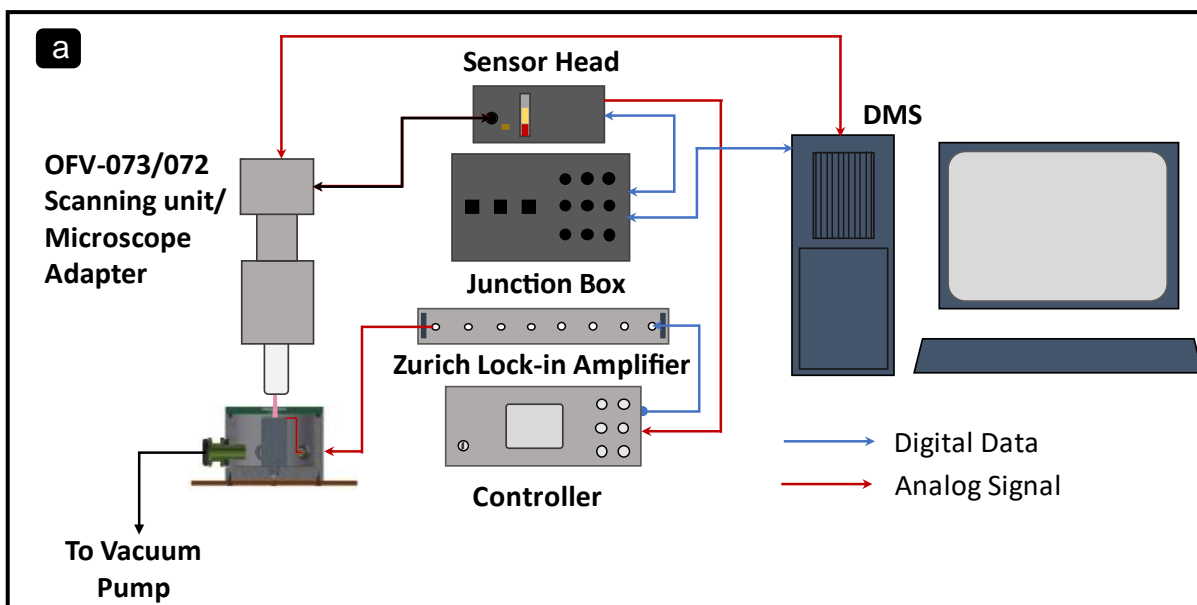
*Figure 6-9: **a)** LDV custom setup **b)** LDV's measurement principle.*

6.4.1 Equipment setup validation

The LDV setup was validated by modal testing a resonator with a known fundamental frequency. A silicon cantilever with a rectangular mass at its end and dimensions as shown in Figure 6-10 was used. It was first modelled in ANSYS Mechanical APDL to find its modal frequencies. The first five frequencies for the cantilever are given in the second column of Table 6-1.

Mode Number	Frequency (kHz)	Frequency 2 (kHz)
1	18.770	18.469
2	24.655	24.253
3	95.650	93.677
4	226.63	222.84
5	233.02	228.77

Table 6-1: Natural frequencies for silicon cantilever structure

To get the frequency response plot, a harmonic analysis was additionally run, an arbitrary force of 100 N was used for the analysis. The material properties of silicon were taken as follows, density 2329 kg/m^3, Young's modulus 169 MPa, Poisson's ratio 0.29. The variational frequency sweep harmonic analysis option in ANSYS was used for the frequency range 18 kHz to 19 kHz. The frequency response plot from the analysis is presented in Figure 6-10c.
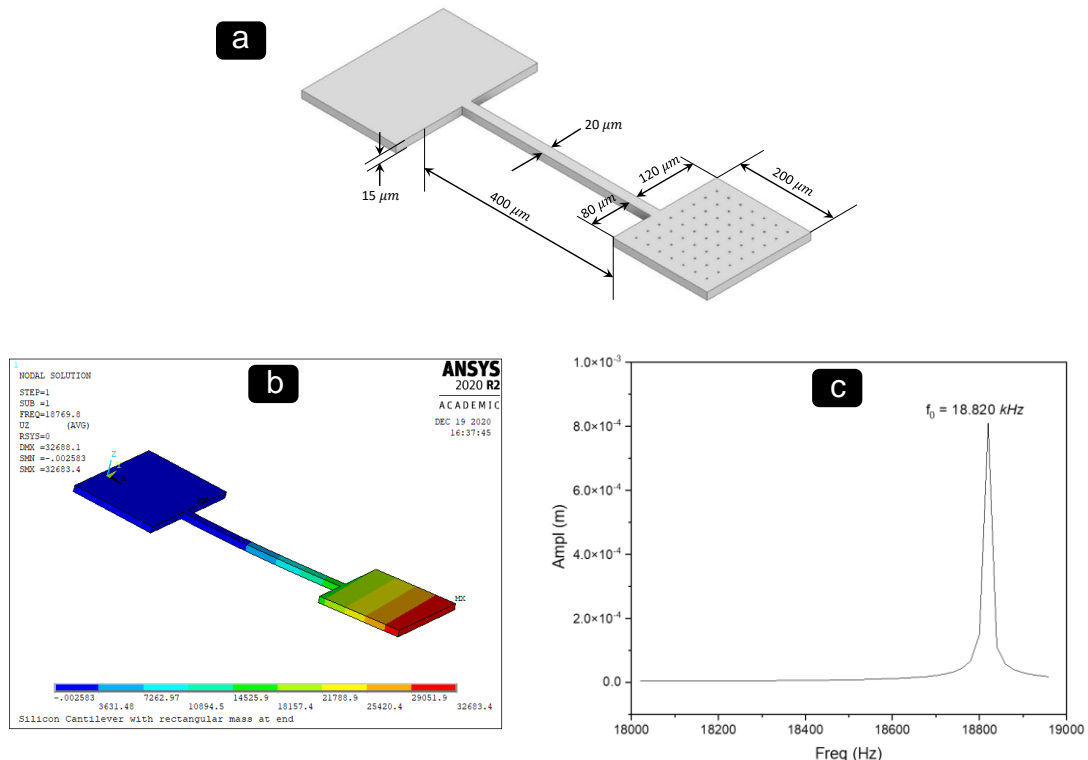
Figure 6-10: ***a)*** *Silicon cantilever with end rectangular mass* ***b)*** *Mode shape for f$_0$ = 18.77 kHz* ***c)*** *Frequency response plot from FEA harmonic analysis*

The die with the silicon resonator was glued to the piezoelectric disc and connected with the setup for the low frequency LDV as described in Chapter 5:. The Zurich Lock-in amplifier receives the signal from the vibrometer controller and processes it to provide frequency plots of the signal. A frequency sweep from 10 kHz to 100 kHz was done. Figure 6-11 shows the frequency plot for the sweep, showing the fundamental frequency of the silicon cantilever at 18.47 kHz and the third mode frequency at 85.04 kHz. The second resonant mode is an in-plane mode, therefore it does not feature in the frequency plot since the vibrometer only measures out-of-plane vibration. The experimental frequencies are slightly lower than those from the ANSYS FEA results. This could be due to added mass on the cantilever; some residue can be seen on the cantilever in the scan image (Figure 6-11a) and could be source of the added mass on the cantilever. To model this, minute increments were made to the dimensions of the rectangular mass at the end of the cantilever model and the modal analysis rerun; the new results are presented in the third column of Table 6-1. With the new values, the experimental fundamental frequency is in agreement with the FEA results; since the other resonance modes are harmonics of the fundamental frequency, their frequencies do not quickly converge to the experimental values. However, validation of the vibrometer setup was still considered successful and validated for measurements on the graphene devices.
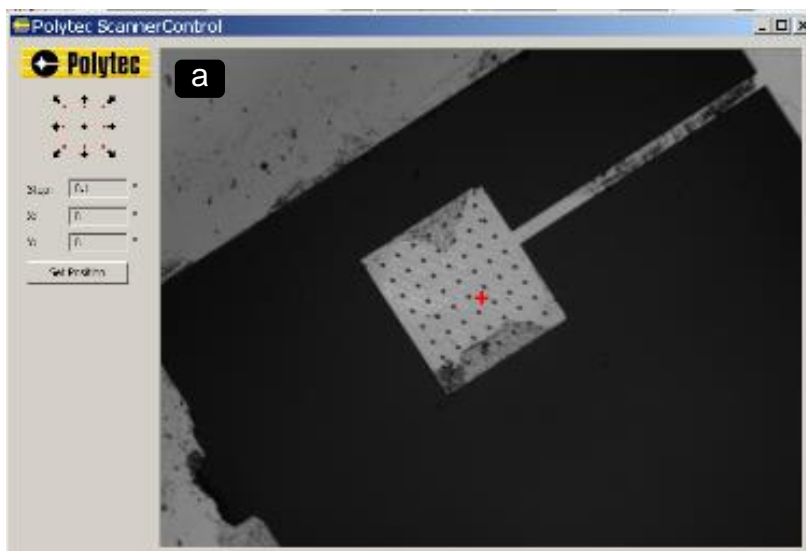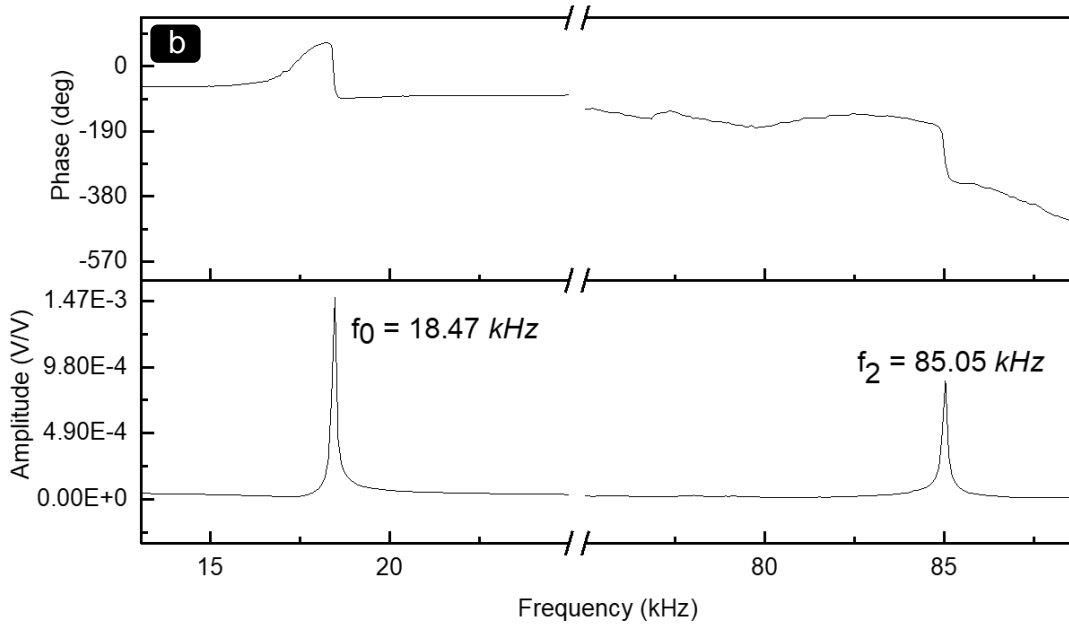
*Figure 6-11: **a)** Scan point on cantilever **b)** Frequency plot of cantilever response to 10 to 100 kHz sweep drive voltage.*

6.4.2 Modal testing of graphene bridges

The sensor platforms with the graphene composite bridges were glued to the piezoelectric disc as was done with the silicon resonator. Frequency sweeps were made from 100 kHz to 1 MHz to determine the fundamental frequency of the bridges in line with the estimated fundamental frequency determined numerically. The response plots are shown in Figure 6-12. It was not possible to measure the frequency parameters for the bridges, as can be seen in the frequency plots, the measurements made on the composite bridges had a lot of background interference from the resonances of the piezo support structure and showed the same form as measurements made directly on the support structure. The unsuccessful attempt to measure the vibrational response of the bridges is suspected to be due to the stress stiffening of the bridges induced by the very large deflection of the structure during the microfabrication process. Additionally, the problems with reflection of the structures as demonstrated during the surface profile measurements were same with the vibrometry measurements and resulted in very low signal strength and signal to noise ratios. The small target area was another causal factor in the unsuccessful measurement process. Having designed bigger sized resonators after the unsuccessful modal testing with the 3 μm structures, hardware problems with the LDV, specifically the laser focusing unit, did not allow for the measurement laser beam to be focused on the

155

resonators. Resonators with large target areas, e.g. the silicon cantilever, easily deal with this problem. Low drive voltage may have also been an issue in the measurement due to the impedance properties of the piezoelectric actuator. A high-frequency, high-voltage amplifier will be needed to achieve amplification at the frequencies required for the modal analysis.
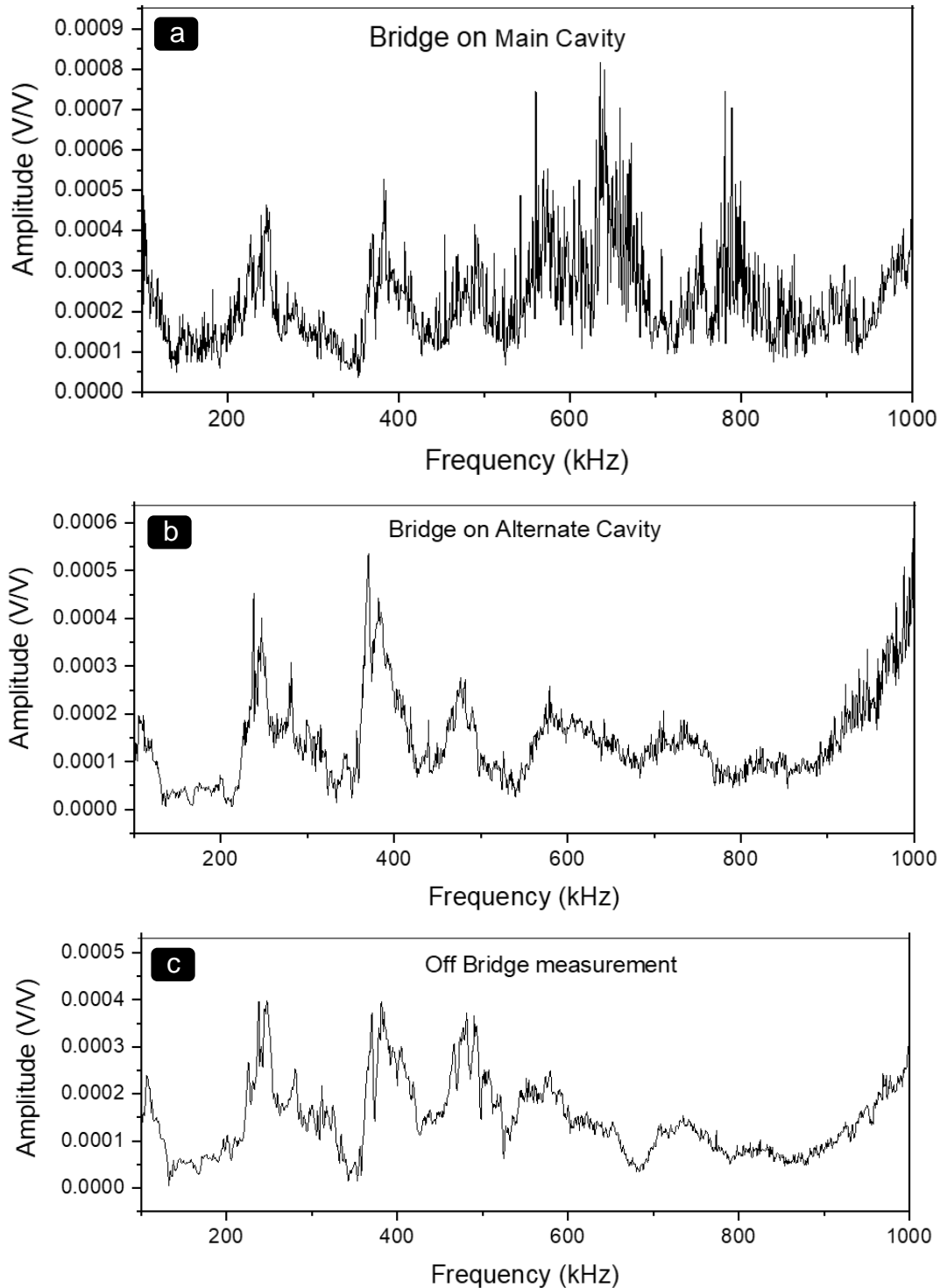
*Figure 6-12: Frequency plots for Ti/Au/Ti/Gr **a)** bridge on main cavity **b)** bridge on alternate cavity **c)** completely of the bridge*

6.5   Conclusion

The graphene bridges microfabricated in Chapter 5 were characterized in this chapter. First, the Raman spectra for suspended SLG and BLG were presented. The spectra did verify the material to be graphene, with the characteristic G and 2D bands. The G band peak for SLG was at 1587.53 cm^{-1} and the peak for 2D was at 2680.25 cm^{-1}. Even though the 2D band was fit with a single Lorentzian, its FWHM was almost twice that reported in the literature. The presence of defects in the crystal structure of the graphene was noted with the presence of the D band. In addition, an unusually large I(G)/I(2D) ratio of 1.3 may also be an indication of the presence of charged impurities in the graphene structures. The spectra for BLG were deviant from what has been reported in literature, with the spectra looking more like the spectra for SLG than for BLG. The 2D band which famously fits four Lorentzians due to the evolution of its electronic band and is the major fingerprint for identifying BLG sheets, fitted only two Lorentzians. This was thought to be due to the stacking achieved during the production and transfer of the sheets to the substrates. Next, surface profiling of the graphene structures was presented and discussed. With graphene being transparent, surface profiling with a Zygo surface profiler using white light interferometry was not possible. Thin layers of gold were deposited on the graphene to enable them to be profiled. High metal deposition rates resulted in rupturing of the suspended structures, hence the use of low metal deposition rates. The surface profiling of bridges microfabricated using lithographic processes revealed very large deformations, up to 1.85 μm for a composite bridge of thickness $\sim 75\ nm$. These large deformations were suspected to be one of the reasons the vibrational response of the bridges could not be measured in a modal test. Frequency peaks were expected at about 0.79 MHz and 0.43 MHz, but were not seen.

Chapter 7: Conclusion and future work

7.1   Introduction

This work set out to develop graphene resonators capable of ultra-sensitive mass detection. This chapter summarizes the work done as presented in this thesis.

7.2   General discussions

Graphene sheets have been shown to offer great advantages as mechanical resonators. However, production of high quality sheets, handling, achieving suspended structures, microfabrication, etc. have remained challenging. Several advancements have been made in many of these areas, one of which is the commercial production of high quality graphene. The design, fabrication and analysis of graphene resonators was carried out over the course of this study. Several works have been done on the vibration analysis of graphene sheets. This was explored extensively in Chapter 3. The vibration of graphene sheets has been modelled using atomistic modelling and continuum mechanics techniques. Atomistic modelling techniques yield very accurate results but are limited to nanosized graphene sheets because they are computationally expensive. Emphasis is therefore laid on the use of continuum mechanics. However, when established local continuum models are applied to nano- and micro-sized sheets, they yield inaccurate results. To deal with this, a small-scale parameter, e_0a, is incorporated in the local equations to account for the size of the sheets. The importance of e_0a in the modelling of nanosheets is well documented and published, and only implied for micro-sized sheets. Typical values of e_0a range between 0 and 2. This work establishes the importance of e_0a for micro-sized sheets. But unique to micro-sized sheets is the fact that the specific value of e_0a has no effect on the model but must be included to scale down the overestimated frequencies.

Chapters 5 and 6 present the design, fabrication and characterization of bilayer graphene resonators. Sensor platforms which act as substrates for the transfer of graphene were designed and fabricated using photolithography. Four types of platforms were made based on cavity sizes. The choice of cavity sizes was made based on the intended optical calibration of the resonators. Previous smaller sized resonators could not be calibrated due to the limit in focusing the laser measurement beam of the equipment. Graphene transfer to the substrates were

done commercially by Graphenea, Spain. Bilayer suspended graphene sheets were mostly achieved on 16 μm by 6 μm cavities but could not be achieved on the bigger 32 μm by 9 μm cavities. Focused ion beam microfabrication was found to be the best option for microfabricating the suspended structures. 3 μm by 0.5 μm bridges and similar sized trampolines were microfabricated with FIB. Due to inaccessibility to FIB facilities, ebeam and UV lithography were resorted to. 16 μm by 3.5 μm composite bridges (with Ti/Au) were achieved with UV lithography. The lithography process involved masking graphene with Ti/Au; the deposition of hot metal caused the graphene membrane to warp with deflections that were > 2000% of its thickness.

The Raman spectra of the suspended structures featured the characteristic G and 2D peaks of graphene. However, the presence of crystal defects was noted (by the occurrence of D peak), the BLG were turbostratic in nature meaning they were not AB stacked as graphite, thereby having a single Lorentzian 2D peak fit. Also, the unusually high I(G)/I(2D) ratio was an indication of the presence of charge impurities in both SLG and BLG. The effects of these impurities on the quality and integrity on graphene as an ultra-sensitive mass resonator will need to be investigated.

It must be mentioned in concluding this writing, that several challenges were faced during the course of this work which severely hampered progress and resulted in the little that has been achieved and reported in this work. From the mighty COVID-19 which was bigger than anyone could mitigate against when it first happened, to technical difficulties in achieving suspended graphene, problems with equipment, availability of equipment, etc. As is highlighted in the recommendations for future work, a lot is still left to be done in this area.

7.3   Conclusion

The design, fabrication, calibration, and analysis of rectangular graphene resonators were attempted in this work. A laid down process for achieving rectangular graphene resonators up to 22 μm was established. In addition, this work has shown that for analytical vibration analysis of micro-sized graphene resonators, the small-scale parameter $e_0 a$ must be incorporated into the local equations to achieve more accurate results. The value of $e_0 a$ chosen is not significant for micro-sized sheets but should be $0 < e_0 a \leq 2$.

7.4   Future work

The achievement of an ultra-sensitive mass sensor requires several stages of multi-field research, design, analysis, and development. Extensive work still needs to be done in addition to what has been done here. These are outlined as follows

1. Extensive modal testing of different sized rectangular graphene structures needs to be carried out to provide adequate experimental data for the validation of analytical and FEA models.

2. The effects of metal deposition at various rates and temperatures on the mechanical and physical properties of graphene membranes need to be explored and documented. With the market share value of graphene growing exponentially as well as its popularity among product designers and manufacturers, processes that affect the material properties and behaviour of graphene need to be well understood.

3. Smart device designs need to be developed to allow for graphene resonators to be driven in micro fluids, since most biological testing is done liquid.

4. Magnetomotive and capacitive driving is recommended and improved designs of both setups are needed.

5. Design of circuitry to process the electrical signals from the resonators and provide user ready results via portable displays.

6. Biofunctionalization protocols for the resonators will need to be established for various biological target molecules and the measurement performance and sensitivity of the mass sensor evaluated.

References

1. S. Wagner, C. Weisenstein, A. D. Smith, M. Östling, S. Kataria and M. C. Lemme, Microelectronic Engineering 159, 108 (2016)

2. L. Syedmoradi, M. Daneshpour, M. Alvandipour, F. A. Gomez, H. Hajghassem and K. Omidfar, Biosensors and Bioelectronics 87, 373 (2017)

3. D. R. Thévenot, K. Toth, R. A. Durst and G. S. Wilson, Biosensors and Bioelectronics 16 (1–2), 121 (2001)

4. S. Balaji and T. Steve, Journal of Laboratory Automation 20 (4), 365 (2015)

5. G. Wu, R. H. Datar, K. M. Hansen, T. Thundat, R. J. Cote and A. Majumdar, Nat Biotech 19 (9), 856 (2001)

6. K. S. Hwang, J. H. Lee, J. Park, D. S. Yoon, J. H. Park and T. S. Kim, Lab on a Chip 4 (6), 547 (2004)

7. G. Zheng, F. Patolsky, Y. Cui, W. U. Wang and C. M. Lieber, Nat Biotechnol 23 (10), 1294 (2005)

8. G. Lai, L. Wang, J. Wu, H. Ju and F. Yan, Analytica Chimica Acta 721, 1 (2012)

9. J. X. Wang, X. W. Sun, A. Wei, Y. Lei, X. P. Cai, C. M. Li and Z. L. Dong, Applied Physics Letters 88 (23), 233106 (2006)

10. X.-L. Luo, J.-J. Xu, Y. Du and H.-Y. Chen, Analytical Biochemistry 334 (2), 284 (2004)

11. X. Wang, Y. Li, H. Wang, Q. Fu, J. Peng, Y. Wang, J. Du, Y. Zhou and L. Zhan, Biosensors and Bioelectronics 26 (2), 404 (2010)

12. D. Tang, R. Yuan, Y. Chai, Y. Fu, J. Dai, Y. Liu and X. Zhong, Biosensors and Bioelectronics 21 (4), 539 (2005)

13. R. F. Dutra and L. T. Kubota, Clinica Chimica Acta 376 (1–2), 114 (2007)

14. W. U. Dittmer, T. H. Evers, W. M. Hardeman, W. Huijnen, R. Kamps, P. de Kievit, J. H. M. Neijzen, J. H. Nieuwenhuis, M. J. J. Sijbers, D. W. C. Dekkers, M. H. Hefti and M. F. W. C. Martens, Clinica Chimica Acta 411 (11–12), 868 (2010)

15. J. L. Arlett, E. B. Myers and M. L. Roukes, Nat Nano 6 (4), 203 (2011)

16. K. S. Novoselov, A. K. Geim, S. V. Morozov, D. Jiang, Y. Zhang, S. V. Dubonos, I. V. Grigorieva and A. A. Firsov, Science 306 (5696), 666 (2004)

17. X. Du, I. Skachko, A. Barker and E. Y. Andrei, Nat Nanotechnol 3 (8), 491 (2008)

18. S. V. Morozov, K. S. Novoselov, M. I. Katsnelson, F. Schedin, D. C. Elias, J. A. Jaszczak and A. K. Geim, Physical Review Letters 100 (1), 016602 (2008)

19. J. Sabio, C. Seoánez, S. Fratini, F. Guinea, A. H. C. Neto and F. Sols, Physical Review B 77 (19), 195409 (2008)

20. K. S. Kim, Y. Zhao, H. Jang, S. Y. Lee, J. M. Kim, K. S. Kim, J.-H. Ahn, P. Kim, J.-Y. Choi and B. H. Hong, Nature 457 (7230), 706 (2009)

21. A. Reina, X. Jia, J. Ho, D. Nezich, H. Son, V. Bulovic, M. S. Dresselhaus and J. Kong, Nano letters 9 (1), 30 (2008)

22. S. Park and R. S. Ruoff, Nat Nano 4 (4), 217 (2009)

23. T. Seyller, A. Bostwick, K. V. Emtsev, K. Horn, L. Ley, J. L. McChesney, T. Ohta, J. D. Riley, E. Rotenberg and F. Speck, Physica Status Solidi (b) 245 (7), 1436 (2008)

24. L. Zhi and K. Mullen, Journal of Materials Chemistry 18 (13), 1472 (2008)

25. L. Peng, Y. Zheng and C. Tianhong, Applied Physics Letters 101 (9), 093111 (2012)

26. Y. Ohno, K. Maehashi, Y. Yamashiro and K. Matsumoto, Nano Letters 9 (9), 3318 (2009)

27. L. Peng and C. Tianhong, Journal of Micromechanics and Microengineering 25 (7), 075022 (2015)

28. A.-S. Juan, M. Tengfei and B. Marc, Applied Physics Letters 106 (8), 083103 (2015)

29. Y. Zhang, Y.-W. Tan, H. L. Stormer and P. Kim, Nature 438 (7065), 201 (2005)

30. M. G. Chung, D. H. Kim, H. M. Lee, T. Kim, J. H. Choi, D. k. Seo, J.-B. Yoo, S.-H. Hong, T. J. Kang and Y. H. Kim, Sensors and Actuators B: Chemical 166–167, 172 (2012)

31. L. Ganhua, E. O. Leonidas and C. Junhong, Nanotechnology 20 (44), 445502 (2009)

32. G. Ko, H. Y. Kim, J. Ahn, Y. M. Park, K. Y. Lee and J. Kim, Current Applied Physics 10 (4), 1002 (2010)

33. F. Schedin, A. K. Geim, S. V. Morozov, E. W. Hill, P. Blake, M. I. Katsnelson and K. S. Novoselov, Nat Mater 6 (9), 652 (2007)

34. H. J. Yoon, D. H. Jun, J. H. Yang, Z. Zhou, S. S. Yang and M. M.-C. Cheng, Sensors and Actuators B: Chemical 157 (1), 310 (2011)

35. M. Chen, C. Hou, D. Huo, H. Fa, Y. Zhao and C. Shen, Sensors and Actuators, B: Chemical 239, 421 (2017)

36. J. Kim, S. Y. Park, S. Kim, D. H. Lee, J. H. Kim, J. M. Kim, H. Kang, J. S. Han, J. W. Park, H. Lee and S. H. Choi, Scientific reports 6, 31984 (2016)

37. B. Liu, S. Salgado, V. Maheshwari and J. Liu, Current Opinion in Colloid and Interface Science 26, 41 (2016)

38. G. F. Schneider, S. W. Kowalczyk, V. E. Calado, G. Pandraud, H. W. Zandbergen, L. M. Vandersypen and C. Dekker, Nano Lett 10 (8), 3163 (2010)

39. S. L. Burrs, M. Bhargava, R. Sidhu, J. Kiernan-Lewis, C. Gomes, J. C. Claussen and E. S. McLamore, Biosensors and Bioelectronics 85, 479 (2016)

40. S. M. Cruz, A. F. Girao, G. Goncalves and P. A. Marques, Sensors (Basel, Switzerland) 16 (1), (2016)

41. Y. Huang, X. Dong, Y. Shi, C. M. Li, L. J. Li and P. Chen, Nanoscale 2 (8), 1485 (2010)

42. B. Zhang, Q. Li and T. Cui, Biosensors and Bioelectronics 31 (1), 105 (2012)

43. L. Zhou, H. Mao, C. Wu, L. Tang, Z. Wu, H. Sun, H. Zhang, H. Zhou, C. Jia, Q. Jin, X. Chen and J. Zhao, Biosensors & bioelectronics 87, 701 (2016)

44. M. Trojanowicz, Main Concepts of Chemical and Biological Sensing. In *Combinatorial Methods for Chemical and Biological Sensors*, Springer, (2009), pp 25

45. H. Nakamura and I. Karube, Analytical and Bioanalytical Chemistry 377 (3), 446 (2003)

46. R. F. Taylor and J. S. Schultz, *Handbook of chemical and biological sensors*. CRC Press, (1996),

47. M. Yemini, Y. Levi, E. Yagil and J. Rishpon, Bioelectrochemistry 70 (1), 180 (2007)

48. Y. Wang, Q. Chen and X. Zeng, Biosensors and Bioelectronics 25 (6), 1356 (2010)

49. W. Sant, M. L. Pourciel-Gouzy, J. Launay, T. Do Conto, R. Colin, A. Martinez and P. Temple-Boyer, Sensors and Actuators B: Chemical 103 (1–2), 260 (2004)

50. J.-G. Guan, Y.-Q. Miao and Q.-J. Zhang, Journal of Bioscience and Bioengineering 97 (4), 219 (2004)

51. M. Piliarik, H. Vaisocherová and J. Homola, Biosensors and Biodetection, 65 (2009)

52. V. Nanduri, S. Balasubramanian, S. Sista, V. J. Vodyanoy and A. L. Simonian, Analytica Chimica Acta 589 (2), 166 (2007)

53. M. L. Antonelli, C. Spadaro and R. F. Tornelli, Talanta 74 (5), 1450 (2008)

54. M. L. Antonelli, G. D'Ascenzo, A. Laganà and P. Pusceddu, Talanta 58 (5), 961 (2002)

55. A. Janshoff, H.-J. Galla and C. Steinem, Angewandte Chemie International Edition 39 (22), 4004 (2000)

56. M. C. Dixon, J Biomol Tech 19 (3), 151 (2008)

57. R.-Z. Hao, H.-B. Song, G.-M. Zuo, R.-F. Yang, H.-P. Wei, D.-B. Wang, Z.-Q. Cui, Z. Zhang, Z.-X. Cheng and X.-E. Zhang, Biosensors and Bioelectronics 26 (8), 3398 (2011)

58. J. Cai, C. Yao, J. Xia, J. Wang, M. Chen, J. Huang, K. Chang, C. Liu, H. Pan and W. Fu, Sensors and Actuators B: Chemical 155 (2), 500 (2011)

59. Q. Chen, W. Tang, D. Wang, X. Wu, N. Li and F. Liu, Biosensors and Bioelectronics 26 (2), 575 (2010)

60. C. Yao, Y. Qi, Y. Zhao, Y. Xiang, Q. Chen and W. Fu, Biosensors and Bioelectronics 24 (8), 2499 (2009)

61. K. Länge, B. E. Rapp and M. Rapp, Analytical and Bioanalytical Chemistry 391 (5), 1509 (2008)

62. D. S. Ballantine Jr, R. M. White, S. J. Martin, A. J. Ricco, E. T. Zellers, G. C. Frye and H. Wohltjen, *Acoustic wave sensors: theory, design and physico-chemical applications*. Academic press, (1996),

63. M. Berger, A. Welle, E. Gottwald, M. Rapp and K. Länge, Biosensors and Bioelectronics 26 (4), 1706 (2010)

64. D. H. Dinh, É. Pascal, L. Vellutini, B. Bennetau, D. Rebière, C. Dejous, D. Moynet, C. Belin and J.-P. Pillot, Sensors and Actuators B: Chemical 146 (1), 289 (2010)

65. S. Rupp, M. von Schickfus, S. Hunklinger, H. Eipel, A. Priebe, D. Enders and A. Pucci, Sensors and Actuators B: Chemical 134 (1), 225 (2008)

66. R. Dahint, M. Grunze, F. Josse and J. Renken, Analytical Chemistry 66 (18), 2888 (1994)

67. V. Ferrari and R. Lucklum, Overview of Acoustic-Wave Microsensors. In *Piezoelectric Transducers and Applications*, Arnau Vives, A., Ed., Springer Berlin Heidelberg, Berlin, Heidelberg, (2004), pp 39

68. I. Y. Huang, M. C. Lee, C. H. Hsu and C. C. Wang, Sensors and Actuators B: Chemical 162 (1), 184 (2012)

69. J. C. Pyun, H. Beutel, J. U. Meyer and H. H. Ruf, Biosensors and Bioelectronics 13 (7–8), 839 (1998)

70. K. L. Ekinci and M. L. Roukes, Review of Scientific Instruments 76 (6), 061101 (2005)

71. JensenK, K. Kim and ZettlA, Nat Nano 3 (9), 533 (2008)

72. H.-Y. Chiu, P. Hung, H. W. C. Postma and M. Bockrath, Nano Letters 8 (12), 4342 (2008)

73. B. Ilic, H. G. Craighead, S. Krylov, W. Senaratne, C. Ober and P. Neuzil, Journal of Applied Physics 95 (7), 3694 (2004)

74. ChasteJ, EichlerA, MoserJ, CeballosG, RuraliR and BachtoldA, Nat Nano 7 (5), 301 (2012)

75. Y. T. Yang, C. Callegari, X. L. Feng, K. L. Ekinci and M. L. Roukes, Nano Letters 6 (4), 583 (2006)

76. T. P. Burg, M. Godin, S. M. Knudsen, W. Shen, G. Carlson, J. S. Foster, K. Babcock and S. R. Manalis, Nature 446 (7139), 1066 (2007)

77. K. S. Novoselov, D. Jiang, F. Schedin, T. J. Booth, V. V. Khotkevich, S. V. Morozov and A. K. Geim, Proceedings of the National Academy of Sciences of the United States of America 102 (30), 10451 (2005)

78. A. K. Geim and K. S. Novoselov, Nat Mater 6 (3), 183 (2007)

79. D. Gray, A. McCaughan and B. Mookerji, Physics for solid state applications. WVU, Boston, (2009)

80. A. H. Castro Neto, F. Guinea, N. M. R. Peres, K. S. Novoselov and A. K. Geim, Reviews of Modern Physics 81 (1), 109 (2009)

81. L. M. Malard, M. A. Pimenta, G. Dresselhaus and M. S. Dresselhaus, Physics Reports 473 (5–6), 51 (2009)

82. J. S. Bunch, A. M. van der Zande, S. S. Verbridge, I. W. Frank, D. M. Tanenbaum, J. M. Parpia, H. G. Craighead and P. L. McEuen, Science 315 (5811), 490 (2007)

83. C. Lee, X. Wei, Q. Li, R. Carpick, J. W. Kysar and J. Hone, physica status solidi (b) 246 (11-12), 2562 (2009)

84. R. R. Nair, P. Blake, A. N. Grigorenko, K. S. Novoselov, T. J. Booth, T. Stauber, N. M. R. Peres and A. K. Geim, Science 320 (5881), 1308 (2008)

85. O. L. Blakslee, D. G. Proctor, E. J. Seldin, G. B. Spence and T. Weng, Journal of Applied Physics 41 (8), 3373 (1970)

86. C. Lee, X. Wei, J. W. Kysar and J. Hone, Science 321 (5887), 385 (2008)

87. V. Singh, D. Joung, L. Zhai, S. Das, S. I. Khondaker and S. Seal, Progress in Materials Science 56 (8), 1178 (2011)

88. K. I. Bolotin, K. J. Sikes, Z. Jiang, M. Klima, G. Fudenberg, J. Hone, P. Kim and H. L. Stormer, Solid State Communications 146 (9–10), 351 (2008)

89. A. A. Balandin, S. Ghosh, W. Bao, I. Calizo, D. Teweldebrhan, F. Miao and C. N. Lau, Nano Letters 8 (3), 902 (2008)

90. P. Blake, E. W. Hill, A. H. C. Neto, K. S. Novoselov, D. Jiang, R. Yang, T. J. Booth and A. K. Geim, Applied Physics Letters 91 (6), 063124 (2007)

91. S. Swapp, Scanning Electron Microscopy (SEM). (2017), Vol. 2018,

92. S. Chatterjee, S. S. Gadad and T. K. Kundu, Reson 15 (7), 622 (2010)

93. E. Meyer, Progress in Surface Science 41 (1), 3 (1992)

94. U. K. Sur, Reson 15 (2), 154 (2010)

95. T. M. G. Mohiuddin, A. Lombardo, R. R. Nair, A. Bonetti, G. Savini, R. Jalil, N. Bonini, D. M. Basko, C. Galiotis, N. Marzari, K. S. Novoselov, A. K. Geim and A. C. Ferrari, Physical Review B 79 (20), 205433 (2009)

96. R. S. Deacon, K. C. Chuang, R. J. Nicholas, K. S. Novoselov and A. K. Geim, Physical Review B 76 (8), 081406 (2007)

97. M. Orlita, C. Faugeras, G. Martinez, D. K. Maude, M. L. Sadowski, J. M. Schneider and M. Potemski, Journal of Physics: Condensed Matter 20 (45), 454223 (2008)

98. A. C. Ferrari, J. C. Meyer, V. Scardaci, C. Casiraghi, M. Lazzeri, F. Mauri, S. Piscanec, D. Jiang, K. S. Novoselov, S. Roth and A. K. Geim, Phys Rev Lett 97 (18), 187401 (2006)

99. M. S. Dresselhaus, G. Dresselhaus, R. Saito and A. Jorio, Physics Reports 409 (2), 47 (2005)

100. A. Das, B. Chakraborty and A. K. Sood, Bulletin of Materials Science 31 (3), 579 (2008)

101. J. S. Park, A. Reina, R. Saito, J. Kong, G. Dresselhaus and M. S. Dresselhaus, Carbon 47 (5), 1303 (2009)

102. C. Mattevi, H. Kim and M. Chhowalla, Journal of Materials Chemistry 21 (10), 3324 (2011)

103. Y. Wang, Y. Zheng, X. Xu, E. Dubuisson, Q. Bao, J. Lu and K. P. Loh, ACS Nano 5 (12), 9927 (2011)

104. P. Gupta, P. D. Dongare, S. Grover, S. Dubey, H. Mamgain, A. Bhattacharya and M. M. Deshmukh, Scientific reports 4, 3882 (2014)

105. T. Hallam, C. F. Moldovan, K. Gajewski, A. M. Ionescu and G. S. Duesberg, physica status solidi (b) 252 (11), 2429 (2015)

106. C. A. Volkert and A. M. Minor, MRS bulletin 32 (05), 389 (2007)

107.   J. Gierak, A. Madouri, A. L. Biance, E. Bourhis, G. Patriarche, C. Ulysse, D. Lucot, X. Lafosse, L. Auvray, L. Bruchhaus and R. Jede, Microelectronic Engineering 84 (5–8), 779 (2007)

108.   F. Molitor, J. Güttinger, C. Stampfer, D. Graf, T. Ihn and K. Ensslin, Physical Review B 76 (24), 245426 (2007)

109.   M. Y. Han, B. Özyilmaz, Y. Zhang and P. Kim, Physical Review Letters 98 (20), 206805 (2007)

110.   J. Güttinger, F. Molitor, C. Stampfer, S. Schnez, A. Jacobsen, S. Dröscher, T. Ihn and K. Ensslin, Reports on Progress in Physics 75 (12), 126502 (2012)

111.   A. V. Krasheninnikov and K. Nordlund, Journal of Applied Physics 107 (7), 071301 (2010)

112.   W. S. Lim, Y. Y. Kim, H. Kim, S. Jang, N. Kwon, B. J. Park, J.-H. Ahn, I. Chung, B. H. Hong and G. Y. Yeom, Carbon 50 (2), 429 (2012)

113.   P. S. Spinney, D. G. Howitt, S. D. Collins and R. L. Smith, Nanotechnology 20 (46), 465301 (2009)

114.   L. Tapaszto, G. Dobrik, P. Lambin and L. P. Biro, Nat Nano 3 (7), 397 (2008)

115.   , (!!! INVALID CITATION !!!)

116.   B. Arash and Q. Wang, Journal of Nanotechnology in Engineering and Medicine 2 (1), (2011)

117.   Y. Zhang, L. W. Zhang, K. M. Liew and J. L. Yu, Composite Structures 144, 86 (2016)

118.   W. L. Jorgensen, J. D. Madura and C. J. Swenson, Journal of the American Chemical Society 106 (22), 6638 (1984)

119.   L. G. Dunfield, A. W. Burgess and H. A. Scheraga, The Journal of Physical Chemistry 82 (24), 2609 (1978)

120.   N. Allinger, Calculation of molecular structure and energy by force-field methods. In *Advances in physical organic chemistry*, Elsevier, (1976), Vol. 13, pp 1

121.   N. L. Allinger, Journal of the American Chemical Society 99 (25), 8127 (1977)

122.   N. L. Allinger, K. Chen and J.-H. Lii, Journal of Computational Chemistry 17 (5-6), 642 (1996)

123.   N. L. Allinger, Y. H. Yuh and J. H. Lii, Journal of the American Chemical Society 111 (23), 8551 (1989)

124.   P. K. Weiner and P. A. Kollman, Journal of Computational Chemistry 2 (3), 287 (1981)

125.   W. L. Jorgensen and J. Tirado-Rives, Journal of the American Chemical Society 110 (6), 1657 (1988)

126.   W. D. Cornell, P. Cieplak, C. I. Bayly, I. R. Gould, K. M. Merz, D. M. Ferguson, D. C. Spellmeyer, T. Fox, J. W. Caldwell and P. A. Kollman, Journal of the American Chemical Society 117 (19), 5179 (1995)

127.   T. A. Halgren, Journal of Computational Chemistry 17 (5-6), 490 (1996)

128.   T. A. Halgren, Journal of the American Chemical Society 114 (20), 7827 (1992)

129.   A. Vedani and D. W. Huhta, Journal of the American Chemical Society 112 (12), 4759 (1990)

130.   H. Sun, The Journal of Physical Chemistry B 102 (38), 7338 (1998)

131.   S. J. Weiner, P. A. Kollman, D. A. Case, U. C. Singh, C. Ghio, G. Alagona, S. Profeta and P. Weiner, Journal of the American Chemical Society 106 (3), 765 (1984)

132.   T. Belytschko, S. P. Xiao, G. C. Schatz and R. S. Ruoff, Physical Review B 65 (23), 235430 (2002)

133.   J. Tersoff, Physical Review B 38 (14), 9902 (1988)

134.   D. W. Brenner, Physical Review B 42 (15), 9458 (1990)

135.   D. W. Brenner, Physical Review B 46 (3), 1948 (1992)

136.   S. J. Stuart, A. B. Tutein and J. A. Harrison, The Journal of Chemical Physics 112 (14), 6472 (2000)

137.   X. Xu and K. Liao, Materials Physics and Mechanics 4, 148 (2001)

138.   D. Srivastava, M. Menon and K. Cho, Physical Review Letters 83 (15), 2973 (1999)

139.   K. M. Liew, C. H. Wong, X. Q. He, M. J. Tan and S. A. Meguid, Physical Review B 69 (11), 115429 (2004)

140.   A. Sakhaee-Pour, M. Ahmadian and R. Naghdabadi, Nanotechnology 19 (8), 085702 (2008)

141.   H. Zhao, K. Min and N. R. Aluru, Nano Letters 9 (8), 3012 (2009)

142.   F. Scarpa, S. Adhikari and A. Srikantha Phani, Nanotechnology 20 (6), 065709 (2009)

143.   C. Li and T.-W. Chou, Physical Review B 73 (24), 245407 (2006)

144.   S. Thomas and K. M. Ajith, Procedia Materials Science 5, 489 (2014)

145.   F. Lin, Y. Xiang and H.-S. Shen, Composites Part B: Engineering 111, 261 (2017)

146.   R. Rafiee and R. M. Moghadam, Composites Part B: Engineering 56, 435 (2014)

147.   J. Peddieson, G. R. Buchanan and R. P. McNitt, International Journal of Engineering Science 41 (3-5), 305 (2003)

148.   C. W. Lim and L. H. He, International Journal of Mechanical Sciences 46 (11), 1715 (2004)

149.   S. Kitipornchai, X. He and K. Liew, Physical Review B 72 (7), 075443 (2005)

150.   X. He, S. Kitipornchai and K. Liew, Nanotechnology 16 (10), 2086 (2005)

151.   K. Behfar and R. Naghdabadi, Composites science and technology 65 (7-8), 1159 (2005)

152.   K. Y. Xu, X. N. Guo and C. Q. Ru, Journal of Applied Physics 99 (6), 064303 (2006)

153.   Y. M. Fu, J. W. Hong and X. Q. Wang, Journal of Sound and Vibration 296 (4), 746 (2006)

154.   X. Q. He, M. Eisenberger and K. M. Liew, Journal of Applied Physics 100 (12), 124317 (2006)

155.   K. M. Liew, X. Q. He and S. Kitipornchai, Acta Materialia 54 (16), 4229 (2006)

156.   T. Murmu and S. C. Pradhan, Journal of Applied Physics 105 (6), 064319 (2009)

157.   L. L. Ke, Y. Xiang, J. Yang and S. Kitipornchai, Computational Materials Science 47 (2), 409 (2009)

158.   S. C. Pradhan and J. K. Phadikar, Journal of Sound and Vibration 325 (1), 206 (2009)

159.   S. C. Pradhan and J. K. Phadikar, Physics Letters A 373 (11), 1062 (2009)

160.   W. H. Duan and C. M. Wang, Nanotechnology 20 (7), 075702 (2009)

161.   R. Ansari, R. Rajabiehfard and B. Arash, Computational Materials Science 49 (4), 831 (2010)

162.   J. Yang, L. L. Ke and S. Kitipornchai, Physica E: Low-dimensional Systems and Nanostructures 42 (5), 1727 (2010)

163.   L. Shen, H.-S. Shen and C.-L. Zhang, Computational Materials Science 48 (3), 680 (2010)

164.   E. Jomehzadeh and A. R. Saidi, Composite Structures 93 (2), 1015 (2011)

165. E. Jomehzadeh and A. Saidi, Computational materials science 50 (3), 1043 (2011)

166. J. R. Mianroodi, S. A. Niaki, R. Naghdabadi and M. Asghari, Nanotechnology 22 (30), 305703 (2011)

167. M. H. Mahdavi, L. Y. Jiang and X. Sun, Physica E: Low-dimensional Systems and Nanostructures 43 (10), 1813 (2011)

168. A. Farajpour, M. Mohammadi, A. R. Shahidi and M. Mahzoon, Physica E: Low-dimensional Systems and Nanostructures 43 (10), 1820 (2011)

169. S. Pradhan and A. Kumar, Composite Structures 93 (2), 774 (2011)

170. R. Ansari, B. Arash and H. Rouhi, Computational materials science 50 (11), 3091 (2011)

171. J. Wang, X. He, S. Kitipornchai and H. Zhang, Journal of Physics D: Applied Physics 44 (13), 135401 (2011)

172. E. Jomehzadeh, A. Saidi and N. Pugno, Physica E: Low-Dimensional Systems and Nanostructures 44 (10), 1973 (2012)

173. S. H. Hashemi, H. Mehrabani and A. Ahmadi-Savadkoohi, Composites Part B: Engineering 78, 377 (2015)

174. L. W. Zhang, Y. Zhang and K. M. Liew, Applied Mathematical Modelling 49, 691 (2017)

175. L. W. Zhang, Y. Zhang and K. M. Liew, Composites Part B: Engineering 118, 96 (2017)

176. Y. Zhang, K. Liew and D. Hui, Composites Part B: Engineering 145, 197 (2018)

177. L. Sekaric, J. M. Parpia, H. G. Craighead, T. Feygelson, B. H. Houston and J. E. Butler, Applied Physics Letters 81 (23), 4455 (2002)

178. K. L. Ekinci, Small 1 (8-9), 786 (2005)

179. K. L. Ekinci, Y. T. Yang and M. L. Roukes, Journal of Applied Physics 95 (5), 2682 (2004)

180. A. N. Cleland, New Journal of Physics 7, 235 (2005)

181. F. Mohd-Yasin, D. J. Nagel and C. E. Korman, Measurement Science and Technology 21 (1), 012001 (2009)

182. A. N. Cleland and M. L. Roukes, Journal of Applied Physics 92 (5), 2758 (2002)

183. N. A. Fleck, G. M. Muller, M. F. Ashby and J. W. Hutchinson, Acta Metallurgica et Materialia 42 (2), 475 (1994)

184. D. C. C. Lam, F. Yang, A. C. M. Chong, J. Wang and P. Tong, Journal of the Mechanics and Physics of Solids 51 (8), 1477 (2003)

185. J. S. Stölken and A. G. Evans, Acta Materialia 46 (14), 5109 (1998)

186. N. A. Fleck and J. W. Hutchinson, Journal of the Mechanics and Physics of Solids 49 (10), 2245 (2001)

187. J. Hutchinson and N. Fleck, Advances in applied mechanics 33, 295 (1997)

188. F. Yang, A. C. M. Chong, D. C. C. Lam and P. Tong, International Journal of Solids and Structures 39 (10), 2731 (2002)

189. A. C. Eringen, Journal of Applied Physics 54 (9), 4703 (1983)

190. N. Radić and D. Jeremić, Composites Part B: Engineering 97, 201 (2016)

191. T. Murmu and S. C. Pradhan, Computational Materials Science 46 (4), 854 (2009)

192. B. Arash and Q. Wang, Computational materials science 51 (1), 303 (2012)

193. F. Ebrahimi and M. R. Barati, Composite Structures 159, 174 (2017)

194. C. W. Lim, G. Zhang and J. N. Reddy, Journal of the Mechanics and Physics of Solids 78, 298 (2015)

195. A. K. Rappe, C. J. Casewit, K. S. Colwell, W. A. Goddard and W. M. Skiff, Journal of the American Chemical Society 114 (25), 10024 (1992)

196. G. Dresselhaus and S. Riichiro, *Physical properties of carbon nanotubes*. World scientific, (1998),

197. R. Ansari and H. Ramezannezhad, Physica E: Low-dimensional Systems and Nanostructures 43 (6), 1171 (2011)

198. R. M. Lin, Computational Materials Science 53 (1), 44 (2012)

199. P. Ribeiro and T. R. C. Chuaqui, International Journal of Mechanical Sciences 150, 727 (2019)

200. I. S. Raju, G. V. Rao and K. K. Raju, Journal of Sound and Vibration 49 (3), 415 (1976)

201. Y. Chandra, R. Chowdhury, F. Scarpa, S. Adhikari, J. Sienz, C. Arnold, T. Murmu and D. Bould, Materials Science and Engineering: B 177 (3), 303 (2012)

202. C. M. Wang, G. T. Lim, J. N. Reddy and K. H. Lee, Engineering Structures 23 (7), 838 (2001)

203. R. Ansari, S. Sahmani and B. Arash, Physics Letters A 375 (1), 53 (2010)

204.   H.-T. Thai and D.-H. Choi, Composites Part B: Engineering 43 (5), 2335 (2012)

205.   H.-T. Thai and D.-H. Choi, Composite Structures 106, 754 (2013)

206.   T. Y. Wu and G. R. Liu, Computational Mechanics 24 (3), 197 (1999)

207.   C. W. Bert and M. Malik, Applied Mechanics Reviews 49 (1), 1 (1996)

208.   C. Shu and H. Du, International Journal of Solids and Structures 34 (7), 837 (1997)

209.   F. Tornabene, F. Ubertini and E. Viola, The Generalized Differential Quadrature Method for Solving Initial-value Problems in Linear Dynamics. In *International Symposium on Recent Advances in Mechanics, Dynamical Systems and Probability Theory (MDP2007)-Palermo, Italy*, (2007), pp 3

210.   T. Y. Wu and G. R. Liu, International Journal for Numerical Methods in Engineering 50 (8), 1907 (2001)

211.   R. Bellman and J. Casti, Journal of mathematical analysis and Applications 34 (2), 235 (1971)

212.   C. W. Bert, S. K. Jang and A. G. Striz, Computational Mechanics 5 (2), 217 (1989)

213.   S. K. Jang, C. W. Bert and A. G. Striz, International Journal for Numerical Methods in Engineering 28 (3), 561 (1989)

214.   C. Shu, *Differential quadrature and its application in engineering.* Springer Science & Business Media, (2012),

215.   C. Shu, W. Chen, H. Xue and H. Du, International Journal for Numerical Methods in Engineering 51 (2), 159 (2001)

216.   A. W. Leissa, Journal of Sound and Vibration 31 (3), 257 (1973)

217.   W. J. Bottega, *Engineering vibrations.* CRC Press, (2014),

218.   K. Lee, A. P. Chandrakasan and J. Kong, IEEE Electron Device Letters 32 (4), 557 (2011)

219.   S. Debroy, S. Sivasubramani, G. Vaidya, S. G. Acharyya and A. Acharyya, Scientific reports 10 (1), 6240 (2020)

220.   AZoM, Titanium (Ti) - The Different Properties and Applications. (2013), Vol. 2020,

221.   I. W. Frank, D. M. Tanenbaum, A. M. v. d. Zande and P. L. McEuen, Journal of Vacuum Science & Technology B: Microelectronics and Nanometer Structures Processing, Measurement, and Phenomena 25 (6), 2558 (2007)

222. S. Shivaraman, R. A. Barton, X. Yu, J. Alden, L. Herman, M. V. S. Chandrashekhar, J. Park, P. L. McEuen, J. M. Parpia, H. G. Craighead and M. G. Spencer, Nano Letters 9 (9), 3100 (2009)

223. A. M. van der Zande, R. A. Barton, J. S. Alden, C. S. Ruiz-Vargas, W. S. Whitney, P. H. Pham, J. Park, J. M. Parpia, H. G. Craighead and P. L. McEuen, Nano Lett 10 (12), 4869 (2010)

224. C. Chen, S. Rosenblatt, K. I. Bolotin, W. Kalb, P. Kim, I. Kymissis, H. L. Stormer, T. F. Heinz and J. Hone, Nat Nano 4 (12), 861 (2009)

225. Y. Zhang, Z. Jiang, J. P. Small, M. S. Purewal, Y. W. Tan, M. Fazlollahi, J. D. Chudow, J. A. Jaszczak, H. L. Stormer and P. Kim, Physical Review Letters 96 (13), 136806 (2006)

226. M. O. Goerbig, Reviews of Modern Physics 83 (4), 1193 (2011)

227. M. O. Goerbig, R. Moessner and B. Douçot, Physical Review B 74 (16), 161407 (2006)

228. W. C. Tang, T.-C. H. Nguyen and R. T. Howe, Sensors and Actuators 20 (1), 25 (1989)

229. A. A. Trusov and A. M. Shkel, Journal of Micromechanics and Microengineering 17 (8), 1583 (2007)

230. M. Z. Iqbal, A. K. Singh, M. W. Iqbal, S. Seo and J. Eom, Journal of Applied Physics 111 (8), 084307 (2012)

231. Z. H. Ni, T. Yu, Z. Q. Luo, Y. Y. Wang, L. Liu, C. P. Wong, J. Miao, W. Huang and Z. X. Shen, ACS Nano 3 (3), 569 (2009)

232. P. Lespade, A. Marchand, M. Couzi and F. Cruege, Carbon 22 (4-5), 375 (1984)

233. W. Bao, F. Miao, Z. Chen, H. Zhang, W. Jang, C. Dames and C. N. Lau, Nature Nanotechnology 4 (9), 562 (2009)